BNL 51443
UC-28
UC-34d
(Particle-Accelerators and High-Voltage Machines; Physics — Particles and Fields TIC-4500)

ISABELLE

PROCEEDINGS OF THE 1981 SUMMER WORKSHOP

JULY 20 — 31, 1981

BNL--51443 Vol. 3

DE82 008395

VOLUME 3
EXPERIMENTAL AREAS
LARGE DETECTORS

BROOKHAVEN NATIONAL LABORATORY
ASSOCIATED UNIVERSITIES, INC.
UNDER CONTRACT NO DE-AC02-76CH00016 WITH THE
UNITED STATES DEPARTMENT OF ENERGY

DISCLAIMER

Printed in the United States of America
Available from
National Technical Information Service
U.S. Department of Commerce
5285 Port Royal Road
Springfield, VA 22161

NTIS price codes:
Printed Copy: A16; Microfiche Copy: A01

FOREWORD

The ISABELLE Summer Workshop, held at BNL from July 20 through July 31, was attended by 259 physicists representing 72 institutions. The discussions covered experimental areas, large detectors and detector technology, with a primary emphasis on physics opportunities, both with a phased and a full luminosity ISABELLE.

There was a consensus that physics with Phase I ($E_{cm} \approx 700$ GeV and $L \sim 2 \times 10^{31}/cm^2/sec$, with bunched beams) was feasible, important and exciting. It has been known for years that the orthodox gauge theories will be critically tested by studying the $W^{\pm}$, Z^0 and high $p_\perp$ phenomena. The Z^0 has a reasonable chance of being found at the $\bar{p}p$ colliders if luminosities reach $10^{30}/cm^2/sec$, but its properties will be difficult to decipher. Seeing the $W^{\pm}$'s or new heavy quarks is less probable and measuring their properties is even less likely. At ISABELLE these phenomena can all be studied with high precision. But the more exciting conclusion which emerged from the workshop was related to the question of what generates the ~100 GeV masses of the W's and Z's. The answer could involve Higgs, technicolor, or other particles with masses ranging from 10.8 GeV to 1 TeV, with an intermediate mass scale of 200-300 GeV being a possible region of strong interest. Some of these models predict spectacular experimental signatures. It is clear that only ISABELLE with $L \sim 10^{32} - 10^{33}$, has an opportunity of addressing and resolving such questions.

The great interest in ISABELLE physics was also evidenced by the variety of large detectors (6 to date) that have evolved - characterized by magnetic field configurations ranging from solenoid through dipole and toroid to no field at all. The ability to extract the physics was re-examined, leptons and γ's being straightforward, with greater attention being paid to analyzing jet and multijet events and defining their properties, masses, $p_\perp$, etc. Many advances were also reported in detector R&D, for example, imaging Cerenkov counters, precision drift chambers, scintillating optical fibers. Although there were many problems to be solved, such as data handling and vertex detectors, there was

more confidence and less apprehension about our ability to solve them. Experimental areas look fine except for the rerouting of some trenches and exchanging areas #10 and #12 to more easily accomodate the ep option.

The question of options was discussed at length and in quite some depth. It seems natural to augment ISABELLE with an ep capability, ep[illegible]y with a separate ring. Electron energies of 10-20 GeV with lum[illegible] of $10^{31} - 10^{32}$ look achievable and have stimulated great [illegible] The addition of a booster, Phase II, would also naturally allow f[illegible] the study of heavy ion interactions for which enthusiasm seems to be growing, especially in the light of ISR results.

In summary, the Workshop was a very upbeat, enthusiastic, and successful meeting. With the opportunities for carrying out high energy experiments being limited at present and more so in the future, the community is beginning to reaffirm even more strongly the great physics potential of ISABELLE. The consensus is to get on with the project, get it done and perform the physics. A turn-on in '86 or '87 is what is desired.

N.P. Samios
S.C.C. Ting
Co-Chairmen

INTRODUCTION

The Workshop and these proceedings were organized into five parts:

		Organizers
1.	Lectures	Ling-Lie Chau
2.	Physics	M.A.B. Beg Ling-Lie Chau V. Fitch A. Mann
3.	Experimental Areas	R. Lanou S. Aronson
4.	Large Detectors	C. Baltay H. Gordon
5.	Detector Research and Development	W. Carithers T. Ludlam

During the two weeks of the Workshop authors gave us their drafts and figures. These were put into final form by BNL typists and draftsmen. Under the extremely tight time constraints we could not guarantee that everything has come out perfectly - we did the best job we could.

The Workshop and Proceedings were truly a herculean job and could not have been accomplished without the gracious help of many people. Kit McNally and Joyce Ricciardelli coordinated the Workshop from its inception. During the Workshop, they were joined by Penny Baggett and Pat Tuttle at the conference desk. The various amenities were organized by Pat Glynn, Bill Love, Mike Schmidt, Tom Rizzo, Larry Trueman and Peter Yamin.

For the Proceedings, Ken Foley served as managing editor, organizing the entire production in less than a month. The sections were ordered and edited by Ling-Lie Chau, Bob Lanou, Sam Aronson, Tom Ludlam and Frank Paige. We had an army of hard-working typists: Donna Early, Judy Ferrero, Barbara Gaer, Rae Greenberg, Isabell Harrity, Pat Knisely, Pat Lebitski, Sharon Smith, Kathy Tuohy, Pat Valli, and Diana Votruba. Drafting the myriad of figures was skillfully accomplished by Randy Bowles, Rip Bowman, Kathy Brown, Bill Dieffenbach, Sal Morano, and Sue Norton. The enormous job of copy preparation was done by Fern Coyle, Liz Russell and Joyce Ricciardelli. None of this would have been possible without the complete support of the Technical Photography and Graphic Arts Division.

Neil Baggett deserves special mention for his incomparable efforts in making this Workshop successful.

Howard A. Gordon
Editor-in-Chief

21 August 1981

Table of Contents

VOLUME 1

VOLUME 2

SECTION II - Physics

Page No.

VOLUME 4

SECTION V - Detector Research and Development

Participants
ISABELLE Summer Workshop July 20-31, 1981

Participant's name	Institution
K. Abe	University of Pennsylvania
A. Ali	DESY
K. Amako	University of Pennsylvania
E. W. Anderson	Iowa State University
T. W. Appelquist	Yale University
S. Aronson	BNL
F. V. Ascolese	BNL
V. Ashford	BNL
M. Atac	Fermilab
M. Atiya	Columbia University
J. Babcock	Carnegie-Mellon University
T. Bacon	Imperial College
N. Baggett	BNL
P. Baggett	BNL
N. Baker	BNL
C. Baltay	Columbia University
A. J. Baltz	BNL
Z. J. Banas	BNL
Z. Bar-Yam	Southeastern Massachusetts University
A. Bassetto	University of Trento, Italy
L. Baumel	Yale University/BNL
U. Becker	Massachusetts Institute of Technology
M. A. B. Beg	Rockefeller University
E. W. Beier	University of Pennsylvania
S. Beingessner	Carleton University
O. Benary	University of Tel-Aviv
J. Bensinger	Brandeis University
D. Berley	National Science Foundation
M. Bernias	BNL
K. Black	Yale University
S. Blatt	Yale University/BNL
B. Blumenfeld	Johns Hopkins University
S. Borenstein	York College of the C.U.N.Y.
G. Bozoki	BNL
P. Braccini	INFN-Pisa/CERN
J. Branson	Massachusetts Institute of Technology
M. Bregman	Nevis Laboratory
G. Bunce	BNL
M. Capell	Massachusetts Institute of Technology
W. Carithers	Lawrence Berkeley Laboratory
L.-L. Chau	BNL
M. Chen	Massachusetts Institute of Technology

S.-P. Chen	Institute of Atomic Energy, Beijing/BNL
C.P. Cheng	Institute of High Energy Physics, Beijing
Y. Cho	Argonne National Laboratory
T. S. Chou	BNL
J.H. Christenson	New York University
S. U. Chung	BNL
P. Clarke	SUNY, Stony Brook/BNL
W. E. Cleland	University of Pittsburgh
D. Coon	University of Pittsburgh
J. W. Cooper	University of Pennsylvania
P. Coteus	Columbia University
S. Csorna	Vanderbilt University
E. D. Courant	BNL
G. T. Danby	BNL
J. F. Donoghue	University of Massachusetts
J. Dowd	Southeastern Massachusetts University
D. S. Du	Institute of High Energy Physics, Beijing
P. Duinker	NIKHEF/DESY
R. Edelstein	Carnegie-Mellon University
F. Eiseler	CUNY
J. Elias	Fermilab
R. Engelmann	BNL
A. Erwin	University of Wisconsin
G. Y. Fang	Massachusetts Institute of Technology
R. Fernow	BNL
R. Field	University of Florida
J. Fischer	BNL
K. J. Foley	BNL
S. Frankel	University of Pennsylvania
W. Frati	University of Pennsylvania
W. R. Frisken	York University
G. Gammel	BNL
G. Giacomelli	University of Bologna
B. G. Gibbard	BNL
M. Goldhaber	BNL
P. Gollon	BNL
H. Gordon	BNL
P. D. Grannis	SUNY, Stony Brook
R. Gustafson	University of Michigan
S. Hagopian	Florida State University
V. Hagopian	Florida State University
H. Hahn	BNL
C. Hargrove	National Research Council of Canada
J. C. Herrerra	BNL

J. Hettema	BNL
H. Hilke	CERN
S. Holmes	Columbia University
H.-C. Hseuh	BNL
K. Huang	Massachusetts Institue of Technology
J. W. Humphrey	BNL
V. W. Hughes	Yale University
Y. Inagaki	BNL
N. Isgur	University of Toronto
J. Jackson	BNL
K. Jaeger	BNL
D. Jensen	University of Massachusetts
H. Jensen	Fermilab
R. Johnson	BNL
S. Kabe	KEK-Japan
T. Kalogerpoulos	Syracuse University
S. Kahn	BNL
G. Kane	University of Michigan
A. Kanofsky	Lehigh University
G. Kantardjian	CERN
H. Kasha	Yale University
S. Katcoff	BNL
E. Keil	CERN
K.-Y. Keung	BNL
J. Kirz	SUNY, Stony Brook
B. Knapp	Nevis Laboratory
H. Kraner	BNL
P. Kunz	SLAC
B. P. Kwan	BNL
T. F. Kycia	BNL
R. E. Lanou	Brown University
K. W. Lai	BNL, University of Arizona
L. Lasker	BNL
W. Lee	Columbia University
Y.Y. Lee	BNL
L. B. Leipuner	BNL
K. Li	BNL
P. Limon	Fermilab
S. Lindenbaum	BNL/CCNY
L. Littenberg	BNL
R. S. Longacre	BNL
W. A. Love	BNL
D. I. Lowenstein	BNL
D. Luckey	Massachusetts Institute of Technology
T. Ludlam	BNL

D. Makowiechi	BNL
K. Manivannan	SUNY, Stony Brook
A. K. Mann	University of Pennsylvania
V. Manzella	BNL
W. Marciano	Northwestern University
J. Martin	University of Toronto
J. Marraffino	BNL/Vanderbilt University
J. Marx	Lawrence Berkeley Lab
M. Marx	SUNY, Stony Brook
G. Massaro	NIKHEF/Amsterdam
T. Matsuda	Osaka University/ MIT
D. Maurizio	BNL
M. May	BNL
R. McCarthy	SUNY, Stony Brook
K. McDonald	Princeton University
A. Melissinos	University of Rochester
A. Metz	BNL/Harvard University
T. Meussen	BNL
D. Miller	Northwestern University
T. Miyachi	INS - Tokyo
M. Month	Department of Energy
W. M. Morse	BNL
A. H. Mueller	Columbia University
M. J. Murtagh	BNL
S. Murtagh	BNL
K. Nakagawa	University of Naples
A. Nappi	University of Pisa
P. Nemethy	Lawrence Berkeley Laboratory
J. Niederer	BNL
S. Nussinov	Massachusetts Institute of Technology
T. O'Halloran	University of Illinois
J. Okamitsu	Columbia-Nevis
B. Ovryn	BNL/University of Rochester
H. Paar	Columbia University/NIKHEF
F. E. Paige	BNL
J. A. Paradiso	Massachusetts Institute of Technology
Z. Parsa	Northwestern University
E. A. Paschos	BNL/Universitat Dortmund
A. Pascolini	University of Padua
R.M. Patel	McGill University
R. Peierls	BNL
A. Pevsner	Johns Hopkins University
O. Piccioni	University of California
H. Piekarz	BNL
J. Piekarz	BNL
R. Plano	Rutgers University
E. Platner	BNL

B. Pope	Princeton University
A. Prodell	BNL
S. Protopopescu	BNL
M. Pusterla	BNL
G. Rubinowitz	BNL
S. Raby	SLAC
V. Radeka	BNL
D. Rahm	BNL
R. R. Rau	BNL
G. Reiter	BNL
T. G. Rizzo	BNL
J. Roberts	Rice University
N. Rofail	BNL
C. Roos	Vanderbilt University
J. Rosen	Northwestern University
E. Rosenberg	Iowa State University
L. Roseuson	Massachusetts Institute of Technology
J. A. Rubio	JEN-Madrid
R. Rückl	University of Munich
J. Russell	Southeastern Massachusetts University
M. Sakitt	BNL
J. Sanford	BNL
J. Sandweiss	Yale University
D. Schildknecht	University Bielefeld
M. Schmidt	Yale University
L. S. Schroeder	Lawrence Berkeley Laboratory
W. Selove	University of Pennsylvania
W. P. Sims	BNL
A. Sinha	SUNY, Stony Brook
W. Sippach	Columbia University
E. J. Siskind	BNL
J. Skelly	BNL
P. Skybic	University of Oklahoma
S.D. Smith	BNL
G. Snow	University of Maryland
J. Spiro	BNL
R. M. Sternheimer	BNL
A. Stevens	BNL
H. Sticker	Rockefeller University
R. Strand	BNL
K. Strauch	Harvard University
I. Stumer	BNL
L. Sulak	University of Michigan
S. Sumorok	University of Birmingham/CERN
Y. Suzuki	Brown University
M. Tanaka	BNL
X. W. Tang	Institute of High Energy Physics, Beijing

M. J. Tannenbaum	BNL
S. Terada	BNL
G. Theodosiou	University of Pennsylvania
D. Theriot	Fermilab
J. Thompson	University of Pittsburg
S.C.C. Ting	Massachusetts Institute of Technology
F. G. Tinta	BNL
A. Tollestrup	Fermilab
M. Tran	University of California, Los Angeles
T. L. Trueman	BNL
M. Valdata-Nappi	INFN-Pisa
G. Voss	DESY
A. Walenta	BNL
W. G. Walker	BNL
W. Wallenmeyer	Department of Energy
P. Wanderer	BNL
J. Warnock	Massachusetts Institute of Technology
W. Weisberger	SUNY, Stony Brook
D. Wheeler	BNL
D. H. White	BNL
S. White	Rockefeller University
B. Wiik	DESY
A. Wijangco	BNL
B. F. Wilczek	University of California, Santa Barbara
H. H. Williams	University of Pennsylvania
W. Willis	CERN
R. R. Wilson	Columbia University
Y. S. Wu	Institute of Theoretical Physics, Beijing/ Institute for Advanced Study
P. Xue	Beijing/MIT
T. Yamanouchi	Fermilab
P. Yamin	BNL
C. N. Yang	SUNY, Stony Brook
T. Ypsilantis	Ecole Polytechnique
J. Zingman	Yale University; BNL

SECTION III

EXPERIMENTAL AREAS

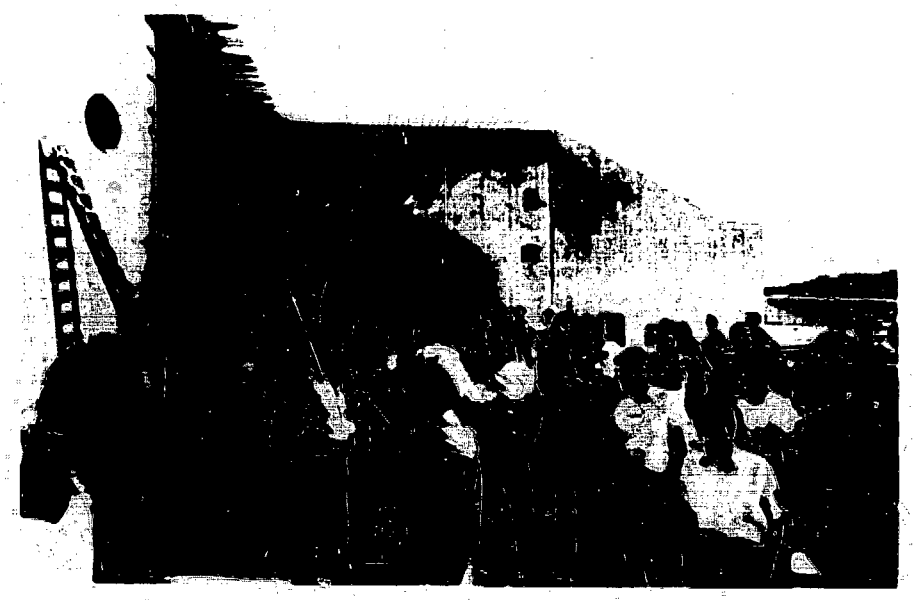

EXPERIMENTAL AREAS GROUP

S. H. Aronson, Brookhaven National Laboratory
R.E. Lanou, Brown University

INTRODUCTION AND SUMMARY

In this section we present the papers which resulted from work in the Experimental Areas portion of the Workshop.

We took as the immediate task of the group to address three topics. The topics were dictated by the present state of ISABELLE experimental areas construction, the possibility of a phased ISABELLE and trends in physics and detectors. Previous summer studies and planning by ISABELLE Experimental Facilities Division had recommended and carried out a construction program for experimental areas which can best be seen by reference to Fig. 1. In it we have a plan view of ISABELLE with the areas placed in a clockwise, hourly sense: Area 2, the narrow angle hall (intended* for low p physics and containing a "stub" for use as a test beam or spectrometer); Area 4, an "open" or blockhouse area (intended for small or modest, demountable experiments); Area 6, the wide angle hall (intended primarily for large p physics; it also contains beam extraction pipes); Area 8, a major facility hall (intended for a very large, general purpose detector); Area 10, recommended as a second major facility hall; and Area 12, recommended as a second open area. At the time of this workshop, Areas 2,4,6 and 8 were well under construction each to serve the purpose indicated above. Drawings of the areas appear as Figs. 1-4 in the report of the Area Upgrades Group, in these proceedings. However, all of the planned features had not actually been included in the construction contracts and thus one of the tasks to be addressed in this workshop was, given present knowledge, to develop an ordered list of items needed to bring areas 2,4,6 and 8 to an adequate level of usefulness for experiments generally. This list to serve as a guide for further construction after action by a Program Committee studying experimental proposals.

*Proceedings of the 1975, 1977 and 1978 ISABELLE Summer Studies provide a more detailed discussion of the considerations and recommendations made prior to this one.

The second task concerned Areas 10 and 12. The construction of these areas had not begun. They were reserved for construction at a time closer to the ISABELLE completion date when more current knowledge of physics trends and detector developments might recommend new choices. Hence, the present time was deemed appropriate to raise the question: What should be done with Areas 10 and 12 now or in the near future?

The third task was to evaluate what the implications were for the present and future experimental areas if a Phase II booster or an electron-proton option were to be adopted.

A group of physicists (see Table I) volunteered to work on these tasks. Three subgroups were formed, referred to as the "Upgrade" Group (Areas 2,4,6 and 8), the "10 and 12" Group (Areas 10 and 12) and the "e-p Option Group". Several questions, such as the implications of a booster generally were handled by discussions among all of the subgroups.

In order to inform ourselves on several specialized topics and experience at other laboratories we had several talks early in the workshop by experts - some of these very helpful talks are included in this portion of the Proceedings.

Reports, with their recommendations, were completed by each of the working subgroups and these reports immediately follow.

These reports contain the specifics concerning each task but we attempt to briefly summarize here their main points, points of contact between them, and some more general ideas they raise.

1. It was recommended not to begin construction of Areas 10 and 12 until experimental proposals are received and acted upon by the Laboratory. For a major detector hall, it was felt that the shorter construction time and smaller cost of the hall relative to those of the detector it would house and possible special properties of the detector recommend this policy. For experiments more appropriate to an open area, Areas 2,4,6 and 8 might suffice at turn-on and if not there is still time to construct an appropriate area after study of experimental proposals by a Program Committee.

2. Cryogenics and other permanent utilities should not be placed under experimental floors. Evidence is mounting that beam to floor height may be a problem in present and future areas requiring greater freedom for detectors in the vertical depth. Future options for a booster or e-p collisions also recommend this.

3. Complications of the vacuum pipe (such as a third pipe) in interaction regions should be avoided. They add to the cost of detectors which must surround them and they provide the potential for compromising experiments. For this reason, placement of e-p options, placement and transfer from a booster, and the extraction/dump system should be carefully considered or reconsidered.

4. Several general purpose improvements of Areas 2,4,6 and 8 (such as some additions of assembly, counting and cryogenic space and addition of crane capacity or coverage) will insure that these areas serve as the locus of a varied experimental program at early turn-on and will provide flexibility for their future utility.

5. For the assembly and preparation of detectors for the first round some attention should be given several matters. How and where will detectors be assembled and transported to areas which will not have their own assembly area or building? Will the first ISABELLE ring to be commissioned with circulating protons be capable of sending high energy particles down the "stub-test beam" for use in early detector checkout?

6. At the time of construction for the next major detector hall, choice should probably be made to place it at Area 12 rather than Area 10 since present indications are that a booster or e-p option might affect Area 10.

In addition to the considerations which led to the above comments and recommendations, discussion was begun (through a set of informal lunch discussions) by the Areas Group as a whole on planning and funding for an experimental program: for example, level and modes of support on construction, installation and operation of detectors in these ISABELLE experimental areas. This is a topic of great concern to the experimental community and it deserves the widest possible discussion.

TABLE I
EXPERIMENTAL AREAS WORKING SUBGROUPS

Name	Working Group Areas	10-12 Upgrade	e-p
ARONSON, S., BNL		X	
ASHFORD, V., BNL	X		
BECKER, U., MIT	X		
BRANSON, J., MIT	X		
FOLEY, K., BNL			X
GOLLON, P., BNL		X	
GRANNIS, P., SUNY - Stony Brook	X		
JENSEN, D., Univ. of Massachusetts	X		
KANTARDJIAN, G., CERN	X		X
LANOU, R., Brown University		X	X
LOWENSTEIN, D., BNL	X*		
LUCKEY, D., MIT	X		
MATSUDA, T., MIT	X		
MILLER, D., Northeastern University	X	X	
NEMETHY, P., LBL		X	
PAAR, H., NIKHEF			X*
POPE, B., Princeton University		X*	
STEVENS, A., BNL			X
THERIOT, D., FNAL		X	
TING, S., MIT	X		
WALKER, W., BNL	X	X	

*Working Group Convener

FIGURE CAPTIONS

Fig. 1. ISABELLE site plan showing location of the experimental areas.

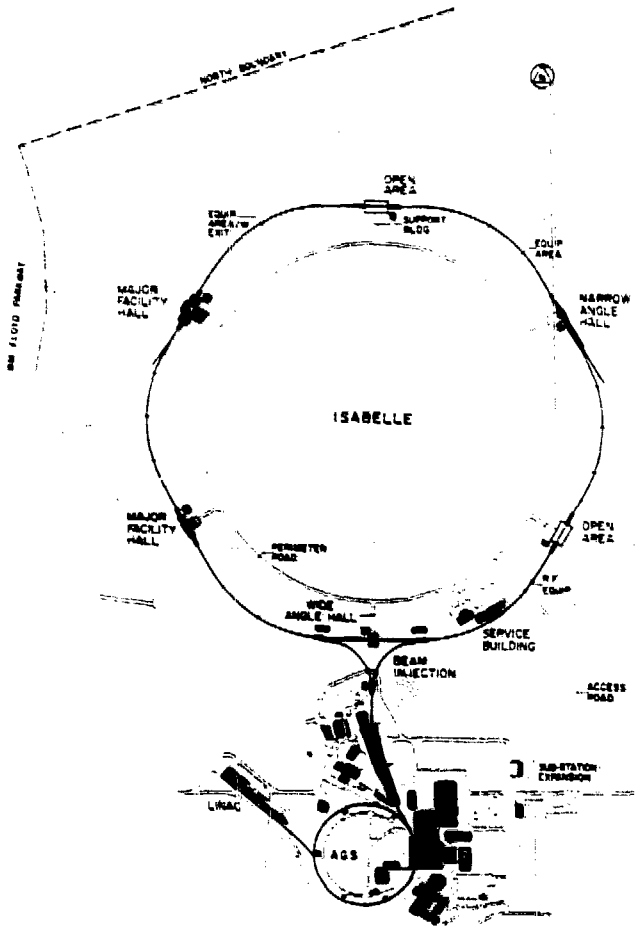
NORTH BOUNDARY
OPEN AREA
EQUIP AREA
MAJOR FACILITY HALL
NARROW ANGLE HALL
ISABELLE
MAJOR FACILITY HALL
OPEN AREA
PERIMETER ROAD
RF EQUIP
WIDE ANGLE HALL
SERVICE BUILDING
BEAM INJECTION
ACCESS ROAD
SUB-STATION EXPANSION
LINAC
AGS

Fig. 1

REPORT OF THE SUBGROUP ON EXPERIMENTAL AREA UPGRADES

S. Aronson, BNL
P. Collon, BNL
G. Kantardjian, CERN
R. Lanou, Brown
D. Miller, Northwestern
B. Pope, Princeton
D. Theriot, FNAL
W. Walker, BNL

I. INTRODUCTION

Four of ISABELLE's six experimental areas are in an advanced stage of construction. These are

1. Area 2 (Small Angle Hall - see Fig. 1)
2. Area 4 (Open Area - see Fig. 2)
3. Area 6 (Wide Angle Hall - see Fig. 3)
4. Area 8 (Major Facility Hall - see Fig. 4)

This subgroup has been charged with the task of reconsidering these areas from the point of view of useability in the ISABELLE experimental program. As a result we have developed an ordered list of suggested improvements to each of the areas. The list is presented area-by-area below, after some introductory remarks on the design considerations behind the present areas. The purpose of the list is to indicate the eventual scope of ISABELLE experimental areas, not to suggest that these upgrades should be put in place now. Indeed, although most of these additions will be needed regardless of which experiments are carried out, we think it prudent to wait for experiment approvals before final design and installation of the suggested improvements.

The designs for the four present areas were fixed in the 1978-1980 period subject to a number of constraints:

1. Fixed scope and budget (roughly $8 M in FY79 dollars) for all experimental areas, including support buildings.
2. All six areas to be developed for physics; four completed buildings plus 2 open areas.
3. A varied experimental program to be carried out in specialized areas.
4. Areas limited by the proximity of injection, extraction and cryogenic equipment.

The Experimental Areas Division of ISABELLE supplied physics related design criteria for each of these areas. These were developed from the work of previous summer studies and from the output of the Experimental Areas Discussion Group,* which considered experiments for each of the areas in some detail. Table I lists the experiments considered for each area and the written output (Proceedings of the 1978 ISABELLE Summer Workshop and ISABELLE Technical Notes) on each. Table II lists the dimensions of the resulting designs.

Much criticism of the existing halls has surfaced in regard to their overall dimensions. These grievances may be redressed in the two remaining areas or, at some future date and with sufficient physics justification, by major reconstruction of the present areas.

However, in this subgroup we have stayed more or less within the framework of the four existing areas which we regard as useful for much of the early physics at ISABELLE, and have sought to optimize them.

II. AREA 2 (SMALL ANGLE HALL)

At present, there is no assembly building foreseen for this area. While it is possible that the first round detector(s) can be constructed in the research area, any major modifications to these or any second-round experiment would need an assembly building. The logical place for such a building (area comparable to that of the research building) would be on the hardstand in front of the demountable wall. This would imply severely restricted access for the cranes needed to dismount the wall for apparatus moving. Consequently the assembly area could surround the demountable wall and include a 20-ton crane that would construct the shielding wall.

The 20-ton crane in the research area is thought to be adequate for the types of experiments to be employed in this area. However, the cryogenics pit

*S. Aronson, V. Ashford, A. Carroll, G. Danby, R. Engelmann, K. Foley, E. Fowler, B. Gibbard, D. Jensen, H. Jostlein, K. Lai, T.Y. Ling, M. Marx, R. McCarthy, F. Paige, B. Pope, L. Read, T. Romanowski, A. Thorndike, and W. Walker

under the concrete floor is thought to be an unnecessary impediment to future expansion of the area and it is recommended that the cryogenics line be run over the roof of the research building.

The small angle stub is envisaged as an extremely useful test beam facility at ISABELLE and it is recommended that the area at its end be developed in the following manner: hardstand should be added to the cut in the berm at this point (elevation 62') and an EEBA-style building (40' x 40' area) should be erected over the area. A support area equivalent to 2 portakamps or trailers would satisfy experimenters requirments. Access to this stub is possible from both Sixth Avenue or Railroad Avenue.

III. AREA 4 (OPEN AREA)

Area 4 has been designed such that a number of experiments can be contained within a large quantity of shielding blocks. These experiments would tend to be small, and to be of finite lifetime. This results in a configuration of shielding blocks that will change as a function of time. On the basis of the experience of the AGS neutrino experiment E734, it is thought that an EEBA-style building covering the area is not necessary. A flexible blockhouse can be made from the shielding blocks and weatherproofed (with polyurethane foam). Changes in the configuration of detectors or shielding will be made with an external movable crane.

The flexible nature of the area has several implications. The hardstand area which at present will cover only 115' along the beam direction should be extended to the full 188' between the berm retaining walls. A fixed assembly building is not thought to be necessary in Area 4 and it is suggested that the experimental support groups investigate the possibility of assembling equipment in buildings such as the EEBA building at the AGS. Similarly the experiment support buildings (counting rooms) would most appropriately be housed in several movable trailers such that they can be placed as close as posible to the experiment.

A major lack of flexibility to area 4 (as area 2) is the presence of the cryogenics pit under the area. We propose that the cryogenics line be routed

outside of the beam tunnel (at the present elevation of 75'-79') and either taken around the edge of the hardstand on stanchions of height 13' or taken further away until the sloping berm reaches this elevation. The detailed routing of the cryogenics depends on whether truck access is required to area 4 from the outside of the rings. The presently existing cryogenics pit is likely to prove invaluable as a flexible means of running cable between the research area and the support buildings.

IV. THE 6 O'CLOCK AREA

Because of its construction with shielded walls, area 6 contains the largest volume presently planned for a research area but with no provision for an assembly area. It is recommended that an assembly area of comparable size (at the minimum) be added on the inside of the rings. A 25' x 25' opening in the north wall of the present research area would lead to the assembly area. This opening could be closed with shielding blocks. The assembly area should be equipped with a 40 ton crane and thus would permit the assembling of the first round detector while the machine is being built. A second round detector (or extensive additions to the first) could be built while ISABELLE is in operation.

The 20-ton crane for the research area is thought to be inadequate and, as the present rails are rated for 40 tons, it should be replaced with a 40 ton crane (or, at least, another 20 ton crane should be added to the rails). It is unfortunate that the existing structure does not allow continuous crane coverage between the research hall and the proposed assembly area.

We have compared the presently available space in the support building (1200 sq. ft.) with needs for similar areas at the ISR, AGS and FNAL and find it to be somewhat small. An additional 500-1000 sq. ft. would improve the support area considerably and, if two experiments were attempting to co-exist in area 6, much more space would be required. Note that ≈ 1000 square feet could be obtained by adding a balcony to the existing building.

We note that it is likely that an experiment using area 6 would use a superconducting magnet and thus will need a building for a heat

exchanger/refrigerator (perhaps 20' x 20'). This building should not be too close to the support area because of noise and vibration problems and therefore fairly long lines will be required.

Lastly, we feel that it is appropriate to mention an extremely important upgrade that is possible for area 6. At present, it is foreseen that this area contains the vacuum pipes for the beam extraction and dumping system. It is certainly possible that the resulting background radiation will render area 6 unusable for any kind of physics. The 6 o'clock hall is a well defined (i.e. existing) area for wide-angle physics while some other areas are not yet defined (or built!). One or more such areas could even be left unused in the early running. It is our opinion that any scenario of ISABELLE utilization consider the possibility of moving the extraction system to another straight section.* In any case, it seems to us impossible for an experiment to be set up in this hall during the first running of ISABELLE. Many measurements of particle flares and of induced radiation will have to be made before the effects of beam extraction and dumping are understood.

V. AREA 8 (Major Facility Hall)

Based on experience at PEP and on the CDF hall design for BØ at FNAL, the worry was expressed that the assembly building presently being constructed in this area is too small. It is probably adequate for first round construction of the detector, assuming a tight-fitting shielding tunnel is built around the beams. It may not, however, be sufficient to house the detector plus its attached electronics house when they are retracted from the beam. This depends on the experiment actually approved, of course; still we recommend looking at the problem of expanding the assembly area in the future. Assembly areas for the apparatus to go into the forward areas should also be considered.

We assumed that the magnet(s) for the approved experiment would be cryogenic. There is no provision for housing the required refrigerator/compressor/heat exchanger complex. A plan for locating this facility could be worked out before its actual configuration is known.

*For additional details on this possibility see P.J. Gollon and A.J. Stevens, p. _____ these proceedings.

We believe (again informed by experience elsewhere) that any large experiment or facility in this area will require more than the 1200 sq. ft. of experimental support space provided. A cheap way to augment this would be to add a mezzanine in the existing support building. A better way would be to expand the present building toward the ring road.

With regard to cranes, it was noticed that the high crane in the assembly building is not part of the contract; it must be bought before the shield wall is needed. As far as the main (40-ton) crane is concerned, it should be mounted on its rails so as to give maximum coverage at the back wall of the research hall.

Table I.
Summary of Experiments Studied in Evaluating Hall Designs
For Areas 2, 4, 6, 8

Area	Ref.	Experiments
2	1978 Summer Study p.303 Tech Note 125 (1979)	- single-arm spectrometer for large x_F inclusive reactions - stub design - high energy test beam - 4π σ_T detector - coulomb-nuclear interference measurement of ρ - diffraction dissociation experiment (including neutron and π° detection) - intermediate angle (50-250 mrad) spectrometer - "rapidity plateau" spectrometer ($\|y\| \leq 3$, $p_\perp \leq 1$ GeV/c)
4	1978 Summer Study p.295 Tech Note 113 (1979)	- 4π σ_T detector - 4π optical chamber (early topology survey) - intermediate angle spectrometer - inclusive n and V° spectrometers - quark search - large $p_\perp$ $e\bar{e}$, γ, π° spectrometer pair
6	1978 Summer Study p.278	- large $p_\perp$ hadron and jet spectrometer pair with particle identification
8	Tech Note 141 (1979)	- BNL dipole - UA1, UA2 - Toroidal magnet spectrometer (Pope) - SREL cyclotron detector - R807 - SPS multimuon proposal (Becker) - FNAL design study (pre-CDF) - Assorted "large" devices conceived at ISABELLE Summer Studies (1977 and 1978)

Table II
Summary of Hall Dimensions (m)

Area	Length	Width	Beam Height	Hook Ht/ Cap. (t)
2. Small Angle				
Central Hall	28	12	1.7	6.1/20
Forward Experimental Building	68	7.9	1.7	5.3*
"Stub"	91	2.4	1.0	2.0*
4. Open Area 4	57+	37+	2.2	--*
6. Wide Angle	16	32	4.3	10/2x20
8. Major Facility				
Central Hall	19	15	5.2	11/40
Forward Experimental Buildings (2)	16	9	3.3	6.6*
Assembly Building	19	19	5.2	11/40 + 14/7.5

*No crane - ceiling height given
+Pad dimensions given

FIGURE CAPTIONS

Fig. 1. Area 2 (Small Angle Hall)

Fig. 2. Area 4 (Open Area)

Fig. 3. Area 6 (Wide Angle Hall)

Fig. 4. Area 8 (Major Facility Hall)

NARROW ANGLE HALL

Fig. 1

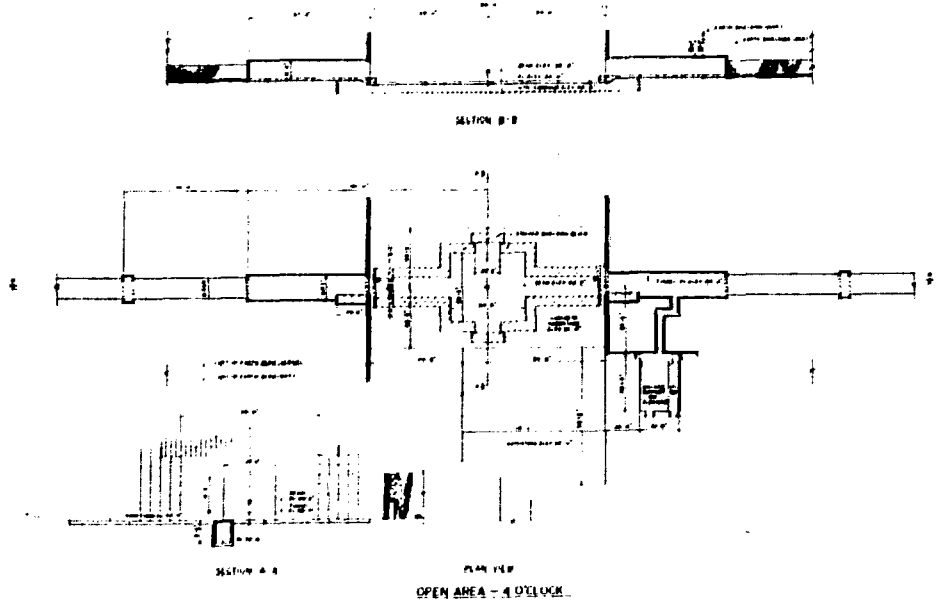

Fig. 2

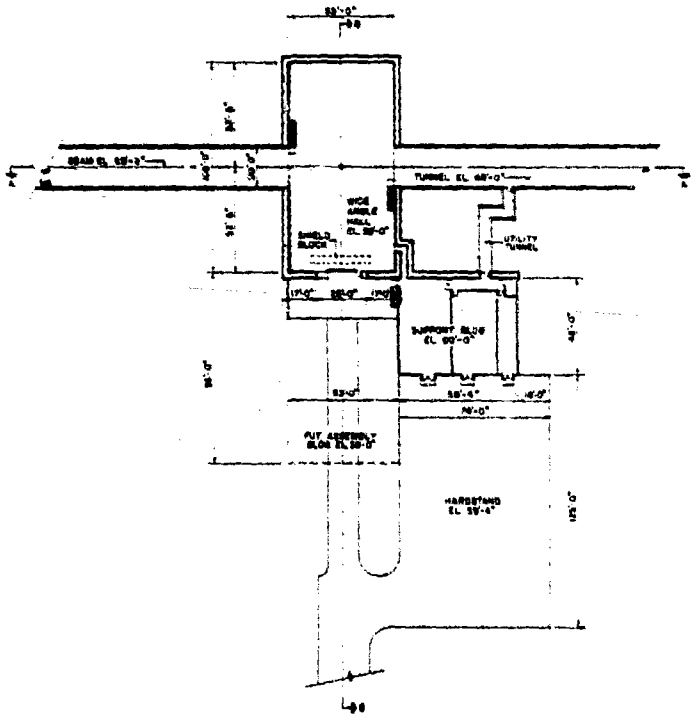

WIDE ANGLE HALL

Fig. 3

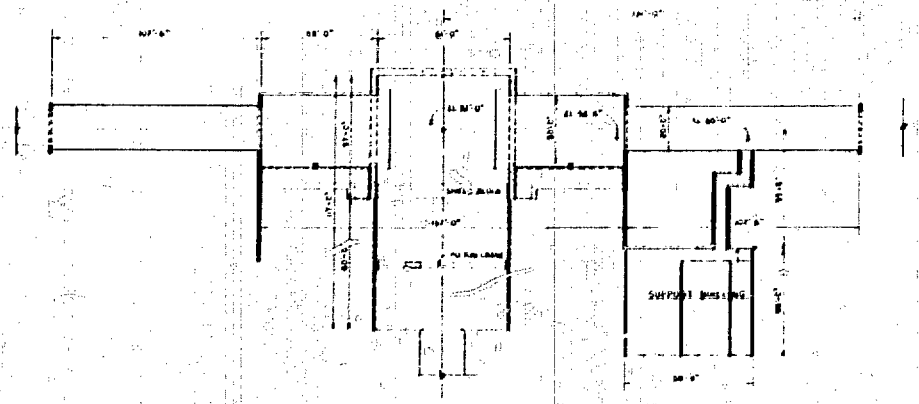

PLAN VIEW
MAJOR FACILITY HALL

Fig. 4

REPORT OF EXPERIMENTAL AREAS 10 AND 12 GROUP

S. Aronson, BNL
V. Ashford, BNL
U. Becker, MIT
J. Branson, MIT
P. Grannis, SUNY Stony Brook
R.E. Lanou, Brown University
D.I. Lowenstein, BNL
D. Luckey, MIT
S.C.C. Ting, MIT
W. Walker, BNL

The question that has been put forth is how to proceed with the last two undeveloped experimental areas, 10 and 12. This has been reviewed with the boundary conditions of a 1986 or a 1988 ISA turn-on date and the possible options of a booster and an additional electron ring. In all cases, the final conclusion is to do the minimum required for the completion of the accelerator and wait until the approval of the first round of experiments to design and construct the experimental areas.

It is presently envisaged that at least one of the two areas would contain a "major" detector. The concept of "major" is defined to be a large detector of greater than $\$\simeq 3\times10^6$. Up to date costing of detectors that are presently under construction at other accelerators or under design for ISABELLE bear out this scale. Thus, the still unconstructed major detector region is presently expected to be as large as or larger than any present colliding beam experimental area, with a construction cost of the order of $\$5\times10^6$. Similarly, the physical size of these detectors is seen to be pushing the limits of present hall sizes and therefore the next large hall at ISABELLE should be larger than Area 8. The critical parameters such as the beam height, which was reported to us to have a major impact on the cost, and the shielding required, can only be determined after one knows what experiment has been approved for this area. We have discussed most of the existing as well as proposed large detectors and for the moment, the M.I.T. multimuon device is the one that makes the greatest demands on the physical size. Specifically, it needs a large expanse of floor approximately 7 meters below the beam tube. On the other hand, this device might be economical on the shielding demands since a good fraction of it is self shielding. A building design should incorporate this feature if the experiment were approved.

Since the last ISABELLE Workshop in 1978, there has been a change in the physics emphasis and much additional experience in the construction and running of large detectors at PEP, PETRA and CERN. We therefore decided to reevaluate several previous assumptions and design considerations and we here review their validity in the light of new data. The first of five points is that up to now, few major detectors have been dismantled prior to the cessation of operations of the colliding beam machine. Major detectors are typically not moved, they are modified and accumulate more components. Thus, a major detector hall should be basically built to accommodate this one device for the life of the machine. The second point is that a major detector hall is very expensive. In absolute terms, $\$5 \times 10^6$ is a lot of money but the hall cost will be only 10-15% of the entire detector. This tells us that one should not rush into putting up halls until the experiment is approved. One should optimize the costs of the hall and detector as a package. It is expensive to modify these areas once built. The third point is that it has been standard dogma that the routing of cryogenic transfer lines was a critical path in the accelerator construction. We do not find this to be the case. A temporary line can always be installed for example directly under the machine vacuum pipe, so as not to interfere with the decision of the experimental floor height. We lament the fact that one was too hasty to position the cryogenic transfer trench beneath the beam line of Area 4. The fourth point is that we have more than enough time to approve and construct the major detectors. We believe this is not so. For the 1986 turn-on, we should have already approved some experiments and for the 1988 turn-on, one should be considering proposals now. The very large detectors will require the order of 5-6 years to design, construct and debug. Thus, the hall construction will have little impact upon the machine turn-on. The fifth point was that a third pipe for electrons or a booster passing through a major detector area designed for p-p physics would be a small complication. This, we feel, is not the case. The response is that this would seriously compromise most dedicated p-p experiments. For example, the multimuon detector appears to be incompatible with a third pipe. Given the present knowledge of detector configurations and in the

absence of an explicit design for a booster or an e-p machine inside the ISABELLE tunnel, the only sure way to avoid interference at p-p interaction regions is to have these options in a four or five-fold by-pass or separate tunnel.

The question of the second area was also investigated. There seems to be no danger in letting future proposals determine what should be done in detail with this area. It is quite conceivable that this area just be initially an enlarged version of the ring structure to house a class of small experiments that can be done quickly during the first two years of operation. For example, total rate and small angle scattering, and quark search experiments might require no more than an enlarged beam tunnel.

The question of a machine physics intersection region for the first year of operation was brought up. We have been told by machine physicists in ISABELLE that this is not necessary and that we may look forward to physics experiments in all six areas.

THE IMPACT OF THE e-p OPTION ON ISABELLE EXPERIMENTAL AREAS

K.J. Foley, Brookhaven National Laboratory
G. Kantardjian, CERN
R. Lanou, Brown University
H. Paar, NIKHEF
A. Stevens, Brookhaven National Laboratory

I. INTRODUCTION

There have been many suggestions for the expansion of existing or planned storage rings to include high energy e-p collisions. We will not discuss the physics potential here, but there is a general concensus that a facility with protons colliding with electrons and positrons of selectible helicity would provide great insight into weak interactions, nucleon structure, etc., in a way not duplicated at e^+e^-, pp, nor $\bar{p}p$ machines. In this report we will comment on some aspects of the addition of a 10-20 GeV electron ring to Isabelle.

II. ASSUMPTIONS

As a model for the electron ring we have used a machine radius of 360 m and have added straight sections of ± 125 m about the e-p interaction point for the beam gymnastics needed to rotate the electron polarization from the natural transverse orientation to the desired longitudinal direction.

We have assumed that Isabelle is primarily a p-p collider whose prolific physics output will deter long shutdowns. In considering possible ep collision points we have avoided the existing large facility hall at 8 o'clock, since that will clearly contain a relatively permanent setup, and the wide angle hall at six o'clock, since in that area the experiments would be severely limited by the need to dump the Isabelle proton beams.

III. LOCATION OF THE ELECTRON RING

There are at least three possible locations for the electron ring:

A. Located in the same tunnel as the pp rings, providing the possibility of ep collisions at any interaction region.

B. Located in a separate tunnel outside the main tunnel, providing ep collisions at one interaction region only. The two possible locations are the 2 and 4 o'clock areas as shown in Fig. 1.

C. Located in a separate tunnel tangent to the main ring, at two straight sections. The arcs joining the two straight sections can be either within or outside the region enclosed by the ISABELLE tunnel.* The interaction regions are at 4 o'clock and 10 o'clock as shown in Fig. 2.

Each of these has advantages and disadvantages. We just mention those that affect the ISABELLE experimental areas design:

1. Option A allows up to 6 ep interaction regions and areas, option B just one and option C up to two.
2. Option A constrains the design of ep interaction region severely, in particular the straight sections with the polarization rotators must be accommodated within the straight section of the ISABELLE tunnel. Options B and C with the outside arcs do not have this constraint.
3. Option A has an extra beam pipe, containing the stored electron beam, passing through pp interaction regions. This is at least a nuisance for the pp detectors. We know of one solution where the electron beam passes through each pp interaction diamond. Its beam can be within the confines of the pp vacuum pipe at least over the length of a central detector. Figure 3 gives a three dimension impression of this arrangement.

---

* In order to reduce the interference with the pp rings, the ring totally inside has a radius of 300 m with 200 m straight section. The outside version has a radius of $\simeq$ 600 m with 300 m straight sections.

4. Option A would have the most interference between the electron ring and the proton rings during installation and operations. Option C has less interference, and option B has the least.
5. Option C underlines the desirability of moving the second major facility hall, now planned for 10 o'clock, to 12 o'clock in order to leave 10 o'clock available for ep physics.

IV. THE ep INTERSECTION

It has been recently proposed (BNL Proposal: Electron-proton Interaction Experiment by Y. Cho et al., May 1981) that the electron beam cross over in vertical plane (see Figure 4). Near the ep interaction point, a zero-degree crossing angle is established by means of vertical bending magnets. Strong quadrupoles produce the low β necessary for high luminosity. Further away from the intersection point, a spin rotator is present at each side. They rotate the electrons spin from transverse as it leaves the arc, to longitudinal at the intersection and back to transverse upon entering the next arc. The total length is about 250 meters or 125 meters on each side of the interaction region. The position of the magnets is totally antisymmetric with respect to the intersection region. This means that the electron beam is below the proton beams upon entering the straight section and above it upon leaving it (or above it upon entering and below it upon leaving). The maximum excursions are 1 meter in the vertical and 0.5 m in the horizontal plane while in the arcs the electron beam is at least 0.5 m above or below the proton beams. These are only estimates since the final design of the spin rotators is not yet available. The final design should be taken into account in determining the elevation of the proton rings in order to avoid later excavation.

V. EXPERIMENTAL HALLS FOR e-p COLLISIONS

In order to estimate the size of the hall we have examined earlier proposals for ep experiments, in particular the most recently proposed ep detector (Fermi Lab Proposal 659). In all cases the apparatus would fit comfortably in the Isabelle straight sections and the length of any

existing hall is adequate though if the small angle hall is used, the larger section should be in the direction of the protons. The typical radius of the apparatus is 3-4 m so a deeper floor would be required (maybe 5 m below the beam) than exists in the areas at 2 and 4 o'clock. The ep detectors are no different in this than the pp central detectors. The polarization rotators are located within the ISABELLE tunnel. It should be noted that these considerations are independent of actual location of the electron ring: that is, independent of which option of Section III is chosen. With this in mind we suggest very strongly that any machine plumbing and electrical connections be kept well away from the beam region -- for example, the existing trenches in the open area must not be used for permanent connections.

VI. SUMMARY

The ep option should be kept in mind at all phases in the construction of ISABELLE. The following points are immediately obvious:

1. The second open area should be moved from 12 o'clock to 10 o'clock.
2. The location of the proton beam should be compatible with the spin rotators.
3. For the ep detector, the floor should be $\approx$ 5 m below the beam.
4. Permanent plumbing and cabling should not be close to the intersection points.

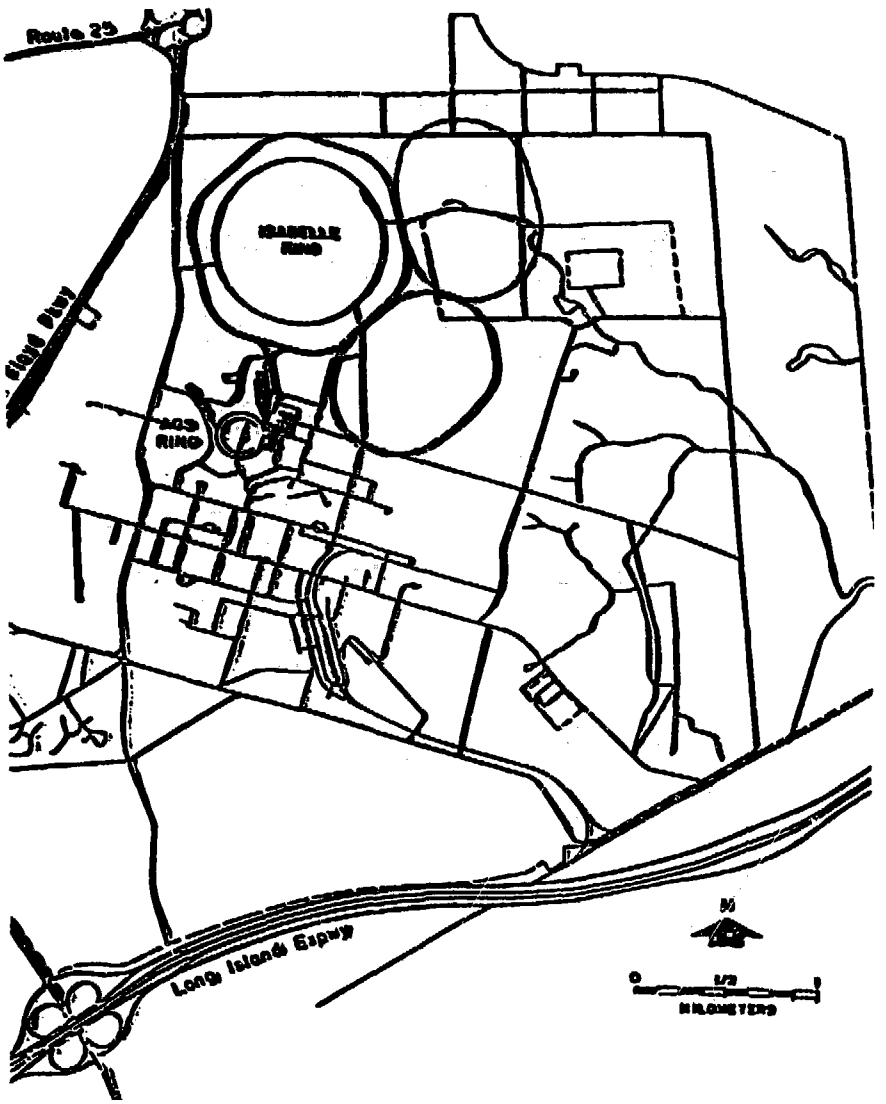

Figure 1: Possible Arrangements for Option B

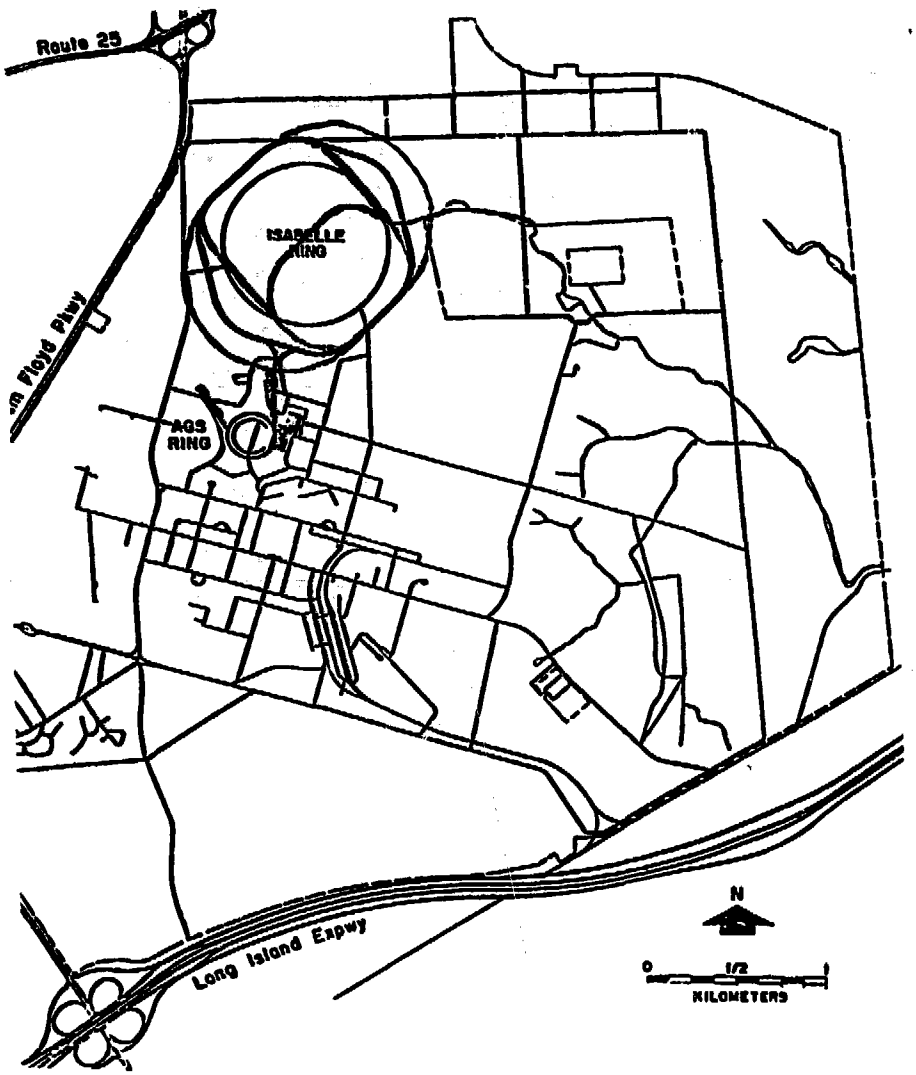

Figure 2: Possible Arrangements for Option C

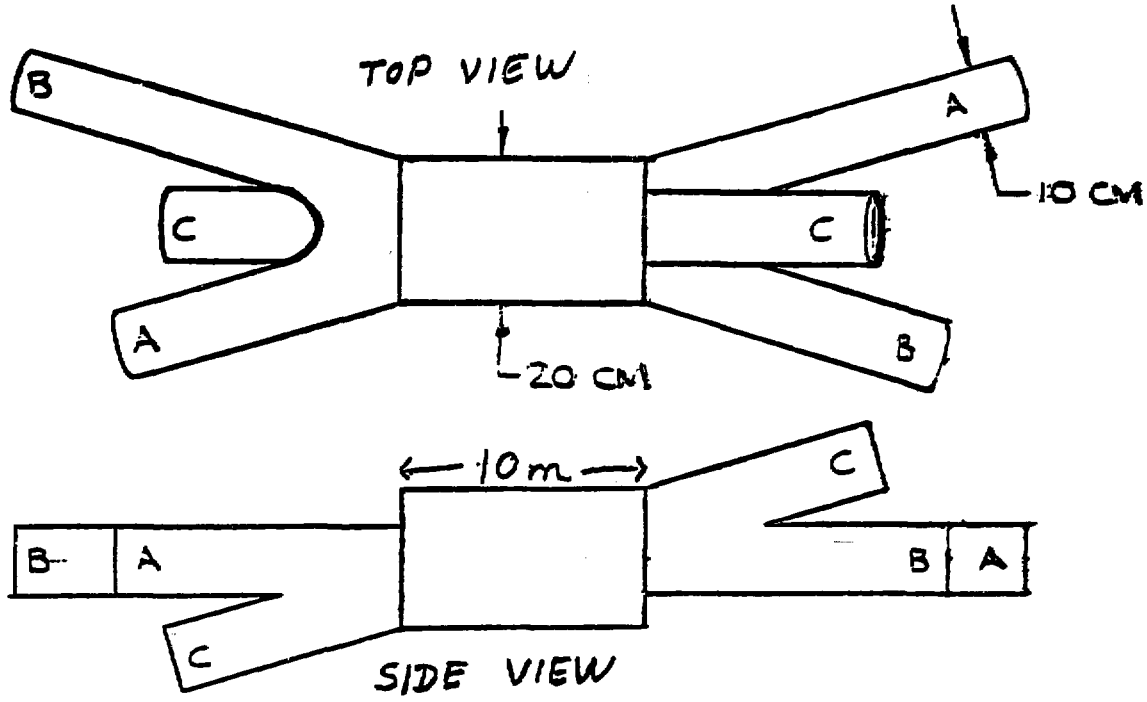

Figure 3: A Possible Beam-Pipe Configuration

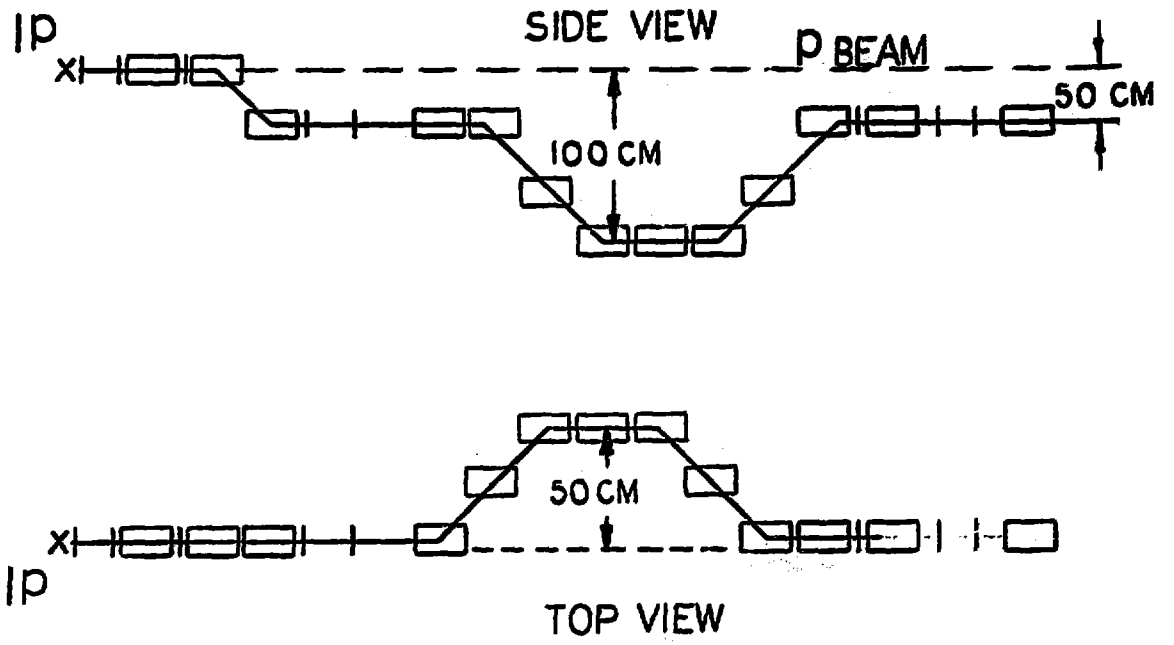

Figure 4: The Electron Spin Rotator

LARGE EXPERIMENTAL HALLS

David Luckey, Massachusetts Institute of Technology

If 100 GeV physics has such particles as the Z_o with a narrow width and low multiplicity decays then some detectors will need resolutions of the order of this width (1%). In constrast to recent hadronic physics, we will have to measure high momenta well, and this will be a major challenge to detector designers in terms of BL^2 and mechanical accuracy.

Large detectors last as long as or longer than the accelerators at which they are built and are not likely to be replaced. This is particularly true of the large magnets involved.

I see no reason to make a universal building but would rather minimize the cost of experiment plus building taken a whole. It will be necessary to commission a detector at the same time as the accelerator, so it is necessary to the detector at physics turn-on time. The mechanics of this will be made difficult if complicated mechanical drives are necessary from different floor levels and from floor depth. Since a large detector will take longer to build than a building, one should pick some of the building parameters after the proposal acceptance and after the mechanical support is designed. One could then pick just the right floor level.

A large detector will take much assembly area and one will need large areas at BNL for the superconducting coil and central drift chamber. Ideally, one should not try to do them at the experimental hall, but rather transport them at the appropriate time.

The initial design of the MIT multi-muon detector could be assembled in an area with the same square footage as the major hall, but needs about 7 meters from beam to floor. Various building designs have shown that it costs about 1M$ per meter of floor depth below the "standard" 8 o'clock hall, so one should find the economic minimum of detector support vs building cost. Given early proposal approval, this should not cause excessive delays in building construction.

CLEANING UP AREA 6

Peter J. Gollon and Alan J. Stevens, Brookhaven National Laboratory

The possibility of a booster at 4 o'clock has resulted in expressions of concern by some experimenters who fear that the presence of the ring there will "ruin another area for physics". The physics at 6 o'clock is already compromised, it is said, by the scraping and extraction systems, so 4 o'clock should be protected at all costs. We raise the question here - but do not answer it - of whether that argument should be turned around. If the usefulness of the otherwise very nice Wide Angle Hall is compromised by the extraction and scraping systems, maybe they should be moved somewhere else. The most logical alternate locations are an undeveloped 10 o'clock area, or 4 o'clock if that location is to be encumbered with a proton booster. The choice between these locations need not be made yet.

What are the physical and radiation safety considerations regarding the locations of these systems? First, they must be located in one or more of the straight sections. There is simply not enough drift space in the arcs to fit them in.

Second, the dumps fit much more conveniently at an outward moving intersection (2, 6, 10) than at an inward moving one (4, 8, 12). This is a simple result of the geometry. The extraction is downward, and the extraction line should continue, with the minimum length and number of magnets, until it extends out past the tunnel floor, where the dumps will go. This consideration favors area 10 over area 4, but does not rule the latter out.[1]

Third, because of the reduced energy of an ISABELLE using Fermilab magnets, the existing muon shielding lobes will be quite adequate for extraction septum losses[2] of 0.1%. This is true even for Phase II ISABELLE, and for the dumps in any location. (It is not true for some locations for a 400 GeV machine.[3])

Fourth, the reduction in ISABELLE energy with Fermilab magnets also provides an improvement of a factor of 20 to 40 in the offsite muon doses for a given beam loss.[4] This factor, combined with the results of Ref. 3 indicate the maximum allowed scraping loss at area 10 in the clockwise direction to be

3%. This is less than the 10% scraped at the ISR. (At 400 GeV the scraping limit for the same location would be 0.075%.)

Fourth, for a 400 GeV ISABELLE, a 6 o'clock location for scrapers is even more marginal for environmental reasons than 10 o'clock scrapers at 355 GeV, since only 0.18% scraping is allowed there in the clockwise direction.[5] Of course, one can always add more sand to the shields of area 10 or 6 to gain from absorption what is not provided by distance. Thus, if the scrapers receive any significant use at full machine energy they will be a worse environmental problem than the extraction lines to the dumps. However, they may not be as bad as is feared by the experimenters, since (a) they involve no extra beam pipes; (b) only one tenth of the particles being scraped interact in the finger upstream of the crossing region, with the remaining protons striking a collimator downstream of the experiment[5]; and (c) experimenters should have advance warning of scraping operations in order to reduce high voltages on PMT's and chambers.

It is clearly a little too early to decide where, if anywhere, to move the dump and scraper systems, but nobody is happy with them at 6 o'clock. We should not immediately exclude the seemingly distasteful possibilities of putting the scrapers and dumps in the different straight sections, and even of locating the two scrapers in different straight sections. Each solution has its drawbacks, whether of an environmental, experimental, or financial nature. There will be lots of complaints no matter what location is chosen. What must be done in the next 6 months or so is to decide if the present location is still the "best" one, although "best" will depend on the realities of machine operation and will not be known until turn-on.

REFERENCES

1. It is worth pointing out that the preferred method of injection is into the outer ring. Doing this (at 30 GeV) at 6 o'clock determines the beam direction in each ring. Placing a booster at 4 o'clock would mean either (a) injecting at 100 GeV into the inner rings, or (b) reversing the presently established sense of rotation. Option (b) would reduce the usefulness of the stub at 2 o'clock.
2. It is claimed that if the total extraction losses on the septum exceed 0.1% of 6×10^{14} protons, the septum will be damaged. This presents a severe limit on the design of the extraction system.
3. "Muon Shielding Requirements for Present Configuration", A.J. Stevens and A.M. Thorndike, ISABELLE Technical Note 65 (1978). Calculations in this reference, as well as all others made or referred to here assume 500 fillings of each ring per year.
4. The factor of 20 is based on background experience at Fermilab, when the accelerator energy was reduced from 400 to 350 GeV (D. Theriot, private communication). The factor of 40 comes from rough calculations based on muon shielding calculations done at Fermilab: "Muon dE/dx and Range Tables...", D. Theriot, NAL TM-229 (1970) and "Muon Shielding: Studies of Homogeneous Shielding for a Neutrino Facility", D. Theriot and M. Awschalom, NAL TM-259 (1970). We believe the latter number to be more relevant to the present situation.
5. "Beam Scraping and Limiting Aperture Collimators at ISABELLE", A.J. Stevens ISA TN-110 (1979). The only location which has large distances to the site boundary in both directions is area 4 (cw 3.4 km; ccw 2 km). The largest distances to the site boundary are at area 4 (cw 3.6 km), area 6 (ccw 3.6 km) and area 8 (ccw 3.6 km).

LIMITATIONS OF A "SELF-SHIELDING" EXPERIMENT

Peter J. Gollon, Brookhaven National Laboratory

It has been suggested several times that one or another particularly massive (and expensive) experiment might be able to economize on shielding by getting recognition for the shielding provided by the apparatus itself. Let us see under what circumstances this may be done.

Figure 1 shows an experimental arrangement in which the interaction region is surrounded by many interaction lengths of calorimeter or magnet yoke. The detector D does provide more than enough attenuation of high energy particles originating from beam-beam interactions at the crossing point. However, it provides essentially no attenuation for the spray of secondaries coming from other beam-loss locations such as the quadrupole Q.

One solution to this problem is to place portable shielding around the beamline on either side of the central detector (left side of Fig. 2). This particular arrangement minimizes the amount of shielding used, but is must be unstacked to open up the ends of the detector. The shielding arrangement of the right side of Fig. 2 avoids this difficulty at the cost of using more concrete blocks. Probably neither of these schemes would appear attractive compared to a fully shielded hall if the concrete block shielding weren't considered "free" because it already exists. (Of course, the existing inventory of concrete blocks will go only so far, after which additional blocks must be bought with real money.)

The scheme shown in Fig. 3 attains a "self-shielding" configuration without lots of stacked concrete by placing everything but the massive central detector in widened sections of the machine tunnel. It saves the expense of stacked shielding by limiting the room for growth of the experiment, and by providing no access to the ends of the detector. Proponents of the MIT detector would not be happy with a scheme such as this, which would force them to move the entire detector out of the beam in order to remove an endcap to gain access to the central calorimeter and chambers. A differently designed massive detector, with access from the side rather than the end, would be a better candidate for a self-shielding layout.

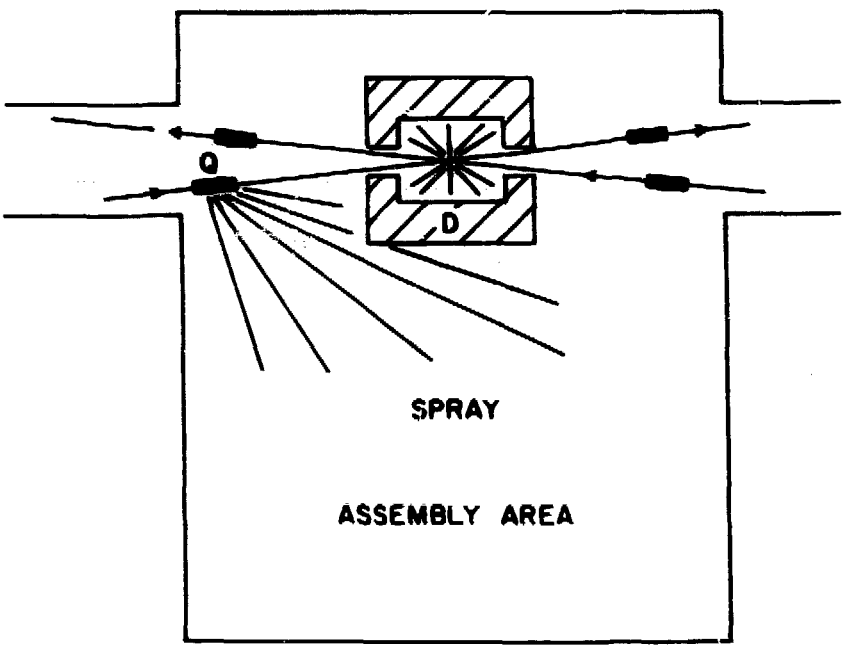

Fig. 1

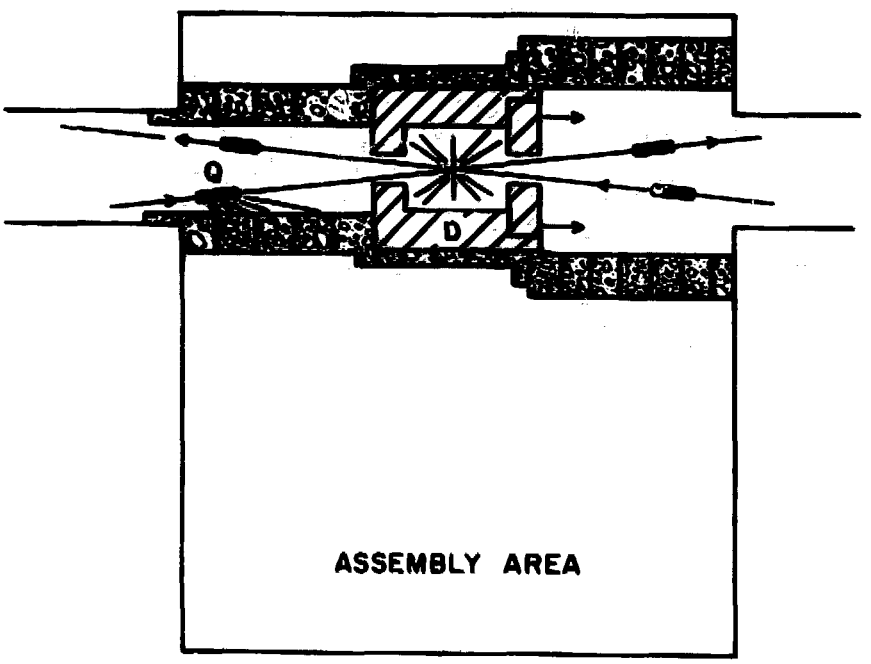

Fig. 2

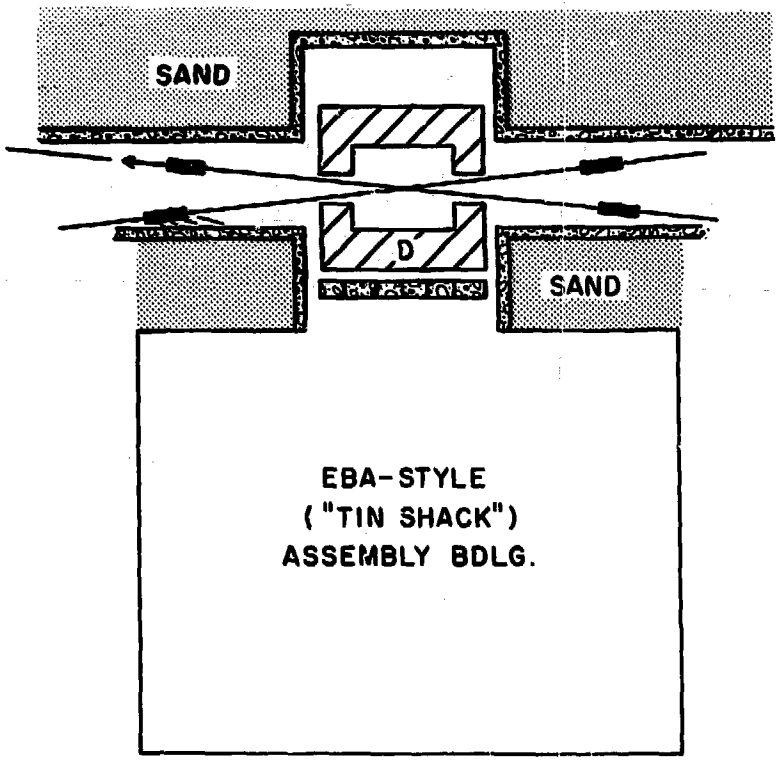

Fig. 3

REVIEW OF THE EXPERIMENTAL AREAS AT CERN COLLIDERS

G. Kantardjian, CERN

This note is an attempt to give an overall picture of experimental areas for the various CERN colliders:

1. ISR with a long experience on proton-proton colliding beams but which had valso successes with other particles such as deuterons, alphas and very recently antiprotons;
2. SPS which is just now operating as a proton-antiproton collider;
3. LEP, an electron-positron storage ring project, which the construction is expected to start very soon.

I. ISR EXPERIMENTAL AREAS

Out of the 8 intersecting regions 6 are allocated for physics experiments, one for beam dumping (number 3) and one for analyses of beam conditions (number 5). Matter of fact, a small set up for monopole research has also been installed in the latter region (number 5).

The ISR has four different types of configuration of the experimental halls.

Intersection 1 is surrounded by a larger hall but enclosed in a shielding construction made of removable concrete blocks for the walls and concrete beams for the roof. The outer wall (thickness = 4.8 m) has not yet been demounted. The inner wall (thickness = 3.2 m) was demounted and remounted several times (about 2 days for each operation) for the installation, repair or reinstallation of the superconducting solenoid (weight $\sim$ 70t) and for the construction of transmission lines channels. The introduction of large equipment up to 40t is possible by removing the concrete beam of the roof (which is 1.5 day of work). Small equipment but not hand-portable can be introduced via Intersection 2 or 8.

The intersecting region separates the large hall in two nonsymmetric halls. The smaller looking towards the center of the ring houses the cryogenic system and the assembly area for the superconducting solenoid as well as the counting room. The hall looking towards outside the ring is divided in

areas for assembly of experimental equipment, small workshop, unloading area, power supplies and test of magnets.

At Intersections 2 and 8 the tunnel is wider by 3 meters looking towards the inside. But no crane capability is available in the extra region and many ad-hoc lifting equipment had to be invented in order to install equipment in Intersection 8 (calorimeters and cerenkov counters for experiment R807) or Intersection 2 (20 kA power supplies for the system magnets of experiment R201).

These two intersections have a large pit, the floor being at 3.86 m below the beam height. Nevertheless special pits have been dug in Intersection 2 (for access to the bottom equipment of experiment R209) and in Intersection 8 (for the supporting jacks of the magnet for experiment R807).

Intersection 6 has a very large hall as well as an assembly hall which was created for the construction of the 1,000 ton magnet called SFM. Due to space and crane capabilities (see table below) the installation of large and heavy experimental equipment is easier and quicker than in the other intersections.

Intersections 5, 6 and 7 have the same width as the normal ISR tunnel (15 meter). The floor is only at 1.46 m for the beam height which has been a constant drawback. To meet the requirements of the various experiments in Intersection 6 we had to dig special pits. The same operation had also to be carried out in Intersection 7 in order to locate the bottom streamer chamber of experiment R703T-UA5.

Normal ISR tunnel: long spectrometers up to 40 m were installed alongside or above the ISR magnets (see experiments R201, R202, R802).

Counting rooms: except for Intersection 1 which was already mentioned before all the counting rooms are located on top of the tunnel. The electrical and transmission lines for the detectors are installed in the three vertical shafts.

Crane capability: Intersection 4 is equipped with a 60 ton crane and 7.5 m hook height above the beam. All the other Intersections are supplied by the 6 standard 30 ton ring cranes allowing a modest 2.5 m hook height above the beam. A possibility of coupling two cranes exists in order to reach a 60 ton capacity. Well after the construction of the ISR we had two smaller 2x2 ton cranes installed which enable us to gain an extra 1.5 m hook height. Due to

a lack of the overhead cranes coverage and/or capacity we often have to introduce a portable crane in the various areas. The turn over of the superconducting solenoid for assembly of the cryostat is a good illustration.

Access into the experimental regions for the equipment: The uneasy situation of Intersection 1 has been discussed earlier. All other intersection regions have a 4.5 m wide and 4.7 m high shielding door which can be opened easily in about 5 minutes. Intersection 4 has an extra demountable shielding wall of 12 m wide and 10 m high. The demounting of the wall takes about 1.5 days. Only Intersection 1 and 4 have the possibility to roll-in heavy and large equipment from an assembly area to a data-taking position.

Some comments: From my experience in preparing and installing experiments around the ISR I can state that assembly areas attached to the research areas are indispensable. Specially now when the detectors are becoming more and more complex. We would save time, unnecessary failures due to transport and panic on the first days of a shut down period.

Also the floor should be at 5 m below the beam height. If this distance is less than 4 m a strong risk exists having to do civil engineering work which is really not recommended when the machine is already operating.

And last, as some equipment has to be carried over the machine or the experimental set-up quite often it is necessary to have a good crane clearance, 7 meters of hook height above the beam line seems reasonable.

II. EXPERIMENTAL AREAS AT SPS-$p\bar{p}$ COLLIDER

Two underground halls have been constructed around the middle point of two long straight sections of the SPS which are called LSS4 and LSS5.

Underground area of LSS 4: This underground hall located at about 61 m below the ground level has a cylindrical shape of 21.4 m in diameter and a total length of about 44 meters divided in 11 m for the research area. 5 m of demountable shielding - 21 m of assembly area and 7 m for counting room purposes. The useful floor width is 15.5 meters its level situated at 5.5 m below the beams level. The maximum height of the hall equals 18 m and the crane hook height is 13 m above the floor level.

There are two accesses. The first is a 8 m diameter vertical shaft for the transport of heavy and large equipment. The second vertical shaft of

5.1 m diameter is equipped with a lift for personnel and small equipment (PIT). Inside the assembly area a 40 ton crane is available and a smaller crane of 10 ton capacity is spanning the interacting area.

Underground Area LSS5: The floor level of LSS5 underground area is situated at about 28 m below the ground level. The interaction hall has a vertical shaft form of 20 m diameter terminated by a dome. The experimental equipment has a stand-by location which is also a vertical shaft of 20 diameter. This large shaft ends up directly in the surface hall and the transportation of the equipment from the surface hall to the underground area is made through the vertical shaft. A rectangular passage joins the two quasi-circular surfaces. The total length of the underground floor adds up then to about 47 meters. The useful height and floor width for rolling in equipment are respectively about 13.8 m and 13.2 m. The mounting and demounting of the shielding wall is carried out through a special rectangular chimney.

The floor level is 6.3 m below the beams height. The interaction area has a rotating overhead crane.

III. EXPERIMENTAL HALLS FOR LEP

LEP a e^+e^- colliding machine will provide eight interaction regions to be reached by experimental areas. The floor level of the eight experimental halls will vary between 40 m and 600 m below the ground level. Three of these regions will be very deep underground and access will only be possible by long horizontal tunnels (about 1% slope). The other five halls will be accessible by vertical shafts as the LSS4 underground area described under section II). The following table summarizes the position and access of the eight experimental halls as well as their description.

Underground Hall

A underground hall will have a cylindrical form of 21.4 m in diameter and 55 m long. The useful floor width will be about 15.5 m. The maximum height of the hall will reach about 18 m and the crane hook height above the floor is foreseen to be between 12 and 13 meters. The floor level will be 5.5 m below the beams line. The total length is divided between the interaction region, some shielding (equivalence of 1.5 m of concrete), the assembly area which should be free of the overhead vertical shaft, and counting rooms purposes.

There will be a vertical shaft of 9 m in diameter for the introduction of the experimental equipment. Transport of the equipment inside the hall will be by means of a 40 ton overhead crane. A separate vertical shaft is also designed for the introduction of the machine element and access to the LEP tunnel.

A garage to introduce or remove large detectors (installation of central detectors into solenoids) is foreseen in the assembly area.

Intersection 1 will probably be dedicated to two-photon experiments. To accommodate the forward detectors two extensions along the beam will be needed. This experimental area could be extended in the direction transverse to the beam later, if needed.

Deep Underground Halls

The areas 3 and 5 will look much like the underground areas which are described above. The main difference concerns the horizontal access tunnels of about 4 m in diameter which replace the vertical shafts.

Interacting area 4 will have the longest access tunnel of about 3,000 meters. This hall will be also cylindrically shaped but somehow reduced in diameter to about 15 meters. The length of the experimental hall will be 55 m from the beam line to the far end of the counting room area.

The diameter of the access tunnel will only be 3 meters which will prevent the introduction of very large pieces of equipment. The experimental set-ups which will be installed in Interaction region 4 will have to be designed in modular and compact units. Due to this specific reduced and remoted access space a long technical support hall is present at the far end of the access tunnel before reaching the experimental hall. Its diameter will also be of 15 meters and its length should approximately be 70 meters.

Table of ISR Experimental Areas

Areas	Length (m)	Width (m)	Height (m)	Beam height (m)	Crane hook above beam (m)	Crane capacity
Inner I1 hall	48	10	25	11		40 tons
Intersection I	12	15	10	5.06	2.5	30 tons, 2x2 and 40 tons if roof is removed.
Outer I1 hall	50	22	25	11		40 tons
Intersection 2 & 8	32	18	8.9	3.86	2.5	30 tons, 2x2 tons
Aasembly hall I4	45	14	10	5.06	3.5	40 tons
Intersection 4	70	25	17.6	5.06	7.5	60 tons
Intersection 5, 6 and 7	ISR tunnel	15	6.5	1.46	2.5	30 tons, 2x2 tons

Table of LEP Experimental Halls

REGIONS	DEPTH BELOW GROUND LEVEL (m)	ACCESS TO THE HALL	DESCRIPTION
1	∿ 51	Vertical Shaft	See underground hall special area for 2-γ physics/also ep option
2	∿ 41	Vertical shaft	See underground hall
3	∿ 150	Tunnel ∿650 m long	See deep underground hall
4	∿ 600	Tunnel ∿3000 m long	See deep underground hall
5	∿ 300	Tunnel ∿300 m long	See deep underground hall
6	∿ 73	Vertical Shaft	See underground hall
7	∿ 67	Vertical Shaft	See underground hall
8	∿ 51	Vertical Shaft	See underground hall

FIGURE CAPTIONS

Fig. 1 Plan view of intersection I1 at the ISR.
Fig. 2 Plan view of intersections I2, 5, 6, 7, 8 at the ISR.
Fig. 3 Plan view of intersection I4 at the ISR.
Fig. 4 Side view of intersection LSS4 at the SPS.
Fig. 5 Plan view of intersection LSS4 at the SPS.
Fig. 6 Side view of intersection LSS5 at the SPS.
Fig. 7 Plan view of intersection LSS5 at the SPS.
Fig. 8 Layout of the interaction regions at LEP.
Fig. 9 Proposal for a LEP experimental hall.

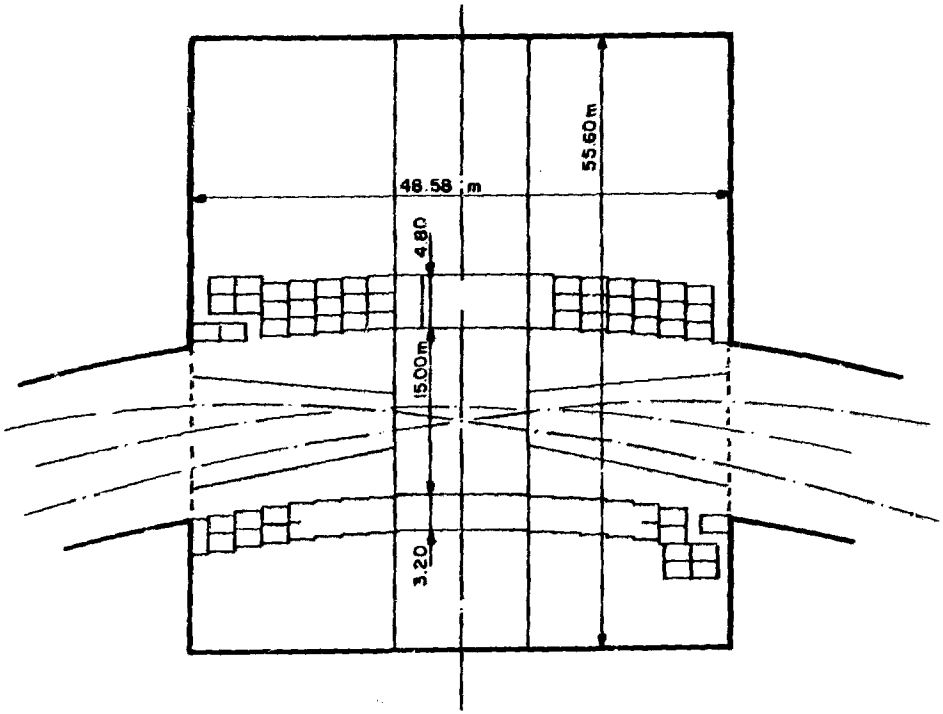

ISR - INTERSECTION 11

Fig. 1

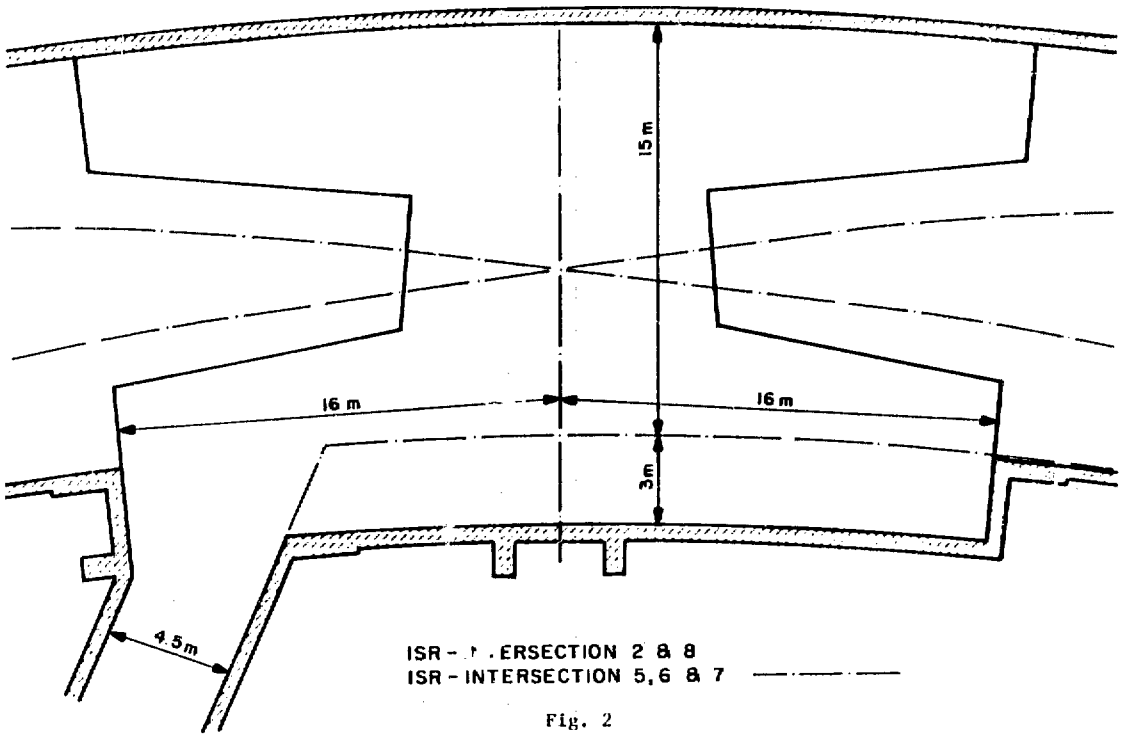

Fig. 2

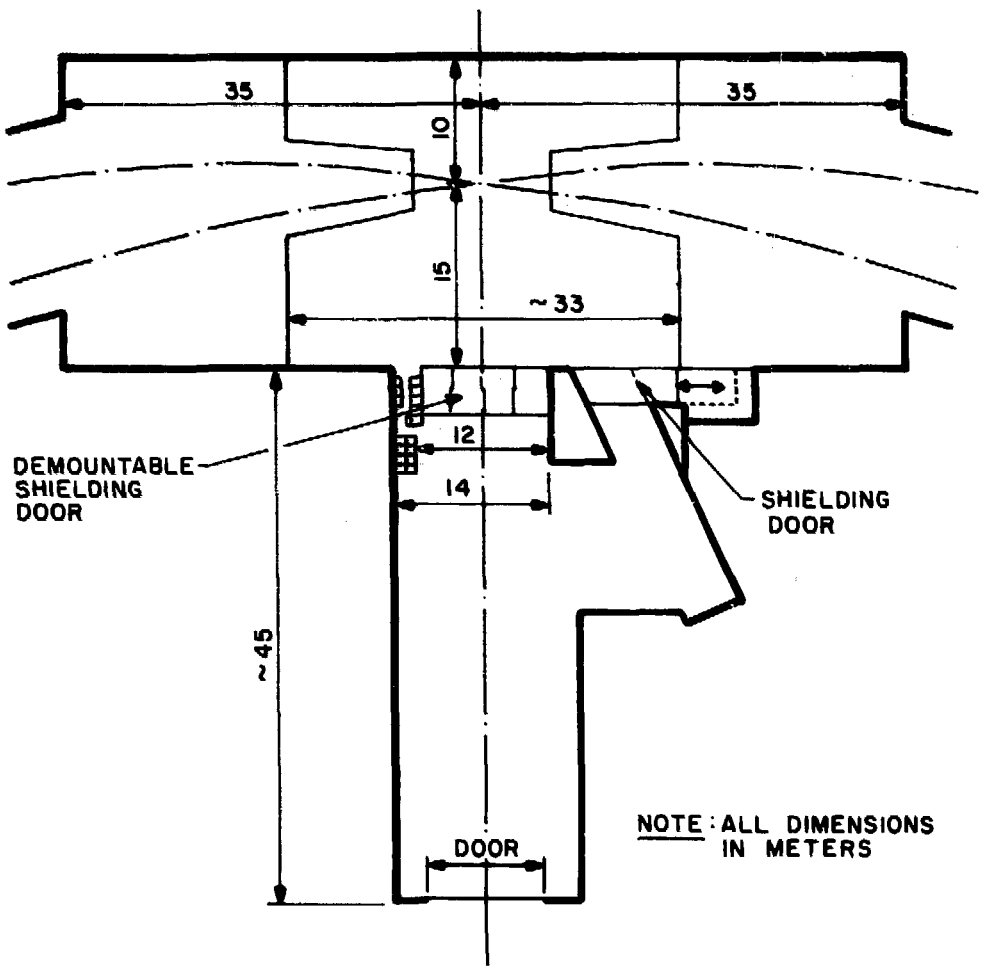

ISR – INTERSECTION I4

Fig. 3

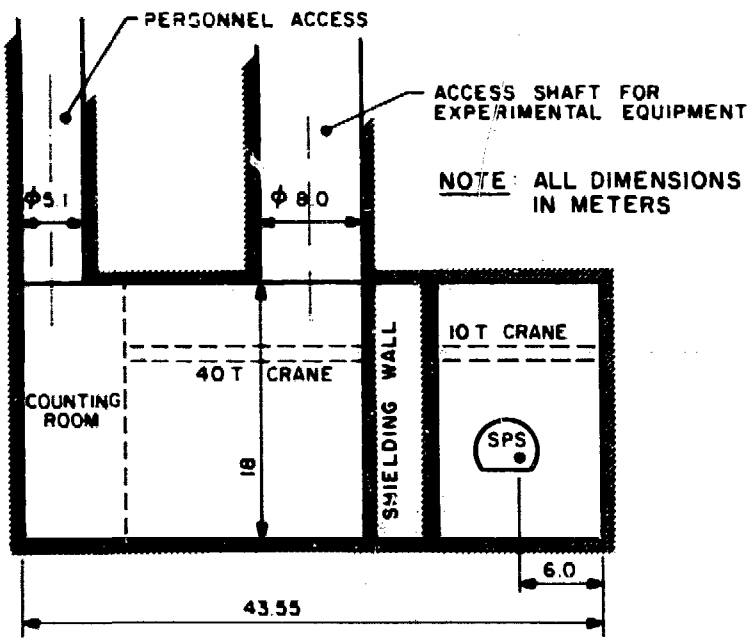

SPS-LSS4 UNDERGROUND AREA
SIDE VIEW

Fig. 4

Fig. 5 SPS-LSS4 UNDERGROUND AREA
PLAN VIEW

Fig. 6 SPS-LSS5 UNDERGROUND AREA
SIDE VIEW

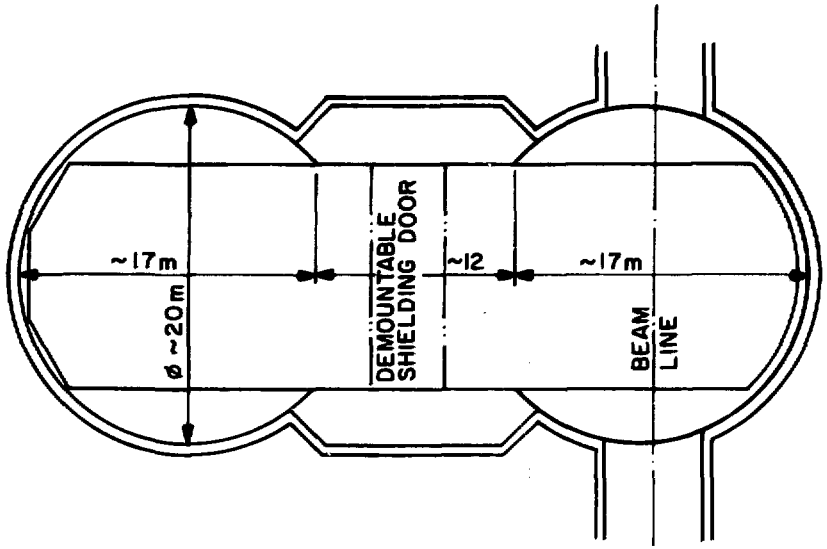

Fig. 7 SPS - LSS5 UNDERGROUND AREA
PLAN VIEW

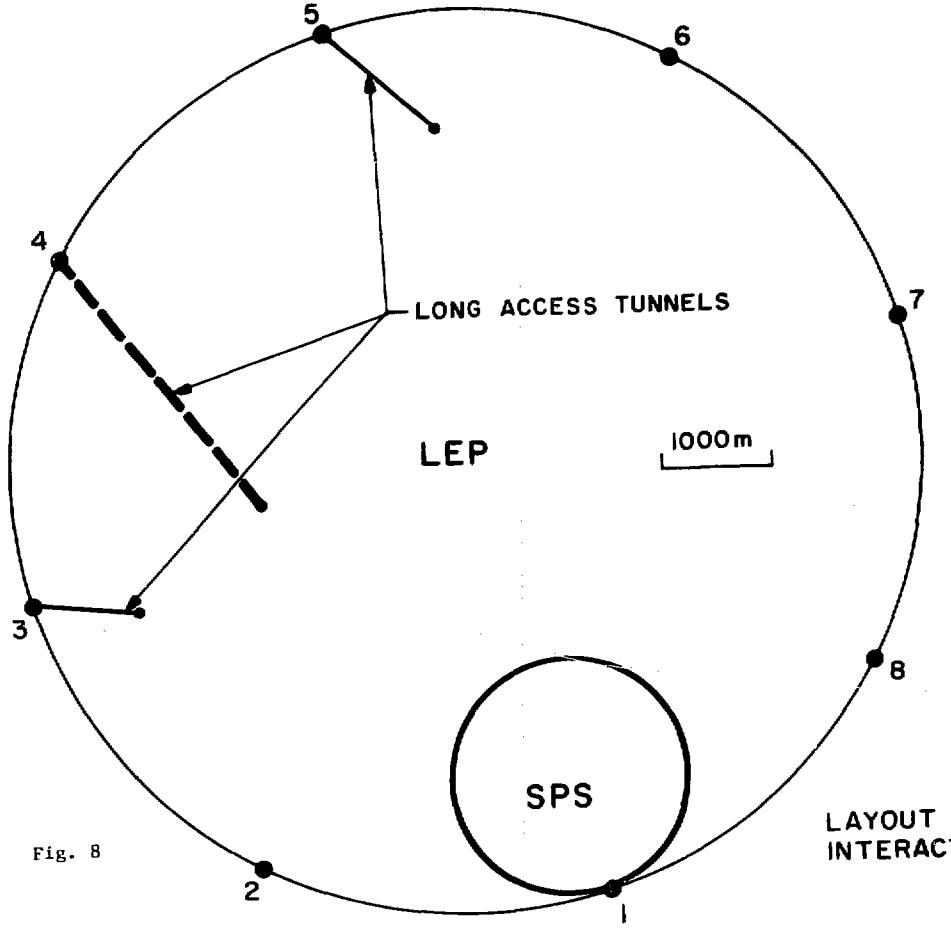

Fig. 8

LAYOUT OF THE 8
INTERACTION AREAS

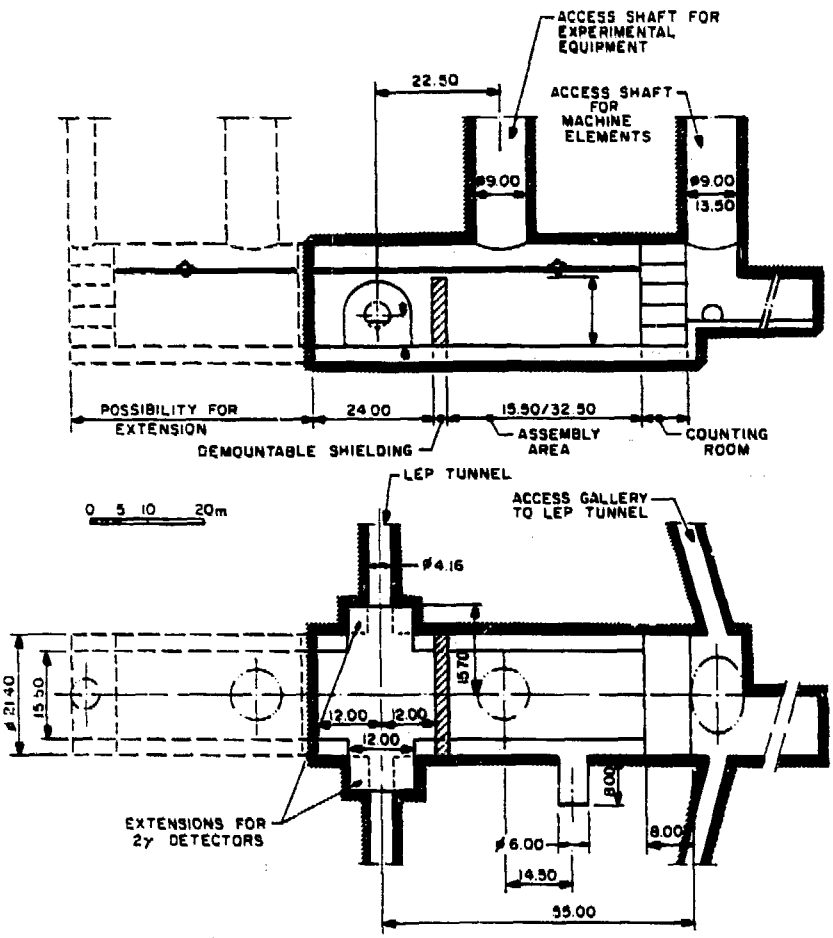

PROPOSAL FOR A LEP EXPERIMENTAL HALL

Fig. 9

EXPERIMENTAL AREA FOR THE FNAL COLLIDER DETECTOR FACILITY

D. Theriot, Fermilab

The Fermilab Collider Detector Facility is a Fermilab-based consortium of national laboratories and universities from the United States, Japan and Italy currently engaged in the design of a general purpose detector to be used in $\bar{p}p$ collisions at 2000 GeV in the center of mass at the Fermilab Tevatron accelerator. The detector uses a 1.5 T superconducting solenoid, 3.0 m in diameter, 5.0 m long for a central magnet. This is filled with a cylindrical drift chamber and surrounded by electromagnetic calorimeters, hadronic calorimeters, and muon detection. I will give a brief overview about the CDF detector (for details on detector see H. Jensen in these proceedings), but will concentrate on the experimental area itself and the interaction of the CDF detector and the experimental area.

A side view of the central detector is shown in Fig. 1. The calorimeters are divided into tower structures which point back to the interaction point. This is shown schematically in the upper right quadrant of the detector.

Figure 2 shows a side view of the backward arm ($\bar{p}$ direction) of the CDF detector. The two large toroidal magnets are used for triggering and measuring the momenta of muons emerging in this direction. The large toroid close to the central detector covers an angular region between 10° and 30°. The rear toroid covers between 2° and 10°. Located between these two toroids is a set of calorimeters to measure both the electromagnetic and hadronic components emerging from the central detector end plug below 10°. Figure 3 shows an isometric view of the entire assembled apparatus in position in the collision hall. In addition to the components previously discussed, a set of calorimeters has been added in the forward (p) direction.

Figure 4 shows a cross section of the CDF experimental area. This area is located at straight section B-$\bar{0}$ of the Fermilab Tevatron. Physically this is one sixth of the way around the ring from Wilson Hall, the high rise office building, near the present industrial buildings. The experimental area consists of three parts: an underground collision hall located around the accelerator, an assembly area located in a pit whose floor is the same level

as the collision hall, and a ground level service area. A ground level building covers both the assembly area and ground level service area. The collision hall is connected to the assembly area by a tunnel 34' x 34' square and 36' long which is plugged with 14' of shielding during accelerator operations. The lowest level occupied by the central detector is 706' above sea level. The forward and backward detectors rest at 710'. The assembly area has floors at both of these levels also. The surface service area is at 743'. The counting rooms are located on two levels of the three level structure which is located between the collision hall and assembly pit over the connecting tunnel.

Figure 5 shows a plan view of the CDF experimental area with the floor loadings and crane coverages. The collision hall is 100' long with the central 50' being 50' wide and two end regions each 25' long and 36' wide for a total of 4300 sq. ft. At the present time we have no plans for a crane in the central region. The forward-backward regions may be serviced by small cranes. All major servicing of the detector is planned to be done in the assembly area. The central detector can move directly out to an alternate location for servicing (shown in the assembly area). The end detectors move in and out of the collision hall on equipment transporters which make up the difference in floor heights (706' to 710') and have capacity to carry the units. The assembly and surface service area are covered by a 50 T crane.

It is envisioned that the magnet yoke for the central detector will be built in place in the assembly area, a pit roughly 73' wide and 87' long. The calorimeters for the central detector will be built elsewhere and installed in the assembly area. The central calorimeter modules (see Fig. 1) form free standing arches which can be assembled anywhere in the assembly area and rolled into place onto the magnet yoke. The backward toroids and the forward and backward calorimeters will be constructed in the assembly area and moved into the collision hall on the equipment transporters.

In the event that the magnet is not ready when collisions are available, the central calorimeters and forward-backward calorimeters can be assembled in a nonmagnetic configuration for early detector operations.

A tentative schedule is given in Table 1 which shows first operations in July 1984.

Table I
Tentative Schedule for CDF Experimental Area

July 15, 1981 - 70% Title I
August 31, 1981 - Final Title I
October 1, 1981 - Site Preparations
December 1, 1981 - Assembly Area Started
June 1, 1982 - Collision Hall Started
January 1, 1983 - Occupancy
July 1, 1984 - $\bar{p}p$ Collisions at 2 TeV
July 1, 1985 - Complete Detector

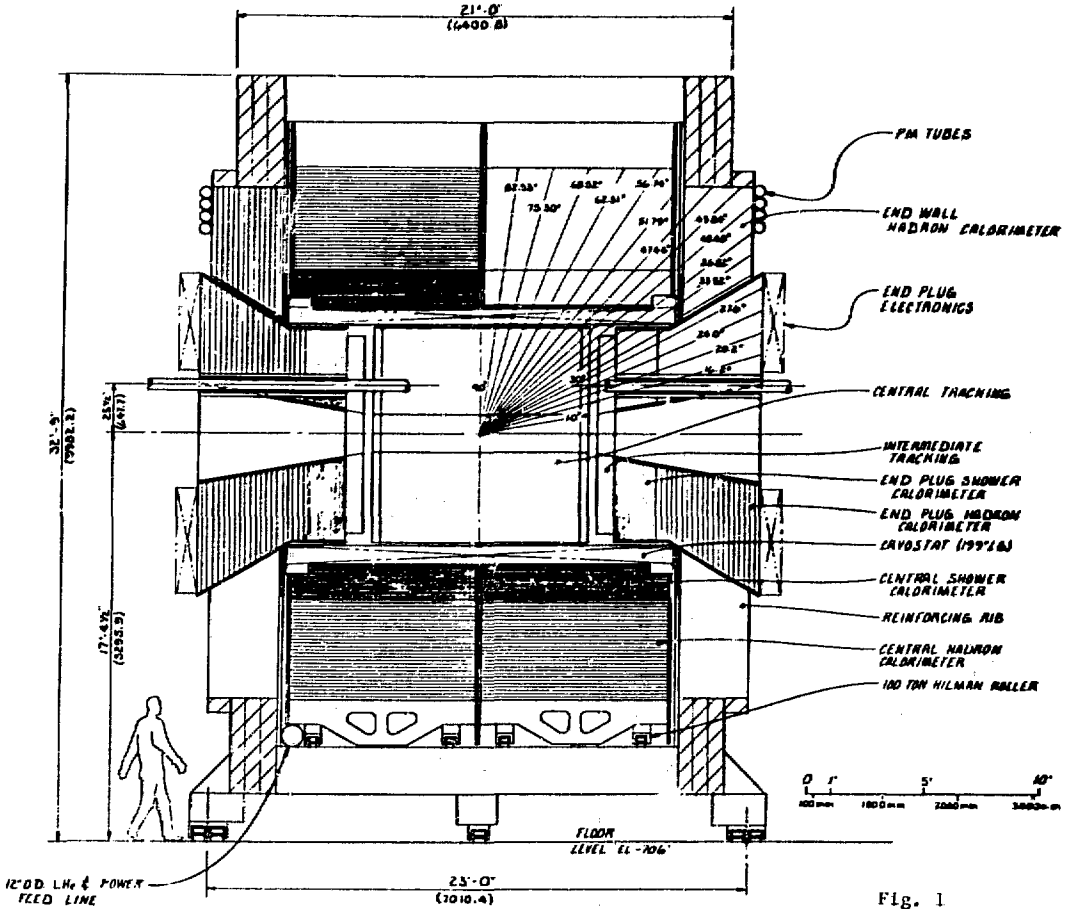
21'-0"
(6400 Δ)
PM TUBES
END WALL HADRON CALORIMETER
END PLUG ELECTRONICS
CENTRAL TRACKING
INTERMEDIATE TRACKING
END PLUG SHOWER CALORIMETER
END PLUG HADRON CALORIMETER
CRYOSTAT (1.99"Δ)
CENTRAL SHOWER CALORIMETER
REINFORCING RIB
CENTRAL HADRON CALORIMETER
100 TON HILMAN ROLLER
32'-6"
(9902.2)
25"
(647.7)
17'-4.9"
(5295.9)
FLOOR
LEVEL EL -106'
12"OD LHe & POWER
FEED LINE
23'-0"
(7010.4)
0
1'
5'
10'

Fig. 1

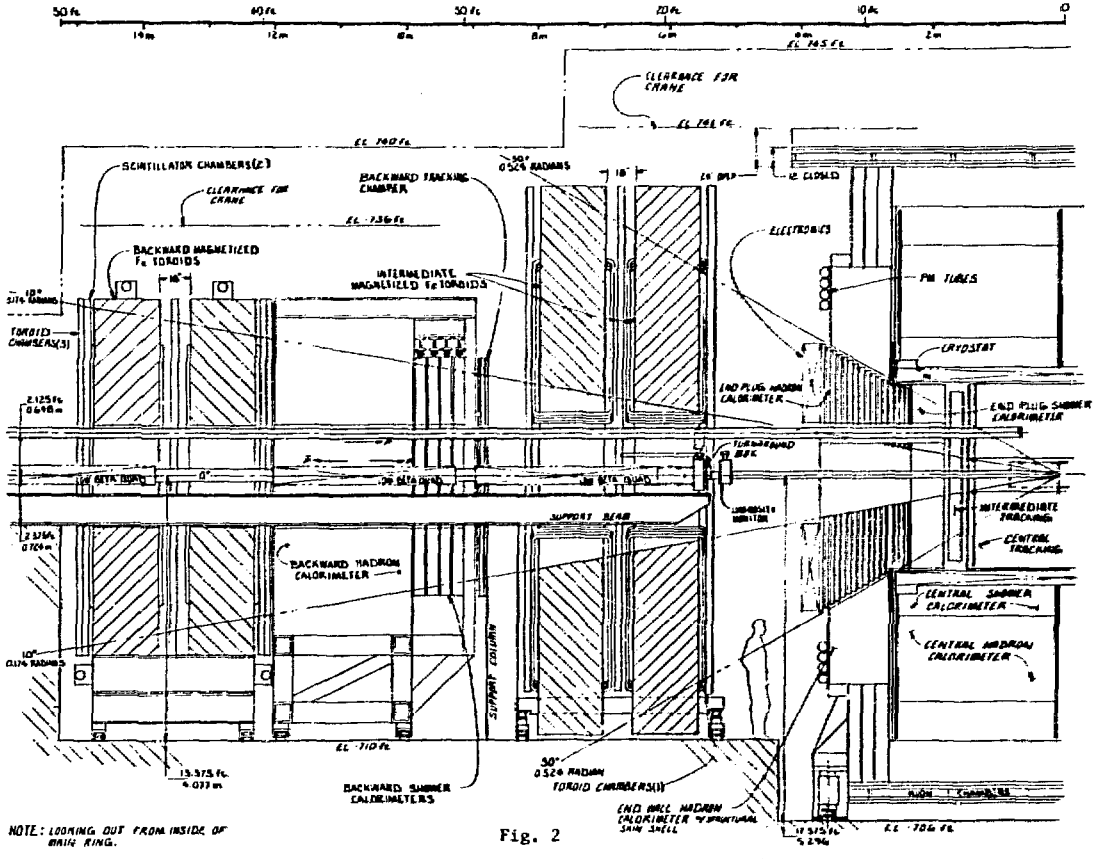
SCINTILLATOR CHAMBERS(2)
CLEARANCE FOR CRANE
BACKWARD TRACKING CHAMBER
BACKWARD MAGNETIZED Fe TOROIDS
INTERMEDIATE MAGNETIZED Fe TOROIDS
TOROID CHAMBERS(3)
ELECTRONICS
PM TUBES
CRYOSTAT
END PLUG HADRON CALORIMETER
END PLUG SHOWER CALORIMETER
TORSION BAR
INTERMEDIATE TRACKING
CENTRAL TRACKING
CENTRAL SHOWER CALORIMETER
CENTRAL HADRON CALORIMETER
BACKWARD HADRON CALORIMETER
SUPPORT BEAM
SUPPORT COLUMN
BACKWARD SHOWER CALORIMETERS
TOROID CHAMBERS(3)
END WALL HADRON CALORIMETER
EL 760 Ft
EL 736 Ft
EL 710 Ft
EL 706 Ft
NOTE: LOOKING OUT FROM INSIDE OF MAIN RING.

Fig. 2

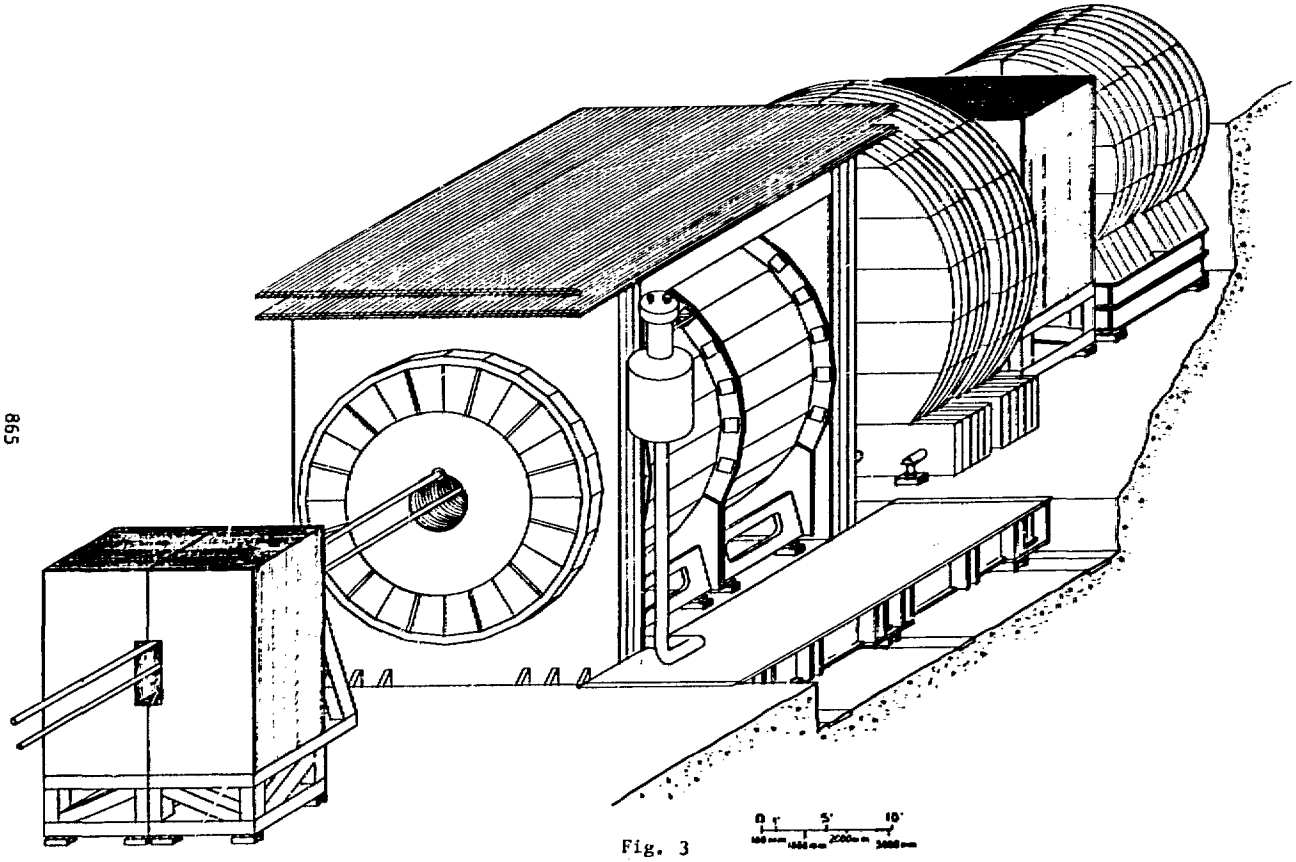

Fig. 3

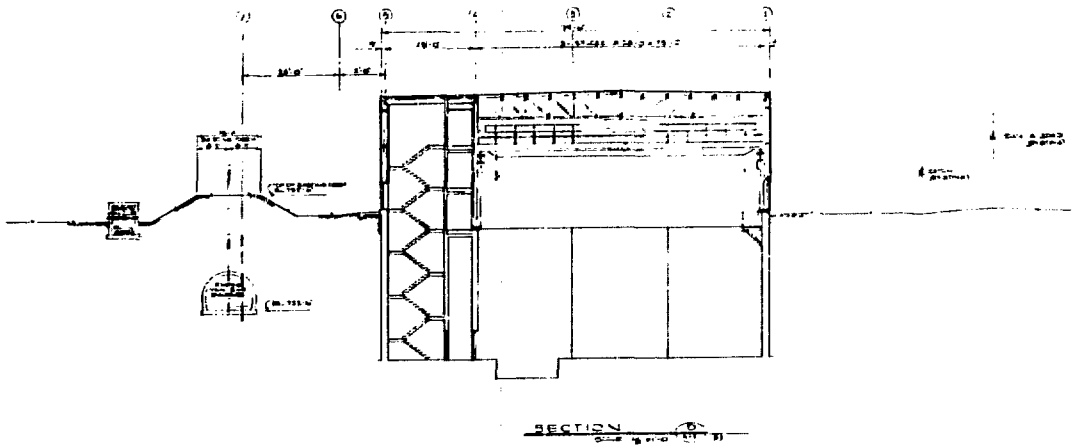

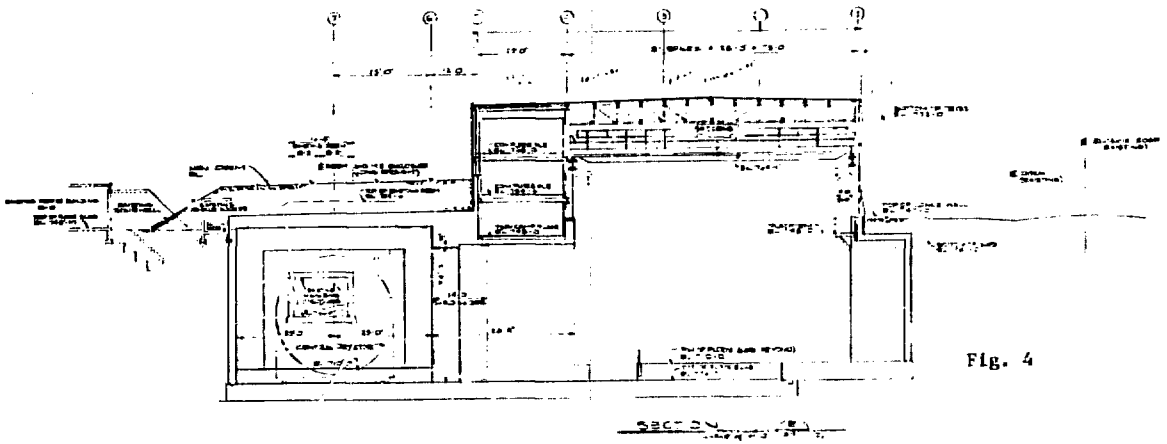

Fig. 4

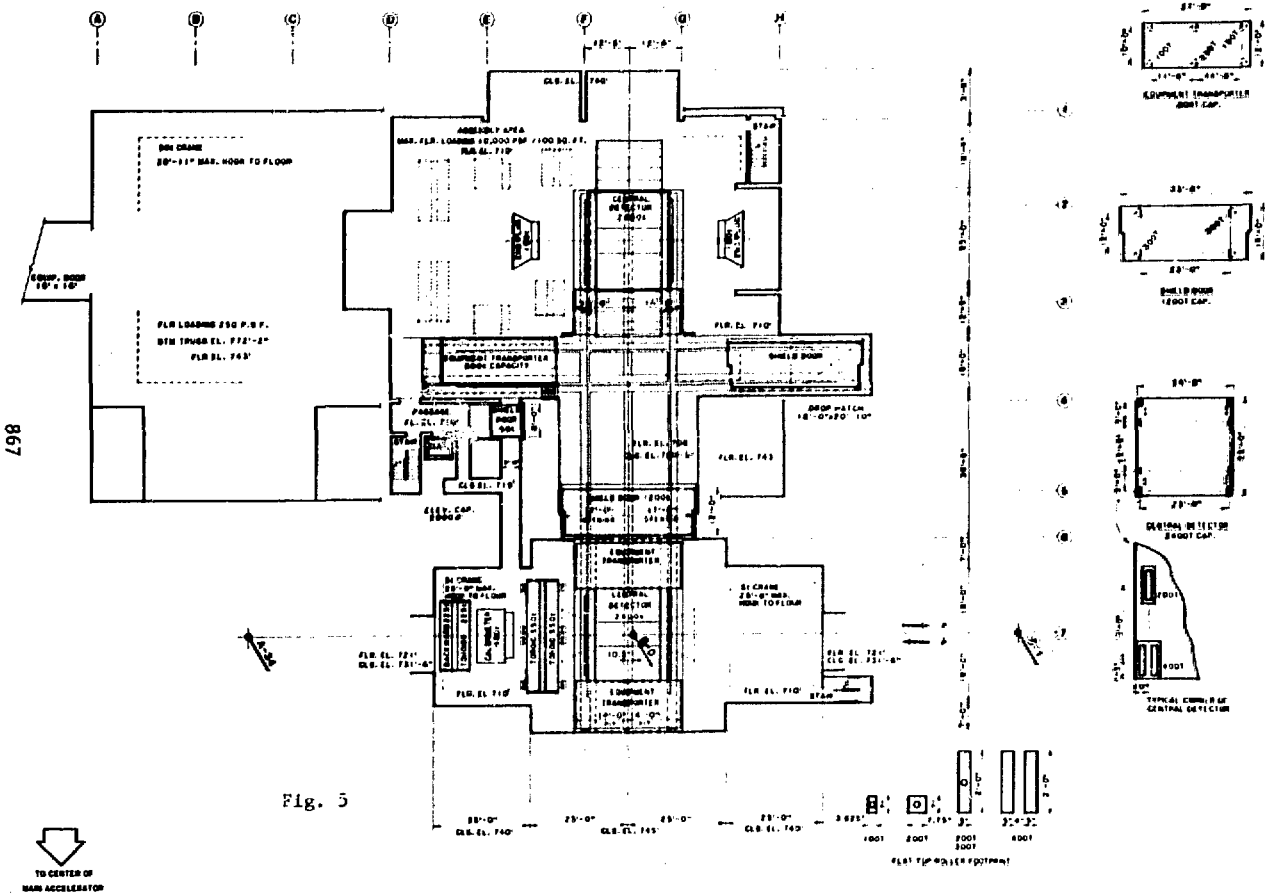

Fig. 5

EXPERIMENTAL AREAS: THE PEP EXPERIENCE

Peter Nemethy, LBL

I will take a before and after look at the PEP interaction regions. We had to design the experimental areas before the submission of proposals and the approval of experiments. The design started from the experimental ideas of several summer studies. Although the experiments finally approved did not much resemble the summer study ones, the fit of the experimental halls to the experimental program turned out to be surprisingly good.

Figure 1 shows our "standard" experimental area; 4 out of 6 halls are like this. The heavy part of the building is built into a hillside which provides shielding but prevents access from one side. A shielding wall separates this beam crossing region from the assembly area, a light steel frame building. The two regions are serviced by a single crane and share a common reinforced concrete floor.

Table I lists the interaction region halls and the experiments. Two experiments, the time projection chamber and 2 photon, coexist in IR-2 (Fig. 3). IR-6 is a nonstandard push/pull area; the terrain allowed access to both sides here. This hall was occupied by the free quark search (FQS) until this summer. We are in the midst of a changeover to the high resolution spectrometer (HRS), our heaviest PEP detector. The other special area, IR-10 is deep underground with access only through the machine tunnels. It contains the Monopole search experiment.

Figure 2 shows the typical dimensions of a standard area (they vary slightly from one to another) with a detector and its movable counting house in the "on-beam" and "service" positions. The chosen floor area is a good fit to all our experiments, although it is very crowded in IR-2 where TPC and 2 have to coexist (Fig. 3). At times the logistics of assembly got very difficult with all parts of the floor occupied.

The standard beam height of 4m (except in IR-10, not meant for experiments originally) was needed for all experiments, including the smaller ones. A small central trench was needed to accommodate the magnet yoke of the

HRS. Among the twenty proposed experiments only one would have gotten us into trouble with a much greater beam height requirement.

The only case, perhaps, of overkill was the insertion length, chosen as ± 9 m on the basis of the summer study result that experiments could not possibly exist with less free length. For the impressive benefits of mini-beta, a solution was found for bringing the first injection quads to ± 6m Fig. 4) compatible even with the 2γ experiment. We are implementing the change this summer.

Our standard crane capacity of 50 tons (100 tons for HRS) was quickly saturated, like any new urban highway. All experiments are using the full crane capacity; sometimes the needs exceed it by $(1 + \epsilon)$.

Rapid equipment access to detectors is very desirable in a colliding ring, where work on one detector requires the shutdown of the entire ring. Figure 5 shows our solution, a concrete precast shielding curtain riding on rails and spanning our standard IR above a stacked shielding wall. The curtain is moved by coupling it to the crane. This scheme has worked very well, allowing crane lifts across the shielding within a half-hour of shutting down the ring. In our open IR-6 we have a concrete blockhouse with a concrete beam roof enclosing the beam crossing region. In IR-10, originally meant for machine physics only, the lack of access caused difficulties even for the "totally passive" monopole search setup.

Our movable counting houses (of the order of 1000 sq.ft.) contain the front-end, parallel electronics. The fixed counting houses, with 2400 sq.ft. on 2 floors, house the back-end electronics and data acquisition computers very comfortably for 1 experiment/IR and somewhat tightly for 2 experiments in IR-2.

We had decreed that all experimental setups must be movable without uncabling 10^4 parallel cables, for fast removal from the beam line to deal with any serious repairs. The design goal was 24 hours for removal and 48 hours for reinstallation to match the ring pumpdown time of about a day. However, all initial experiments chose, understandably, to set up directly on the beam line, so that we did not have a test of this "rapid deployment" concept until recently. However, we have just performed the first push/pull changeover between two experiments in IR-6, replacing FQS with HRS during this

summer's shutdown (Fig. 6). We spent 2 1/2 single-shift days to remove all shielding, then 2 1/2 single-shift days to roll in the 2000 ton HRS detector on its multi-ton rollers and with its attached counting house.

The switch went without difficulties and in much less time than scheduled, confirming our belief in the efficacy of the prewired detector/attached movable house scheme. To our consternation, however, the slight floor sag under the weight of HRS tilted our shielding buttresses enough to require our giving a close shave to the shielding house roof blocks.

Table I
Specifications for Experimental Areas

SPECIFICATION	AREA 12	2	4	6	8	10
Length (m)	20	20	16	20	20	20
Width (m)						
Inside	7	7	6	20	10	3.5
Outside	24	24	22	20	31	3.5
Height (m)						
Maximum crane hook clearance above beam	6.5	6.5	6.5		6.5	
Beam elevation above floor	4	4	4	4	4(6)	2
Maximum height of detector (curtain shear line)[a]	4(5)	4(5)	4(5)		4(5)	
Crane (tons)	40(50)	40(50)	40(50)	No	40(50)	No
Nearby Space for Counting House (mxm)	9x11 +10x12	10x12 +10x12	9x22.5		9.5x15 +12x12	No
Alcove	Yes	Yes	No	No	Yes	No
Length (CW) (m)	20	20			20	
Width ± (m)	3.5	3.5			3.5	
+ (m)	3	3			3	
Height - (m)	2	2			2	
Power (MW)						
At 12.4 kV [b]	5	5	5	5	5	5
Installed cooling capacity	1	1	1	1	1	0
House power (480 V 3 ϕ)	0.9	0.9	0.9	0.9	0.9	
Loading Access	outside yard	outside yard	outside tunnel	both sides	outside yard	beam tunnel

[a] If more than 4 m are needed, a special curtain may need to be designed.
[b] Maximum overall limit on 12.4 kV from experimental areas is 15 MW.

FIGURE CAPTIONS

Fig. 1. Standard PEP interaction region hall

Fig. 2. Standard hall size with a detector in in and out position

Fig. 3. Our crowded IR-2

Fig. 4. Original and revised position of last insertion quad

Fig. 5. Shielding curtain scheme

Fig. 6. Push/pull exchange of FQS for HRS

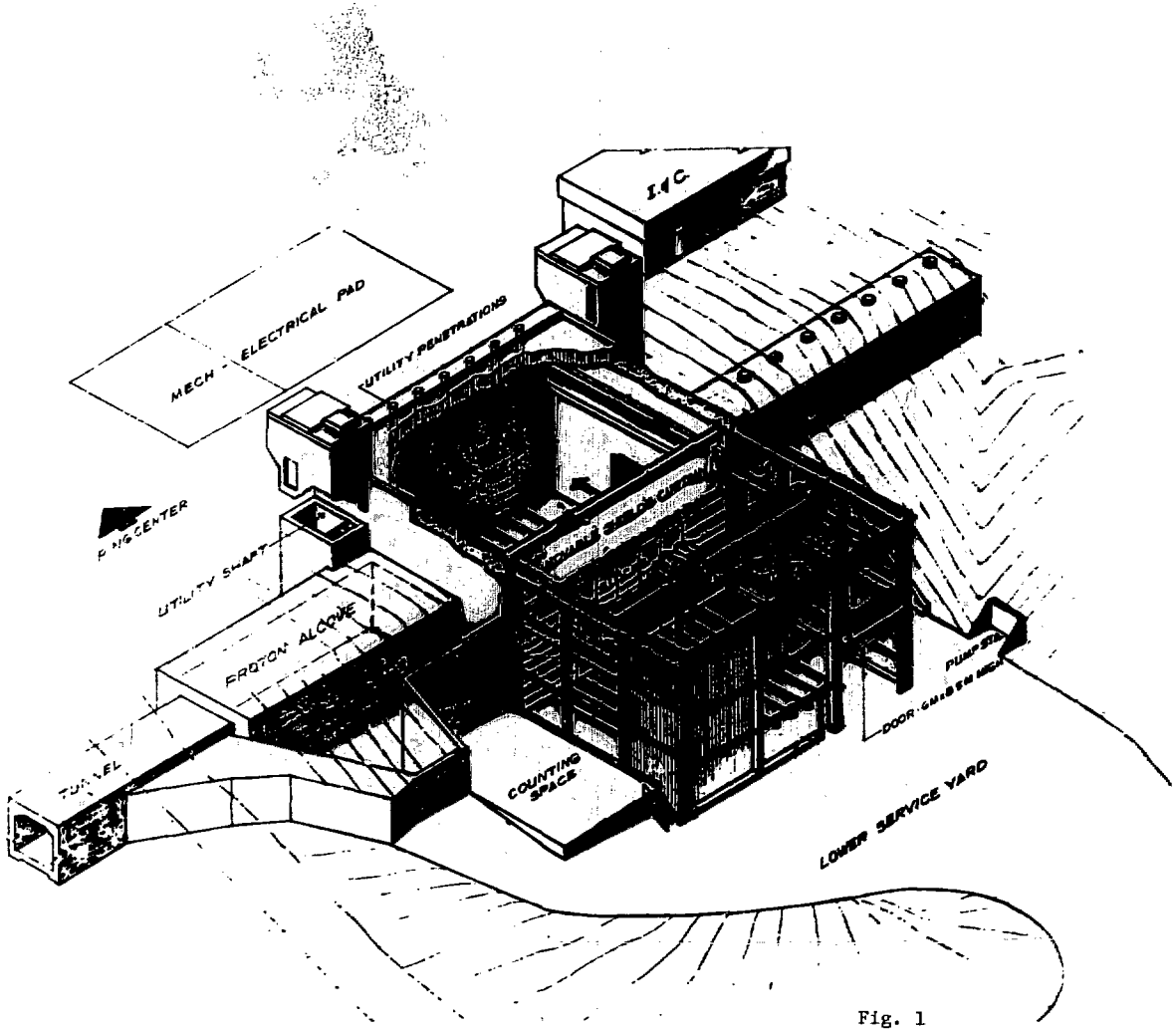
I.C.
MECH. - ELECTRICAL PAD
UTILITY PENETRATIONS
P.N.G. CENTER
UTILITY SHAFT
FROTON ALCOVE
TUNNEL
COUNTING SPACE
LOWER SERVICE YARD

Fig. 1

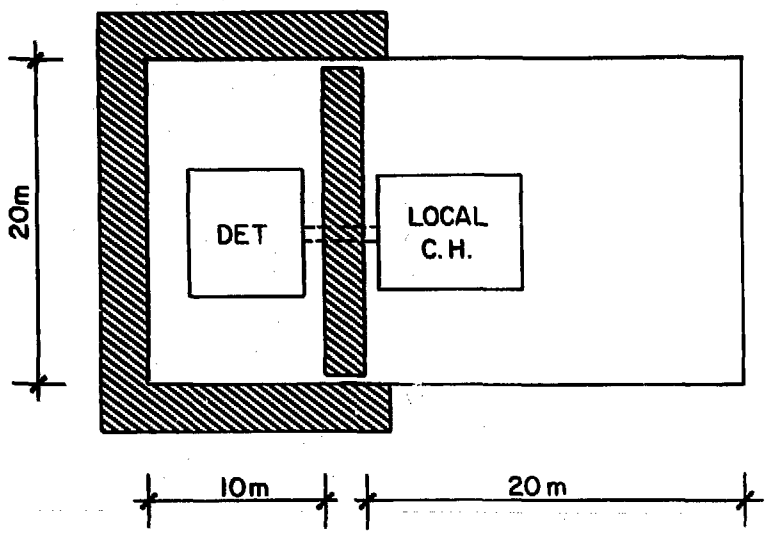

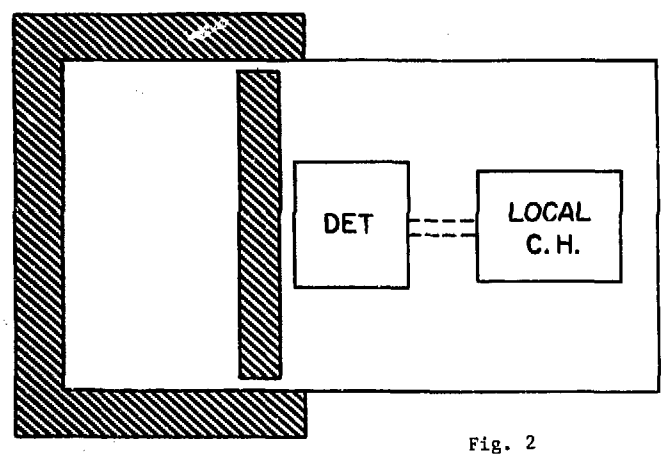

Fig. 2

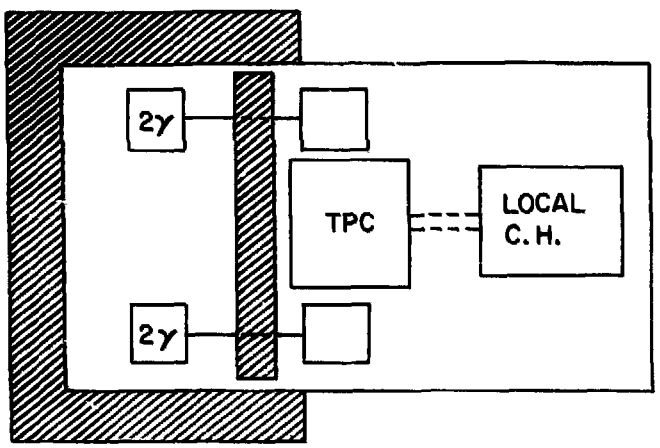

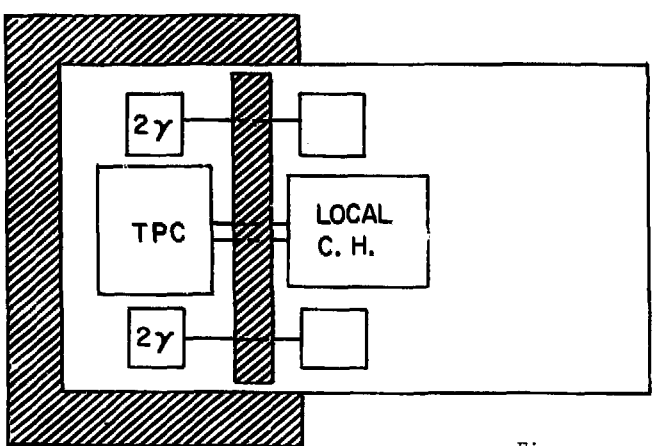

Fig. 3

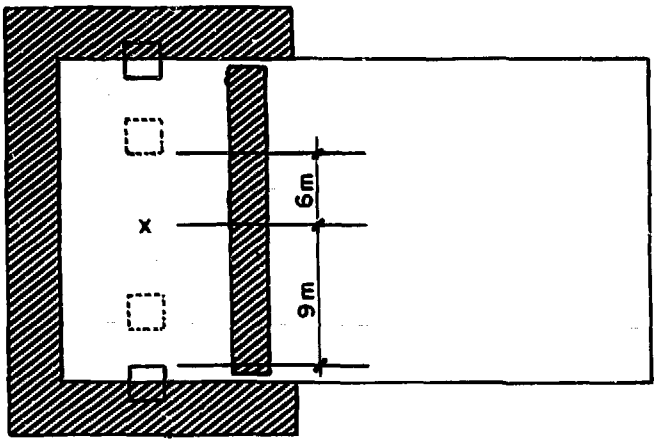

Fig. 4

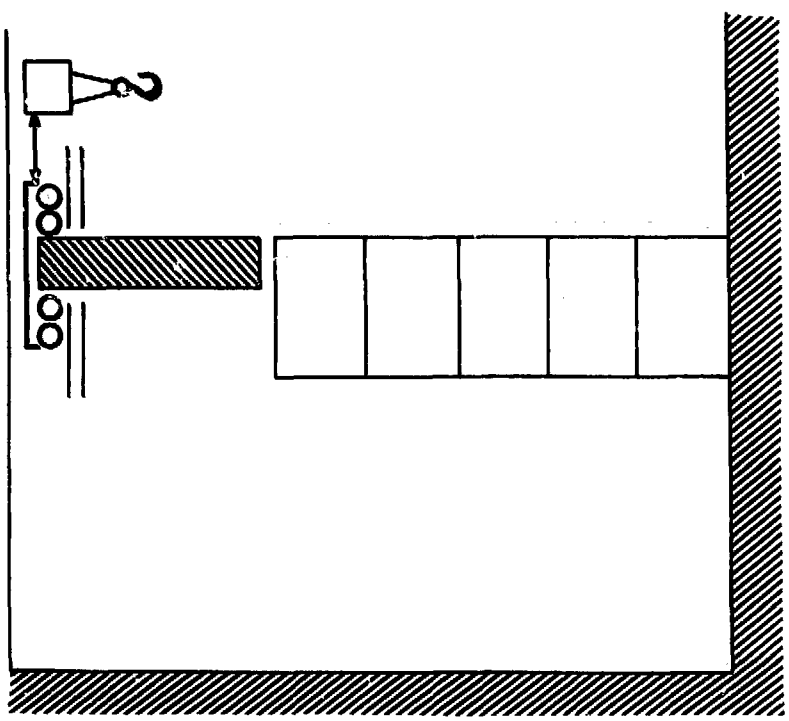

Fig. 5

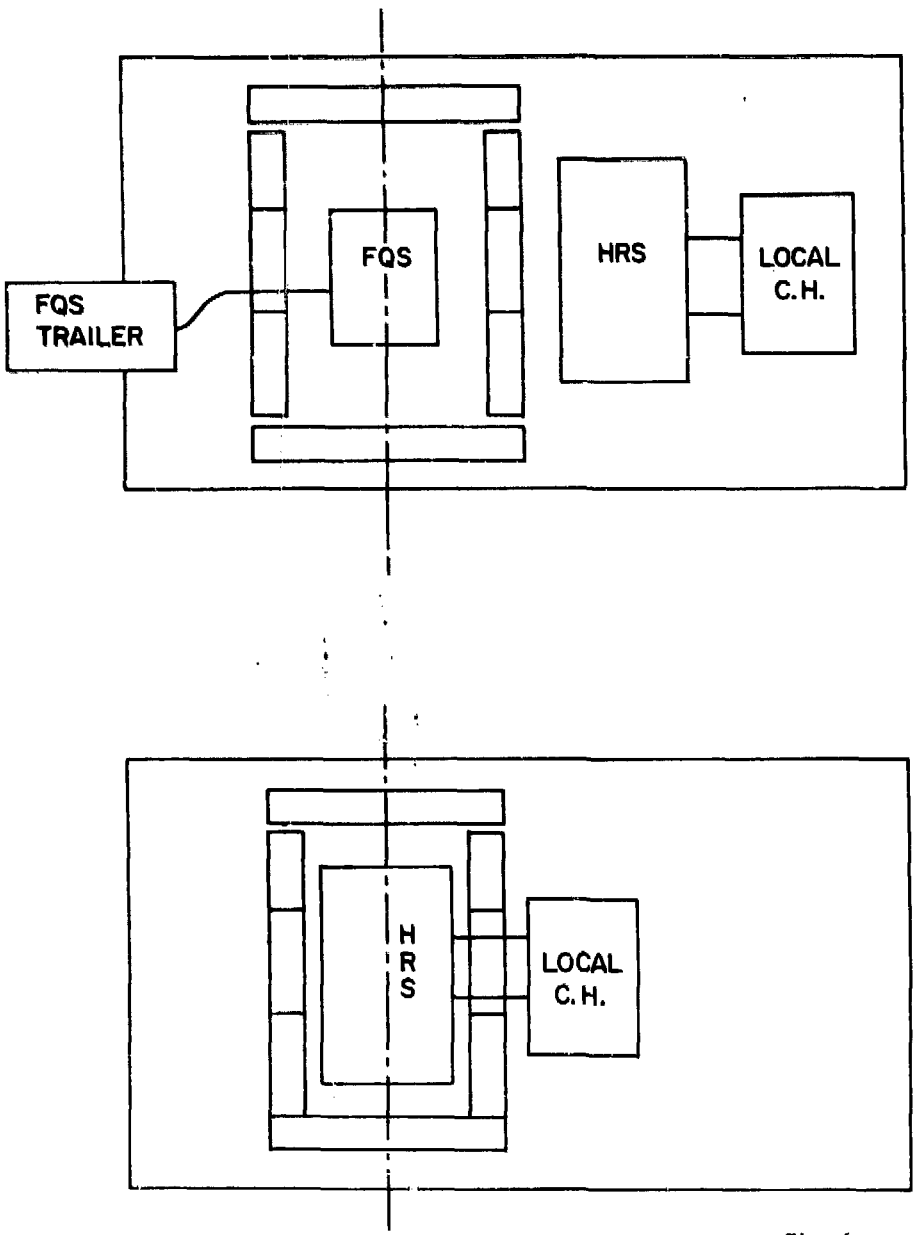

Fig. 6

SECTION IV

LARGE DETECTORS

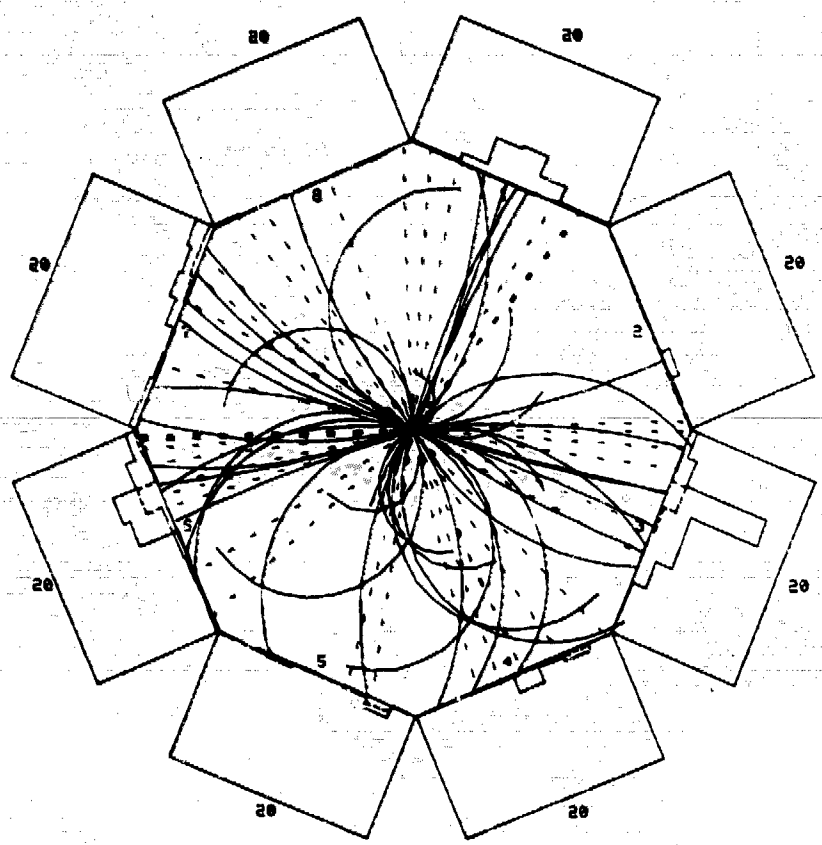

SUMMARY OF THE LARGE DETECTORS GROUP

H. Gordon, BNL
C. Baltay, Columbia University

This group examined the existing designs and plans for large detectors at ISABELLE. Various working subgroups formed. Here we will outline the topics as presented in the following papers. One subgroup tried to identify the physics strengths of each detector and to evaluate whether important physics could be done with them in the proposed Phase I luminosity of 2×10^{31} cm^{-2} sec^{-1}. A survey of various magnetic field configurations was made. Another subgroup analyzed the effect of the bunch structure on these detectors. One working group considered how to handle the Phase II luminosity. A group also studied the important subject of calibration and on line monitoring.

At first we had a series of talks outlining the large detectors in the design stage for ISABELLE as well as those under construction for the $\bar{p}p$ colliders at CERN (talk by Sumorok) and at Fermilab (talk by Jensen).

U. Becker presented the detailed design of the BNL/MIT/NIKHEI/Beijing group for a detector which focuses on measuring muons with excellent momentum resolution. This is achieved by having a hadron calorimeter close to the beam pipe followed by precision drift chambers in a superconducting solenoid. Some details of this detector will be found in other reports of these proceedings, for example, S. C. C. Ting's paper, page 334, papers by Paradiso and Becker.

The BNL/Columbia/Pennsylvania group has concentrated on achieving excellent electromagnetic and hadron calorimetry by using uranium plates in a dipole magnetic field. This field allows detection of particles both forward and sideways while providing an open geometry. The calorimeter is segmented so as to allow good reconstruction of multijet events, as discussed in a paper by Gordon, Stumer and Benary. Smith and Gordon consider several calorimetric triggers.

The BNL/Brown/Stony Brook group has chosen a limited aperture detector in order to focus on electromagnetic particles: π^0, γ, and $e^{\pm}$. The use of

lead glass will optimize the energy resolution as is detailed in the "Lapdog" paper presented by P. Grannis.

Chen explores the notion of a large detector filling a 10 meter cube. Since the quality of a magnet depends on BL^2, this design emphasizes the length by having a low field far from the intersection region.

Ypsilantis presents the concept of using a spherical ring imaging Cerenkov counter for the purpose of excellent particle identification in a weak magnetic field.

The working group organized by Abe considered what capabilities will be required in the detectors in order to pursue specific physics goals. Abe discusses how well the jet-jet invariant mass can be measured by a calorimeter. Csorna studies the inclusive lepton and hadron spectra from QCD jets so as to measure semileptonic branching ratios and find signatures of new flavors. Bacon suggests the requirements necessary to be able to detect multiple vertices in an event.

A review of the strengths and weaknesses of solenoids vs. dipoles vs. solenoids by the subgroup chaired by Pope precedes the section on magnets. Littenberg presents the progress on the design of a large dipole magnet. Bregman reviews why the dipole is preferred by that group. Grannis shows how the idea of the magnet for Lapdog evolved. Luckey and Ting discuss the use of conventional magnets in, for example, the Magnetic Hall Detector mentioned by Chen. Pope explains the virtues of a toroidal magnetic field for many different detectors. The toroid field has no effect on the beams and is closed so that no flux return is required. However, the coils may obstruct a fraction of the solid angle and need quite strong support.

The main effect of the bunched beams is to give 30% of the events which occur with another event in the same bucket. The report of the working group headed by Blumenfeld points out that experiments may need to distinguish these multiple events by using time differences, by reconstructing the vertices, or by finding too much energy via calorimetry. Johnson comments on how to try to resolve multiple interactions.

The next working group led by Morse studies whether detctors that are designed for Phase I luminosity can be upgraded to handle the Phase II

luminosity. Johnson shares some lessons learned at the AGS in an experiment that operated at rates of 10^7/second. Bozoki reminds us that the machine magnets must be quite reliable in order to do any physics.

Finally, a group headed by Sumorok reviews various calibration and monitoring schemes that have been used in large detectors. They then recommend some principles that should be followed in the coming designs.

We concluded that all of these detectors could do important physics in Phase I. A detailed study of Z^0 and $W^{\pm}$ production would be possible, as well as a search for higher mass Z's or W's. Bound new flavor states will be looked for with mass above 40 GeV. The Higgs or technicolor production might be seen. Large transverse momentum jets would be studied to test QCD. We concluded that the development of a high precision vertex detector to allow the direct detection of the decays of charm or bottom particles would be most useful.

HADRON CALORIMETRY AT ISABELLE

H.A. Gordon, I. Stumer, BNL
O. Benary, Tel-Aviv University

I. INTRODUCTION

At very high energies, calorimetric methods have become increasingly more essential for measuring hadronic energy. We present here a study of the capabilities of calorimetry at $\sqrt{s}$ = 800 GeV at 90^{o}.

The rising multiplicity and complexity of the new physics can be easily exemplified by the event in Table I where a pair of $t\bar{t}$ quarks are produced at $\sqrt{s}$ = 800 GeV in a pp interaction. Each outcoming quark has a $p_{\perp}$ = 100 GeV and emerges at y = 0. We are using for this study a QCD Monte Carlo program written by F. Paige and S. Protopopescu.[1]

The two beam fragments will be contained mostly in the beam pipes, but a non-negligible fraction of their particles will contaminate the physical measurements even at 90^{o} (see S.D. Smith and H. Gordon[2]).

In the second section we describe our "idealized-realistic" detector and the showers' parameterization.

In the third section we will try to identify jets by calorimetry; e.g. mass, width.

The fourth section will deal with a "real" problem: can one select Z^{o} events, when Z^{o} decays into two hadronic jets amid the much higher background of two back-to-back jets produced at $\sqrt{s}$ = 800 GeV.

II. THE CALORIMETER, ENERGY DEPOSITION, JET RECONSTRUCTION

Figure I shows an axial view of the trajectories of the particles from a Z^{o} decaying into $t\bar{t}$. The layout of our calorimeter is the following: there are 8 units arranged in an octogonal cylinder around the beam pipes which are perpendicular to the plane of the paper. The front face of each unit is 2.0 meters from the beams. Each of these units is segmented into 20 cm x 20 cm towers which are seperately read out. Each unit covers $\pm 65^{o}$ in theta which is equivalent to a rapidity coverage of $-2<y<2$ out of a maximum of ± 6.7 for $\sqrt{s}$ = 800 GeV.

The magnetic field was of the solenoidal type with a constant B_Z = 10 KGauss. The neutral particles are represented by dashed lines.

Figures 2 and 3 display the energy deposition of the jets in our octants. There are 8 towers across and 40 towers along the beam directions.

Figure 2a shows the points of incidence of different particles on the face of our calorimeter.

Each tower consists of 2 mm uranium plates as an absorber, sampled with 2.5 mm scintillator plates which are read out by wavelength shifters.[3]

Our calorimeter is 1.1 meters deep and has a total of 5.8 absorption lengths and 56.6 radiation lengths.

The energy deposition in each tower is subdivided into two signals: an "electromagnetic" part (pulse height in the first 10 radiation lengths of depth) and the total "hadronic" part.

We have assumed that each hadron (photon) interacts after a distance, Z, the probability distribution of which is given by

$$f(Z) = 1/\lambda \exp(-Z/\lambda)$$

where λ is the nuclear interaction (radiation) length. Once the particles interact we have used the mean longitudinal parameterization suggested by R. Bock et al.[4]

The energy deposited, E, as a function of S is given by

$$dE/dS = f(S)$$

normalized in such a way that a fully contained shower should deposit all of its incident energy, E:

$$\int_0^\infty f(S)dS = E.$$

For an electromagnetic shower of energy, E, at a depth, X, expressed in radiation lengths such as: $X = \beta(S/X_0)$, the energy deposited will be:

$$dE = E \frac{X^{\alpha-1} e^{-x} dx}{\Gamma(\alpha)}$$

where $\alpha = 2.286 \pm 0.7136 \log E$ (E in GeV),

$\beta = 0.5607 \pm 0.0093 \log E$.

The longitudinal profile of a hadronic shower which starts at a depth, S_o, was parameterized by a two component expression of the form:

$$dE = E\left[C\,\frac{X^{\alpha_E-1}e^{-x}dx}{\Gamma(\alpha_E)} + (1-C)\,\frac{y^{\alpha_H-1}e^{-y}dy}{\Gamma(\alpha_H)}\right]$$

where E is the incident energy, $X = \beta_E\cdot(S-S_o)/X_o$ is the number of radiation lengths accumulated since the start, S_o, of the shower multiplied by a dimensionless coefficient β_E, $y = \beta_H\cdot(S-S_o)/\lambda$ is the number of absorption lengths accumulated since the start of the shower multiplied by another dimensionless coefficient, β_H. C represents the "electromagnetic component" of the hadronic shower ($0 \le C \le 1$).

We used the values fitted to the UAl calorimeters after special precautions were taken to insure linear response for hadrons below 2 GeV and photons below 0.5 GeV:

$$C = .4634$$
$$\alpha_H = 0.6165 + 0.3183 \log E \qquad (E \text{ in GeV})$$
$$\beta_H = 0.9099 - 0.0237 \log E$$
$$\alpha_E = \alpha_H$$
$$\beta_E = 0.2198.$$

For the lateral development of the showers, we have used a two-dimensional gaussian distribution where the variance, σ, was taken to be equal to one half of one "equivalent absorption (radiation) length" for hadrons (photons). One equivalent absorption length in our real calorimeter is defined as the total depth of the calorimeter, 110 cm divided by the total of 5.8 λ; for the hadronic component: $\sigma_H \simeq 19$ cm; for the electromagnetic component of the hadron shower and for photons and electrons: $\sigma_E \simeq 2$ cm.

We have also assumed that the scintillators will react only to the "visible energy" which was taken to be 90% out of the electromagnetic showers and 70% of the hadronic showers.

We have assumed that the pulse heights of the scintillators and the wave length shifters do not suffer from attenuation length problems.

We assume a $\Delta E/E = 0.40/\sqrt{E}$ as a hadronic resolution and a $\Delta E/E = 0.15/\sqrt{E}$ as an electromagnetic shower resolution. Those values are actually about 10% worse than the measured ones in similar uranium-scintillator calorimeter.[5]

No other shower development-deposition fluctuations were used for this study.

Figures 2b and 3b display the energy deposition in two of the octants of Fig. 1. The energy deposited in each tower is represented by a vertical line. The scale is indicated by the vertical line in the lower left corner of the figure. All of these energies are projected onto the front face of the calorimeter and a one to one correspondence with the point of incidence displayed in Figs. 2a, 3a should be visible. Sometimes the energy in a tower appears as a double width line: the left part is proportional to the energy deposited in the "electromagnetic floor" (first 10 radiation lengths); the right line represents the total energy of the tower.

The histograms of Figs. 2b and 3b show the energy deposition when one projects all the towers on the two directions. The dashed histograms represent the energy accumulated in the "electromagnetic floor" only.

In this particular shower simulation, all the geometrical effects were taken into account: non normal incidence, side and back leakage.

Pattern Recognition

A rather sophisticated pattern recognition program was made. The program is able to identify subclusters of energy deposited within a jet.

For this paper we have used a simplified pattern recognition program in which every jet was treated as a single cluster and all the energy deposited in the calorimeters was assigned to our jets. This approach should be equivalent to some on-line fast processor pattern recognition to be used in a possible multi-jet trigger. E_i is the summed energy deposited by all the particles into an individual tower. From each hit tower a vector was constructed from the center of the intersection region towards the center of the tower on the calorimeter face, defining a four vector $(\vec{E}_i, E_i)$.

This procedure introduces numerous approximations and systematic biases:

1. The front face of the calorimeter does not represent the "effective plane" where the center of gravity of the shower should be located.

2. The positioning of the shower in the center of the tower does not give the best estimate of the direction of the particles. (Improvements could be done by smaller tower cross sections, by balancing two independent left-right readout of the pulse height of a particular tower, or by

considering the pulse height in adjacent towers to the one struck.)

3. The fact that no mass is assigned to each tower in forming the four vector could bias the measurement of the jet mass.

III. IDENTIFICATION OF JETS VIA CALORIMETRY

First we will address the question of how the magnetic field will affect our measurements of the properties of the jet. 40 GeV u quark jets were generated in ISAJET and projected into our calorimeter. The mass of the jet calculated from ISAJET was m = 12.5 ± 4.8 GeV. In Fig. 4a we show the measured mass in the calorimeter as a function of the magnetic field. For B_Z = 0 KGauss we obtain m = 10.9 ± 3.1 GeV.

One can observe that the mass of light quark jets is independent of the strength of the magnetic field applied. In fact it is also independent of the direction of the field as well.

Of course these statements rely heavily on the way we assume that the quark materializes into hadrons. The total momentum of the jet is affected by the intensity of the magnetic field and this can be seen in Fig. 4b. Nevertheless, for B_Z = 0 KGauss the calorimeter measures a momentum of 39.3 ± 4.6 GeV to be compared with a momentum calculation of 39.4 ± 1.0 GeV from ISAJET.

The shift in mass as calculated by calorimetry in comparison with the direct calculation in ISAJET is most probably due to the biases (1) and (3) mentioned at the end of the previous section. We also remark that the percentage error in the measurement of the mass was not increased by the calorimetric method.

One of the most interesting questions for the future physics is: can one identify the quark by measuring the jet mass? We have assumed a fixed decay chain for the t quark and changed its mass in steps up to 25 GeV. The solid dots in Fig. 5 represent the mass of 40 GeV t jets calculated in ISAJET as a function of the quark mass for B_Z = 0 KGauss. The triangles and the X in the same figure show the calorimetric calculated mass for two different acceptances of the calorimeter: $|\Delta y| \leq 2$ and $|\Delta y| \leq 1$, respectively. One can observe that when the mass becomes non negligible in comparison with the

momentum of the jet, the acceptance of the calorimeter should be maximized.

QCD predicts at $y = 0$, $p_\perp = 40$ GeV, a ratio of 1/1000 for t quarks versus all the other light partons: u, d, s, g. For a calorimeter with a $|\Delta y| \leq 2$ the calorimeter measures m(u jet) = 10.9 ± 3.1 GeV and m(t jet) = 18.6 ± 4.5 GeV (for a t quark mass of 20 GeV). If one selects only jets with a mass bigger than a certain mass, m, we have calculated by how much the t jets/all jets ratio will increase. For example, let us assume that a very sharp trigger threshold can be applied on the mass of the jets. If one accepts only jets with a mass bigger than 18 GeV, only ∿ 1% of the light constituent jets will survive and we will lose ∿ 48% of the t quark jets. Now the ratio t jets/all jets has become approximately 4%. This ratio is displayed in Fig. 6 as a dashed line as a function of the mass cut, m. If one assumes that the t quarks are produced in pairs (i.e. back-to-back $t,\bar{t}$ jets), the rejection over the regular constituent jets is much bigger and the ratio of $t\bar{t}$ jets/all jets can be ∿ 90% (see solid line in Fig. 6).

In the ISAJET Program the mass of the jet increases when the momentum of the jet increases. New technicolor states, like η_T may have masses of ∿ 200 GeV and sizable branching ratios into $t\bar{t}$ pairs. That will require jet identification for momenta of 100 GeV/c. Figure 7a(b) shows the mass of the u(t) quark jet reconstructed through calorimetry when those jets were generated at momentum of 100 GeV/c. One obtains $m_{u\ jet} = 21.0 \pm 5.3$ GeV and $m_{t\ jet} = 28.7 \pm 5.1$ GeV for a t quark of mass 20 GeV. Now, the power of rejection by jet-mass selection against regular constituent jets has become not useful.

In conclusion, the jet-mass should provide a useful tool in selecting heavy quark-antiquark states at $y = 0$. A calorimeter with good solid angle coverage $|\Delta y| \leq 3$ could do the job for masses of the quark of the order of 20 GeV and $p_\perp$ of the order of 50 GeV. We estimate that an increase of the $p_\perp$ to 100 GeV/c or a measurement of the jet at higher rapidity will make the jet-mass identification less useful.

IV. Di JET MASS - IDENTIFICATION OF Z^0

To approximate the detection of the $Z^0 \to u\bar{u}$ or $\to t\bar{t}$, we generated events with the transverse momentum of each jet set to 50 GeV/c and reconstructed

the dijet mass in our calorimeter. The results are shown in Fig. 8. The $u\bar{u}$ spectrum is much sharper than that from the $t\bar{t}$. The reason can be found in the reconstructed momenta spectra, Fig. 9. The low tail in the momentum spectrum in the $t(\bar{t})$ case occurs because of missing the energy of neutrinos and muons. For t jets the average number of neutrinos per jet is 0.81 and the average number of muons per jet is (.4) with mean momentum of 4.3 GeV/c when the jet is at 40 GeV/c. The mass resolutions are shown in Table II.

Other Methods of Differentiating Jets

We studied a variety of other methods of distinguishing jet flavors by constructing simple moments. Some of these are shown in Fig. 10 for u and t jets. Events were generated in ISAJET. Each moment was calculated from the four-vectors assuming a perfect detector. We define

$$<\theta^n> = \sqrt{\frac{\sum_i E_i \theta_i^n}{\sum_i E_i}} - (\bar{\theta})^n$$

where E_i is the energy of the i^{th} particle in the jet and θ_i is the angle between the i^{th} particle and the jet axis. It is clear that $<\theta>$ gives a better separation between the u and t jets than $<\theta^2>$ or $<\theta^3>$.

We also tried various moments involving

$$<Z^\ell p^m> = \frac{\sum_{i=1}^{n} Z_i^\ell p_{\perp i}^m}{n}$$

where Z_i is the fraction of the total jet momentum the i^{th} particle has, and $p_{\perp i}$ is the transverse momentum of the i^{th} particle from the jet axis.

$<Zp_\perp^2>$ gave the largest separation of all those tried ∿ about 10:1 rejection at the cut shown.

REFERENCES

1. F.E. Paige and S.D. Protopopescu, ISAJET: A Monte Carlo Event Generator for Isabelle, BNL 29777 (1980).
2. S.D. Smith and H.A. Gordon, Simple Calorimetric Triggers for Phase I Operation, next paper - these proceedings.
3. O. Botner et al, Nucl. Inst. and Meth. 179, 45 (1981).
4. R.K. Bock et al, EP/80-206 (1980) - Submitted to Nucl. Instr. and Meth.
5. O. Botner et al, IEEE Trans. on Nucl. Sci., NS-28, No. 1, p. 705 (1981).

Table I

Two 90° Jets of $t,\bar{t}$ Quarks with 100 Gev $p_\perp$ Each at $\sqrt{s}$ = 800 GeV

t : $(t\bar{d})\ \rho^0\rho^-\pi^0\pi^-\pi^+K^{*-}\rho^+K^{*-}\phi$

$\quad\llcorner$ $(ub)^*\pi^0\pi^0\pi^-\eta'\pi^0\eta'\eta\rho^+$

$\quad\quad\llcorner$ $(ub)\gamma$

$\quad\quad\quad\llcorner$ $e^+\nu_e\bar{D}^0$

$\quad\quad\quad\quad\llcorner$ $K^0\pi^+\pi^0\pi^0\pi^-$

$\bar{t}$: $(s\bar{t})\eta K^{*0}\pi^0\omega\pi^-\pi^0\pi^+\rho^+\pi^-$

$\quad\llcorner$ $\mu^-\bar{\nu}_\mu(d\bar{b})^*\omega\pi^0\eta'$

$\quad\quad\llcorner$ $(d\bar{b})+\gamma$

$\quad\quad\quad\llcorner$ $F^-\pi^+\pi^0\pi^+\pi^-$

$\quad\quad\quad\quad\llcorner$ $K^0K^-\pi^+\pi^0\pi^-$

beam jet 1: $\Delta^0\rho^+\pi^0\eta'\eta\rho^-\rho^+\pi^-\omega\rho^+$

beam jet 2: $\eta\rho^+\omega\rho^-\rho^+\rho^-\rho^-\pi^+$

Table II

Central Values and Sigmas for Momentum and Invariant Masses Calculated from the Calorimeter

	$p_\perp$ (of each jet generated in GeV/c)	p_{jet} (GeV/c)	m_{jet} (GeV)	m_{dijet} (GeV)
$u\bar{u}$	100	99.0 ± 4.8	21.8 ± 5.2	202.5 ± 6.3
	50	49.5 ± 3.4	13.7 ± 3.1	102.6 ± 4.7
$t\bar{t}$	100	88.6 ±11.7	28.7 ± 5.9	185.7 ±17.9
	50	41.7 ± 7.4	20.9 ± 5.0	93.4 ±10.8

FIGURE CAPTIONS

Fig. 1. Axial view of a $Z^0 \to t\bar{t}$ as seen in the specific calorimeter described in the text.

Fig. 2. Energy distributions and trajectories projected to the front face of the calorimeter in octant 3 for the event in Figure 1.

Fig. 3. Energy distributions and trajectories projected to the front face of the calorimeter in octant 6 for the event in Figure 1.

Fig. 4. a) Mass of the jet measured in the calorimeter versus the magnetic field strength; b) Momentum of the jet measured in the calorimeter versus the magnetic field strength.

Fig. 5. Mass of the jet for various masses for the t-quark.

Fig. 6. Ratio of the number of t jets to all jets observed as a function of the lower limit of quark mass accepted. At m = 0 this implies no mass cut so the value of 0.001 is the ratio of the expected number of t quarks to all quarks produced.

Fig. 7. a) Mass distribution of u quarks with momentum of 100 GeV/c; b) Mass distributions of t quarks with momentum of 100 GeV/c.

Fig. 8. Dijet invariant mass distributions reconstructed from the calorimeters for a) $u\bar{u}$ and b) $t\bar{t}$ events with 100 GeV invariant mass.

Fig. 9. Momentum distribution for 50 GeV/c, a) u and b) t jets, reconstructed from the calorimeter.

Fig. 10. Various moments for u and t jets - see text for details.

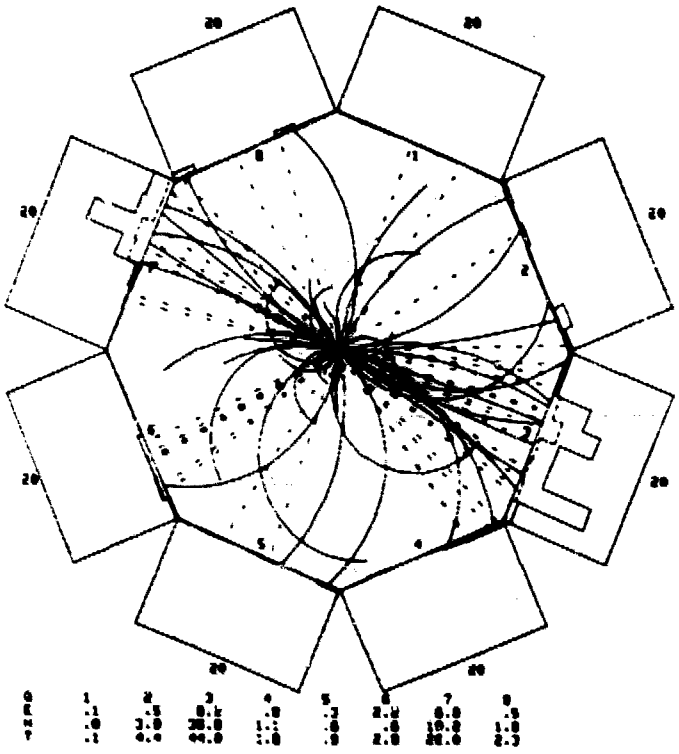

Fig. 1

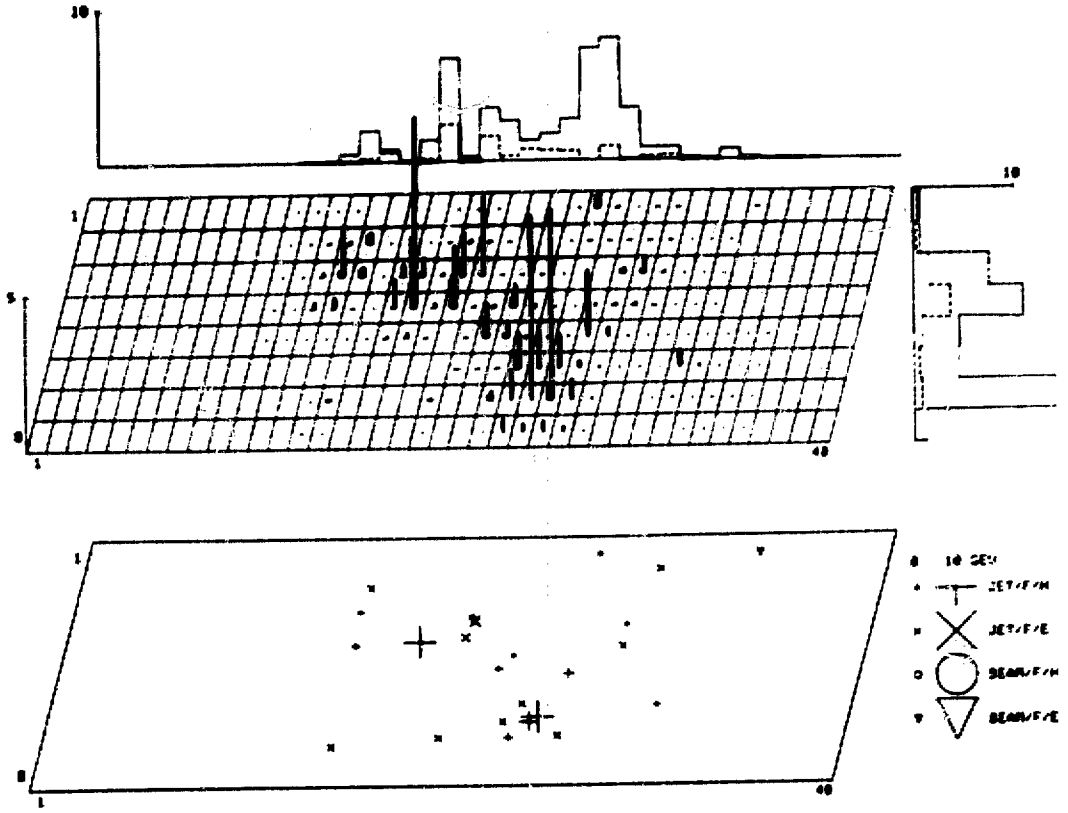

Fig. 2

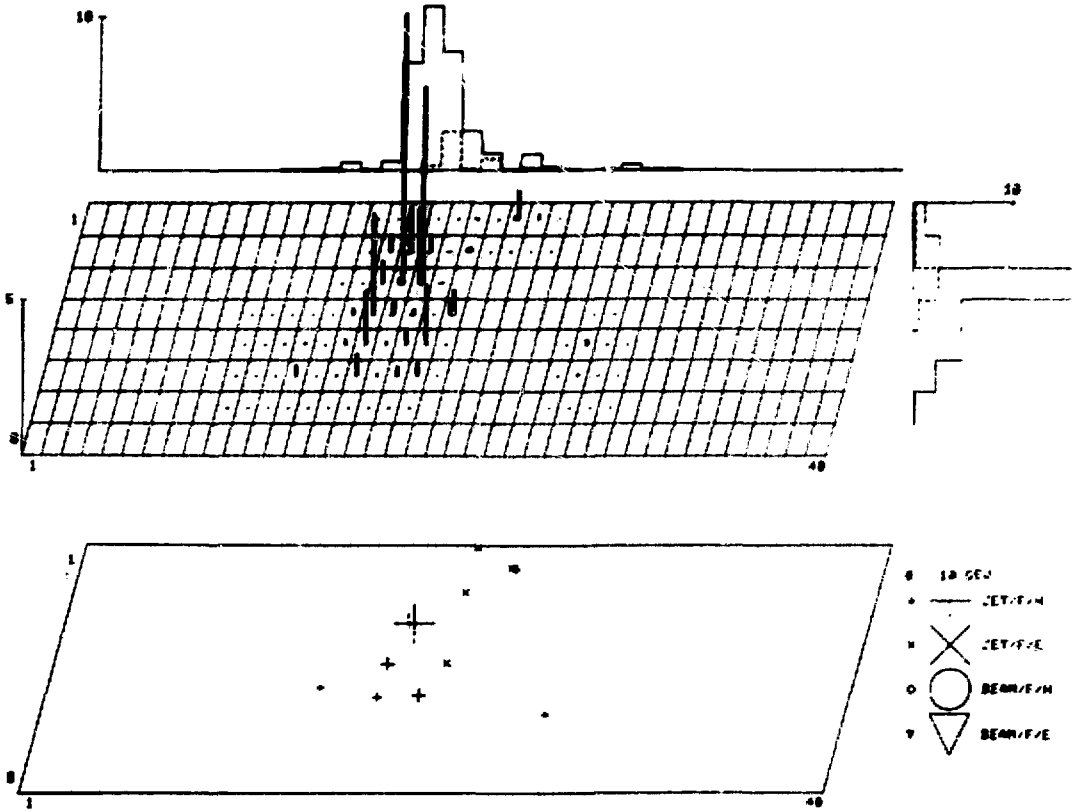

Fig. 3

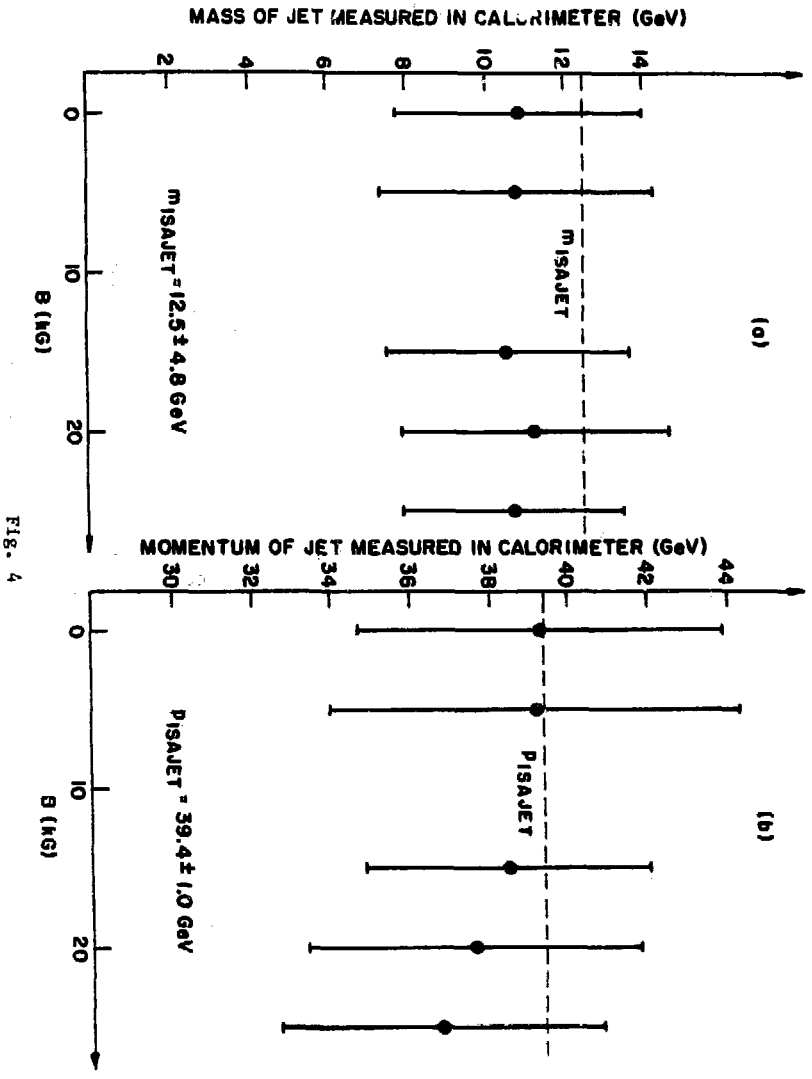
MASS OF JET MEASURED IN CALORIMETER (GeV)
2
4
6
8
10
12
14
0
10
20
B (kG)
m_ISAJET = 12.5 ± 4.8 GeV
m_ISAJET
(a)
MOMENTUM OF JET MEASURED IN CALORIMETER (GeV)
30
32
34
36
38
40
42
44
0
10
20
B (kG)
p_ISAJET = 39.4 ± 1.0 GeV
p_ISAJET
(b)

Fig. 4

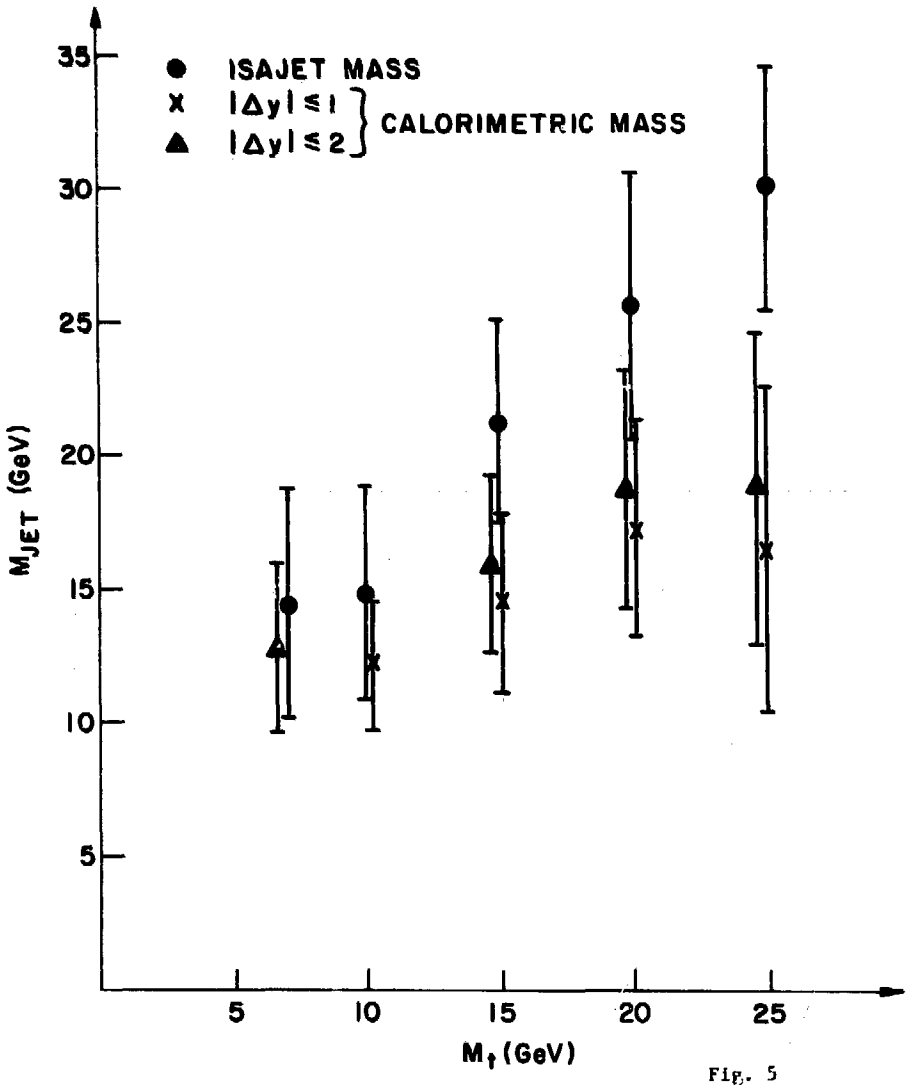
ISAJET MASS
|Δy| ≤ 1
|Δy| ≤ 2
CALORIMETRIC MASS
35
30
25
20
15
10
5
M_JET (GeV)
5
10
15
20
25
M_t (GeV)

Fig. 5

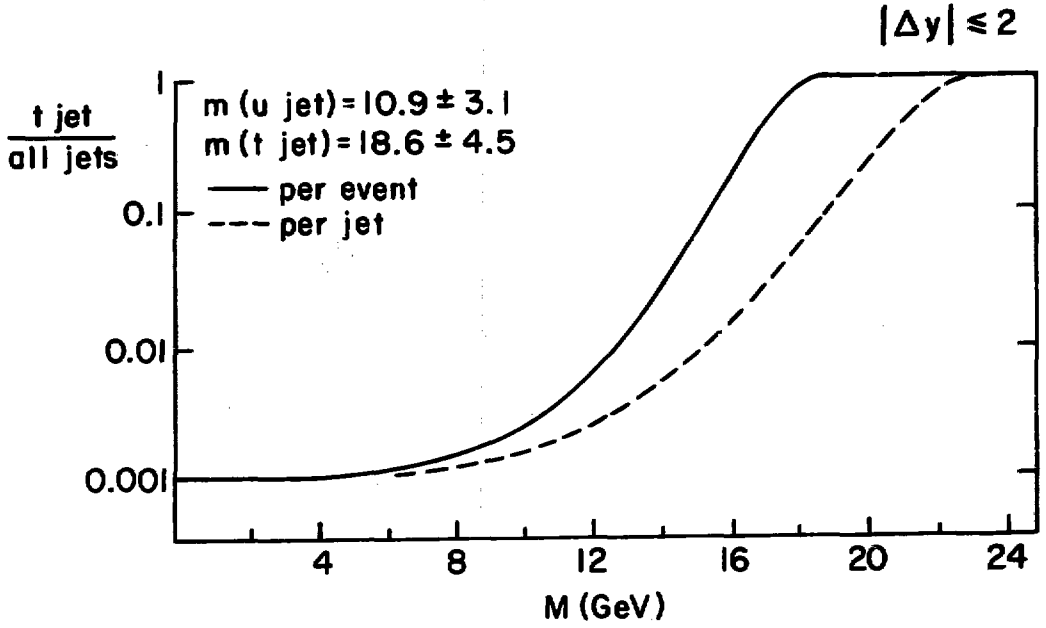
|Δy| ≤ 2
t jet / all jets
m (u jet) = 10.9 ± 3.1
m (t jet) = 18.6 ± 4.5
per event
per jet
1
0.1
0.01
0.001
4
8
12
16
20
24
M (GeV)

Fig. 6

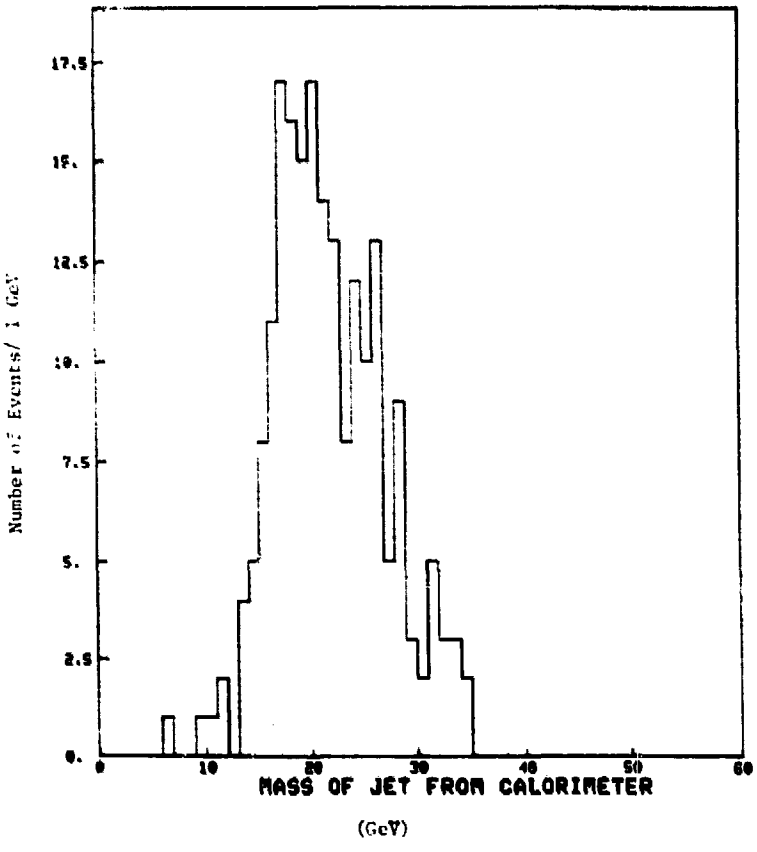
17.5
15.
12.5
10.
7.5
5.
2.5
0.
0
10
20
30
40
50
60
MASS OF JET FROM CALORIMETER
(GeV)

Fig. 7a

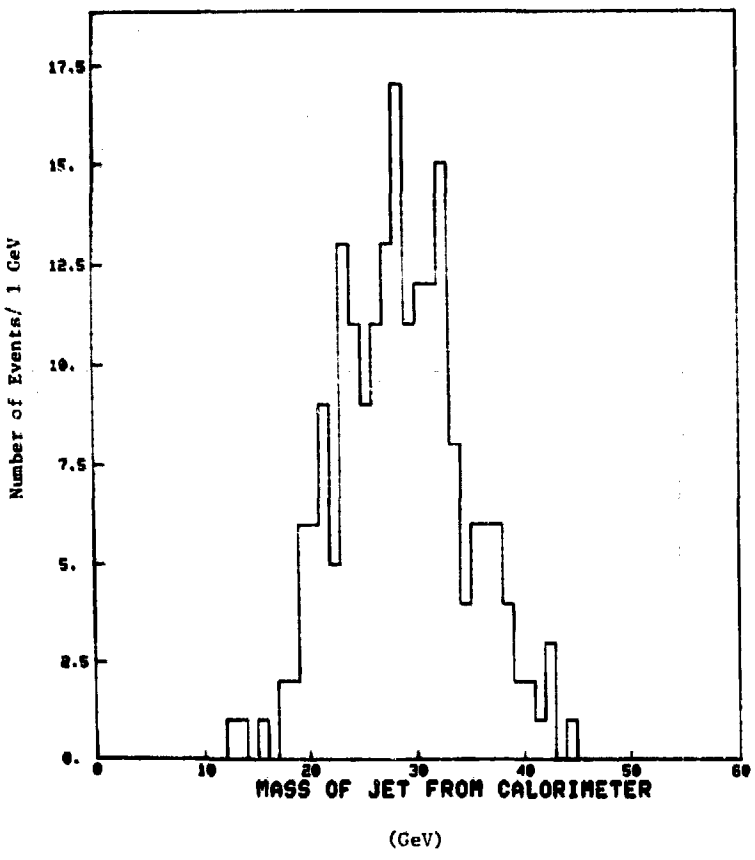
Number of Events/ 1 GeV
17.5
15.
12.5
10.
7.5
5.
2.5
0.
0
10
20
30
40
50
60
MASS OF JET FROM CALORIMETER
(GeV)

Fig. 7b

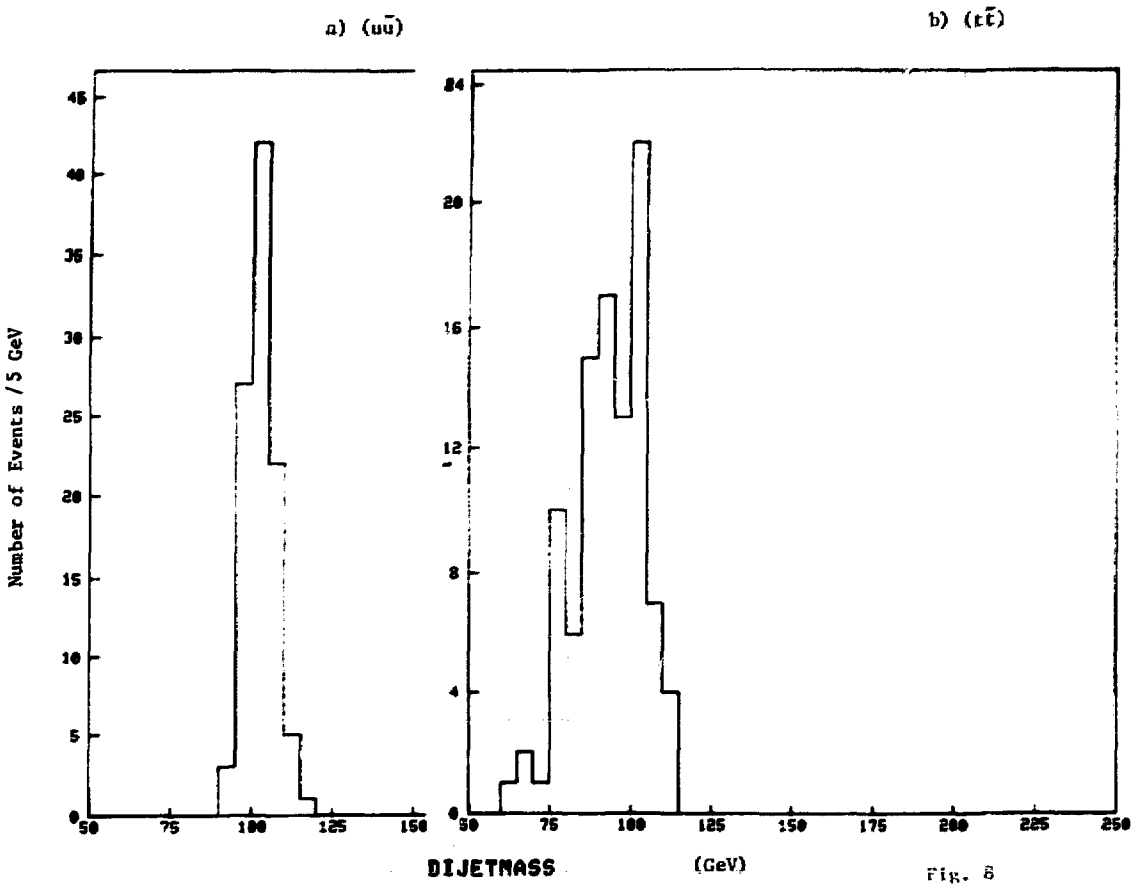

Fig. 8

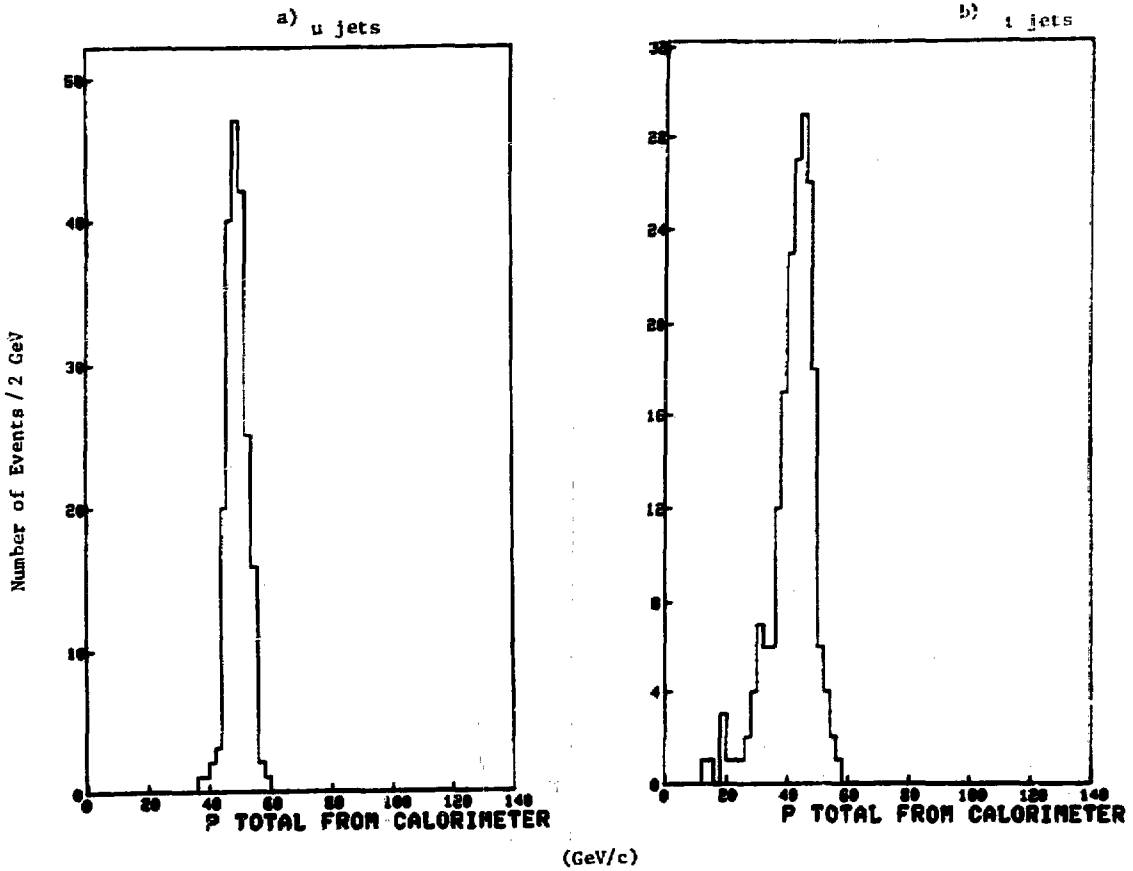
a) u jets
b) s jets
Number of Events / 2 GeV
P TOTAL FROM CALORIMETER
(GeV/c)

Fig. 9

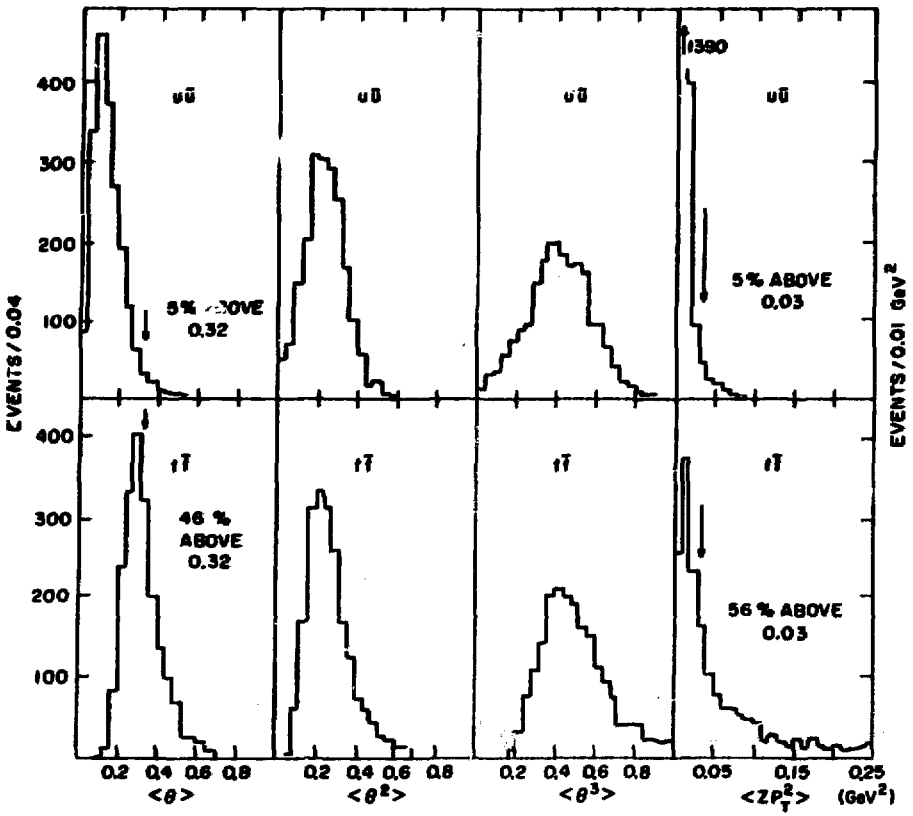
EVENTS / 0.04
EVENTS / 0.01 GeV²
400
300
200
100
uū
tt̄
5% ABOVE 0.32
1390
5% ABOVE 0.03
46 % ABOVE 0.32
56 % ABOVE 0.03
0.2 0.4 0.6 0.8
<θ>
<θ²>
<θ³>
0.05 0.15 0.25
<ZP_T²> (GeV²)

Fig. 10

SIMPLE CALORIMETRIC TRIGGERS FOR PHASE I OPERATION

S. D. Smith and H. Gordon, BNL

We would like to evaluate the usefulness of various analog calorimeter sums as triggers in Phase I. In particular, we are concerned about the effects of multiple minimum bias events within the same RF bucket which we would like to select against. Here, we define minimum bias events as those interactions comprising the bulk of the 50 mb total cross section which do not have high transverse momentum jet structure. If we further define Phase I to be $\mathcal{L} = 2.7 \times 10^{31}$ cm^{-2} sec^{-1} with a 220 ns bucket spacing we can immediately see that the mean number of events/crossing is .3 and the probabilities of seeing 0, 1, 2 or 3 events in any single bucket is

n	P	Frequency (Mc)
0	.741	--
1	.222	1.01
2	.0333	.15
3	.00033	.015

For this study we will imagine a hadron calorimeter which covers the full 2π of azimuth and the entire rapidity interval between $y = \pm 4$ ($2.1^{\circ} \leq \theta \leq 177.9^{\circ}$). We will consider neither the effects of calorimeter resolution nor those of a magnetic field.

First of all, energy sums which are not weighted according to the θ position of the calorimeter elements do not seem to be useful to us as they will be dominated by small $\sin\theta$ low transverse momentum events. If we think that large transverse momentum characterizes interesting events we should, accordingly, make sums over the calorimeter elements such as

$$E \equiv \sum_{i=1}^{N} E_i \sin\theta_i \sim \sum_{\text{particles}} |P_\perp|.$$

Here the sums go over the entire solid angle covered by the calorimeter.

We were able to generate distribtution for $E_T = \sum_{\text{particles}} |P_\perp|$ during the workshop using Frank Paige's Monte Carlo event generation programs for

both minimum bias and QCD jet events. Figure 1 shows the results for the minimum bias case. Typically a minimum bias event has 20–30 particles in the calorimeter depositing only about 8.5 GeV for E_T. The E_T distribution appears surprisingly gaussian with $\sigma \sim 2.6$ GeV. The distribution arising from 2 and 3 simultaneous events is also shown.

In Figure 2 we compare the E_T distributions of QCD jet events with that resulting from the minimum bias events. Note that at this choice of luminosity and crossing frequency that events containing jets of $P_\perp > 20$ GeV/c have an E_T distribution well above that of the minimum bias events. If the mean number of interactions per crossing is increased the minimum bias distribution will flatten out.

It is likely that if the existence of jets is clearly established a more selective jet trigger would be desired. To this end, we imagine a series of overlapping calorimeter sums each of which covers only a limited range in azimuth and rapidity.. After an initial trigger resulting from our E_T sum, we might check to see if the largest of these more restricted sums (defined as E_T^*), is greater than some threshold value. We would like each $\Delta\phi$, Δy area summed over to be large enough to efficiently collect the energy of a jet centered on it but small enough to select against the more diffuse minimum bias events. We have chosen $\Delta\phi = 45^\circ$ and $\Delta y = 1$. Figure 3 compares the E_T^* spectra for minimum bias (including multiple events) and QCD jet events having a jet with $P_\perp > 10$, and 20 GeV. Clearly, the discrimination against minimum bias events has been greatly improved.

In conclusion, the use of sinθ weighted calorimeter sums would appear useful for discrimination against minimum bias events and multiple low $P_\perp$ interactions at Phase I ISABELLE. In particular, the type of restricted sum described in the text should make a good jet trigger. An E_T threshold of $\sim$25 GeV would result in a counting rate $\lesssim$ 10 kc and reasonable signal to noise. E_T^* trigger thresholds anywhere above 10 GeV appear to completely suppress the minimum bias events. If one desires to separate multiple events by detecting a total energy greater than the available $\sqrt{s}$, a calorimeter coverage of at least $|y| \leq 7$ is required. Pseudo-rapidity $y = 7$ corresponds to a polar angle, $\theta \approx 1.8$ mR.

FIGURE CAPTIONS

Figure 1. These are the distributions in E_T arising from one (solid line), two (dashed line) and three (dotted line) minimum bias type events occurring in the same RF bucket. The normalizations are correct for $L = 2.7 \times 10^{31}$ with 220 ns bucket spacing and assuming poissonian statistics.

Figure 2. This graph compares the E_T counting rate distributions arising from all minimum bias events, including multi-event buckets (solid curve) with those arising from QCD jet events having at least one jet of total transverse momentum greater than 10 GeV (dotted curve), 20 GeV (dashed curve) and 30 GeV (dash-dotted curve). The QCD jet curves do not include multiple event effects.

Figure 3. These are the resulting distributions when the largest E_T sum over a limited region ($\Delta\phi = \frac{\pi}{4}$, $\Delta y = 1$) is sought for a trigger. The solid curve arises from all minimum bias events ($n < 4$) while the dotted and dashed curves are due to the QCD jet events where at least one jet has a total transverse momentum greater than 10 or 20 GeV, respectively.

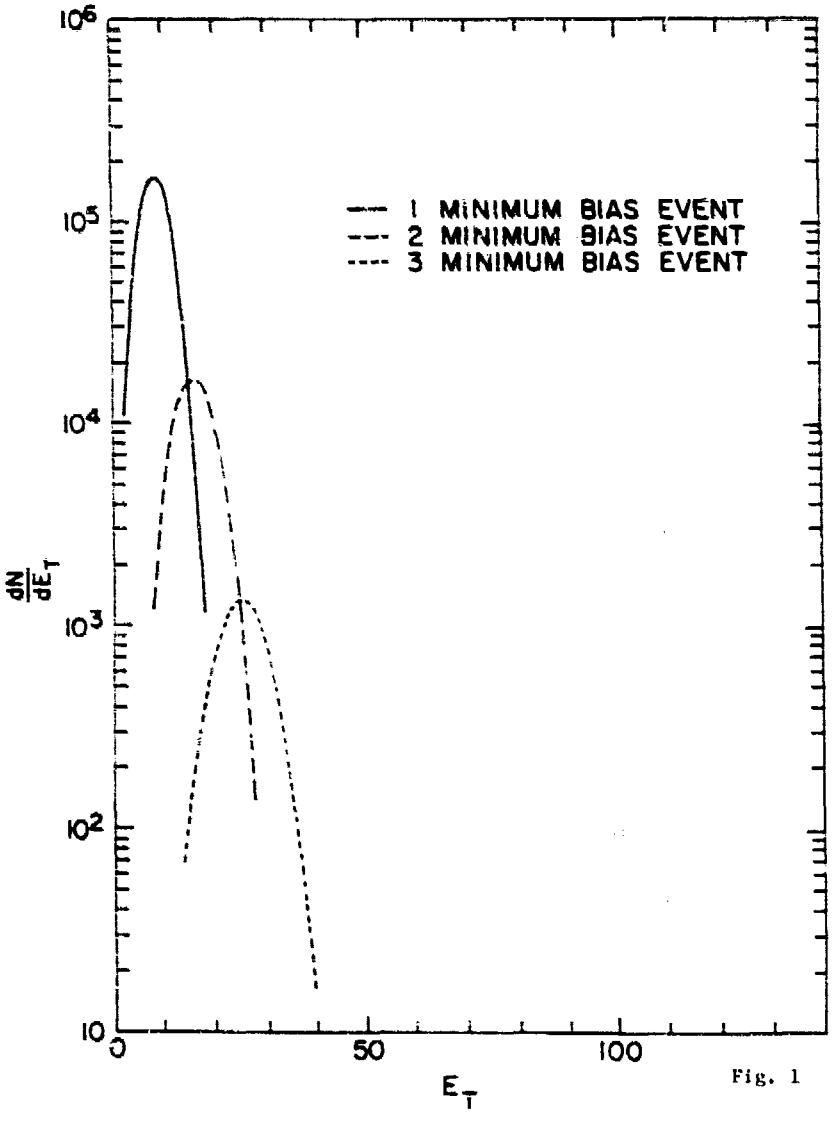
1 MINIMUM BIAS EVENT
2 MINIMUM BIAS EVENT
3 MINIMUM BIAS EVENT
10^6
10^5
10^4
10^3
10^2
10
$\frac{dN}{dE_T}$
0
50
100
E_T

Fig. 1

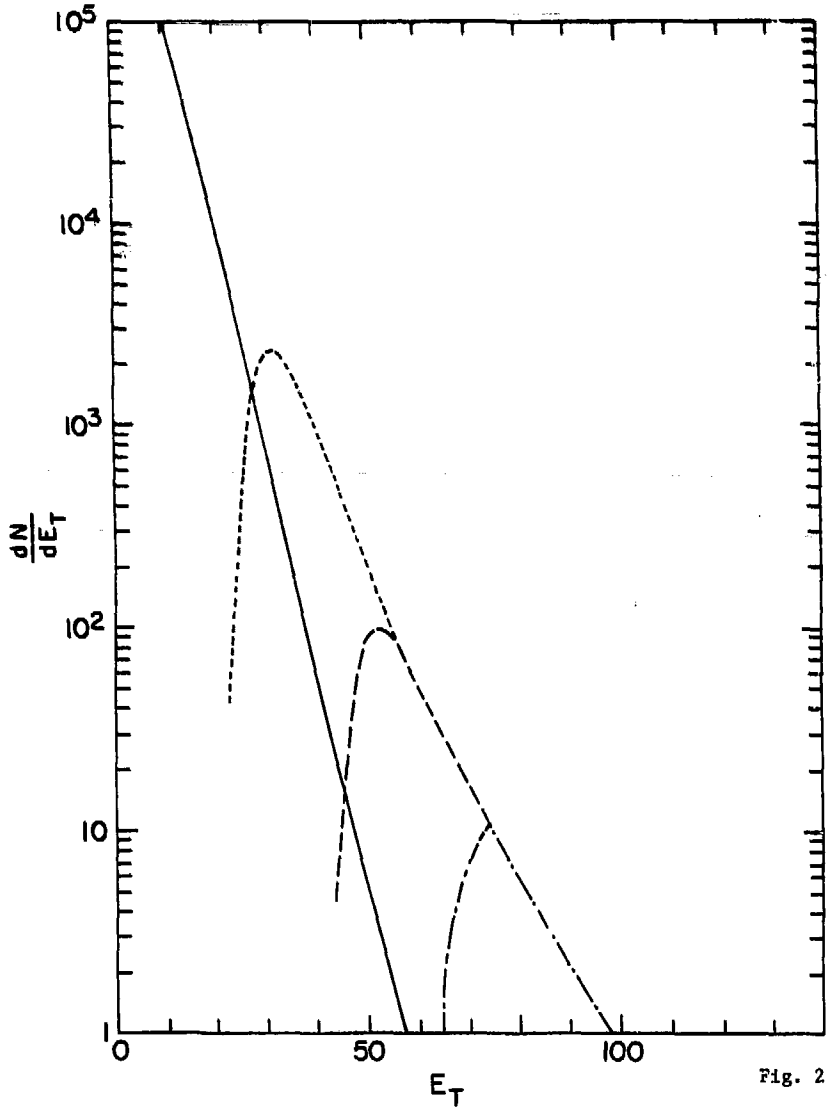

Fig. 2

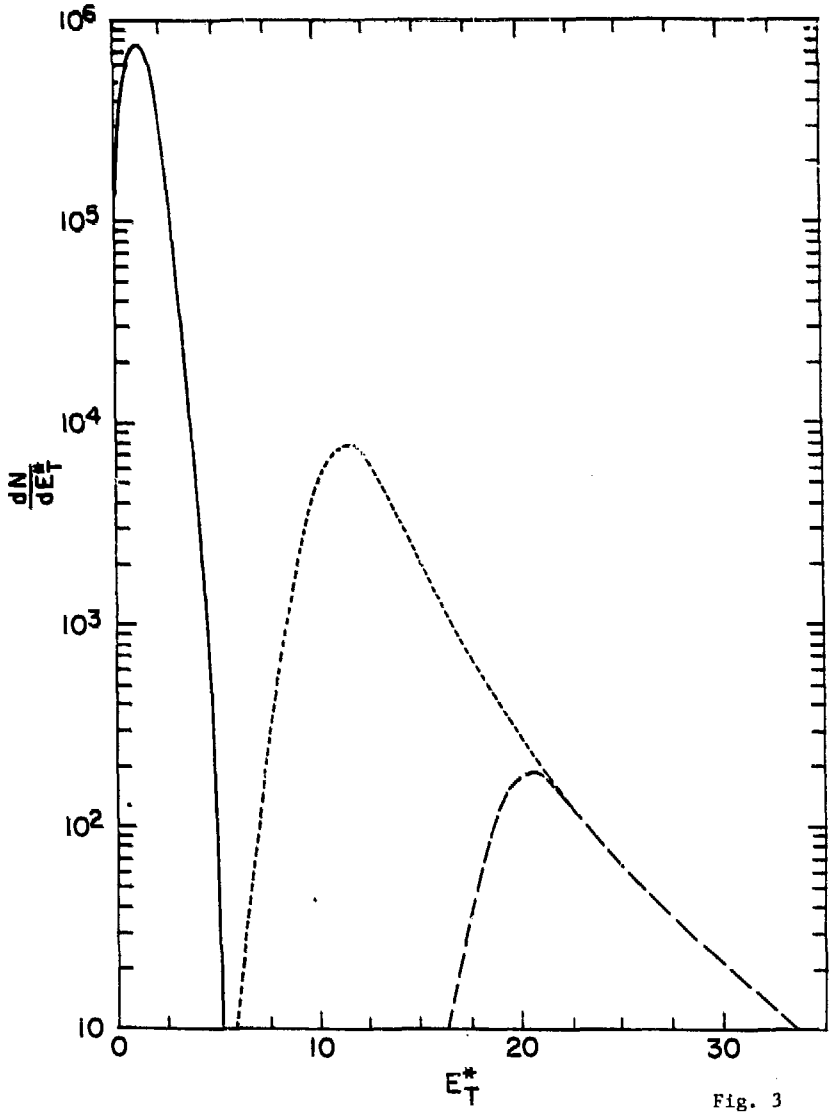

Fig. 3

LAPDOG - A LARGE ANGLE ELECTROMAGNETIC EXPERIMENT FOR ISABELLE

L. Ahrens, S. Aronson, H. Foelsche, B. Gibbard,
P. Wanderer, H. Weisberg, P. Yamin, BNL
D. Cutts, R. Lanou, Brown University
R. Engelmann, P. Grannis, J. Kirz, M. Marx, R. McCarthy, SUNY

In the summer of 1980, a group of physicists from Brookhaven, Brown and Stony Brook held a small workshop to begin development of a proposal for ISABELLE, aimed at high resolution studies of π^0, γ, and electrons. Although we make no pretense of predicting which questions will be most fundamental when beams begin circulating, it seems a very good bet that the high luminosity afforded by ISABELLE, will enable exciting new work in the realm of short distance (high mass and high p_T) phenonema. With our eye on this kind of physics, we have focussed on detection of electrons and gammas, feeling that the widest range of studies can thereby be enabled - without an excessively large detector.

I. PHYSICS GOALS

There are several specific topics which we have used to develop our ideas:

1) Dielectron studies - Either the Z^0 and $(\bar{t}t)$ states will be observed before ISABELLE or not. If not, we would want to be in a position to search for them, if so we must study their properties. The yield of Z^0's is a measurement of QCD scale violations. It will also be crucial to measure the physical width of the Z^0 as an indicator of the number of neutrino species and to search for fine structure in the $(\bar{t}t)$ production, as observed for ψ and Υ. This requires good energy resolution for the electrons; calorimetric measurement of E is better than magnetic determination of p above some energy. We believe it possible to achieve resolutions good enough for these measurements

with a system based on lead-glass shower detectors or the equivalent.

Other aspects of electron production interest us: study of the continuum (Drell-Yan) of e^+e^- yields important information on hadron structure. Observation of $W^{\pm}$ through their leptonic decays is obviously of interest. Finally, we would like to be sensitive to the Higgs boson (or any Goldstone Boson of similar properties). This latter poses a severe experimental challenge if the boson mass exceeds 20 GeV/c^2. A good resolution dilepton experiment may however be sensitive to some possible H^0 channels - viz, $H^0 \to \psi\psi$ or TT, $Z^0 \to H^0$ + massive $e^{\pm}$ pair or $(\bar{t}t) \to H^0 + \gamma$.

2) High p_T particle production - With 700 GeV available in the center of mass we expect to be able to get significant counting rates of high p_T single particles out to 60 GeV/c, a factor of four increase over the presently studied range. We choose to focus on measurement of π^0 and γ, rather than identify $\pi^{\pm}/K^{\pm}/p^{\pm}$ for several reasons. We do not feel that comparison of say π vs K production at the low X_T available is likely to give any insight into small distance physics that has not been better measured at fixed target machines. Charged particle identification is expensive in real estate; we favor doing a good job on electromagnetic particles, judging that such a strategy opens more interesting windows than particle identification. As an example in the high p_T realm, with good EM detection we expect to distinguish single γ from π^0. This is important since current theory suggests quite different characteristics and underlying mechanisms for these two. We note that the precision of $\delta E/E$ measurement for EM particles improves with energy whereas $\delta p/p$ measurements from magnetic deflection get worse. For the geometry discussed below the cross-over is around 20 GeV.

3) Multilepton studies - Many sources of multilepton production can be imagined. Specifically there are the possibilities of Higgs bosons, $W^{\pm}$, new sequential leptons, neutral heavy leptons or naked top states - each of which can decay into cascades of ordinary (e,μ) leptons. Thus a detector that has chosen a focus on electrons in some portion of its solid angle might very usefully be augmented with muon detectors over some remaining solid angle and thereby provide useful information on multileptonic final states. We have not imagined this class of physics to be the main motivation, but rather an interesting area for expansion.

4) Jet studies - Much attention has been devoted in recent years to jet production at high p_T; the hope, somewhat fulfilled, has been that jets may reveal underlying constituent structure more directly than single hadron production. Experimentally, recovery of a clean jet signal awash in a flood of hadrons has been a major challenge in hadron-hadron collisions. We may expect however that at very high p_T, the isolation of jets may become simpler. It is also of great intrinsic interest to study p_T and angle dependence of jet production. It is probably true that, owing to the complexity of the final state, information from several complementary experiments will be useful. We have not chosen to optimize a detector for jet physics; however we foresee that many interesting results could be obtained. For example, we may want to compare jets recoiling against high p_T π^0's and γ's to help distinguish various scattering subprocesses. Sensing the absence of recoiling jets for single high p_T electrons should materially help enhance the $W^{\pm}$ signals.

II. GENERAL DESCRIPTION OF THE APPARATUS

There are several important considerations that have colored our discussions and seem to be central to our thinking.

1) Of the many physics possibilities, we feel most excited by the opportunity to probe the very short distance structure of hadrons and the chance of studying new massive particle states. A natural avenue that focusses on both of these areas is a high p_T experiment which emphasizes detection of π^0, γ and electrons.

2) We find there are many reasons to push for the best available energy resolution of EM particles. We aim for measurement of the width of the Z^0 and resolution within the family of $(\bar{t}t)$ states. Good energy resolution is also essential for discriminating π^0 from single γ. Thus we envision an electromagnetic calorimeter based upon lead-glass Cerenkov counters - or any affordable alternative of comparable resolution. We are willing to sacrifice, for example, full 4π solid angle coverage for the best resolution.

3) For various reasons, we prefer a configuration that does a few experiments very well to a global program which can do some of everything. This

style of experiment seems to be favored by all participants in the study to date. Implied in this style is an intention to resist designing a gargantuan apparatus and to be content with the merely huge. Realistic budgets for such an experiment are limited to $5 million.

4) We feel rather strongly that good first round experiments will be most successful if they are kept relatively simple. Our ideal of course is to find a design that is simple to calibrate and run and which allows straightforward analysis to yield quick physics results. There is some historical precedent to support the feeling that simple experiments will produce the best physics in the early years of running. A corollary to this simplicity argument is that it may be more productive to do experiments where trigger rates can be kept low and thus highly optimized computer analysis is not required. We have, for example, felt the need for a magnetic field but hope to keep the tracking chambers out of the main magnetic volume. Thus - we hope - we preserve most of the simplicity of straight line pattern recognition and fitting.

Several tactical decisions have been made following the adoption of the above considerations.

A) In order to discriminate electrons from charged hadrons with good certainty we need some additional identifying method beyond the energy measurement in the EM calorimeter. We have rejected Cerenkov identification as unwieldy and space consuming; transition radiation detectors introduce a non-negligible mass detrimental to $e^{\pm}$ studies. We opted instead for independent measurement of momentum with a magnetic spectrometer system. Comparison of (E/p) with one seems sufficiently powerful to identify electrons reliably, particularly when coupled with longitudinal shower development information in the calorimeter. In order to keep the calorimeter size to a minimum, the field should be as close to the beams as possible.

B) The calorimeter array, in addition to having good energy resolution, should have reasonably fine position resolution. Part of the reason for this is simply the high multiplicity expected at ISABELLE and the need to avoid spatial overlap of several shower deposits. Fine segmentation is also necessary for the method we have in mind for distinguishing π^0 and γ. Briefly,

this method consists of running with a radiator foil ($\sim$1/3 r.l.) before the magnetic field. Electron pairs from gammas which convert in the foil are then separated by the field and show up in the calorimeter as two distinct energy clusters. If the e^+e^- pair is accompanied by another γ (as in π° or η decay) we expect to see a third energy cluster between the electron hits. Single γ's should present a pattern with no third cluster. Our studies show that for spatial cells in the 5-10 cm range along the bend coordinate, this method effectively separates π° and γ, even in the presence of radiative effects and multiple scattering. The energy resolution of Pb glass plays an important role too, for those cases where the electrons radiate hard γ's and the effective $e^+e^-\gamma$ mass must be computed.

C) The magnet, while essential to our scheme, is not the most important feature of the experiment. It must therefore be simple enough that it neither dominate the budget nor the effort.

D) We recognize that it is likely to be impossible to build or instrument a detector which covers 4π solid angle and has the desired energy resolution, keeping within our presumed budget.

We have discussed at some length a range of compromise solutions in which restricted coverage is achieved. We conclude that, for a fixed area or solid angle affordable, we are better off to keep Δy (or $\Delta\theta$) large at the expense of $\Delta\phi$- rather than the reverse. This is dictated by our choice of high p_T physics. For example, $Z^\circ \to e^+e^-$ decay is expected to give electrons over a rapidity range of about ± 2 units with roughly equal probability; the azimuthal correlation of the two elecrons is great, owing to the large mass and limited p_T of the Z°. Similar conclusions are reached for jet or $W^\pm$ studies. Simply stated, in high p_T pair physics one pays once for restriction in ϕ, but twice for restriction in y.

E) We imagine that our goals can naturally be accommodated in the Wide Angle Hall scheduled for the 6 o'clock insertion at ISABELLE; thus we would like to design a magnet compatible with the beam extraction lines. We also should keep the magnetic field effect on the intersecting beams to a minimum.

The detector which has emerged from our discussions is briefly described here. We chose a magnet which is basically an iron filled toroid with field lines directed azimuthally. Two open wedges in this magnet of approximately

±25° each are made in the horizontal plane and define the azimuthal aperture. Inner and outer toroid radii are 75 and 175 cm; the field integral is about 1.5 Tm. Tracking chambers (drift or PWC) are located inside and outside the magnet for momentum determination and location of particle hit positions at the EM calorimeter. The Pb glass calorimeter begins at r = 225 cm and extends to approximately 300 cm. This calorimeter is built from long rectangular pieces approximately 6.5 x 6.5 cm^2 in cross-section. Many layers (8-10) are then required to achieve the necessary depth for shower containment. Phototubes are mounted on the small area cross sections at top and bottom of the array. At least three PWC's are interleaved in the matrix to give accurate shower positions at several depths and for tracking calibration muons through the array. Sketches of the detector are shown in Figs. 1a and b.

III. MAGNET

The magnet design for this experiment is shown in Figs. 2a and b. It can be considered as an iron toroid with 2 air gaps or as 2 oppositely directed dipole fields. It has been chosen to give reasonable momentum resolution over $\Delta\phi \sim \pi/2$ and $25° < \theta < 165°$. For this type of magnet the bend plane contains the long dimension of the interaction diamond, necessitating chambers near the beam pipe. Figure 3 shows the field strength vs distance from the collisions point. The inner and outer tracking regions contain about 8% and 19% of the total field integral respectively. One quadrant of the field configuration is shown in Fig. 4, which indicates that the field on the lead glass phototubes, or on the beam pipe, can be easily minimized. An attractive feature of this field is that in the beam view (Figure 4) there is very little bending, facilitating tracking and/or triggering. In order to achieve the requisite field integral and minimize power consumption, we expect to use superconducting coils.

This design permits us to retain a great deal of flexibility in the experiment. The magnet can be translated down the beam, or left and right half split and displaced with respect to each other. There is sufficient iron in the return to permit slots for possible muon tracking (there is equal $\int Bdl$

in the vertical plane) or even hadron calorimetry. There is sufficient room to place tracking chambers above and below the beam pipe.

Cost for this magnet, including transport mechanism is about $2 million. Design work of the magnet and transporter have been in progress at Brookhaven this year.

IV. ELECTROMAGNETIC DETECTOR

The electromagnetic detector, which is at the heart of this experiment is designed around lead glass. We will attempt to implement a minimum amount of glass consistent with a $\Delta E/E = 0.04/\sqrt{E} + 0.006$ achieved by Appel et al. In addition we want positional information such that we get good hadron rejection and directional information.

The resulting design, shown in Figs. 1a and b is one with all elements made from blocks 6.5 cm x 6.5 cm x varying length all stacked with the long axis vertical. The 6.5 cm x 6.5 cm size is convenient segmentation for both phototube size and hadron rejection by lead glass alone.

Magnet dimensions and charged particle tracking constrain the array such that the first plane of lead glass is 225 cm away from closest approach to beam line.

Although in principle the coverage in angle can be done in a stack with blocks all in the same plane, this is more costly in lead glass. The presence of the wire chambers makes it awkward to "round the corner" near the end of the magnet by the simple expedient of stacking the blocks like a cross-word puzzle - the chamber edges have to be dealt with anyway. Instead, we divide the detector beyond the magnet end ($\pm$2 meters or $\pm$36.5° from 90°) by four smaller "transition" pieces with stacking identical to that of the "barrel" (see Fig. 1b). These "transitions" pieces cover down to $\theta \approx 25°$ with a dead region of about 2.5° at $\theta \approx 53°$.

There are eight layers of lead glass. In a radial direction at 90° to the beams this presents 21.5 radiation lengths. Wire planes are placed between layers 1 and 2, 2 and 3, and between 4 and 5 and after layer 8. These chambers serve to provide, via their segmentation, several functions: 1)

determination of correction factor for showers developing late in the stack of only 21.5X_0. 2) greater precision in gamma direction determination than obtained from blocks alone (wires free us from necessity of finding vertical position via pulse height division in blocks), 3) again, via improved spatial resolution, they should increase our ability to reject hadrons vs showers; and 4) to track muons through the array for calibration. The placement of the chambers has not been optimized; they are spaced with the following considerations in mind: 1) three z-segmentations seem minimal, 2) the first two divisions were placed after 2.7X_0 and 5.4X_0 to make sure that the probability of getting an early sampling of shower development was high, 3) the third division was made as deep into the stack as seems consistent with being far enough in for late and/or long shower conversions and adequate moment arm for direction measurement but not so far that it was rarely used to provide the third segment for hadron rejection and/ or energy corrections.

The total weight of lead glass is 92 tons and consists of 3400 blocks. In order to contemplate using such a quantity we have embarked on a program to reduce the cost of lead glass without compromising its performance. So far we have shown that it is possible to use blocks which have not had the four long sides cut, ground and polished. The untreated surfaces are very smooth, but in comparison to polished blocks the surfaces are rippled and the corners round. (Fig. 5) This discovery alone is expected to reduce the cost by a factor of 2. We are proceeding with other ideas for savings, such as using blocks that are not "fine" annealed. We have tested an array of 30 of these blocks to compare resolutions with different orientations and to study how well the energy spilled out the back of the array can be predicted from an individual longitudinal shower profile. Preliminary analysis suggests that energy resolution is as good as, or nearly so, that achieved in a single 15 x 15 cm^2 block containing the entire shower. We have also studied pulse height variation with distance from the phototube for a full length (140 cm) bar (Fig. 6) and variation with angle of electron incidence (Fig. 7). We believe that the uniformity of light response is adequate for successful control. We do however feel the need for better energy resolution and calibration studies in high energy electron beams.

At this moment we estimate the glass array will cost $2.5M including glass, phototubes and readout electronics.

The mass resolution for 90 GeV e^+e^- states is wholly dependent on the energy resolution of the lead glass. If we assume resolution of $\sigma_E/E = 0.006 + 0.042/\sqrt{E}$ for the energy measurement ($\sigma_E = 0.94$ GeV at $E = 90$ GeV), our simulations show that σ_m for the Z° mass is 0.75 GeV. With energy resolution σ_E raised to 1.34 GeV, the mass resolution increases to about 1.0 GeV. The physical Z° full width Γ is expected to be about 3 GeV, with an additional 0.2 GeV added for each new neutrino type. A preliminary estimate suggests that about 300 Z° decays, measured with resolution $\sigma_M = 1.0$ GeV, will suffice to measure Γ to the desired accuracy.

V. TRACKING SYSTEM

We expect to have a system of drift chambers around the beam pipe, in front of the lead glass and distributed through the lead glass array. While the momentum measurement is unnecessary for measurements of the Z°, it is crucial for the single $e^\pm$ physics and will be useful in limited jet studies and in calibration work. With presently available chamber resolutions we find $\delta p/p \approx Cp$ with $C = 1.35 \times 10^{-3}$ (GeV/c)$^{-1}$ at $\theta = 90^\circ$ and $C = 0.63 \times 10^{-3}$ (GeV/c)$^{-1}$ at $\theta = 45^\circ$ which is approximately equal to the lead glass resolution for 20 GeV/c e^-. Designs for this system have not been completed.

VI. RATES

We have calculated some rates for the experiment outlined above, using a luminosity of 2×10^{31} (cm^2 sec)$^{-1}$. Using the computed Z° production cross-section of Paige[1] and a branching ratio of 3% into e^+e^-, we find 0.15 Z° detected/hour. The acceptance for $Z^\circ \to e^+e^-$ is found from Monte Carlo simulation to be about 0.04 -- in part because of the limited $\Delta\varphi$ coverage ($\Delta\varphi/2\pi = 1/4$) and in part due to loss of electrons near the beam pipe.

Similarly, for a $(t\bar{t})$ bound state at m = 50 GeV we estimate 0.12 detected events per day.

High p_T π^0's within the rapidity range $|y| < 2.5$ occur in detectable quantity out to p_T = 60 GeV/c. Using current QCD predictions[2] we expect 20 events/hour at p_T = 20 GeV/c and 0.1 events/hour at p_T = 60 GeV/c. Single protons can be detected using the technique discussed above, although a loss in rate is incurred by the need to convert a γ and by trigger selection cuts. Assuming $\gamma/\pi^0 = 0.1$, we find about 2 direct γ/hour detected at 10 GeV/c, dropping to 0.12 per hour at 20 GeV/c. Our Monte Carlo studies indicate that π^0's are misidentified as γ's about 10% of the time so that measurement of γ/π of less than 0.1 becomes difficult.

Studies of multilepton rates are less well understood. An estimate has been made for the case $Z^0 \to t\bar{t}$, based upon instrumentation of magnet return yokes as muon identifiers and muon filters behind the electromagnetic calorimeters and assuming 10% semileptonic decay branching ratios at each step of the quark cascades. We find that three lepton events occur about half as often as detected $Z^0 \to e^+e^-$, whereas four lepton events are seen at about 2% of the $Z^0 \to e^+e^-$ events.

Consideration has been given to some of the backgrounds expected. For the electromagnetic detector the relevant question is the probability of another π^0 or γ hitting a cell already struck by a high p_T particle. With less than one event per bunch crossing, the only background, given adequate shielding to the beams, is that from the same event. We estimate this probability to be 2×10^{-3}, hence on average, an extra 0.6 MeV deposited in the cell. A similar overlap probability may be expected in the tracking chamber cells. Since this experiment would not place a premium upon interaction vertex reconstruction, we do not envision particular difficulty even if the luminosity in bunched beam mode were to rise to give significant multi-interaction crossings.

In summary, we are enthusiastic about the prospects of early turn on of ISABELLE with luminosity of 2×10^{31} $(cm^2\ sec)^{-1}$. We feel confident that our major goals of elucidating the vector boson properties and extending high p_T particle production cross-sections can be achieved. The proposed experiment would enable us to look in previously unexplored regimes of energy,

mass and transverse momentum. We imagine that interesting work can be done in examining multilepton events, multigamma production, and in correlation of jets with high p_T particle production. Higher (unbunched beam) luminosities will greatly aid these studies, but we feel that first round studies at the projected Phase I luminosity will be invaluable in pointing out which aspects most deserve further study at higher rates.

VII. REFERENCES

1. F.E. Paige, BNL-27066 (1979 unpublished).
2. I. Hinchliffe and R.L. Kelly, LBL-12274 (1981 unpublished).

FIGURE CAPTIONS

Fig. 1a. Schematic beam's view.
Fig. 1b. Schematic plan view.
Fig. 2a. Cross section of split toroid/dipole.
Fig. 2b. Plan view split toroid/dipole.
Fig. 3. Toroid field in median plane.
Fig. 4. Field map for one quadrant of detector.
Fig. 5. Lead glass blocks used in optical comparisons.
Fig. 6. Observed pulse height vs distance from phototube in a 140 cm long lead glass bar.
Fig. 7. Variation of pulse height with angle for polished and extruded lead glass bars.

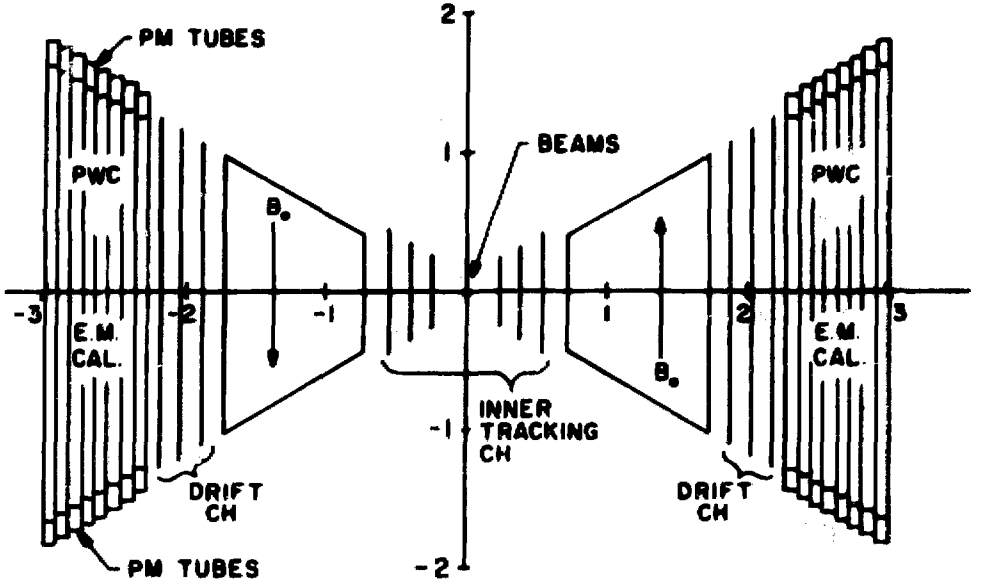

SCHEMATIC BEAM'S VIEW

Fig. 1a

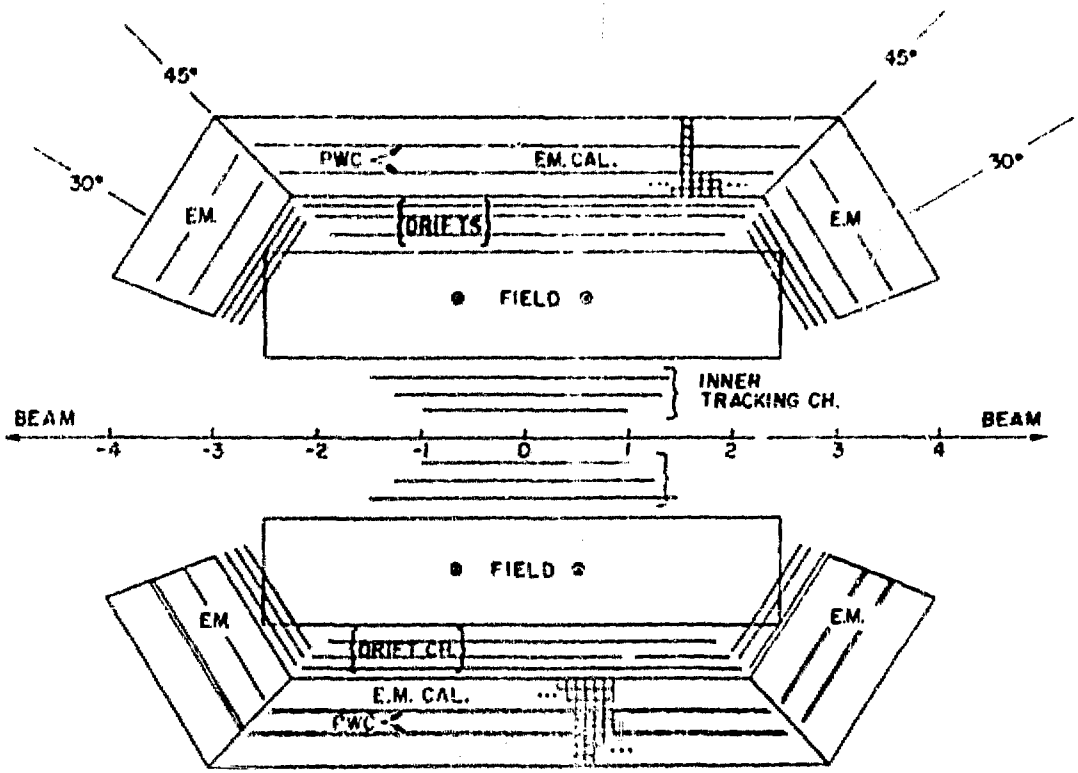

PLAN VIEW

Fig. 1b

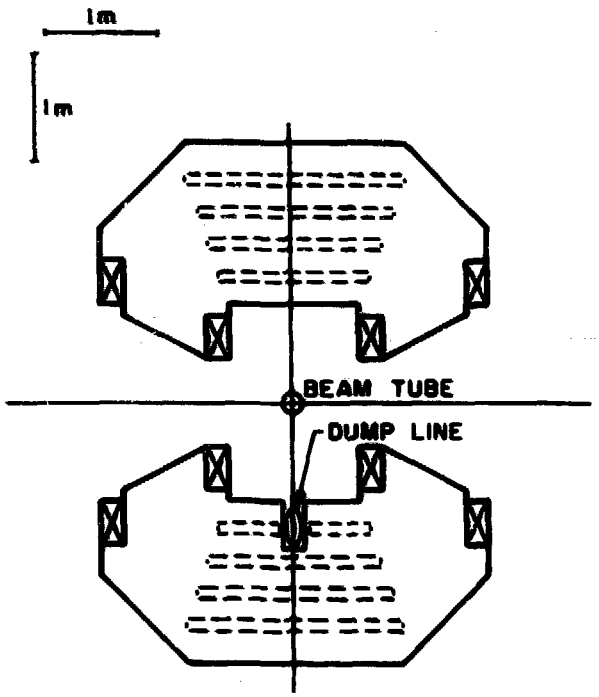

CROSS SECTION OF SPLIT TOROID/DIPOLE

Fig. 2a

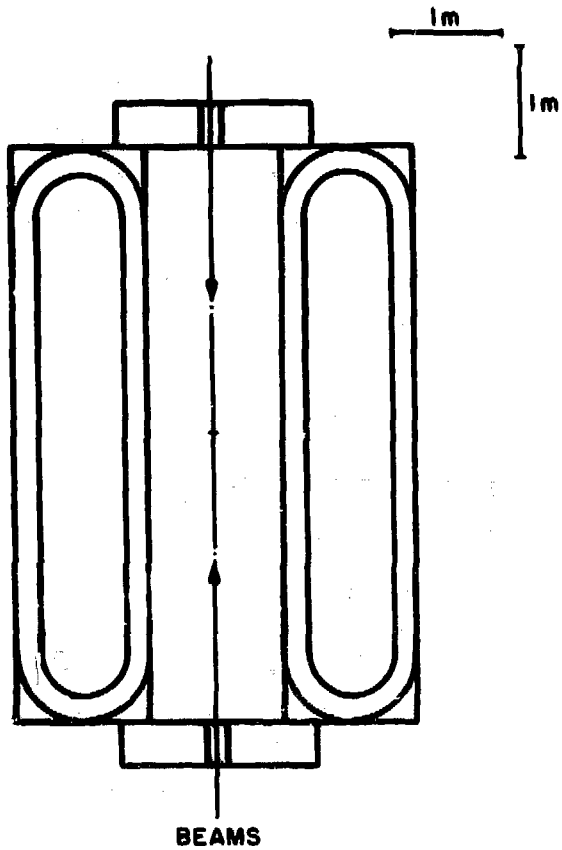

PLAN VIEW SPLIT DIPOLE/TOROID

Fig. 2b

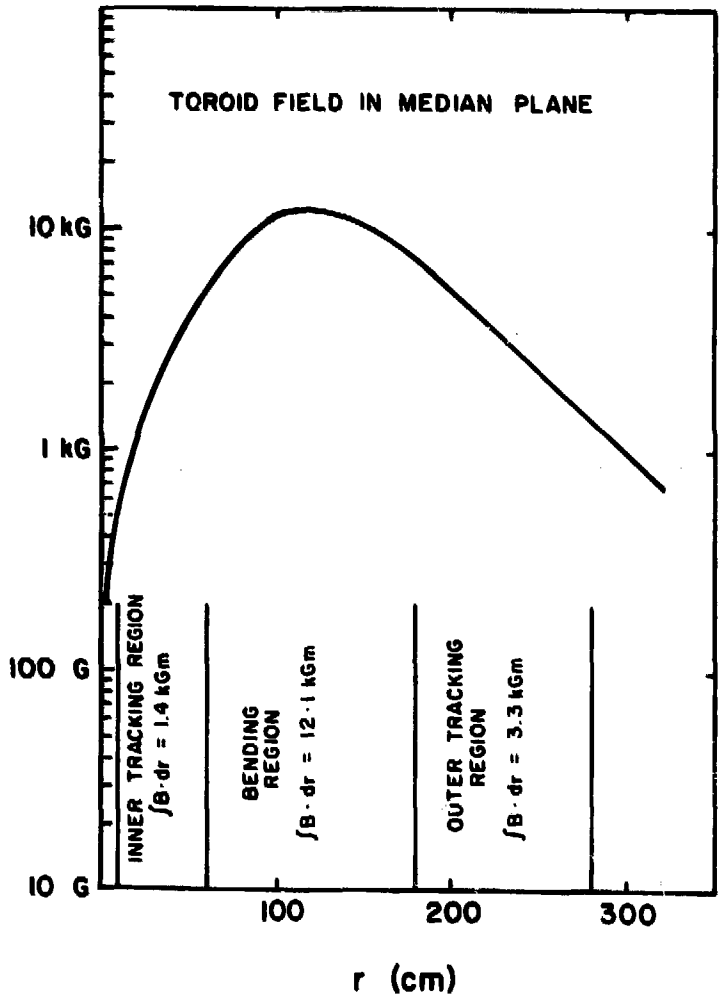
TOROID FIELD IN MEDIAN PLANE
10 kG
1 kG
100 G
10 G
INNER TRACKING REGION
∫B·dr = 1.4 kGm
BENDING REGION
∫B·dr = 12·1 kGm
OUTER TRACKING REGION
∫B·dr = 3.3 kGm
100
200
300
r (cm)

Fig. 3

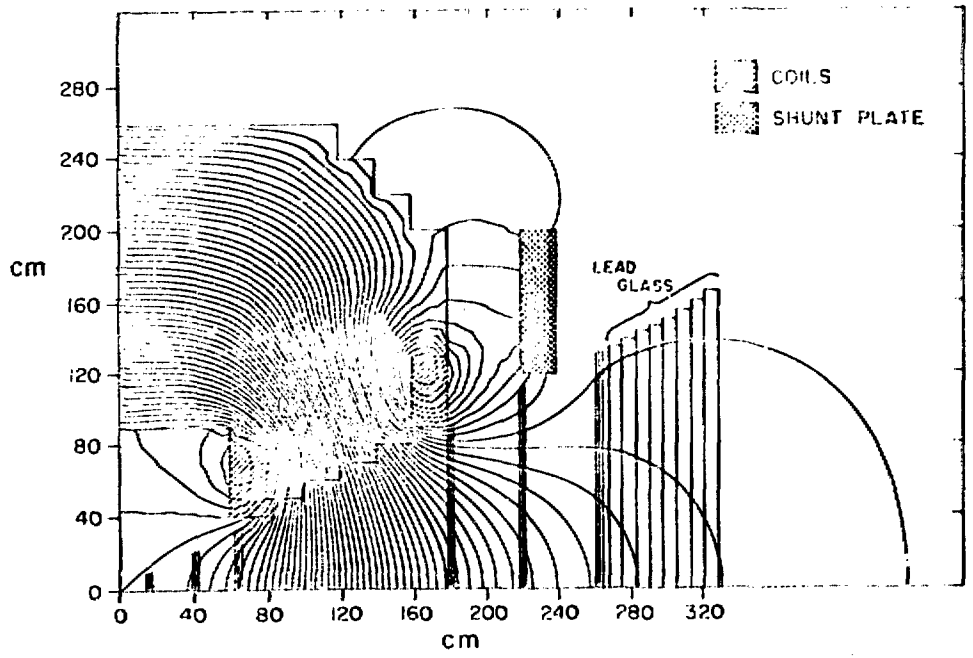
COILS
SHUNT PLATE
LEAD GLASS
cm
280
240
200
160
120
80
40
0
0
40
80
120
160
200
240
280
320
cm

Fig. 4

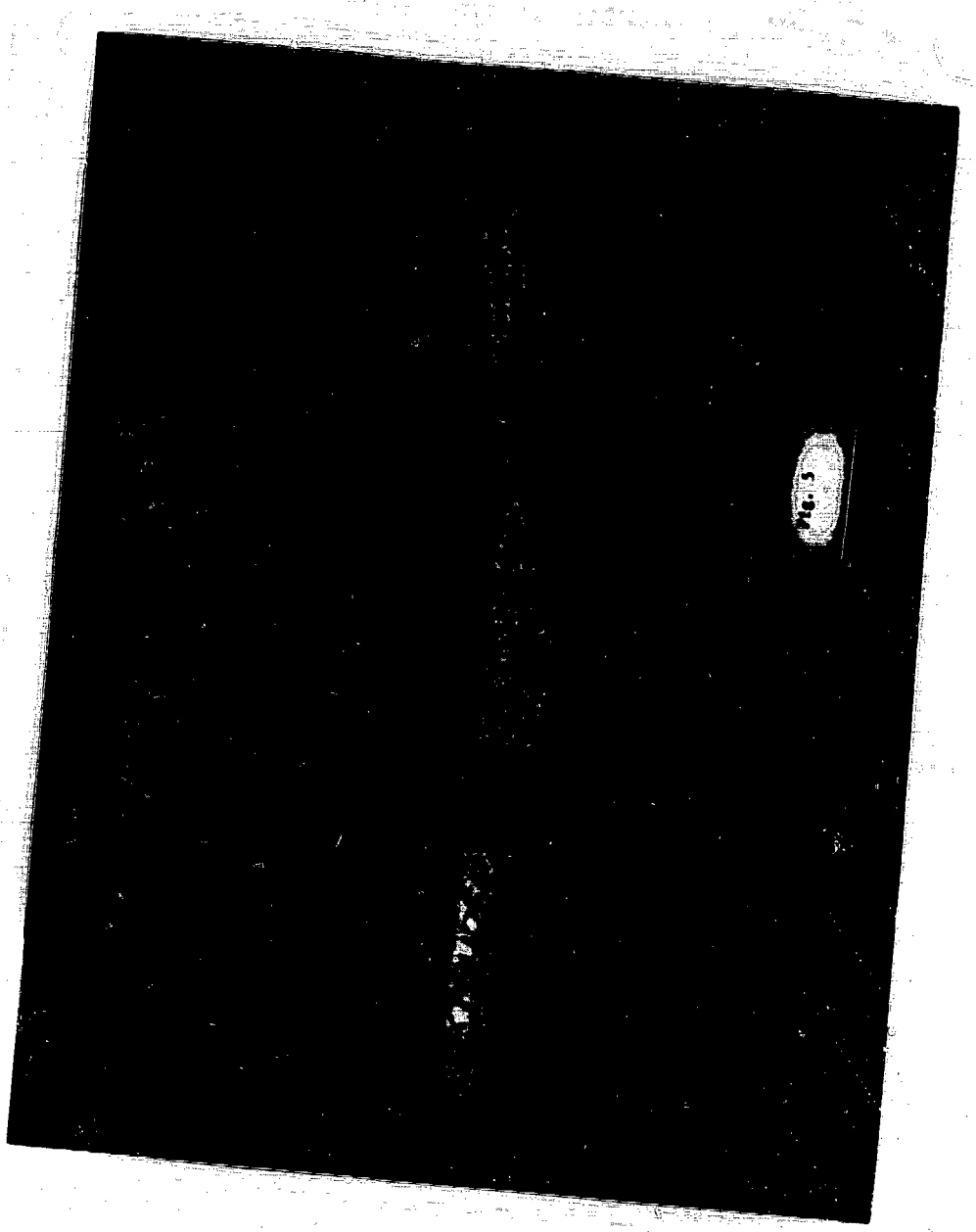

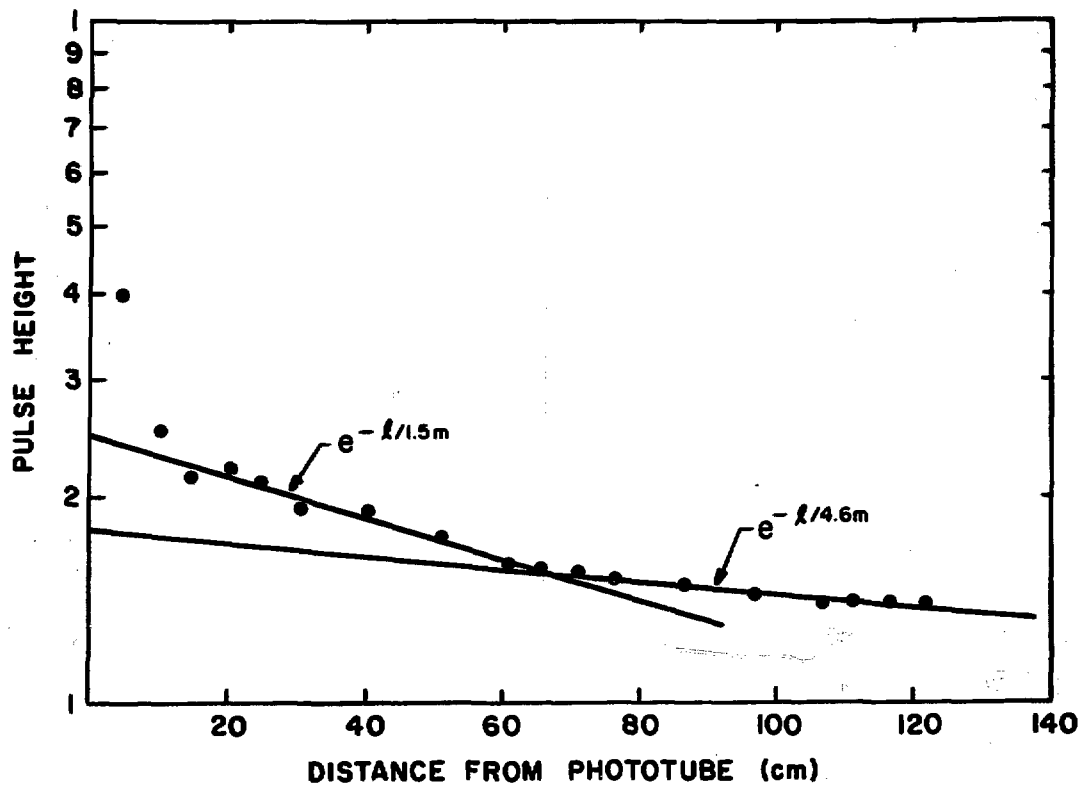
PULSE HEIGHT
DISTANCE FROM PHOTOTUBE (cm)
e^-ℓ/1.5m
e^-ℓ/4.6m
1
2
3
4
5
6
7
8
9
20
40
60
80
100
120
140

Fig. 6

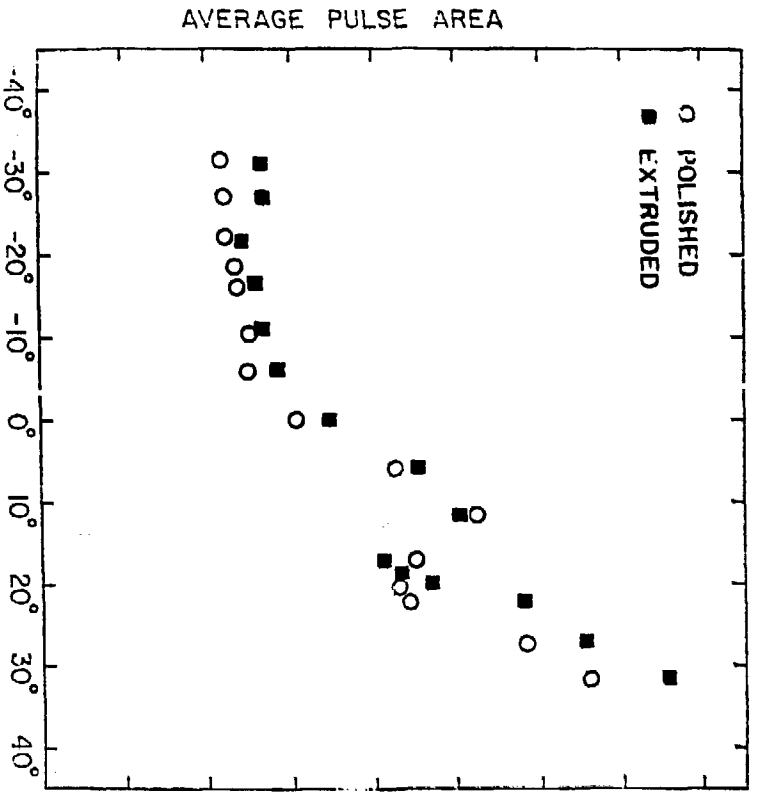
AVERAGE PULSE AREA
POLISHED
EXTRUDED
-40°
-30°
-20°
-10°
0°
10°
20°
30°
40°
BEAM ANGLE

Fig. 7

THE MAGNETIC HALL DETECTOR

M. Chen, MIT, C. Cheng, IHEP Beijing, T. Matsuda, MIT,
H.W. Tang, IHEP Beijing, and J. Warnock, MIT

I. INTRODUCTION

The records of high energy physics in the last decade are full of suprises and successes. Among these are the discoveries of new quarks and leptons and the success of gauge theories. The Glashaw - Weinberg - Salam SU(2)xU(1) model for the electromagnetic - weak interaction and QCD for the strong interaction are the highlights of the latter. However, at present our scheme has not yet been completed; at least one additional quark is yet to be observed, and the discoveries of one or more Z^0 and $W^{\pm}$ either elementary or composite, at the mass values either as predicted by the standard model or their absence, will have perfound impact on particle physics. If the theory of mass generation turns out to be correct, we have also to find the Higgs particle (or the technicolored particles). ISABELLE,[1] the proton-proton collider which presumably comes in operation in 1986 with the center-of-mass energy of 700 GeV and the initial luminosity of 2×10^{31} $cm^{-2}sec^{-1}$, will certainly be one of the best places to study these new phenomena. However, the ultimate goal of ISABELLE could be still beyond these studies. Because of the the large center-of-mass energy and the very high luminosity we can expect brand-new phenomena. Therefore major detectors at ISABELLE should have enough flexibility so that they can be modified in the later stage to look for the as yet unexpected, as well as the capability to study the "standard" phenomena with high precision at the first stage.

Keeping these points in mind we proposed a high resolution muon/flavor spectrometer consisting of a 4KG, large volume ($10\times10\times10$ m^3) solenoidal magnet, high resolution vertex chamber, electromagnetic and hadronic calorimeter and muon chambers as one of the major facilities at ISA.

II. PHYSICS AT ISA

ISA will give us an opportunity to search for new particles at the highest energy ($\sqrt{s}$ = 700 GeV) with a high luminosity of the order of 2×10^{31}

cm^{-2}/sec. With the booster installed and with additional superconductive low-β quadrupoles closer to the intersection region at the later stage, the luminosity can be further increased to 10^{33} cm^{-2}/sec. Assuming an integrated luminosity of 1×10^{38} cm^{-2} for the first year and 10^{40} cm^{-2}/year with the booster, the following physics could result:

This approach that the detector gets more sophisticated as time goes on matches with the increases of luminosity.

1) $Z^0, W^{\pm}$ production and the leptonic decays

a) Masses of Z^0 and $W^{\pm}$

To reveal the nature of the weak force is clearly one of the most fascinating tasks of high energy physics of the '80s. All the experimental evidence from νp, νe,[2] polarized ep[3] and recent high energy e^+e^- data from Petra[4] are so far consistent with the standard SU(2)xU(1) model.

After including the $O(\alpha)$ radiative corrections, the standard model predicts the following values for the $W^{\pm}$ and Z^0 masses to be[5]

$$m_W = 83.0 \pm 2.4 \text{ GeV} \tag{1}$$

$$m_Z = 93.8 \pm 2.0 \text{ GeV} \tag{2}$$

with

$$\sin^2 \theta_W = 0.217 \pm 0.012 \tag{3}$$

Of course, one can obtain $\sin^2\theta_W$ as a function of m_W or m_Z. To determine $\sin^2\theta_W$ with a precision better than that given in Eq. (3), one should strive to measure m_W and m_Z to within 2GeV. If both are precisely determined, their ratio would show if there is any deviation in the parameter ρ

$$\rho = \frac{m_W^2}{m_Z^2 \cos^2\theta_W} \tag{4}$$

which is predicted to be 1 in the standard model.

b) The Z^0 Width

Using $\sin^2\theta_W = 0.217$ and $m_Z = 93.8$ GeV, the lowest order partial decay widths of the Z^0 are predicted to be (in the standard model)[6]

$$\Gamma_o(Z^o \to \ell\bar{\ell}) \simeq 0.092 \text{ GeV} \tag{5a}$$

$$\Gamma_o(Z^o \to \nu_\ell \bar{\nu}_\ell) \simeq 0.181 \text{ GeV} \tag{5b}$$

$$\Gamma_o(Z^o \to \text{hadrons}) \simeq 2.109 \text{ GeV} \tag{5c}$$

where ℓ is a charged lepton ($e,\mu,\tau...$) and $m_t \simeq 20$ GeV has been used in Eq. (5c).

Summing over the three lepton species gives

$$\Gamma_o(Z^o \to \text{all}) \simeq 2.93 \text{ GeV} \tag{6}$$

The quantum chromodynamic corrections are the same as those computed for $R \equiv \sigma(e^+e^- \to \text{hadrons})/\sigma(e^+e^- \to \mu^+\mu^-)$ if we neglect terms of order m_q^2/m_Z^2 (m_q = quark mass). Such calculations yield[7,8]

$$\Gamma(Z^o \to \text{hadrons}) = \Gamma_o(Z^o \to \text{hadrons}) \times \left[1 + \frac{\alpha_s(m_Z)}{\pi} + 1.3\left(\frac{\alpha_s(m_Z)}{\pi}\right)^2\right] \tag{7}$$

Using $\alpha_s(m_Z) \simeq 0.13$ implies about a 4% enhancement in the hadronic width. This including radiactive corrections one finds for the Z^o's predicted total width

$$\Gamma(Z^o \to \text{all}) \simeq 3.02 \text{ GeV} \tag{7}$$

The result in Eq. (7) is for three neutrino species. If the total width is found to be larger it could be interpreted as implying the existence of additional neutrinos. One finds that the number of neutrino species, N_ν, is given by

$$N_\nu = 5.52\ \Gamma(Z^o \to \text{all})/1 \text{ GeV} - 13.7 \tag{8}$$

In order to estimate the accuracy to which Γ_{Z^0}, the width of the Z^0, could be determined from a given number of $Z^0 \to \mu^+\mu^-$ events, the following procedure was adopted. The width was assumed to be 2.9 GeV, and the mass resolution of the detector was taken to be constant at σ = 1 GeV. Furthermore, it was assumed that the cross section followed the Breit-Wigner form, and the background from Drell Yan events was subtracted out. The Breit-Wigner cross section was then smeared using a Gaussian function with σ = 1 GeV, representing the mass resolution of the detector. A Monte Carlo[9] was then used to produce a pair events according to the resulting curve. The events were then gathered into 0.5 GeV bins and the number of events per bin was compared to the number predicted from the curve used to generate the events. A chi squared fit was carried out; the Z^0 width used in the Monte Carlo generation of the events was varied, while holding the Z^0 width constant in the comparison curve. The widths which gave χ^2 value of 1 above the minimum chi square value were taken as defining the 1σ limits on Γ_z. The results were the following; with 800 $\mu^+\mu^-$ events, the width can be measured to $\sim$200 MeV; with 3000 $\mu^+\mu^-$ events $\Delta\Gamma$ = 100 MeV.

The μ pair production rate from Z^0 decays has been calculated (Fig. 1) to be about 2000 per 1000 hours at a luminosity of 2×10^{31} cm^{-2}sec^{-1}. The acceptance of any detector for $Z^0 \to \ell^+\ell^-$ as a function of the minimum detection angle is shown in Fig. 2. For a detector covering 30° to 150° the acceptance is $\sim$40%, or a counting rate of 800 μ pair events per 1000 hours.

As for the accuracy to which the mass can be measured, the statistical error is given by $\Delta m_{Z_0} \sim (\Gamma/2)(1/\sqrt{N})$ giving Δm_{Z_0} = 50 MeV with 800 $\mu^+\mu^-$events observed. When systematic errors are included (for example the uncertainty in the chamber alignment to $\sim$100 μm over 5 m diatance in 4KG magnetic field) Δm_{Z_0} is estimated to be $\sim$200 MeV. This in turn yield $\sin^2\theta_w$ with an accuracy of $\pm$0.001 in the framework of the standard model.

c) <u>$W^\pm \to$ lepton$^\pm\nu$</u>

In order to study the $W^\pm$ at ISA with the proposed detector one would look for the signal from $W^\pm \to \mu^\pm\nu$. The rate for $W^+ \to \mu^+\nu$ is expected to be 18000 per 1000 hours assuming an intial luminosity of 2×10^{31} cm^{-2}sec^{-1}, and for $W^- \to \mu^-\nu$ the rate is predicted to be 12000 per 1000h. With a detector

covering $30° < \theta < 150°$, the detection efficiency is ~75%. This translates into 22500 $W^{\pm}$ events per 1000 hr.

The single μ spectrum from the $W^{\pm}$ in pp interactions will show a significant charge asymmetry due to the V-A structure of the $Wq\bar{q}$ coupling. The expected asymmetry is shown in Fig. 3 as a function of rapidity of the muon.

There are two major backgrounds for the single lepton from $W^{\pm} \to \mu^{\pm}\nu$ decay. One is the lepton from $Z^{o} \to \mu^{+}\mu^{-}$ decay. The other is from the semileptonic decays from the flavored particles s, c, b and t. Their lepton P_T spectrum are shown in Fig. 4.

Two signatures which can be used to distinguish these events from the background are the following. Firstly, the presence of a relatively isolated high P_T muon. If one looks at the total energy of the hadrons along the direction of the muon, one can significantly decrease the background due to the decay of particles with heavy quarks. For the latter type of event, the energy of the hadrons along the direction of the muon is expected to be fairly large, since the muon is associated with the hadron jet, whereas in $W^{\pm}$ decays one would usually expect this energy to be smaller. The two distributions are shown in Fig. 5.

The second signature is a missing P_T from the undetected neutrino. The missing P_T distribution from $W^{\pm}$ decays is compared with that observed in heavy flavor decays in Fig. 6. Another important source of background muons comes from $Z^{o} \to \mu^{+}\mu^{-}$ when one of the muons is missed by the detector. This background can be kept small if the detector can identify leptons in the range $10° < \theta < 170°$ (without necessarily measuring their momenta accurately). Also, experimentally measuring the P_T distribution of the Z^{o} allows one to determine the P_T distribution of the $W^{\pm}$. The distribution obtained in this way can be compared with the distribution obtained from the P_T spectrum of the muons from $W^{\pm}$ decay once the background due to heavy flavor decay and the Z^{o} has been suppressed as discussed above.

The expected $\mu^{\pm}$ spectrum from $W^{\pm}$ decay after one year of running, are shown in Fig. 7 as function of P_T for two different values of M_W. One can determine the mass of the $W^{\pm}$ to within 2 GeV from the P_T distribution of the muons. This corresponds to a $\Delta(\sin^2\theta_W)$ of $\pm.02$.

We studied also the possibility of detecting $W^+ \to t\bar{b}$. A suggestion of using an $\ell^+\ell^+$ trigger doesn't seem fruitful, the effective mass reconstructed (assuming perfect detection of remaining energy) is so smeared because of the missing neutrinos that it is impossible to separate this from $t\bar{t}$ background.

Another possibility is to use charmed particle detection in high mass jets to enrich the sample of heavy quark jets. In $W \to t\bar{b}$ about $\sim$40% of the events have a D (or F) with p> 10 GeV, and $\sim$50% have leptons with p > 4 GeV. Assuming one could identify such events one could calculate the W mass from the two jets. The present D^+ lifetime is $\sim 5 \times 10^{-13}$ sec, for p = 10 GeV/c $\gamma \sim 5$ meaning $c\tau \sim 750$ μm, so one needs detectors near the interaction region that would allow one to reconstruct vertices with $\sigma \sim 200$ μm in order to select charm events.

2) New Sequential Lepton

If a new sequential heavy lepton exists with a mass of less than half that of the Z^0, then one can study its properties by looking at events of the type $Z^0 \to L^+L^-$. We would require that one of the heavy leptons decays into a muon and that the other decays hadronically. The expected rate for this type of event is about 400 per 1000 hours. In the detector one would see an isolated muon opposite to a broad hadron jet. Also one would expect to observe a relatively large missing P_T due to the neutrinos produced. The total width of the Z^0 would also be increased by the presence of the new heavy lepton and its associated neutrino; the total contribution to the width being about 270 MeV.

3) Search for New Neutral High Mass Leptons

Another possibility is a new heavy neutral lepton with a mass $\leq M_{Z^0}/2$ produced in the Z^0 decay; i.e., $Z^0 \to \ell^0\bar{\ell}^0$. Assuming that the new lepton couples with the Z^0 in the same way that neutrinos do, the width of Z^0 will be increased by 180 MeV for each additional type of lepton, which corresponds to 4000 $\ell^0\bar{\ell}^0$ events. This new neutral lepton could be observed by its decay, e.g., $\ell^0 \to \mu\pi$, with a mass resolution of better than 1% in the proposed detector.

4) New Quarks and Onium

If massive quarks exist, heavy vector mesons like J or χ with new flavors will be produced in pp collisions.[10] Assuming the Gaisser scaling law for the heavy vector[11] mesons holds and that the ratio of the production cross section to the Drell-Yan process at $m_{Q\bar{Q}}$ is the same as that of the J and χ,[12] the yield of such a new quarkonium is calculated as a function of its mass. The measured width is dominated by the experimental resolutions. Therefore, the signal-to-noise ratio improves with the mass resolution, which we assumed to be $\Delta m/m = 1\%$. As we see in Fig. 8, we can detect such a particle up to $M_{Q\bar{Q}} \approx 70$ GeV at ISA.

The process $Z^o \to t\bar{t}$ can be observed provided that the mass of the t quark is smaller than half the mass of the Z^o. With an initial luminosity of 2×10^{31} cm^{-2}/sec, we expect the rate for this type of event to be around 4000 per 1000 hours for $m_t \sim 20$ GeV. The signature for this type of event would be two broad jets with total invariant mass $\sim m_z$. Alternatively if we required that one of these jets contain a muon, these $t\bar{t}$ events can be distinguished from the background $Z^o \to u\bar{u}$, $d\bar{d}$, $s\bar{s}$, $c\bar{c}$, $b\bar{b}$ by looking at the P_T of the muon relative to the accompanying hadron jet. The $t\bar{t}$ events can also be produced directly in pp collisions. The production cross-section as a function of the mass t-quark is shown in Fig. 9. The $t\bar{t}$ events give rise to a higher P_T muon on the average than is observed in the events where Z^o decays into lighter flavors and therefore they can be distinguished from each other as shown in Fig. 10 for $m_t = 20$ GeV.

5) Multiple Muon Events

Heavy new flavored particles such as top mesons could be produced at ISABELLE. Their decay into single high P_T muon final states is rather copious. As discussed earlier, the P_T of the lepton with respect to the hadron jet will be higher for heavy quarks than light quarks. Such multiple muon events with multiple secondary vertices will be an important signature of the production of heavy flavored particles.[13] Also, if Higgs particles[14] or technicolor particles are produced[15] at ISABELLE, we could have multiple muon events through their dominant decays into heavy leptons and heavy quarks.

6) Lifetime of Long-Lived Particles

The relatively long-lived particles ($10^{-13} < \tau < 10^{-10}$ sec) produced from e.g., the Z^0 decay can be studied by reconstructing their decay vertices, making full use of the high spatial resolution and the good track separation of the time expansion chamber. With a given resolution of σ, the vertex position along the track direction will be determined with a resolution of σ/θ, where θ is the angle between the two charged secondaries according to which the vertex is reconstructed. Since $\theta_{max} = 1/\gamma = M/E$, the distance from the intersection point to the decay vertex can be determined with a resolution of $\sigma \cdot \gamma$. For the sake of simplicity we have assumed $E \gtrsim M_{Z^0}/2$, which strictly is true only for $\tau^{\pm}$ and high mass leptons. The average decay lengths and resolutions for various particles are shown in in Fig. 11, the distributions of the vertex distance from the interaction point are plotted. It is feasible to measure the lifetimes of the particles if they decay into multi-charged final states with reasonable branching ratios and if their lifetimes are within the range 10^{-13} to 10^{-10} sec.

7) High Mass Z^0 & $W^{\pm}$[16]

Although the present data is consistent with the prediction of the standard model, the intermediate boson structure to be explored at high energies is by no means uniquely determined by what has been observed so far in the low energy regime. This is why weak boson hunting may still turn out to be an exciting adventure in the years to come.

The absolute bound on the mean charged boson mass, $\bar{M}_W \gtrsim 178$GeV, the mass relation and the lower bound on neutral boson production represent roughly everything.[17] which can be said about the carriers of the weak force on fairly general grounds. More detailed predictions in scenarios alternative to the standard model (in the absence of, e.g., a concrete and soluble dynamics of subconstituents) must rely on more specific assumptions, i.e., the choice of undetermined parameters. A specific two boson scenario was worked out by Schildknecht and Kuroda[18] with $\bar{M}_Z = 120$GeV ($\bar{M}_W = 97$GeV) and neutral boson masses $m_1 = 100$ GeV and $m_2 = 180$ GeV. The higher mass boson may be considered as approximating a possible continuum. For details refer to reference 18. Fig. 12 shows the production cross section for pp for the two boson scenario, a single boson model with $M_Z = 120$ GeV, and the standard model.

Experiments at ISA will hopefully decide on the question, whether the carriers of the weak force are indeed the gauge bosons of the standard model, or whether, alternatively, they form a more complex system, perhaps associated with a substructure of leptons and quarks, quite analogous to the role played by the vector mesons[19] in QCD. In this case multiple (>2) lepton or quark jets will provide a dramatic signature which can be unambiguously observed by a detector such as the one proposed here.

III. DETECTOR

The detector we propose here consists of;

1) a 4K Gauss, large volume ($10x10x10m^3$) solenoidal magnet,
2) a high resolution vertex chamber,
3) electromagnetic and hadronic calorimeters, and
4) muon chambers inside and outside the iron return yoke.

At the first stage of the experiment, only the vertex chamber and muon chambers will be installed in the magnetic field. In this stage, we will measure momentum of charged particles, especially muons, with the resolution of $\Delta P/P \simeq 2\%$, search for new particles such as Z^o, $W^{\pm}$, toponium, Higgs particles and the second Z^o etc., in their leptonic decay modes, and determine the masses and the widths of these particles. In the second stage, we will install the electromagnetic and hadronic calorimeters which will enable us to measure missing - P_T, energy-flow of hadron jets and lepton-hadron correlations. Thus, as is discussed in the section II, we can study the heavy flavor productions and search for heavy quarks and leptons in their weak decays, and also Higgs (Technicolor) particles in their heavy particle decay modes.

Beyond this stage, depending on what kind of new physics might come up at ISABELLE at the time, we may modify our detector configuration and add new detector elements in order to identify hadrons, electrons in jets etc. since we have enough space in the magnet.

The side view and end view of the proposed detector in the second stage are shown in Fig. 13.

1) 4K Gauss, Large Volume Solenoidal Magnet

To obtain a 4K Gauss, $10x10x10m^3$ solenoidal magnetic field, we plan to use a conventional aluminum coil magnet. The technical feasibility of this

kind of large magnet, together with some options on coil windings, is discussed in ref. 20. The coil has an inner rectangular cross-section of $10 \times 10 m^2$ and a length of 10m. Since power is expensive, we limit it to 2 Mega watts requiring the coil thickness of ≈60 cm. Total weight of aluminum coil would be 700 tons. The iron surrounding the coil has a thickness of 60 cm (3.5 absorption lengths) to provide for a nonsaturated return yoke.

The iron end caps completing the magnet will reduce the stray magnetic field and will improve the field homogenity. The iron return yoke would weighs ∿2000 tons. To reduce the construction cost, there is a possibility to use a sodium conductor as an alternative to aluminum conductor as is discussed in ref. 20. Fig. 14 shows one of the option of coil winding method utilizing a helix made from aluminum bars welded together at the corners as it is assembled.

2) High Resolution Vertex Chamber

Immediately surrounding the beam pipe, one possibility is to use a cylindrical drift chamber based on the principle of the time expansion chamber[21] with a spatial ($r\phi$) resolution of 10 ∿ 30 μm and a double track separation of 200 μm at atmospheric pressure. In the time expansion chamber the anode signal is kept fast using thin wire and small gap, while the drift of the electrons produced by the track is slowed down by using low electric field. In this way it is possible to obtain an anode signal truly reflecting as a function of time the spatial distribution of the charge density. Measuring the center of gravity of this signal is equivalent to measuring the center of gravity of the spatial distribution which is mostly due to diffusion. By accepting a large fraction of the ionization of the track, the error due to diffusion for a given drift length x (e.g., x=1 cm) is consequently:

$$\Delta x = \sigma_{diff}/\sqrt{n}$$

with σ_{diff} the broadening due to diffusion of a single electron, and n the number of accepted electrons. With $n \simeq 50$ and $\sigma_{diff} = 50$ μm (for x=1 cm), 7 μm is the contribution to the spatial resolution due to diffusion. Careful measurements in pressurized standard drift chambers[22] found a constant contribution for the best gas which would in the time expansion mode have a contribution of

ΔX_o = 10 μm such that we would expect in the time expansion drift chamber a position resolution of

$$\Delta X_{rms} = \sqrt{100 + 50X\ (cm)}\ \ (\mu m).$$

Fig. 15 shows the scheme of the chamber operation. Drift time is measured by the zero-crossing of the induced signal on two potential wires. The width of the signal will give us the information of the track angle. In Fig. 16, the end view of the practical chamber is shown. The inner and outer radii of the chamber are 10 cm and 60 cm respectively and the length is 2 m. The chamber is electrically dividied into 30 segments. Each segment has 2 drift regions and the 40 amplifying cells at the center. The amplifying cell structure is shown in Fig. 17. The drift region is separated from the amplifying region by a carbon-coated nylon mesh which can be stretched accurately to the position. Left-right ambiguity is resolved by having two anode wires for each cell. The z-coordinate is measured by charge division on the anode wires, giving a resolution of $\sigma_z \lesssim 8$ mm.

The chamber is planned to operate at the drift field of E=0.2 KV/cm for 83% Ar-9% CH_4-8% $CH_2(OCH_3)_2$ gas mixture of the normal pressure, a mixture which has been successfully used in first tests with the time expansion chamber. There are indications of mixtures giving smaller diffusion which will be investigated. The drift velocity is $\sim$1 cm/μsec, which corresponds to the maximum drift time of 6 μsec for our chamber design. Due to the time expansion method, we can get a good track separation of $\sim$200 μm, which is demonstrated in Fig. 18. The systematic accuracy will be limited by irregularities in the flatness of the amplifying plane (nylon mesh) and the cathode plane. To minimize mechanical distortions of the chamber body which cuase displacements of the meshes, we plan to isolate the chamber in an aluminum vessel under tight controls of temperature and gas mixture. Several methods of calibration, including the use of a pulsed X-ray and/or a pulsed laser beam, are now under consideration.

3) Electromagnetic and Hadronic Calorimeter

We propose to use an electromagnetic and hadronic calorimeter outside the precision vertex chamber in the second stage of ISA experiment to measure

the electronmagnetic and hadronic energy of the final states. As an example the calorimeter can be a multi-plate sampling device with uranium-tungstun plates and parallel plate avalanche chambers[23] (or "multiplate ion chamber") (McDonald and Walenta).

In this device high voltage is applied across adjacent plates to yield gas amplification of the ionization caused by an electromagnetic or hadronic shower. Although charge is collected during the entire drift time of electrons and ions across the gap, a signal rise time of some 10 nsec can be obtained. This is because the largest part of the prompt signal is due to amplification very close to the anode of the avalanche initiated by electrons which were liberated near the cathod, and hence have a long path for the avalanche.

In an electromagnetic calorimeter made of 1/2 radiation length of lead or tungsten, the expected energy resolution is $\sigma/E \lesssim 22\%/\sqrt{E}$.

In such a hadronic calorimeter the energy resolution is expected to be $\sigma/E \lesssim 80\%/\sqrt{E}$ (including fluctuations in the ionization and fluctuations in the nuclear loss). The cathode (and anode) planes are easily subdivided into strips or pads to measure the transverse coordinates of the EM or hadronic showers.

In Fig. 19 the side view and the end view of the EM and hadronic calorimeter covers $45^\circ<\theta<135^\circ$. The calorimeter is divided into 8 segments as shown in Fig. 19.

The front part of the calorimeter is the electromagnetic calorimeter, with 4 mm tungsten plates and 6 mm gas gap for the parallel plate avalanche chamber. The gas filling is a mixture of Argon + 5% Acetone. There are totally 24 layers of tungsten plate-chamber sandwich blocks, which has a total thickness 27 radiation length (thickness 24 cm). The back part of the calorimeter is the hadronic calorimeter, which 15 mm tungsten plates and 6 mm gas gap for the parallel plate avalanche chamber. There are totally 48 layers of tungsten plate-chamber sandwich blocks, which has a total thickness of 7 nuclear absorption lengths (thickness is 1 meter). The total thickness of the electromagnetic and hadronic calorimeter is 124 cm.

The spatial resolution of the calorimeter is determined by the size of the chamber cells. If we subdivide the cathode (and anode) planes of the

parallel plate avalanche chambers with 4x4 cm^2 pads, we get $\sigma_\phi \lesssim 1.5°$ and $\sigma_z \simeq 4$ cm with Z along the beam axis.

The calorimeter is supported by Al mechanical structure. Some parameters are listed in Table 1.

4) Plane (Muon) Chambers

Outside the vertex chamber (outside the calorimeter in the second stage of the experiment), the type of plane drift chambers similar to our previous experiments at ISR (R209) can be used to reconstract the charged particle trajectories (the muon trajectories in the second stage) and measure their momentum. The chambers will be grouped into several layers to optimize the momentum resolution and the reconstruction efficiency. Outside the iron return yoke same type of plane chamber will be used to reconstruct the muon trajectory. Eight planes of the outer chamber will be enough to trace the muon trajectory back into the inner plane chambers and into the vertex chamber, thus to obtain a sufficient hadron rejection rate. The spatial resolution of the chamber is $\sim$200 μm and total area of the chambers would be 1800 m^2. The angular range covered by the muon chambers outside the iron return yoke is $10° < \theta < 170°$.

5) Resolution and Acceptance

The momentum resolution obtained by the proposed detector is given by the following formula:

$$\frac{\Delta P}{P} \lesssim \frac{27\sigma \sin\theta}{BL^2} \cdot P$$

where L is the track length (m), B the magnetic field (Tesla), σ the spatial resolution of the chamber (m), θ the polar angle of the particle and P the momentum of the charged partial (GeV/c). With $\sigma \lesssim 200$ μm (in the plane chambers) and $BL^2 = 10 T\text{-}m^2$ in the first stage, the formala gives

$$\Delta P/P = 5.4 \times 10^{-4} \cdot \sin\theta \cdot P \text{ (in GeV/c)}$$

For Z^0 decaying into 2 back-to-back muons, the mass resolution will be (Fig. 20)

$$\frac{\Delta m}{m} \simeq \frac{1}{\sqrt{2}} \frac{\Delta P}{P} \simeq 1.7\%$$

Considering the better spatial resolution ($20\sqrt{30}$ μm) and the number of the sampling points ($\sqrt{40}$) in the vertex chamber, the resolution should be substantially improved.

In the second stage of the experiment, after the insertion of calorimeter counter we will measure charged hadron momentum in the vertex chamber and muon momentum in the plane chambers outside the calorimeter. In the vertex chamber the momentum resolution is given by the following formula;

$$\frac{\Delta P_T}{P_T} = \frac{3.3\times10^3}{B(KG)L^2(cm^2)} \cdot P_T \cdot \sigma\sqrt{\frac{750}{N+5}}$$

where N is the number of the sampling points and the other are same as before. With $\sigma=3\times10^{-3}$ cm, N=40 and L=40 cm, the formula gives

$$\frac{\Delta P_T}{P_T} = 6.3 \times 10^{-3} P_T \text{ (GeV/c)}$$

The muon momentum resolution in this stage will be somehow worse by a factor of $2\sqrt{3}$ than in the first stage because of the shorter lever arm. However it is still sufficient to identify and measure the semi-leptic decays of heavy flavor particles with $m \gtrsim 20$ GeV.

The detector covers a polar angle range of 10° to 170° to identify muons. In the angular range of $30° < \theta < 150°$, the momentum resolution ia in the order of $5.4\times10^{-4} P_T$ (GeV). The vertex chamber covers only this angular region to avoid the high particle production rate in the beam directions.

6) Triggering on High P_T Muons

In order to take the full advantage of the high luminosity of the ISA, the detector will be triggered primarily on high P_T muons. High P_T muons can be defined by using

a) scintillation counters D_i outside the return yoke, each 60 cm wide, covering $\gtrsim$ 100 mr in azimuthal angle ϕ.

b) proportional tubes A_i positioned just outside the vertex chamber. There are 1440 such tubes each one with 1 cm diameter and two meter long. Therefore each one covers 16 mr.

c) Plane drift chambers can be used to define the trajectory of the particle and therefore the minimum value of the P_T of the particle.

The trigger can then be achieved in three steps described as follows:

a) Fast trigger ($\sim$ 20 ns) consists of a coincidence of muon counter D with beam gate, i.e. trigger 1 = (ΣD_i)*(Beam gate).

b) Secondary level trigger ($\sim$ 100 ns) consists of a coincidence between a single muon counter D_i with the corresponding proportional tubes in the same azimuthal angle, i.e.

$$\text{trigger 2} = D_i * (A_{i-1} + A_i + A_{i+1}) * \text{Beam gate}$$

c) Slow trigger ($\sim$ μs) consists of coincidence of wires of plane drift chambers in the same azimuthal region, i.e.

$$\text{trigger 3} = \sum_{j=i-1}^{i+1} Ch1_j * \Sigma Ch2_j * \Sigma Ch3_j * \Sigma Ch4_j$$

7) Particle Production Rate, Vertex Reconstruction

The expected luminosity of the phase 1 ISABELLE is 2×10^{31} cm^{-2} sec^{-1} which produces about 0.3 interactions per each beam crossing of 220 nsec intervals. Since our time expansion vertex chamber has a averaged drift time of 3 μsec, the probability having more than one interaction for a trigger would be substantial. However, the recorded tracks of the particles from the interactions in the second beam crossing will be shifted from the real tracks by $\sim$220 ns x drift velocity closer to the cathode plane. In the time expansion chamber of the drift velocity of 1 cm/μsec, these shifts are in the order of 2 mm compared to the spatial resolution of $\sim$30 μm. Therefore, with the proposed configuration of the chamber, the particles from the second beam crossing will not form any significant verticies. Moreover, in the polar angle range of $30° < \theta < 150°$, where the vertex chamber covers, the particle

production rate[24] is estimated to be $\simeq 10^4$ particles/sec/mrad for $\sqrt{s}$=800 GeV and for the luminosity of 10^{33} cm^{-2} sec^{-1} (Fig. 21). For the phase 1 luminosity (2×10^{31} cm^{-2} sec^{-1}), this estimate gives $\sim$5 particle produced into the vertex chamber in 3 μsec in average. Therefore either we would not see any particle from the second interaction or we would separate two events by the verticies.

As the ISABELLE luminosity increases to 1×32^{32} cm^{-2} sec^{-1}, we would have $\sim$10 interactions for a trigger. But again the most of the interactions are low P_T hadric interactions and the number of the particles recorded in the vertex chamber is estimated to be $\lesssim$ 50 in average. Since the time expansion chamber has a good track separation of $\sim$200 μm, we could expect that the event reconstruction and the separation of interesting interactions with high P_T muons (or hadrons) in the same way in the phase 1 will be possible.

SUMMARY

We have proposed the high resolution muon detector consisting of a 4K Gauss, large volume solenoidal magnet, a high resolution vertex chamber and conventional plane drift chambers. This combination will permit us to make very accurate momentum measurement for all charged particles, especially μ's. High spatial resolution together with good multiple-track separation of the time expansion vertex chamber will enable us to measure secondary verticies of long-lived particle and will help us to reconstruct the interesting high P_T muon (hadron) interaction among the other interaction.

In the later stage of the experiment, we can add the calorimeter, thus the detector would stand the higher luminosity and we will be able to study heavy flavor production, possible technicolor (Higgs) production etc.

Finally one of the advantages of the proposed detector is the flexibility for the later modification. After all ISABELLE might disclose a brand-new physics and we should leave some room for it.

REFERENCES

1. M. Samios, Talk at this workshop.
2. P. Langacker et al., in Proceedings of Neutrino '79, International Conference on Neutrinos, Weak Interactions, and Cosmology, Bergen, Norway, 1979, edited by A. Haatuft and C. Jarlskog (Fysik Institutt, Bergen, 1980), Vol. I, p. 276; J.E. Kim et al., University of Pennsylvania Report No. UPR-158T, 1980 (unpublished); I. Liede and M. Roos, Nucl. Phys. B167, 397 (1980); J.J. Sakurai, in Proceedings of Neutrino '79, International Conference on Neutrinos, Weak Interactions, and Cosmology, Bergen, Norway, 1979, edited by A. Haatuft and C. Jarlskog (Fysik Institutt, Bergen, 1980), Vol. I, p. 267; L.M. Seghal, in Proceedings of the Symposium on Lepton and Hadron Interactions, Visegrad, 1979, edited by F. Csikor et al., Technische Hochschule Aachen Report No. PITHA-79/34 (unpublished); L.W. Mo, in Proceedings of the XVth Recontre de Moriond, Moriond, France (to be published).
3. C. Prescott et al., Phys. Lett. 77B, 347 (1978); 84B, 524 (1979).
4. A. Böhm, Proc. of the 20th Internat. Conf. on High Energy Physics, Madison, Wisc., 1980; D. Barbar et al., Phys. Rev. Lett. 46, 1663 (1981); R. Marshall, Rutherford Lab. Report No. RL-80/29, 1980; W. Bartel et al., DESY Report No. 80/123 (1980); Ch. Berger et al., DESY Report No. 80/116 (1980); A. Wagner, Proceedings of the 9th Recontre de Moriond, Moriond, France, 1981.
5. A. Sirlin and W. Marciano, "Radiative Corrections to $\nu_\mu + N \to \mu^- + X$ and their Effect on the Determination of ρ^2 and $\sin^2\theta_W$," to be published in Nucl. Phys. B.
6. Z. Parsa and W. Marciano, "Properties of $W^\pm$ and Z^0," Proceedings of this workshop.
7. D. Albert, W. Marciano, D. Wyler and Z. Parsa, Nucl. Phys. B166, 460 (1980).
8. K. Chetykin, A. Kataev and A. Tkachov, Phys. Lett. 85B, 277 (1979); M. Dine and J. Sapirstein, Phys. Rev. Lett. 43, 668 (1979).
9. A. Paige and S. Protopopescu, BNL-29777 (Informal Report)
10. S. Pakvasa, M. Dechantsreiter, A. Halzen and D.M. Scott, Phys. Rev. 20, 2862 (1979); M. Dechantsreiter, A. Halzen, P. McIntyre and D.M. Scott, Preprint DOE-ER/0081-202, 1981.
11. T.K. Gaisser, A. Halzen and E.A. Paschos, Phys. Rev. D15, 2572 (1977).
12. C. Kourkoumelis et al., Phys. Lett. 91B, 481 (1980); M. Goldhaber and L.L. Wang, Phys. Rev. D18, 2364 (1978).
13. A. Halzen and D.M. Scott, Proceedings of the 20th Internat. Conf. on High Energy Physics, Madison, Wisc., 1981; N. Cabibbo and L. Maiani, CERN-TH2726.
14. H.M. Georgi, S.L. Glashow, M.E. Machacek and D.V. Nanopoulos, Phys. Rev. Lett. 40, 692 (1978); S.L. Glashow, D.V. Nanopoulos and A. Yildiz, Phys. Rev. D18, 1724 (1978); Talks by A. Ali and L.L. Wang. Proceedings of this workshop.
15. S. Dimopoulos, S. Raby and G.L. Kane, UM-HE-80-22 (1980); G. Girardi et al., LAPP-TH-30 (TH3029-CERN), 1981; also talks by M.A.B. Beg, G.L. Kane, L.L. Wang, and C. Baltay, Proceedings of this workshop.
16. D. Schildknecht, Proceedings of this workshop.

17. G.J. Gounaris and D. Schildknecht, BI-TP81/09 (1981) (to be published in Z. Phys. C).
18. M. Kuroda and D. Schildknecht, BI-TP81/22; G. Gerardi, P. Mery and P. Sorba, CERN-TH-3062.
19. It should be noted that about twenty years ago the vector mesons ρ, ω and ϕ were predicted as the gauge particles associated with strong isospin and hypercharge (J.J. Sakurai, Ann. Phys. 11, 1 (1980)), while a rich spectrum of vector meson states has evolved meanwhile.
20. D. Luckey and Samuel C.C. Ting, MIT-LNS Technical 114 (1981) and talk at the ISABELLE Summer Workshop, July 21-31, 1981.
21. A.H. Walenta, IEEE Trans. Nuc. Sci. NS-26, No. 1, Feb. (1979), 73 and talk at the ISABELLE Summer Workshop, July 21-31, 1981.
22. W. Farr, J. Heintze, K.H. Hellenbrand and A.H. Walenta, NIM 154 (1978) 175.
23. K.T. McDonald and A.H. Walenta, Private communication.
24. E.H. Willen, the proceedings of the ISABELLE Summer Workshop, 1977. The Fig. 21 is taken from the "Working Draft of ISA Proposal," MIT-LNS-EMI Group, Jan. 1981.

Table I

Calorimeter	# Layers	W plate thickness (mm)	gas gap (mm)	Total thickness of W	Total thickness (cm)
EM calorimeter	24	4	6	27 r.l. (96 mm)	24
hadronic calorimeter	48	15	6	7 ab. length (72 cm)	100

FIGURE CAPTIONS

Fig. 1 The expected dimuon mass spectrum from the decays of Z^0 produced at ISA with $\sqrt{s}$ = 700 GeV.

Fig. 2 The acceptance of $Z^0 \to \ell^+\ell^-$ as a function of the cutoff angle θ_c of a detector assuming that leptons are detected in the polar angle range of $\theta_c < \theta < 180° - \theta_c$.

Fig. 3 $d\sigma/dy$ for $W^\pm \to \mu^\pm\nu$ at ISA. The charge asymmetry between μ^+ and μ^- is significant.

Fig. 4 The P_T distributions of muons from $W^\pm \to \mu^\pm\nu$ (solid curve), $Z^0 \to \mu^+\mu^-$ (slashed curve) and from the semileptonic decays from quarks. Also shown is the muon spectrum from the semileptonic decays of s, c, b and t quark after the missing P_T cut of 15 GeV/c.

Fig. 5 The distributions of $P_{L,H}$ for $W^\pm \to \mu^\pm\nu$, and quark jets with $10 < P_T^\mu < 15$ GeV/c and with $P_T^\mu > 30$ GeV/c. Here $P_{L,H}$ is defined as the sum of the longitudinal momenta of the hadrons projected along the muon momentum in the same hemisphere ($30° < \theta < 150°$); $P_{L,H} = \sum_h \vec{P}_h \cdot \hat{P}_\mu$.

Fig. 6 The distributions of missing (unbalanced) P_T for $W^\pm \to \mu^\pm\nu$ and for the semileptonic decays of c, b and t-quark.

Fig. 7 The P_T distributions of the single muons from $W^\pm \to \mu^\pm\nu$ with M_W = 79.5 GeV and M_W = 77.8 GeV. The two sets of Monte Carlo data correspond to 1000 hours of data taking at ISA ($L = 2 \times 10^{31}$ cm^{-2} sec^{-1}).

Fig. 8 The lepton pair signals of heavy-quark bound state ($Q\bar{Q}$) of the mass $M_{Q\bar{Q}}$ = 40, 50, 60, 70, 80 and 110 GeV on the Drell-Yan and Z^0 production "background." The quark charge e_Q = 2/3 and 1% mass resolution are assumed. The indicated numbers of events correspond to 1000

hours of data taking at $L = 2 \times 10^{31}$ cm^{-2} sec^{-1} with the detector acceptance of $30° < \theta < 150°$.

Fig. 9 The calculated production cross section of $p+p \to t+\bar{t}+X$ as a function of the mass of t-quark.

Fig. 10 The P_T distributions of the fastest muons from b and c quark, and from t-quark (m_t = 20 GeV) with respect to the hadron jet axis in the same hemisphere ($30° < \theta < 150°$).

Fig. 11 The distributions of the decay distance of various particles from Z^0 decay. Mean lifetimes $c\tau$ of 0.08, 0.3, 0.03 and 0.3 are assumed for τ, D^+, B and L^0, respectively. The mass of L^0 and the spatial resolution of the vertex chamber are assumed to be 10 GeV and 30 μm. Relative yields are strongly dependent on the detection efficiency for each particle.

Fig. 12 The muon pair signatures of Z^0 in the standard model, the single Z^0 model with the Z^0 mass of 120 GeV and the two-Z^0 model for pp collisions at $\sqrt{s}$ = 800 GeV.

Fig. 13 a) The side view of the proposed detector in the second stage.
b) The end view of the proposed detector.

Fig. 14 Coil construction from aluminum bar, either welded or bolted at the corners.

Fig. 15 The scheme of operation of the time expansion chamber.

Fig. 16 The end view (one quadrant) of the time expansion vertex chamber.

Fig. 17 An amplifying cell of the time expansion chamber.

Fig. 18 A demonstration of the double track separation of the time expansion chamber.

Fig. 19 The schematic side view and end view of the calorimeter.

Fig. 20 The momentum resolution (or the mass resolution for the back-to-back muon pairs) of the detector in the first stage as a function of the production angle θ.

Fig. 21 The single particle counting rate as a function of the production angle for $L = 1 \times 10^{33}$ cm^{-2} sec^{-1} and $\sqrt{s} = 800$ GeV.

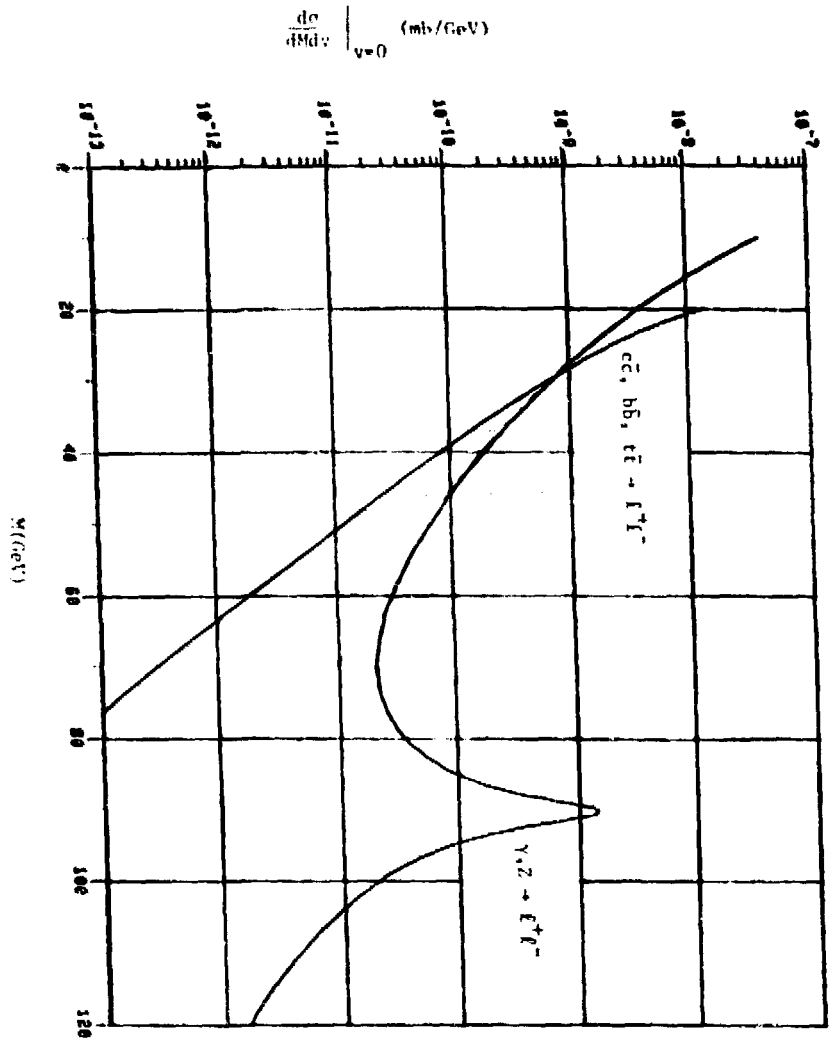
$\frac{d\sigma}{dMdy}\Big|_{y=0}$ (mb/GeV)
10^{-12}
10^{-13}
10^{-11}
10^{-10}
10^{-9}
10^{-8}
10^{-7}
0
20
40
60
80
100
120
M(GeV)
$c\bar{c}$, $b\bar{b}$, $t\bar{t} \to l^+l^-$
$\gamma, Z^0 \to l^+l^-$

Fig. 1

Acceptance for $Z^0 \to \ell^+ + \ell^-$ vs.
the cutoff angle of the detector

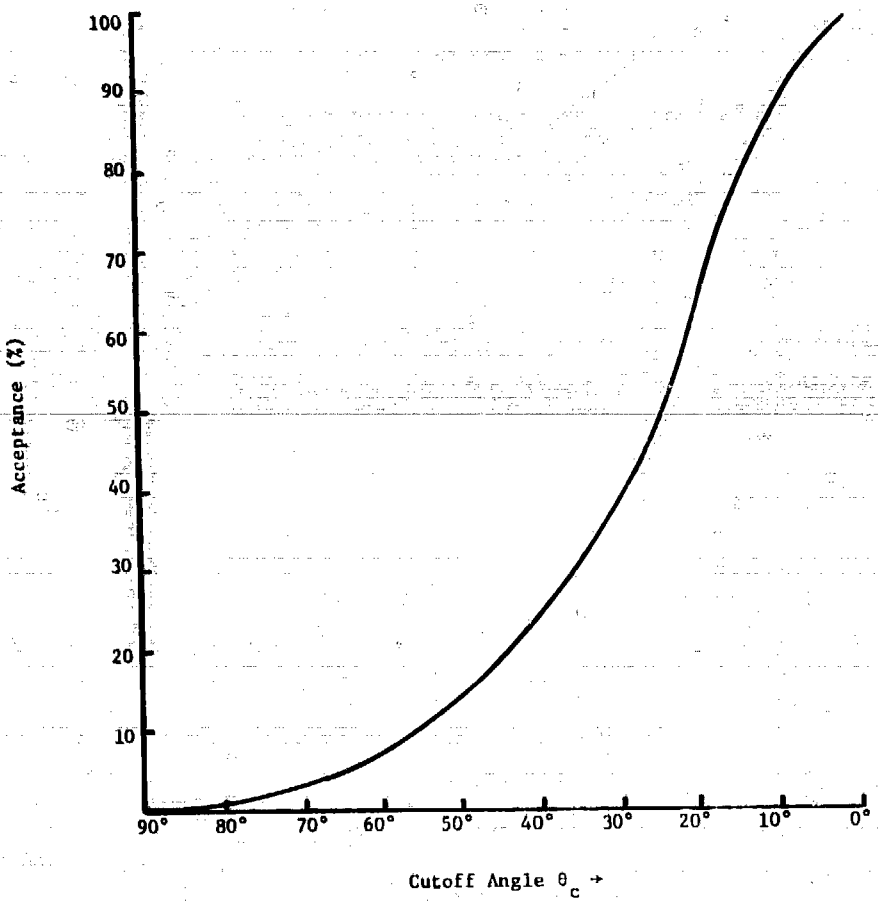

Fig. 2

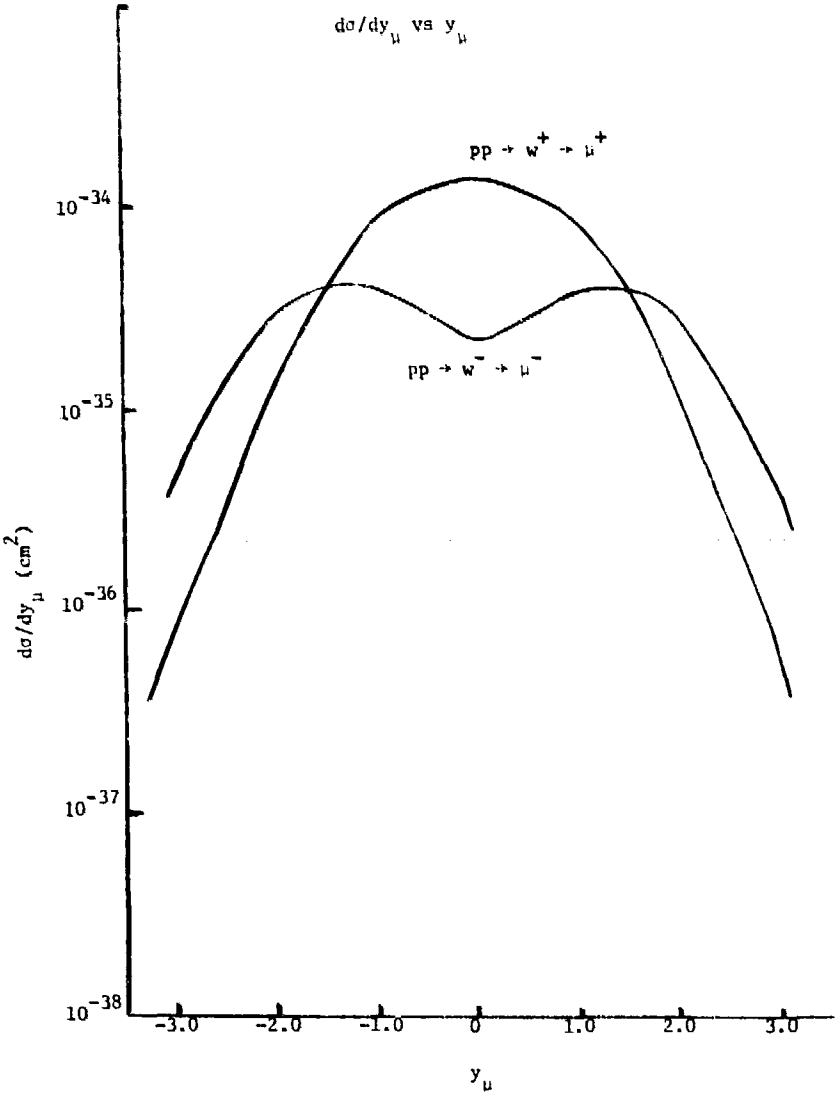
dσ/dy_μ vs y_μ
pp → W⁺ → μ⁺
pp → W⁻ → μ⁻
10⁻³⁴
10⁻³⁵
10⁻³⁶
10⁻³⁷
10⁻³⁸
dσ/dy_μ (cm²)
-3.0
-2.0
-1.0
0
1.0
2.0
3.0
y_μ

Fig. 3

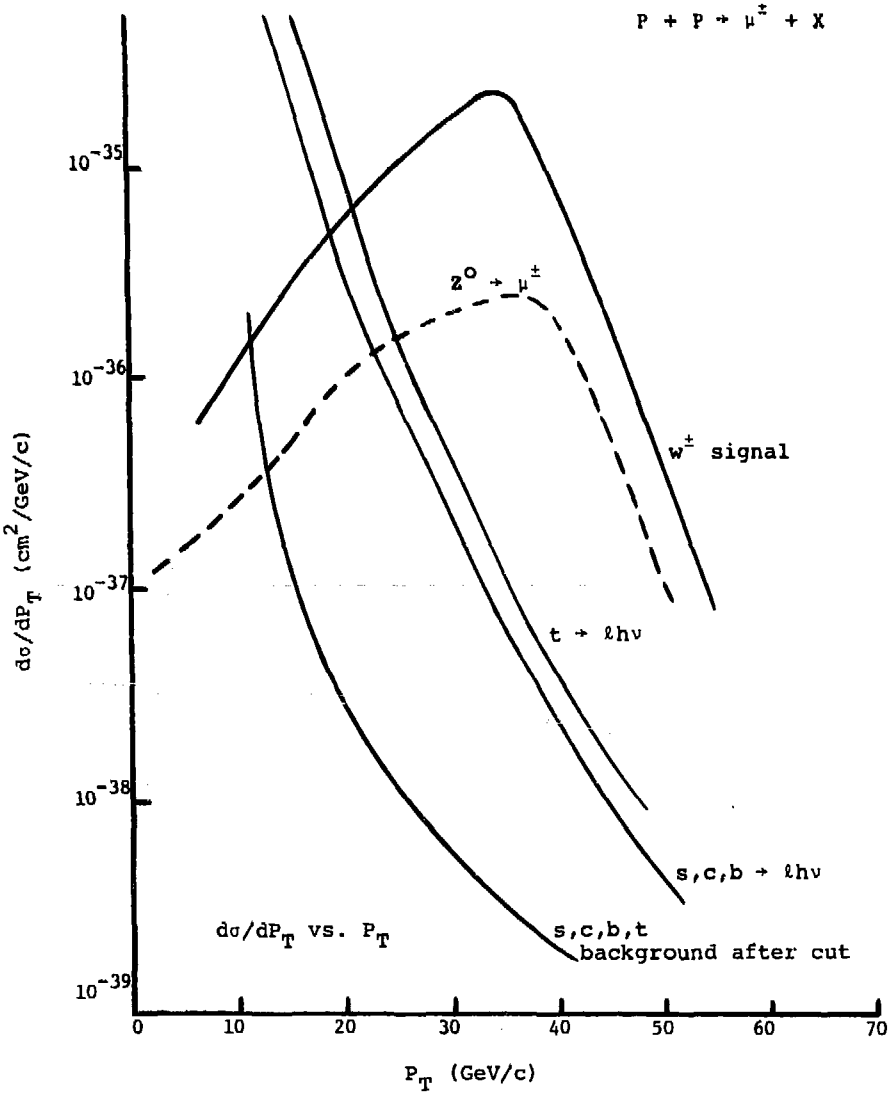
P + P → μ± + X
10^-35
10^-36
10^-37
10^-38
10^-39
dσ/dP_T (cm^2/GeV/c)
Z^o → μ±
w± signal
t → ℓhν
s,c,b → ℓhν
dσ/dP_T vs. P_T
s,c,b,t
background after cut
0
10
20
30
40
50
60
70
P_T (GeV/c)

Fig. 4

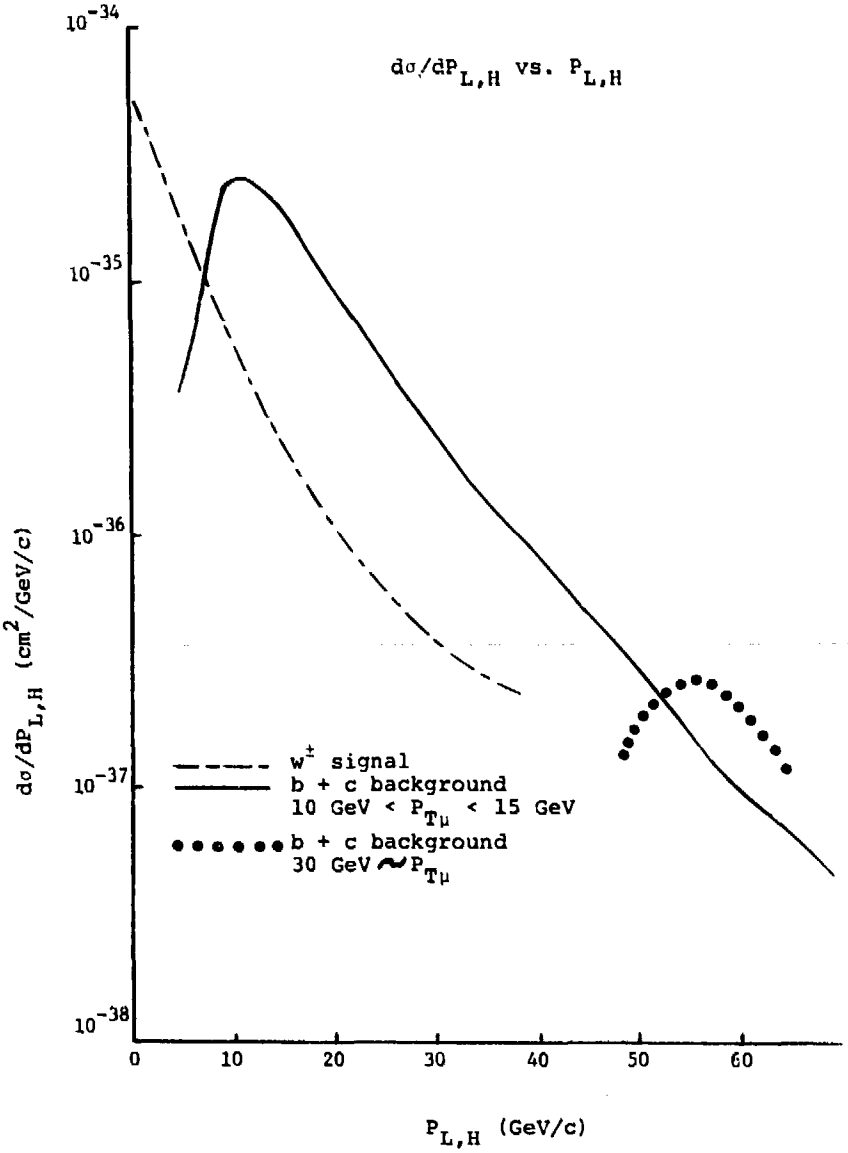
$d\sigma/dP_{L,H}$ vs. $P_{L,H}$
10^{-34}
10^{-35}
10^{-36}
10^{-37}
10^{-38}
$d\sigma/dP_{L,H}$ (cm^2/GeV/c)
$w^{\pm}$ signal
b + c background
10 GeV < $P_{T\mu}$ < 15 GeV
b + c background
30 GeV ~ $P_{T\mu}$
0
10
20
30
40
50
60
$P_{L,H}$ (GeV/c)

Fig. 5

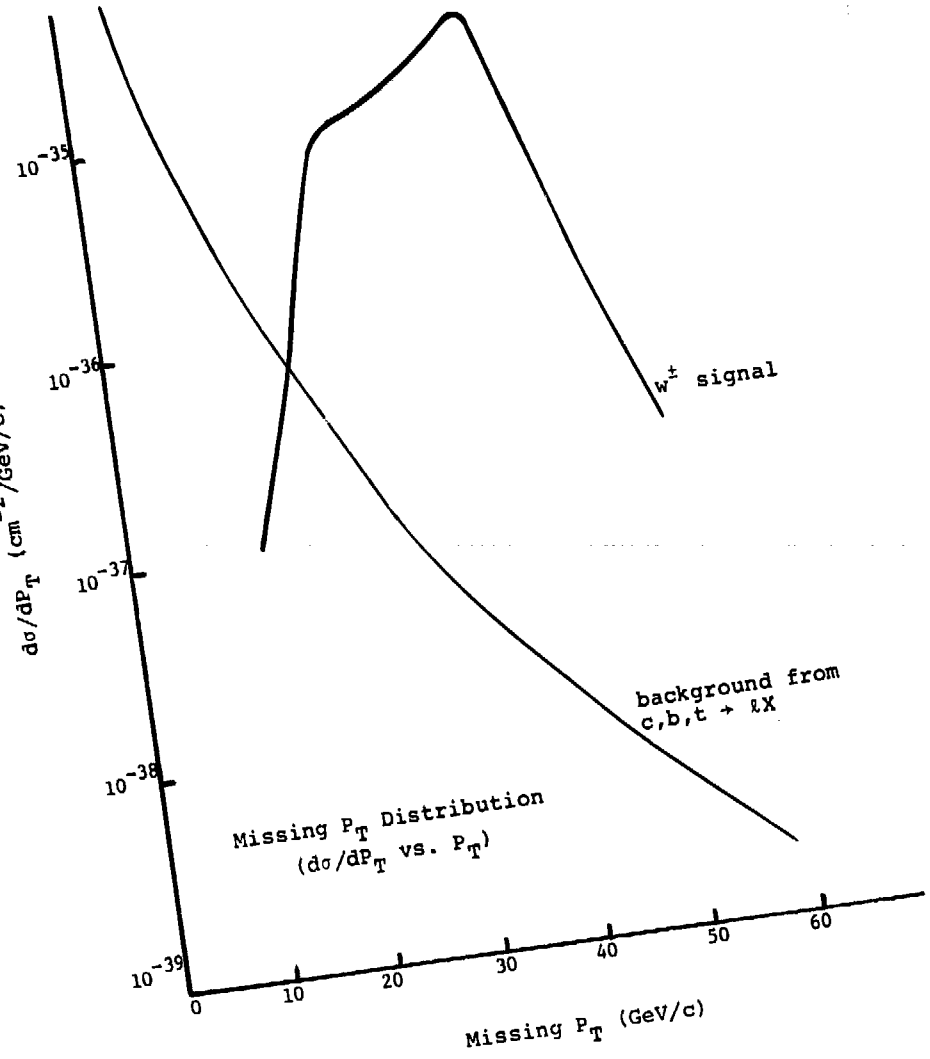
10^{-35}
10^{-36}
10^{-37}
10^{-38}
10^{-39}
$d\sigma/dP_T$ (cm^{-2}/GeV/c)
$W^{\pm}$ signal
background from c,b,t → ℓX
Missing P_T Distribution
($d\sigma/dP_T$ vs. P_T)
0
10
20
30
40
50
60
Missing P_T (GeV/c)

Fig. 6

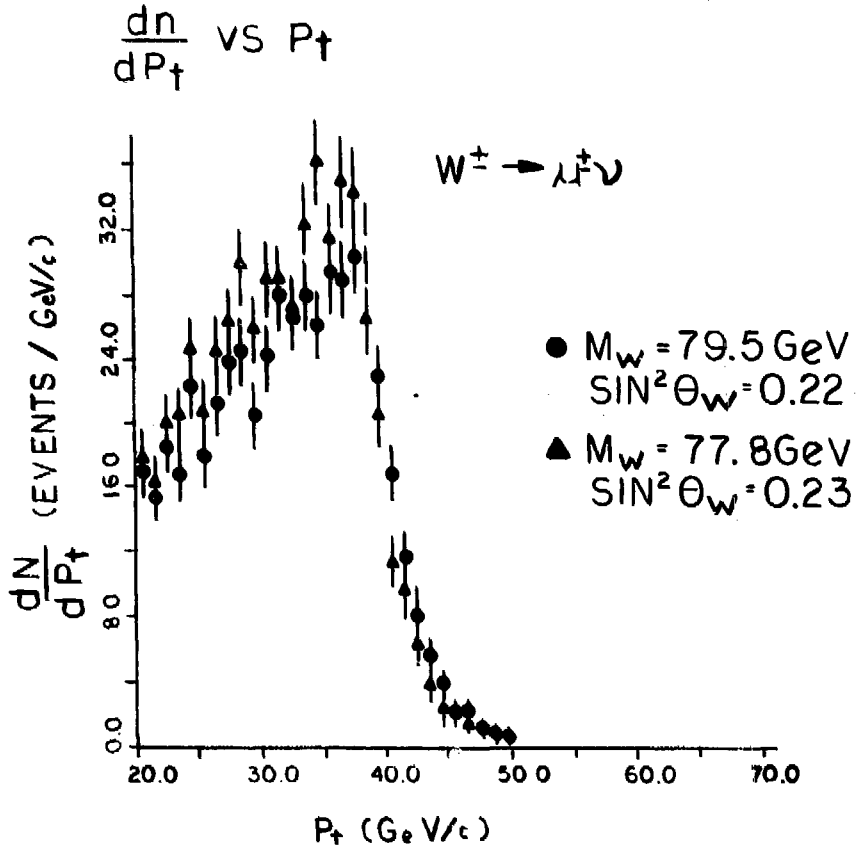
dn/dPt VS Pt
W± → μ±ν
● MW = 79.5 GeV
SIN²θW = 0.22
▲ MW = 77.8 GeV
SIN²θW = 0.23
dN/dPt (EVENTS / GeV/c)
0.0
8.0
16.0
24.0
32.0
20.0
30.0
40.0
50.0
60.0
70.0
Pt (GeV/c)

Fig. 7

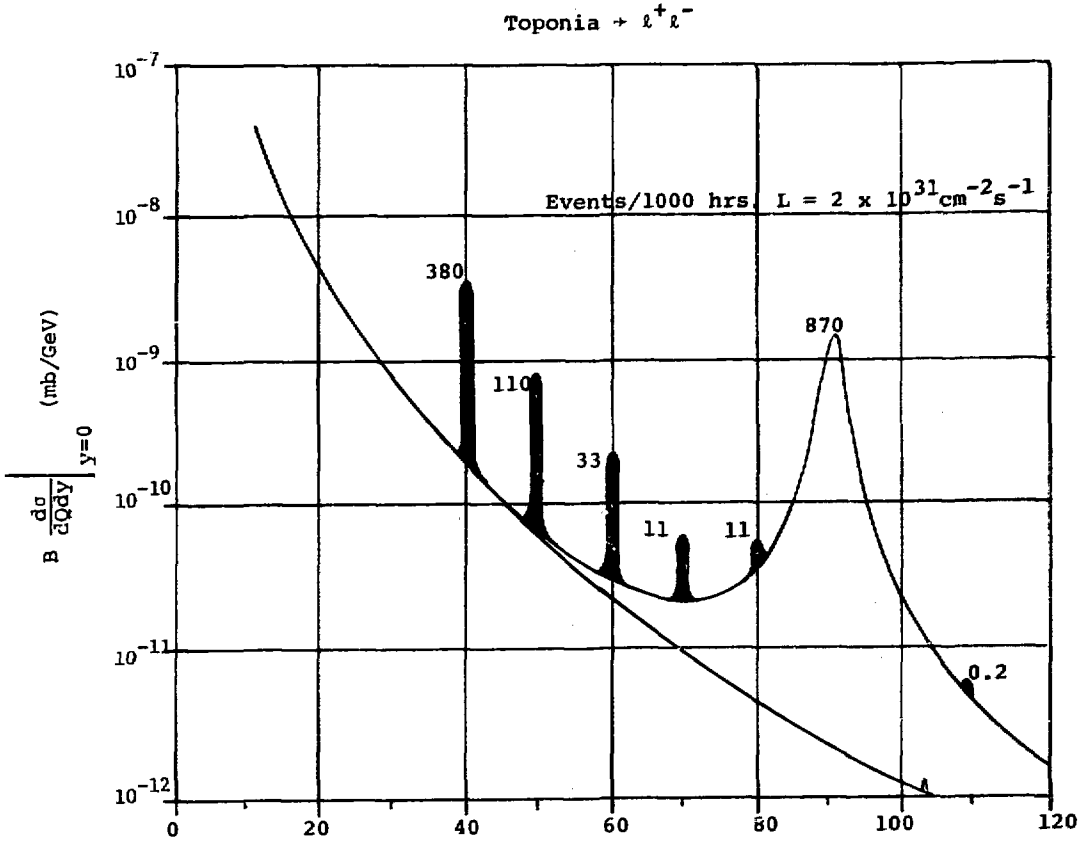
Toponia → $\ell^+\ell^-$
Events/1000 hrs, L = 2 x $10^{31}cm^{-2}s^{-1}$
$B\left.\frac{d\sigma}{dQdy}\right|_{y=0}$ (mb/GeV)
10^{-7}
10^{-8}
10^{-9}
10^{-10}
10^{-11}
10^{-12}
380
110
33
11
11
870
0.2
0
20
40
60
80
100
120
Q (GeV)

Fig. 8

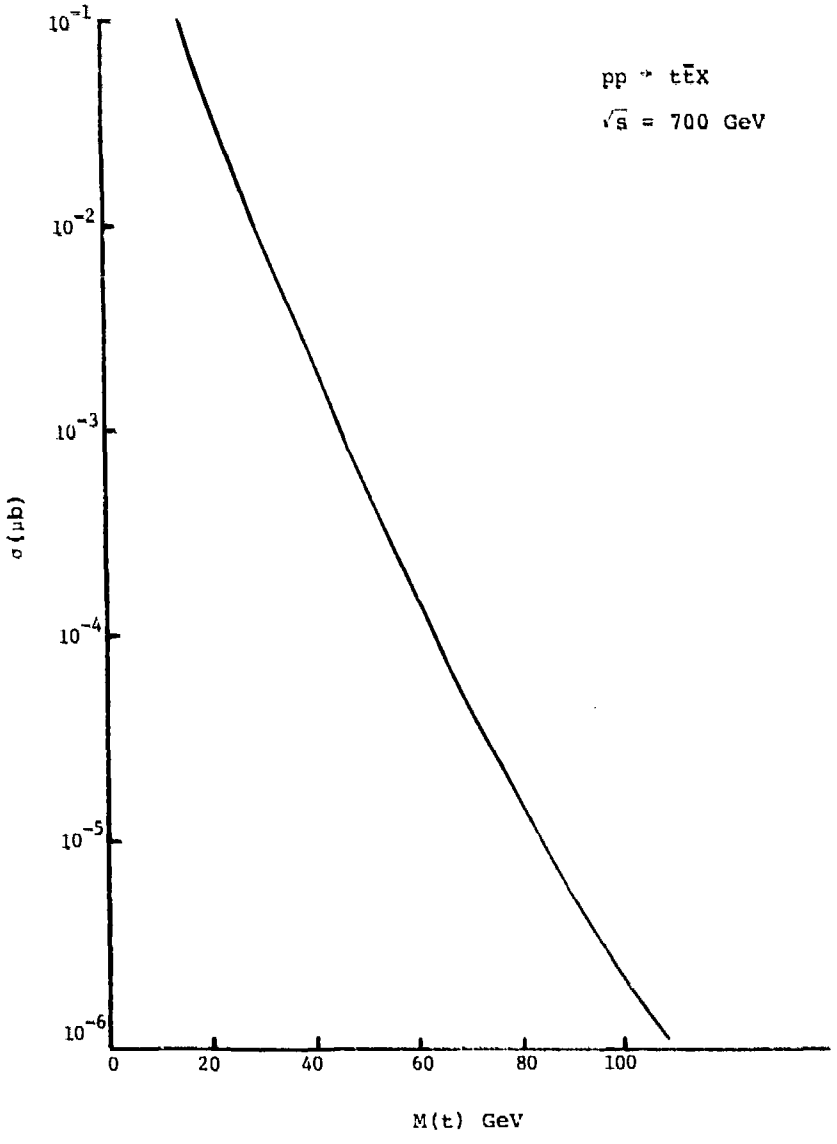
10^{-1}
10^{-2}
10^{-3}
10^{-4}
10^{-5}
10^{-6}
σ (μb)
pp → tt̄X
√s = 700 GeV
0
20
40
60
80
100
M(t) GeV

Fig. 9

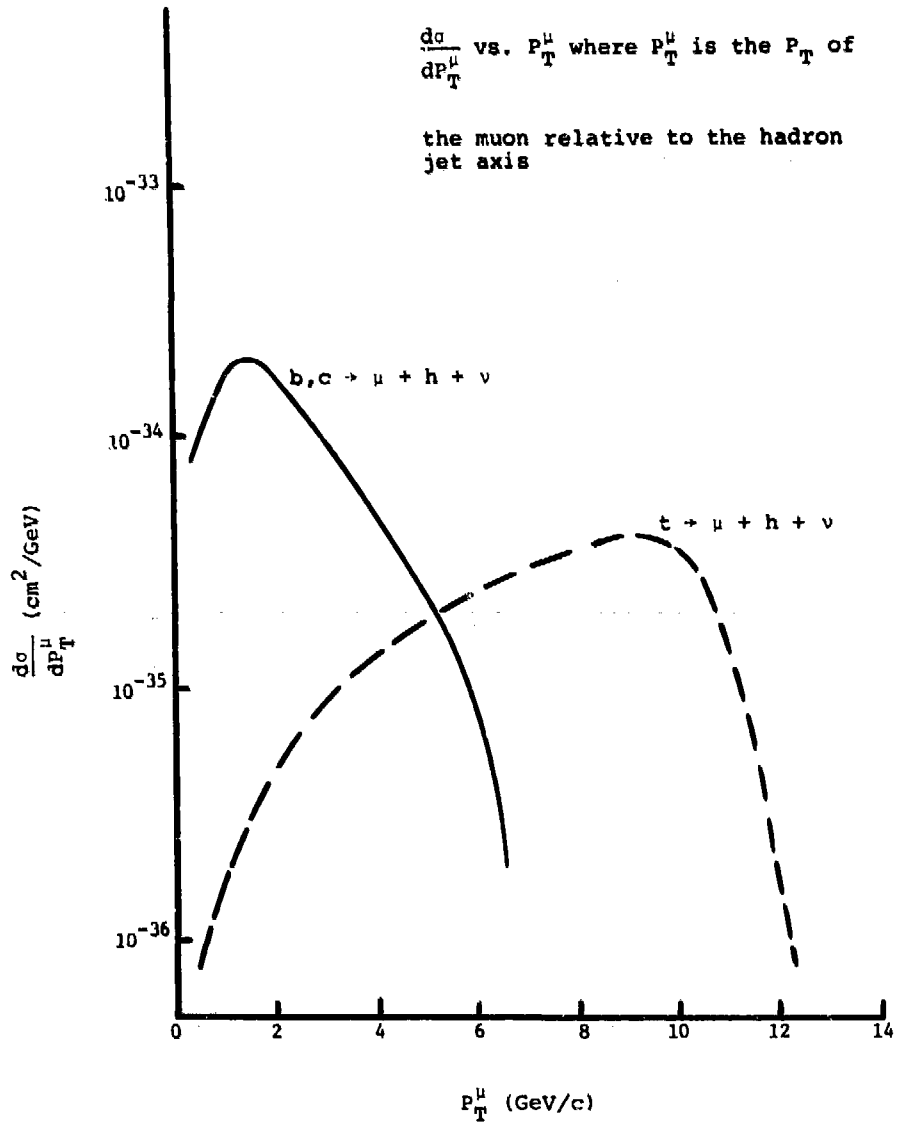
$\frac{d\sigma}{dP_T^\mu}$ vs. P_T^μ where P_T^μ is the P_T of the muon relative to the hadron jet axis
10^{-33}
10^{-34}
10^{-35}
10^{-36}
b,c → μ + h + ν
t → μ + h + ν
$\frac{d\sigma}{dP_T^\mu}$ (cm^2/GeV)
0
2
4
6
8
10
12
14
P_T^μ (GeV/c)

Fig. 10

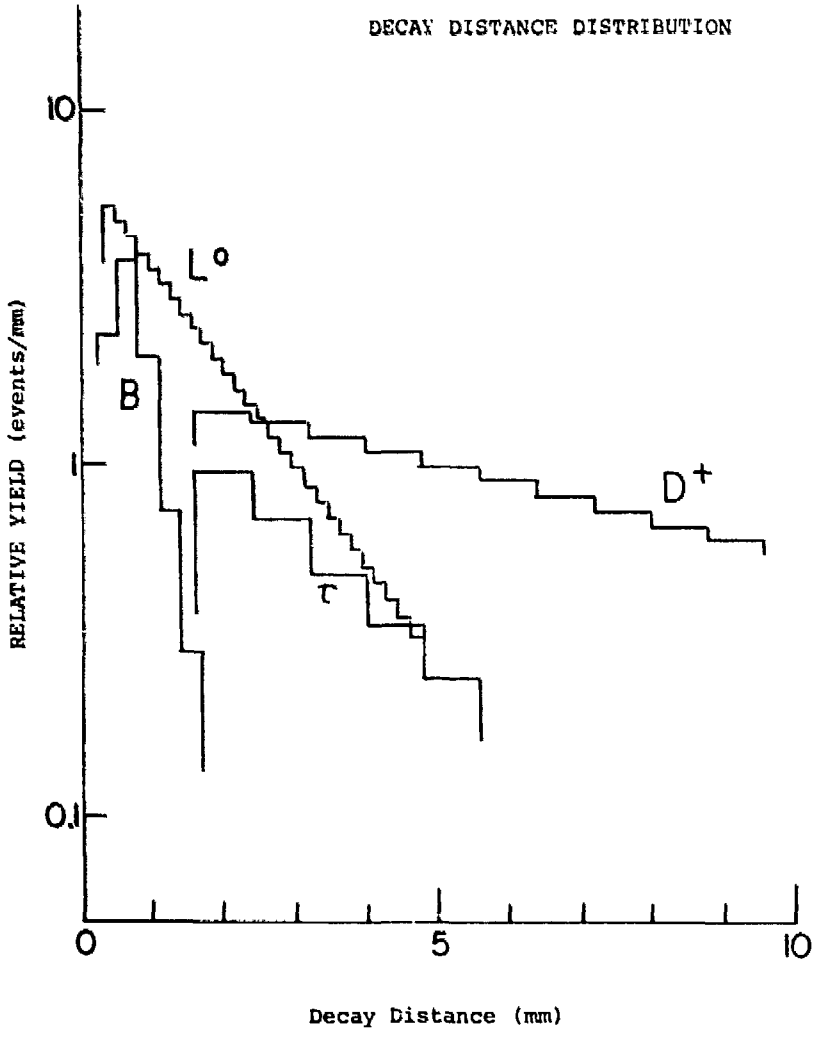
DECAY DISTANCE DISTRIBUTION
10
1
0.1
RELATIVE YIELD (events/mm)
L°
B
D+
τ
0
5
10
Decay Distance (mm)

Fig. 11

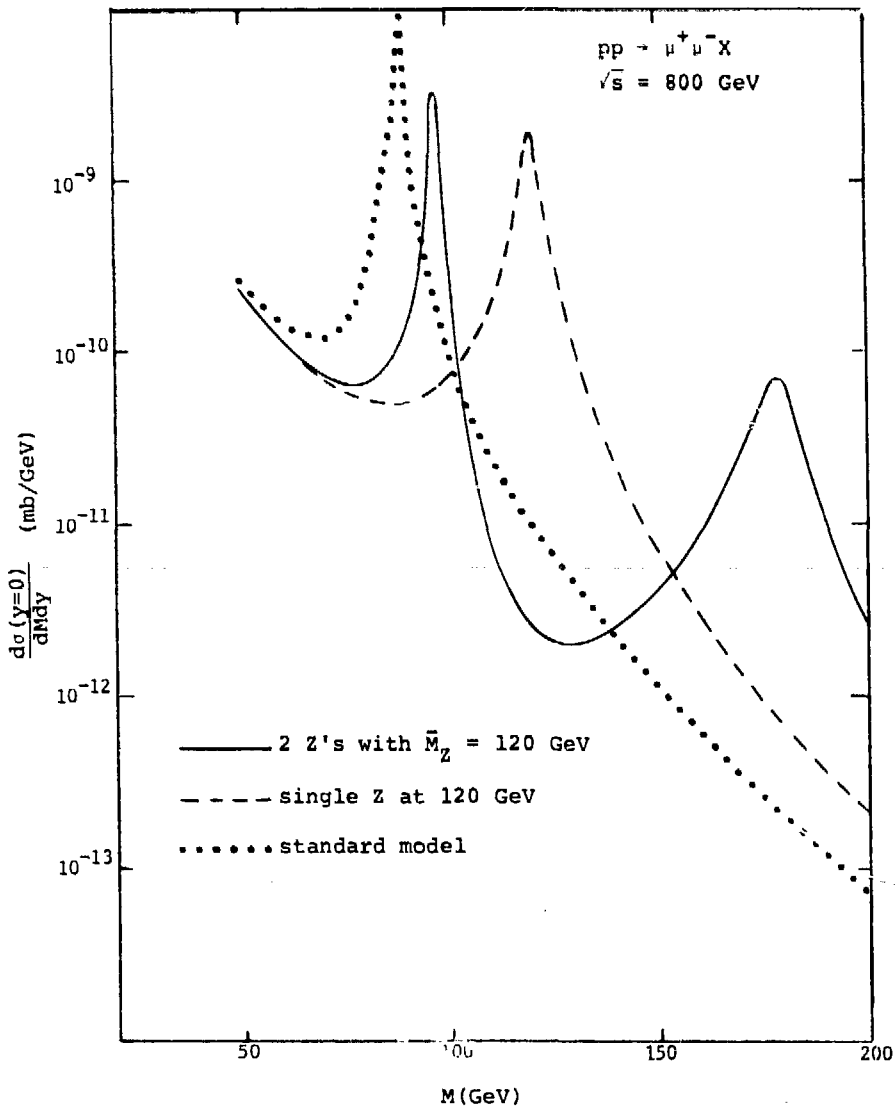
pp → μ⁺μ⁻X
√s = 800 GeV
10⁻⁹
10⁻¹⁰
10⁻¹¹
10⁻¹²
10⁻¹³
dσ(y=0)/dMdy (mb/GeV)
2 Z's with M̄Z = 120 GeV
single Z at 120 GeV
standard model
50
100
150
200
M(GeV)

Fig. 12

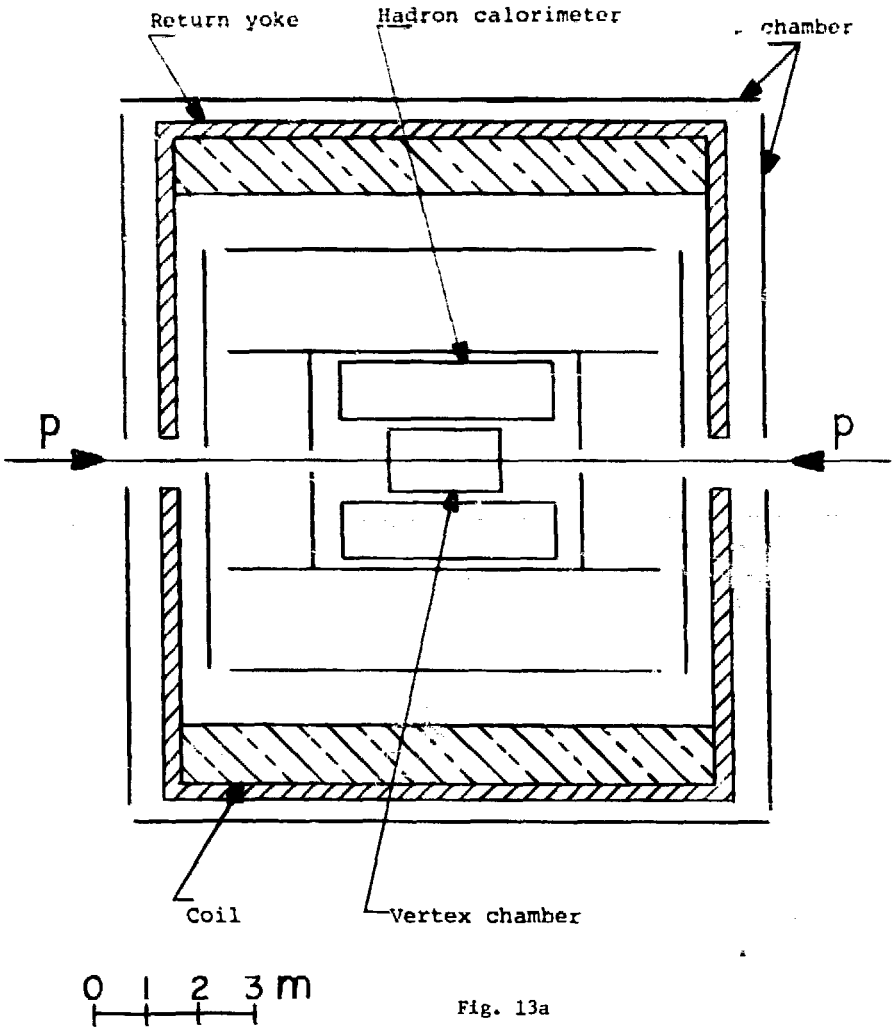
Return yoke
Hadron calorimeter
chamber
p
p
Coil
Vertex chamber
0 1 2 3 m

Fig. 13a

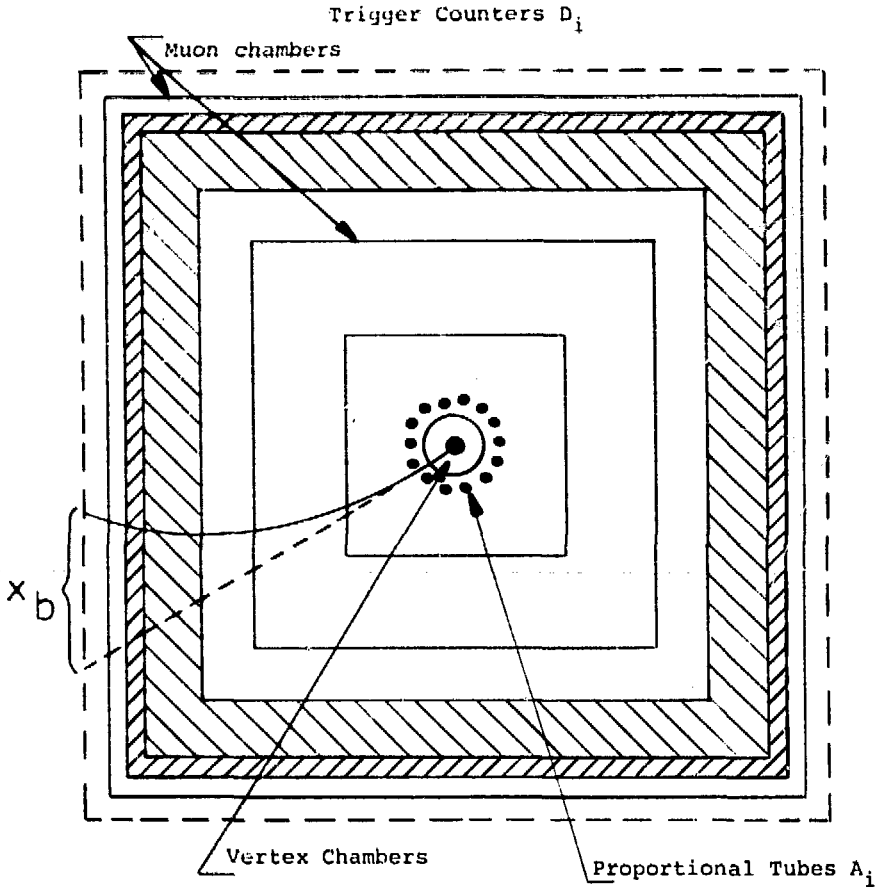

$x_b \sim 30$ cm for $P_\perp \sim 5$ GeV

0 1 2 3 m

Fig. 13b

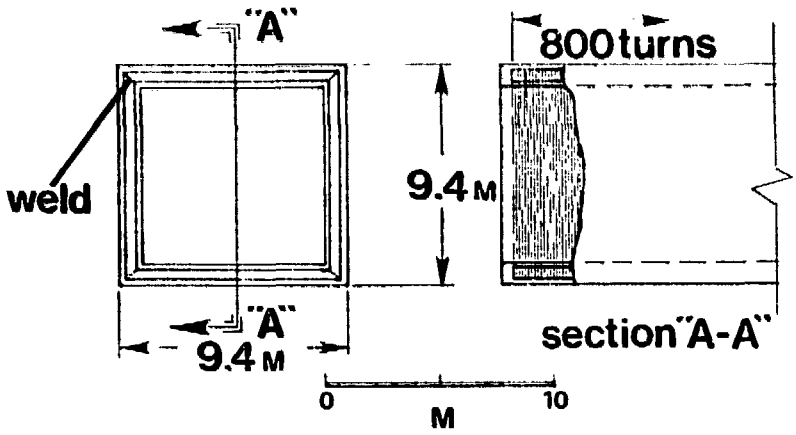
"A"
800 turns
weld
9.4 M
"A"
9.4 M
section "A-A"
0
10
M

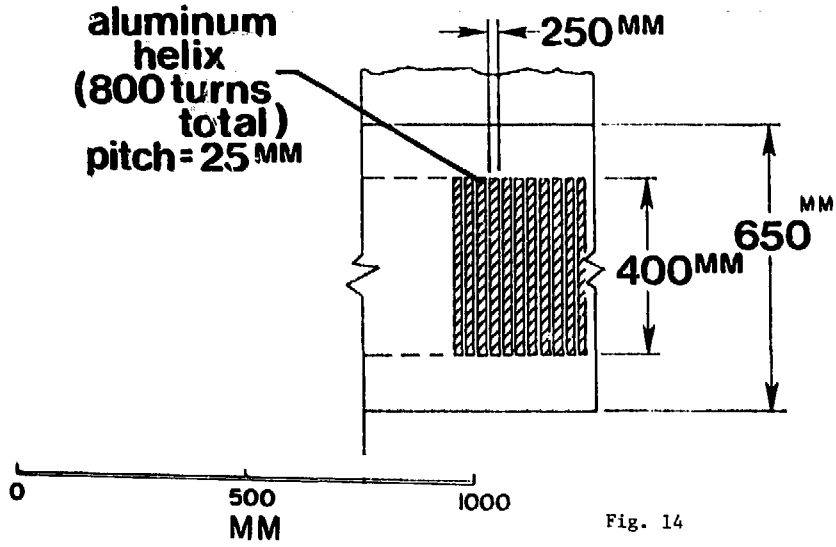
aluminum
helix
(800 turns
total)
pitch = 25 MM
250 MM
650 MM
400 MM
0
500
1000
MM

Fig. 14

SCHEME OF THE HIGH RESOLUTION TIME EXPANSION CHAMBER

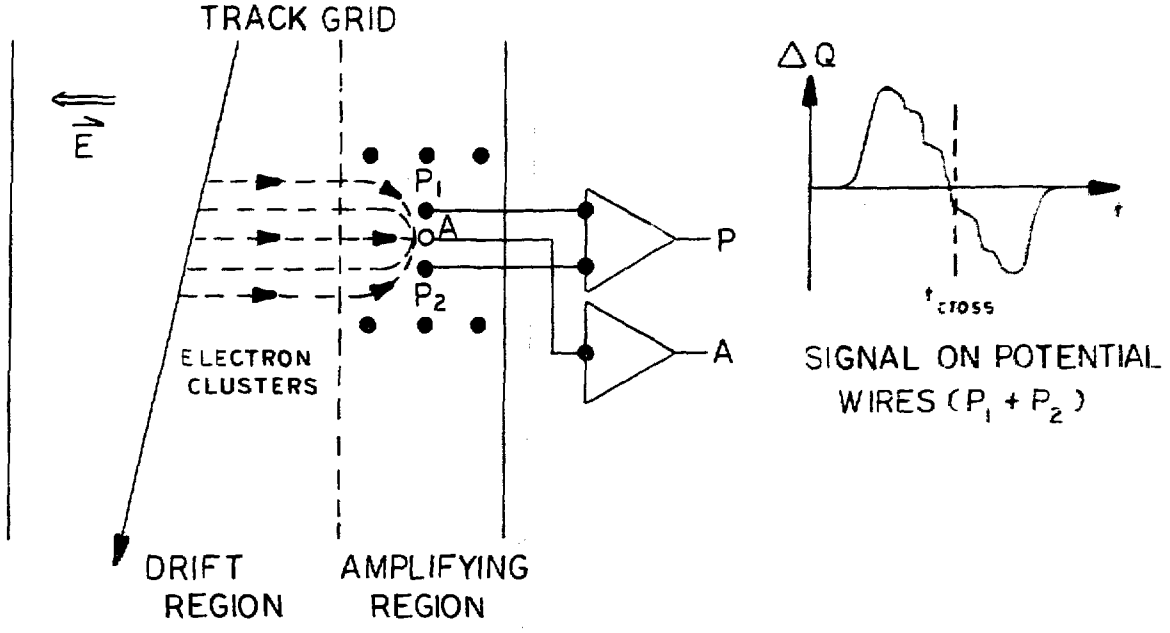

Fig. 15

TIME EXPANSION CHAMBER

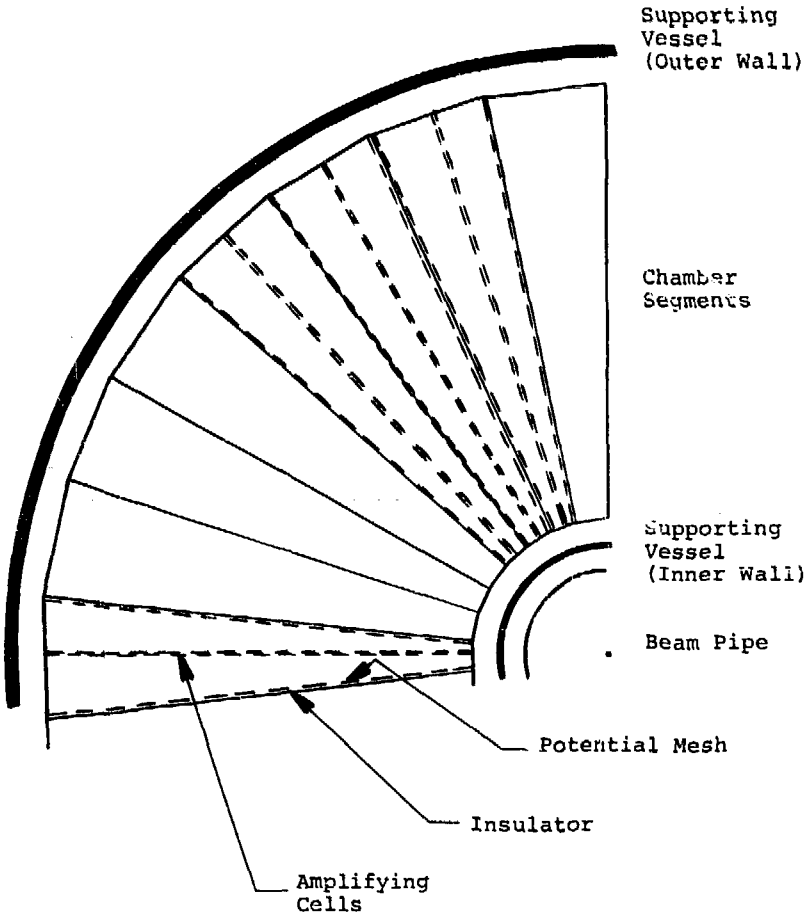

Fig. 16

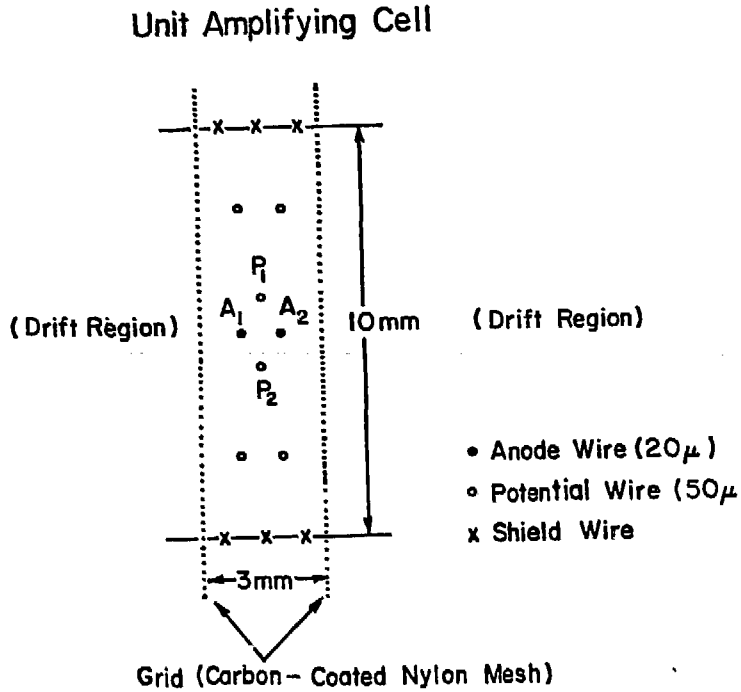
Unit Amplifying Cell
(Drift Region)
P1
A1
A2
10mm
(Drift Region)
P2
• Anode Wire (20μ)
∘ Potential Wire (50μ
x Shield Wire
3mm
Grid (Carbon-Coated Nylon Mesh)

Fig. 17

DOUBLE TRACK RESOLUTION

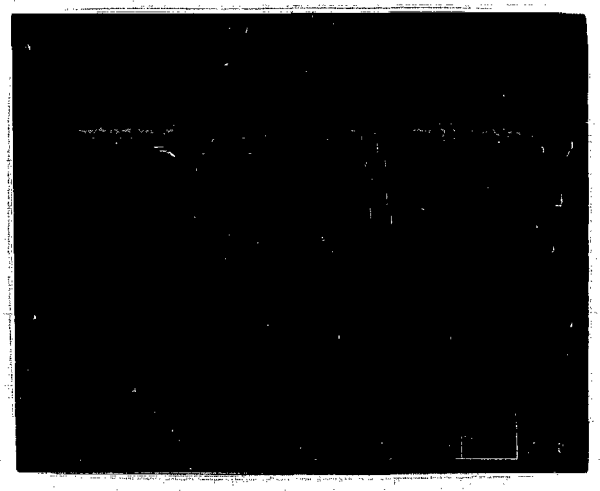

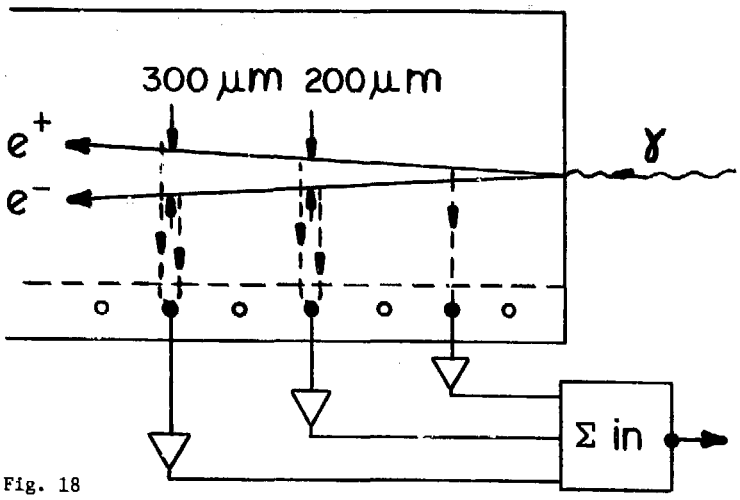

Fig. 18

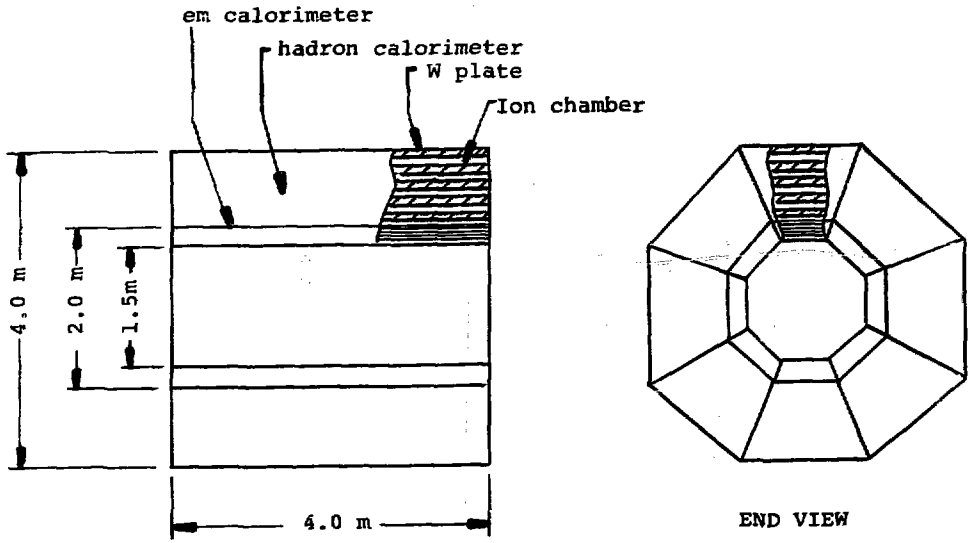
em calorimeter
hadron calorimeter
W plate
Ion chamber
4.0 m
2.0 m
1.5m
4.0 m
SIDE VIEW
END VIEW

Fig. 19

Mass (and momentum) resolution as a function of the lepton (dilepton) angle

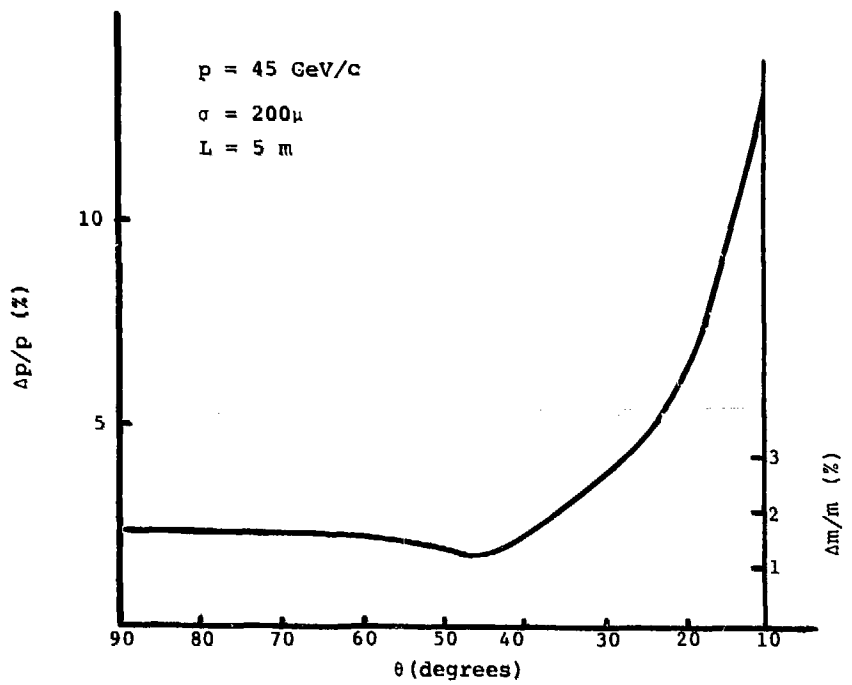

Fig. 20

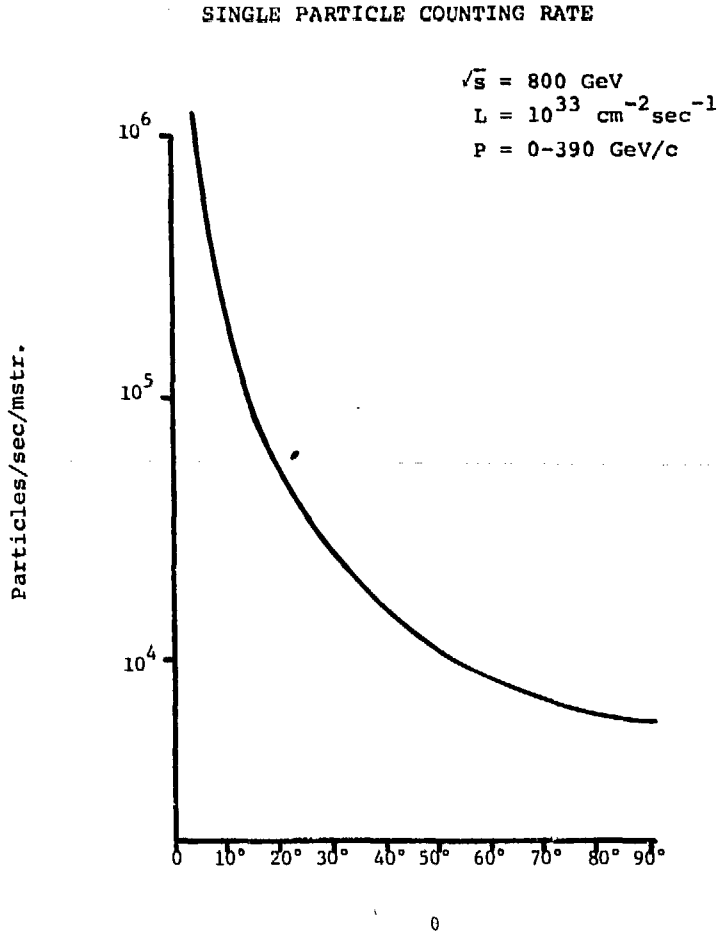
SINGLE PARTICLE COUNTING RATE
$\sqrt{s}$ = 800 GeV
L = 10^{33} $cm^{-2}sec^{-1}$
P = 0-390 GeV/c
Particles/sec/mstr.
10^6
10^5
10^4
0
10°
20°
30°
40°
50°
60°
70°
80°
90°
θ

Fig. 21

SPHERICAL RING IMAGING CHERENKOV DETECTOR SYSTEM WITH A WEAK MAGNETIC FIELD

T. Ypsilantis, M. Urban, J. Sequinot
Ecole Polytechnique, Paris, France
T. Ekelof, CERN

With the successful tests of the Ring Imaging Cherenkov (RICH) photon drift detector shown in Figure 1, where circular ring images containing ten points (converted photoelectrons) have been observed (see Fig. 2 and 3), it is now possible to envision a detector system for colliding beams which has many desirable properties. The photon detector operates with a fused quartz transparent (to 7.5 eV) window with a photoionizing gas TMAE (1 Torr) admixed with methane (759 Torr) thus it contains no exotic (single crystal) components and may be considered as "off the shelf." The value of $N_o = 81\ cm^{-1}$ presently achieved with TMAE is expected to rise to a value of $125\ cm^{-1}$, based on laboratory measurements of the quantum efficiency Q and the transparency T as shown in Fig. 4, with technical improvements of the drift detector. Recall that the number of points on the ring image $N = N_o L \sin^2\theta$ where L is the length of the radiator (cm) and $\cos\theta = 1/\eta\beta$ where η is the refractive index of the radiator and β the velocity of the charged particle.

The spherically symmetric detector system is shown in Fig. 5 and is comprised of a liquid freon 14 (150°K) radiator and detector inside the solenoid wound on an approximately spherical surface. The integrated field between the vertex point and the coil is about .2T-m and the magnet consumes only 200 kW power. The freon radiator is placed just inside the coil and is 2 cm thick ($X = .036X_o$) going from a radius of .73 m to .75 m with a spherical reflecting mirror at .75 m radius. Superinsulation separates the liquid freon radiator from the coil. The detector for the liquid freon radiator is placed between .51 and .55 m radius corresponding to a 4 cm thick spherical drift volume filled with CH_4 + TMAE. Converted photoelectrons drift 20 cm or less along lines of constant ϕ (azimuthal angle) to a picket fence of radial PC wires placed along lines of constant θ (polar angle). A planar version of such a drift detector is shown in Fig. 1. The detectors and radiators are enclosed by spherical quartz windows 2.5 mm thick ($X = .02X_o$) with the cold freon

radiator (150°K) insulated from the warm detector (300°K) by atmospheric pressure, low thermal conductivity, neon gas. The region between the beam pipe and the photon detectors (.50 m radius) is free for installation of a tracking detector and/or a high precision vertex detector. The liquid freon has a refractive index of 1.15 at a photon energy of 6.75 eV and so has a threshold of $\gamma = 2$ for Cherenkov radiation. The quartz windows ($n = 1.6$) start radiating at $\gamma = 1.28$ and cutoff at $\gamma = 2$ due to total internal reflection hence the liquid freon-quartz system is continuously sensitive to charged particles above $\gamma = 1.28$ ($p_\pi = .11$ GeV/c).

The number of points on the ring image from the liquid freon is about 60 ($N_o = 125$ cm^{-1}, L = 2cm) and from the two quartz windows is about 38 (L = .5 cm) so pattern recognition of the circles is possible especially if a tracking detector provides the direction of the particles as they enter the radiator. This has been established by Monte-Carlo simulation of $e^+e^- \to qqg$ jet events at $S = (50\ \text{GeV})^2$ and $S = (100\ \text{GeV})^2$.

The magnetic field lines of force inside and outside the coil are shown in Fig. 6 at a power of 200 kwatts. The integrated field going out along radial lines between 0 and .75 meters is about .2T-m and outside the coil between 1 and 2 meters about 50 gauss-m. This power and field strength has been chosen so that the condition for good ring imaging $\theta_B \leq \Delta\theta_{ms}$ (where θ_B is the bend inside the radiator and $\Delta\theta_{ms}$ the multiple scattering in the radiator) is approximately satisfied. This condition requires

$$\theta_B = \frac{.3BL}{P} \leq \frac{.015}{p\beta}\sqrt{\frac{L/2}{L_O}}$$

or

$$B \leq \frac{.05}{\sqrt{2LL_o}} \quad (B \text{ in tesla, L and } L_o \text{ in meters})$$

For liquid freon 14 (L = .02 m, L_o = .56 m) the condition is that $B \geq .33$T in the radiator and for Argon gas (1 bar, 293°K, L = 1 m, L_o = 118 m) then B < 33 gauss in the radiator. The condition is satisified in the liquid radiator and nearly so in the Argon radiator.

Outside the coil, for the reasons outlined in the previous paragraph, is placed a 1 meter thick Argon radiator from 1 m to 2 m with the detector a spherical drift detector between .97 m and 1.01 m with a 2.5 mm quartz window separating the Argon gas from the detector. The threshold of the Argon gas radiator is $\gamma = 35$ and it will produce images for a $\beta = 1$ particle with 10 points on the circle. The Cherenkov angle for the liquid radiator is 516 mr and for the gas radiator 28.3 mr and these produce images on their respective detector surfaces of 292 mr and 28.3 mr respectively. The aberrations of the ring images have been calculated, from formulas given in reference 1, and are shown in Fig. 7a and 7b for a liquid neon radiator (2.5 cm thick, $n = 1.1$) and for the Argon gas radiator. The liquid neon and liquid freon have similar response and aberrations and was available in graphic form at the meeting. The freon is preferred for cryogenic reasons. The corresponding liquid neon Cherenkov angle (emission) and detection angle are 430 mr and 311 mr. As is seen from this figure the aberrations for the liquid are dominated by multiple scattering and chromatic aberrations and at $\gamma = 50$ give the chromatic limit $\Delta\theta_o = 1$ mr hence $\Delta\theta_o/\theta_o \simeq 3 \times 10^{-3}$ which is the accuracy to which the detected ring radius can be measured. The corresponding values for $\Delta\theta_o$ and θ_o for the Argon gas radiator are .4 mr and 28.3 mr hence $\Delta\theta_o/\theta_o = 1.5\%$. In the previously mentioned tests with the planar detector and Argon radiator we have achieved a resolution of 3.0% which, if a more correct fit function is used (i.e. not a circle) corresponds to the expected 1.5% resolution.

The momentum measurement of a Cherenkov radiating particle is illustrated in Fig. 8 where a spiralling particle in a constant $\vec{B}$ field in the Z direction is assumed. Since the position of the ring image is determined only by the particle direction as it transverses the radiator volume the center of the ring image C and the impact point P of the particle as it transverses the detector will be displaced. The particle bending angle θ_B due to the magnetic field is then

$\theta_B = 2\alpha$	α = angle $\overline{PC}$	if detection point P at the mirror
$" = 4/3\alpha$		if detection point P at half radius
$" = 1.6\alpha$		if detection point P at photon detector

This should be compared to the classicial tracking formula $\theta_B = 8\ S/L$ where S is the sagitta of the track and L the chord over which the track is measured. It may be noted that the first method is between 4 and 6 times more precise for measurement of θ_B than the sagitta method for equal accuracy of measurement of $\sigma(s/L)$. This is understandable if one notes that the ring image method measures a point and a direction of a circle (presumably fixed at the origin = vertex point) where as the sagitta method measures only points on the arc of the circle. As shown in Fig. 8 the accuracy expected for this method should give $\Delta p/p^2 = .6\%/GeV/c$ for an integrated field (to .75 m) of .2T-m. In addition the θ dependence of the precision $\Delta p/p^2$ should vary as $1/\sin\theta$ (with the assumed B field in the Z direction) whereas for a solenoid the dependence (outside the end cap) is $1/\sin^{2.5}\theta$ hence a much less drastic loss of resolution at small θ for the ring imaging method. As shown in Fig. 6 the field lines curve in toward the iron at small θ and with additional shaping of the pole piece one may expect to achieve even a smaller dependence than $1/\sin\theta$ thus approaching isotropic resolution on p. This momenum resolution is quite conquerable to that expected in TPC where the magnetic field is 1.5T over .8m hence 1.2 Tm of integrated field (see Fig. 9).

With the curves of Fig. 7 and the momentum measurements shown in Fig. 8 we have calculated the precision $\Delta p/p$ with which p can be measured by the Cherenkov ring imaging method and also utilising the B field. At low momentum the B field method is limited by multiple scattering to about 8% and is always less precise than the ring imaging method (see Fig. 10). At higher momenta once again the ring imaging method is always more precise up to 100 GeV than the B method except for π's above 36 GeV/c (see Fig. 11). Combining the measurements of p and γ (from the ring image) one may calculate the mass resolution expected

$$\Delta m/m = \sqrt{(\Delta p/p)^2 + \frac{1}{\beta^4}\left(\frac{\Delta\gamma}{\gamma}\right)^2}$$

The number of standard deviations to separate a particle of mass m_A from a particle of mass m_B is

$$\sigma = |M_A - M_B|/\Delta m$$

and this is plotted in Figs. 12 to 15 for the combinations (πK), (KP), ($\pi\mu$), (μe). The three regions labeled quartz, neon or argon indicate when a given radiator is acting as a threshold counter (i.e. a π counts but the K doesn't) hence σ is large. For the regions in between the ring radius makes the identification to the indicated number of σ's. As can be seen from the curves πK separation is possible to 78 GeV/c (3σ level) KP to 53 GeV/c, $\pi\mu$ to about 10 GeV/c and μp to about 30 GeV/c. This covers the range expected for LEP and a good fraction of that expected for Isabelle. Note that $e\mu$ hence even more so $e\pi$ separation is possible by this method hence the study of direct lepton processes will be facilitated with this method. Note also that the number of σ's is large so that a detector which operates less well than expected still has a margin of error. To illustrate with experimental results of the Argon gas radiator tests a measurement with 6.2 GeV/c beam containing π's and e's is shown in Fig. 16. The π radius fit is 17.8 mr and the e fit radius is 28.3 mr. The separation is clear. This corresponds to the same separation for 22 GeV/c π's and K's. This data was taken under conditions where the impact parameter of the incident particle was 16 cm from the center curvature of the mirror (R = 200 cm) hence an impact parameter of 8%. This produces an eccentricity of the image of about 2.5% which is the largest contribution to the measured width of $\Delta\theta/\theta$ = 3% since the fit was made to a simple circle. Even under these conditions clear separation was achieved.

1) T. Ypsilantis, Physica Scripta 23, 723 (1981).

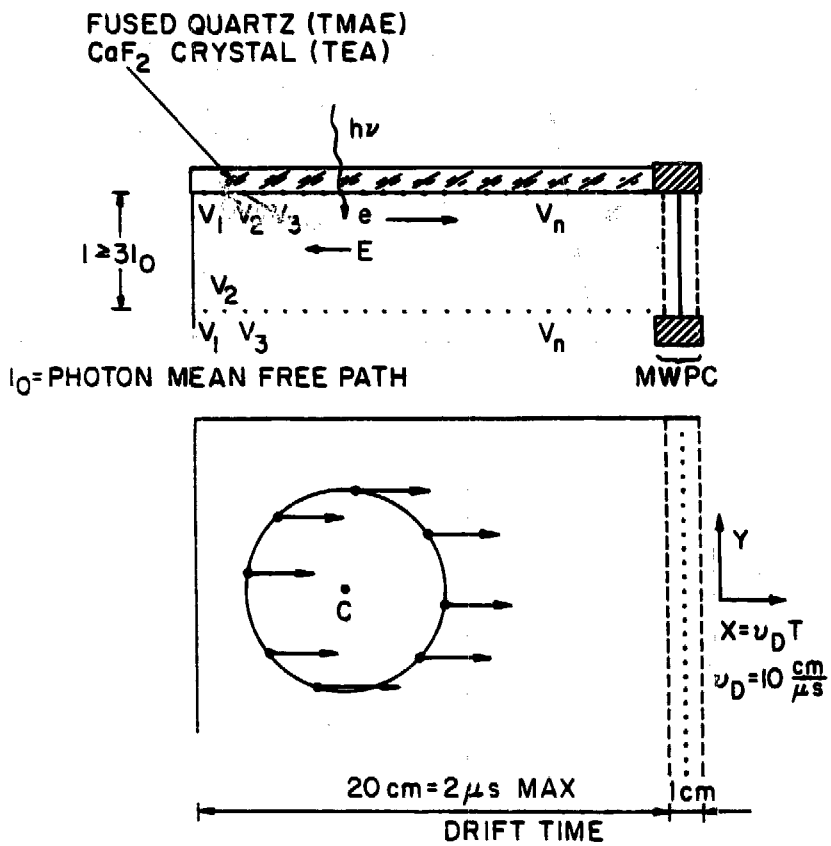
FUSED QUARTZ (TMAE)
CaF2 CRYSTAL (TEA)
hν
V1 V2 V3
e
Vn
E
l ≥ 3l0
V2
V1 V3
Vn
l0 = PHOTON MEAN FREE PATH
MWPC
C
Y
X = vD T
vD = 10 cm/μs
20 cm = 2 μs MAX
DRIFT TIME
1 cm

Fig. 1

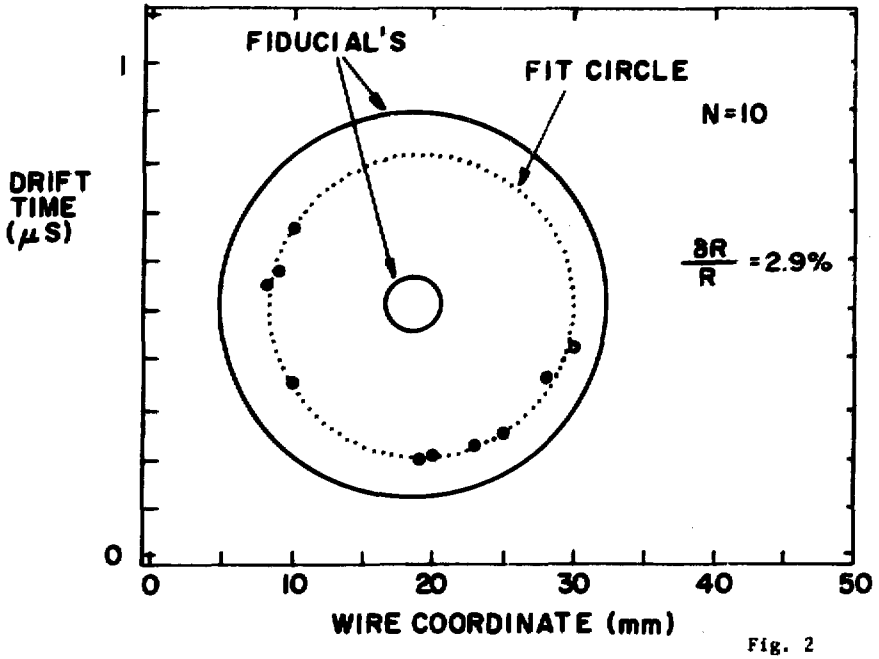
FIDUCIAL'S
FIT CIRCLE
N=10
δR/R =2.9%
DRIFT TIME (μS)
1
0
0
10
20
30
40
50
WIRE COORDINATE (mm)

Fig. 2

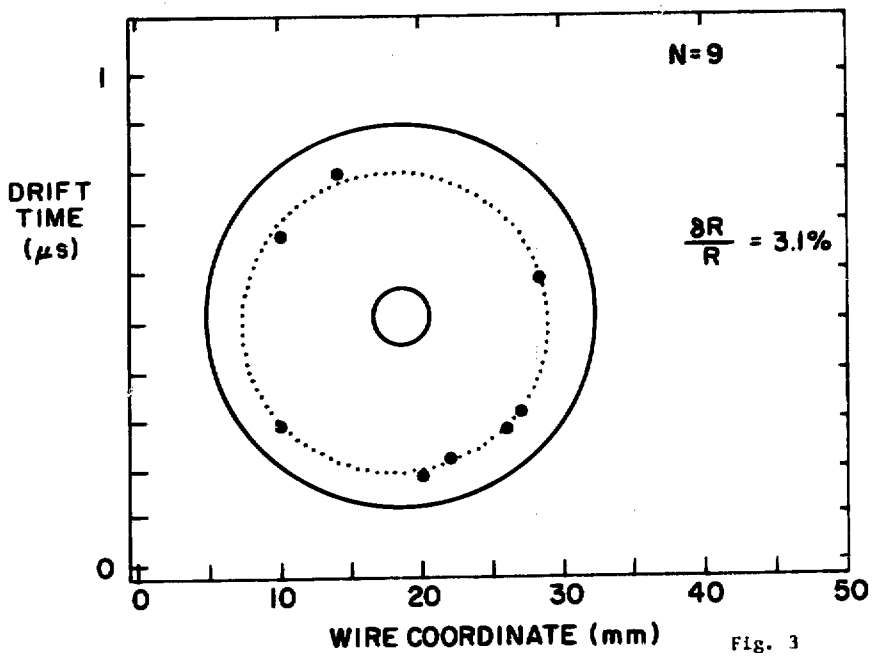

Fig. 3

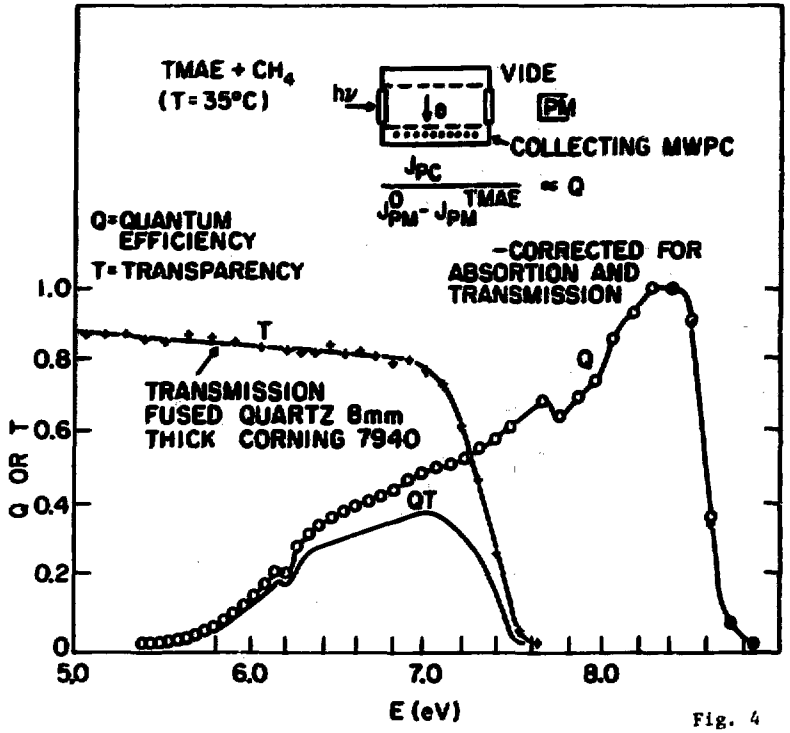
TMAE + CH4
(T=35°C)
hν
e
VIDE
PM
COLLECTING MWPC
JPC / (J0PM - JTMAE PM) ≈ Q
Q=QUANTUM EFFICIENCY
T=TRANSPARENCY
-CORRECTED FOR ABSORTION AND TRANSMISSION
T
Q
QT
TRANSMISSION FUSED QUARTZ 8mm THICK CORNING 7940
Q OR T
1.0
0.8
0.6
0.4
0.2
0
5.0
6.0
7.0
8.0
E (eV)

Fig. 4

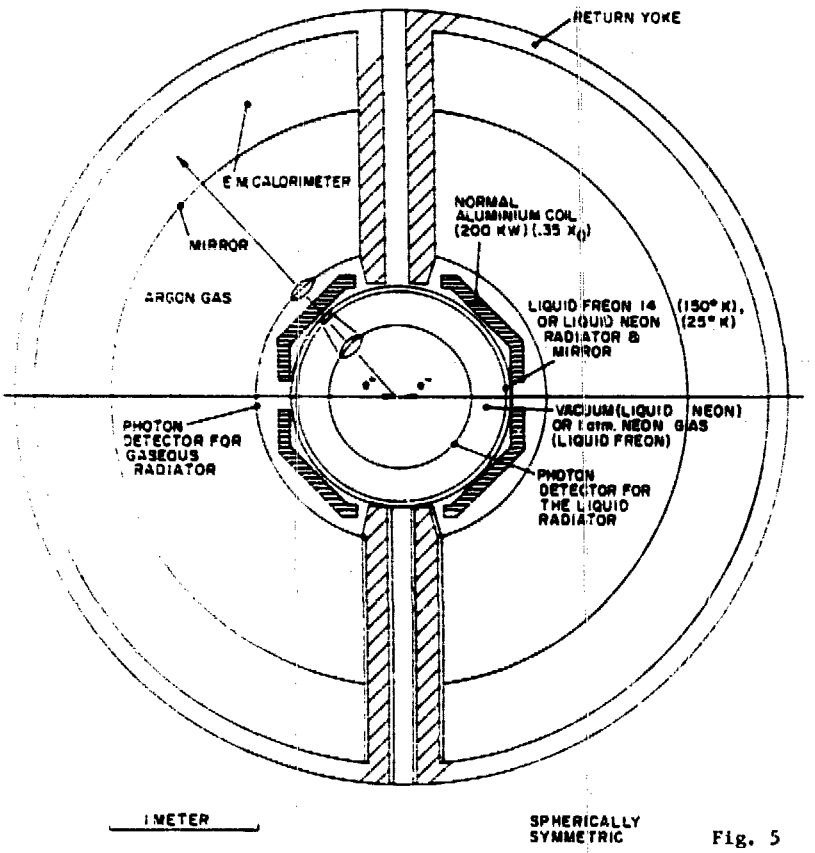
RETURN YOKE
E M CALORIMETER
MIRROR
ARGON GAS
NORMAL ALUMINIUM COIL (200 KW) (.35 X_0)
LIQUID FREON 14 OR LIQUID NEON RADIATOR & MIRROR
(150° K), (25° K)
PHOTON DETECTOR FOR GASEOUS RADIATOR
VACUUM (LIQUID NEON) OR 1 atm. NEON GAS (LIQUID FREON)
PHOTON DETECTOR FOR THE LIQUID RADIATOR
1 METER
SPHERICALLY SYMMETRIC

Fig. 5

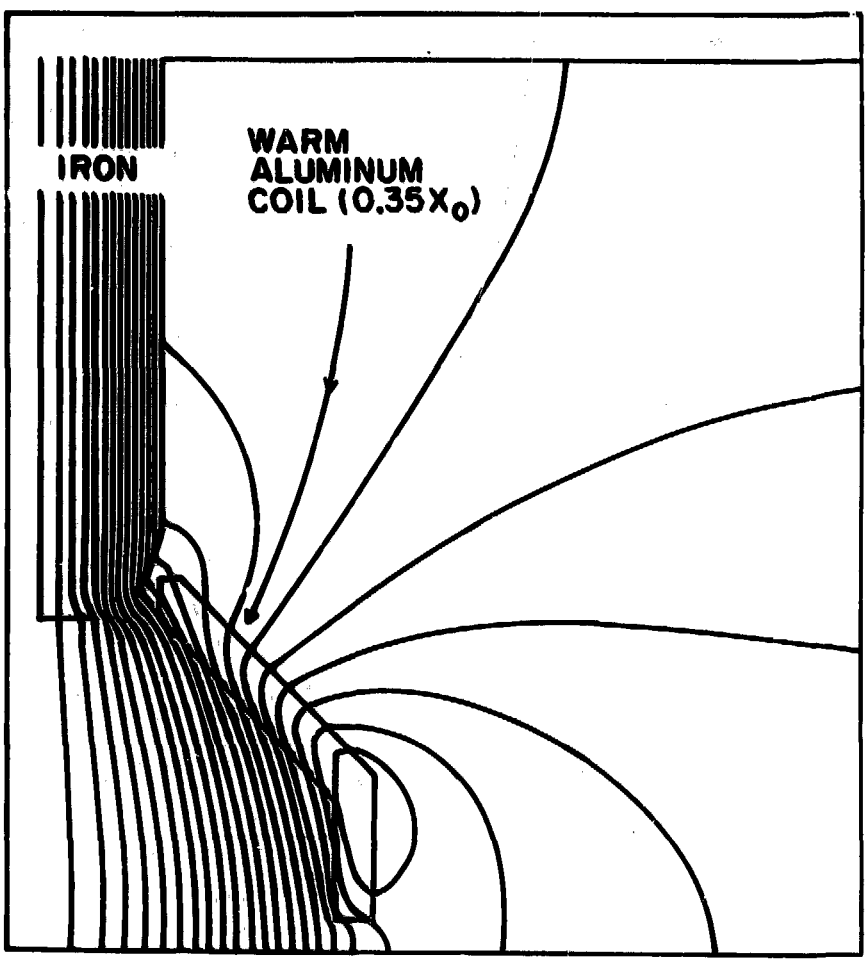

Fig. 6

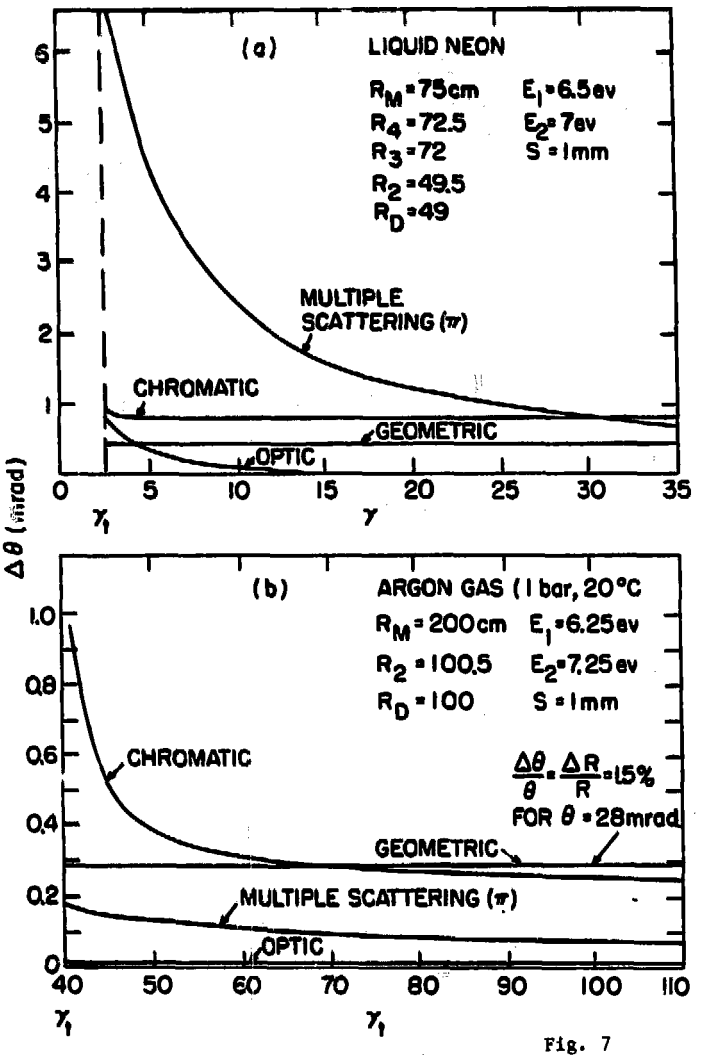
(a)
LIQUID NEON
R_M = 75cm
R_4 = 72.5
R_3 = 72
R_2 = 49.5
R_D = 49
E_1 = 6.5ev
E_2 = 7ev
S = 1mm
MULTIPLE SCATTERING (π)
CHROMATIC
GEOMETRIC
OPTIC
Δθ (mrad)
γ_1
γ
(b)
ARGON GAS (1 bar, 20°C
R_M = 200cm
R_2 = 100.5
R_D = 100
E_1 = 6.25ev
E_2 = 7.25ev
S = 1mm
$\frac{\Delta\theta}{\theta} = \frac{\Delta R}{R}$ = 1.5%
FOR θ = 28mrad
CHROMATIC
GEOMETRIC
MULTIPLE SCATTERING (π)
OPTIC
γ_1
γ_1

Fig. 7

MOMENTUM MEASUREMENT WITH RING IMAGE

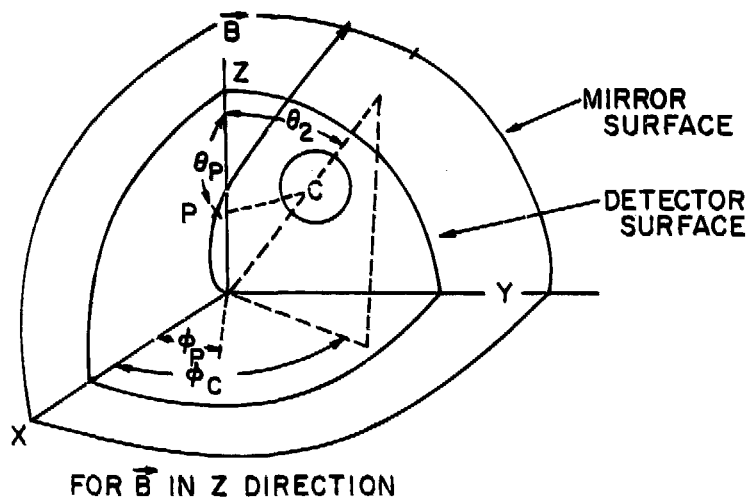

Fig. 8

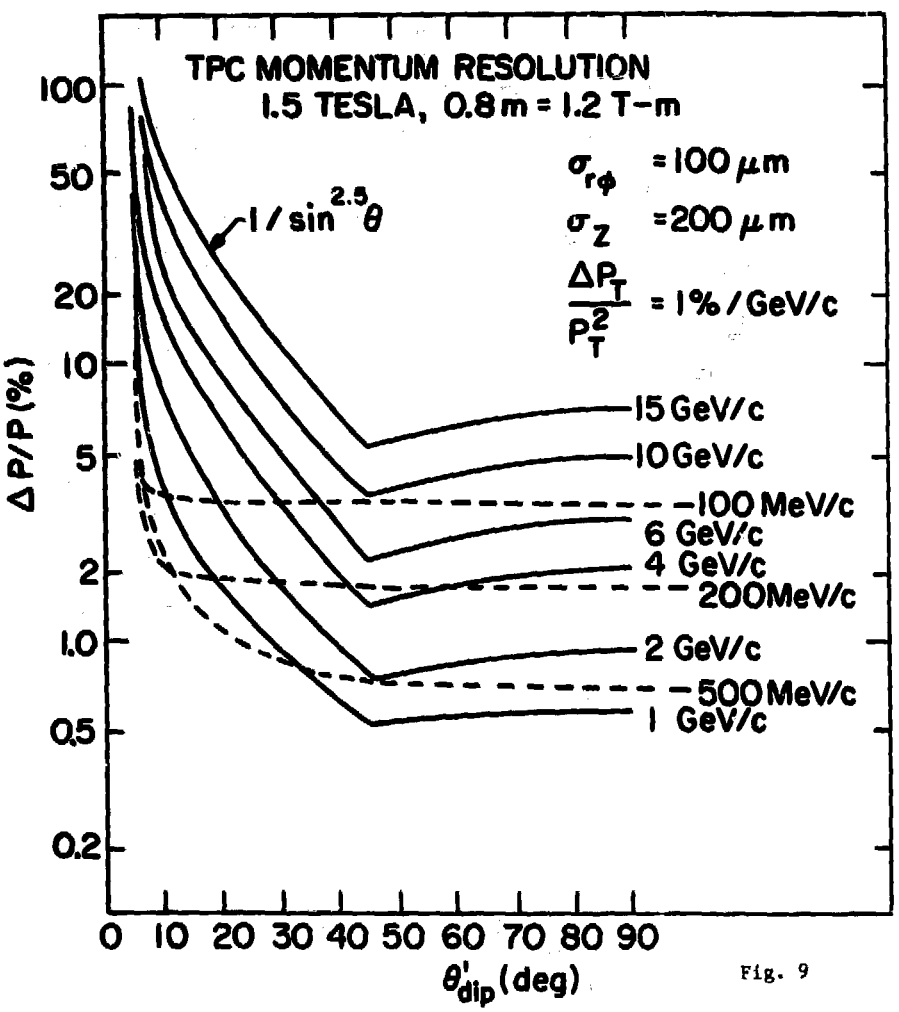
TPC MOMENTUM RESOLUTION
1.5 TESLA, 0.8m = 1.2 T-m
$\sigma_{r\phi}$ = 100 μm
σ_z = 200 μm
$\frac{\Delta P_T}{P_T^2}$ = 1% / GeV/c
$1/\sin^{2.5}\theta$
15 GeV/c
10 GeV/c
100 MeV/c
6 GeV/c
4 GeV/c
200 MeV/c
2 GeV/c
500 MeV/c
1 GeV/c
ΔP/P (%)
100
50
20
10
5
2
1.0
0.5
0.2
0 10 20 30 40 50 60 70 80 90
θ'_{dip} (deg)

Fig. 9

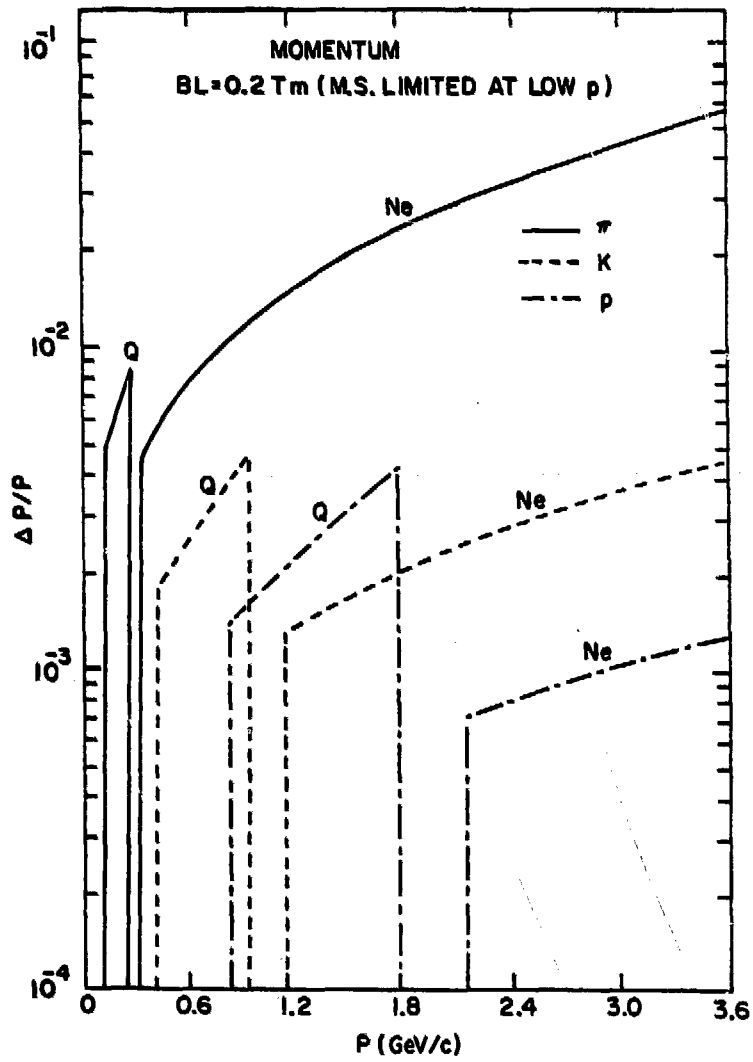
MOMENTUM
BL=0.2 Tm (M.S. LIMITED AT LOW p)
Ne
π
K
p
Q
Q
Q
Ne
Ne
ΔP/P
P (GeV/c)
10⁻¹
10⁻²
10⁻³
10⁻⁴
0
0.6
1.2
1.8
2.4
3.0
3.6

Fig. 10

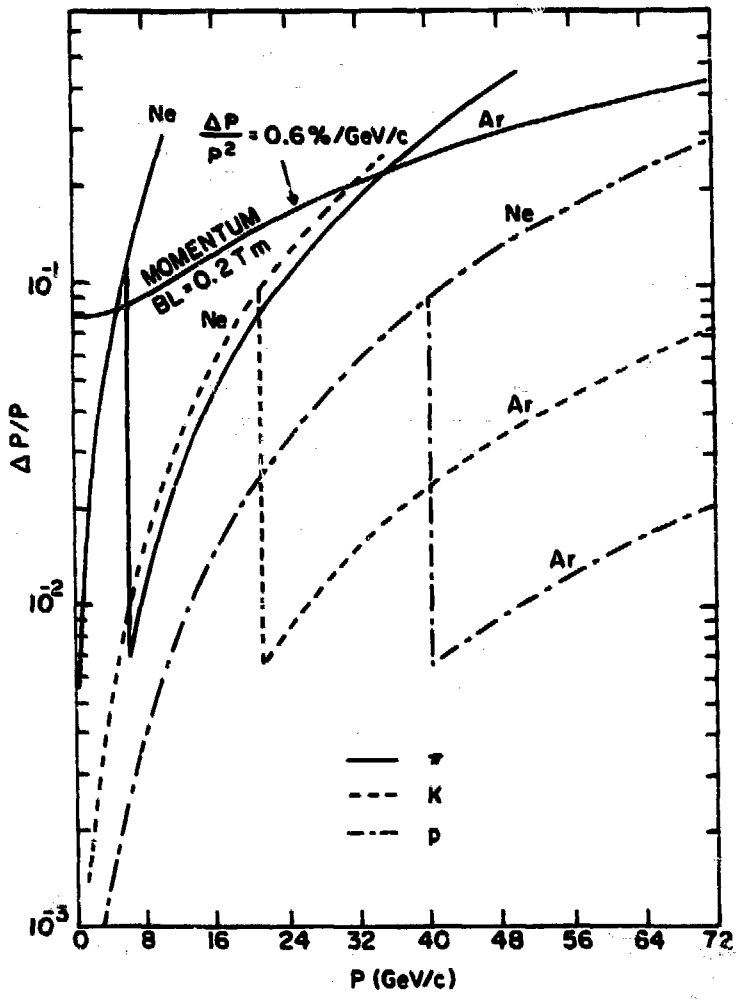
Ne
$\frac{\Delta P}{P^2}$ = 0.6 %/GeV/c
Ar
MOMENTUM
BL = 0.2 T m
Ne
Ne
Ar
Ar
10^{-1}
10^{-2}
10^{-3}
ΔP/P
π
K
p
0
8
16
24
32
40
48
56
64
72
P (GeV/c)

Fig. 11

$$n_{\pi K} = \frac{m_K - m_\pi}{\Delta m_\pi}$$

$$n_{K\pi} = \frac{m_K - m_\pi}{\Delta m_K}$$

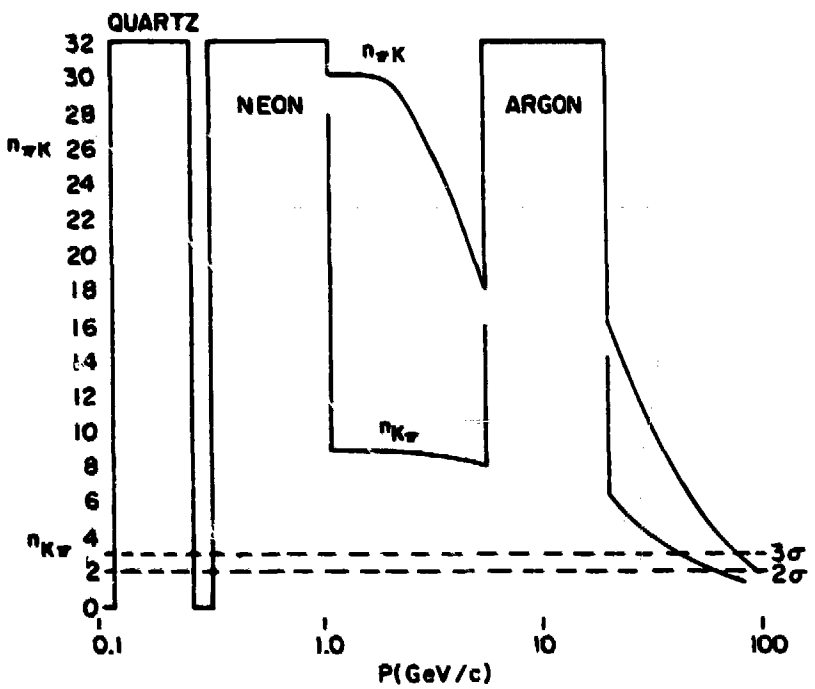

Fig. 12

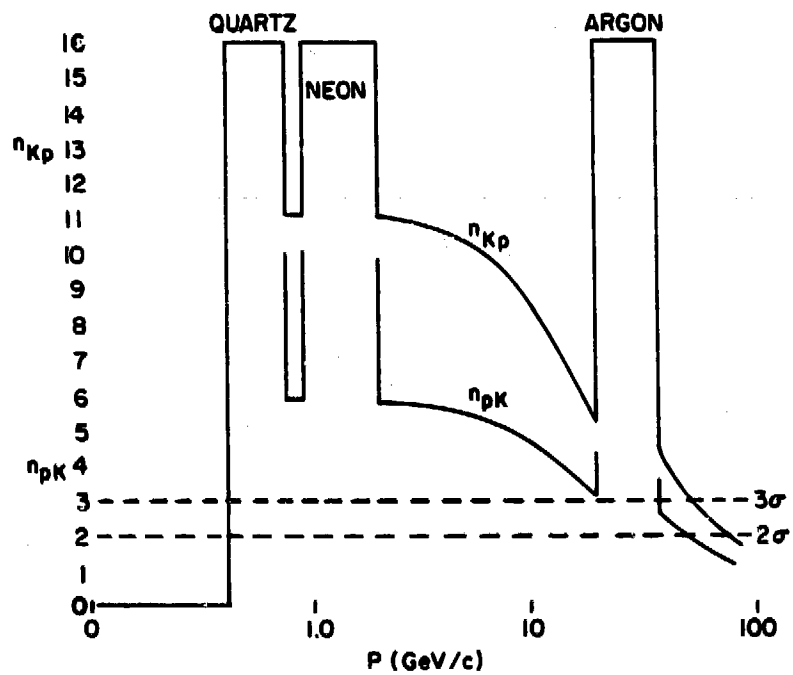
QUARTZ
NEON
ARGON
n_{Kp}
n_{pK}
n_{Kp}
n_{pK}
3σ
2σ
16
15
14
13
12
11
10
9
8
7
6
5
4
3
2
1
0
0
1.0
10
100
P (GeV/c)

Fig. 13

Fig. 14

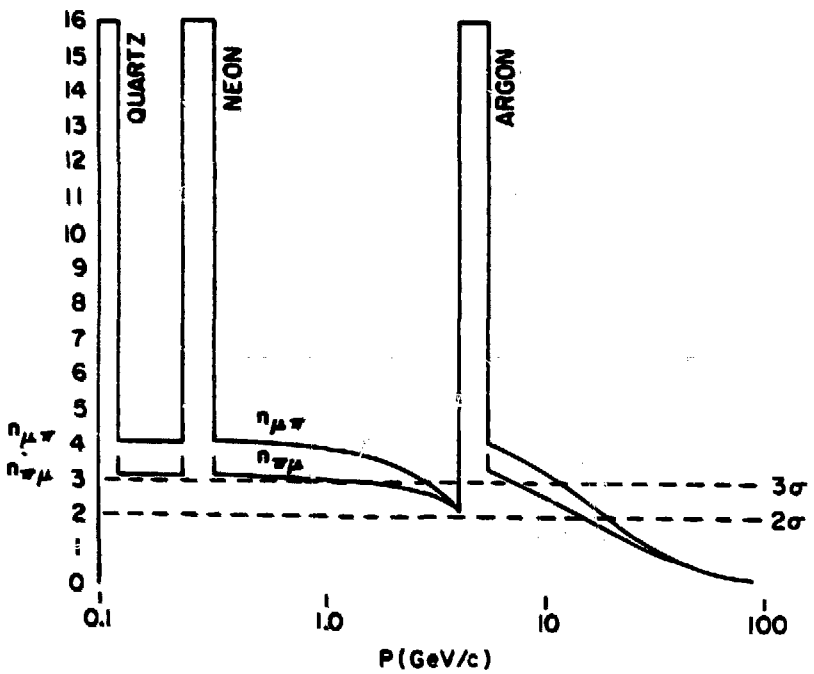
16
15
14
13
12
11
10
9
8
7
6
5
4
3
2
1
0
QUARTZ
NEON
ARGON
$n_{\mu\pi}$
$n_{\pi\mu}$
$n_{\mu\pi}$
$n_{\pi\mu}$
3σ
2σ
0.1
1.0
10
100
P(GeV/c)

Fig. 15

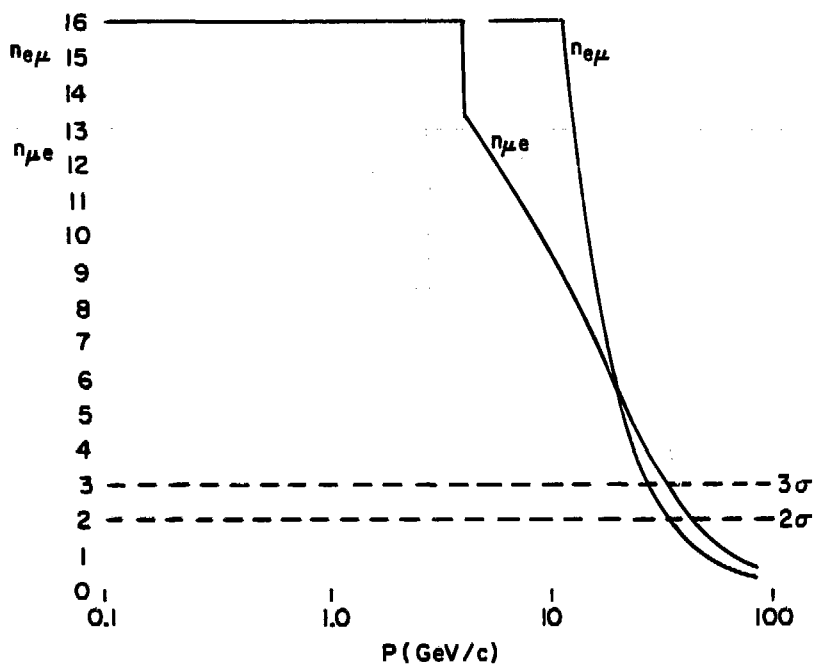
16
15
14
13
12
11
10
9
8
7
6
5
4
3
2
1
0
$n_{e\mu}$
$n_{\mu e}$
$n_{e\mu}$
$n_{\mu e}$
3σ
2σ
0.1
1.0
10
100
P(GeV/c)

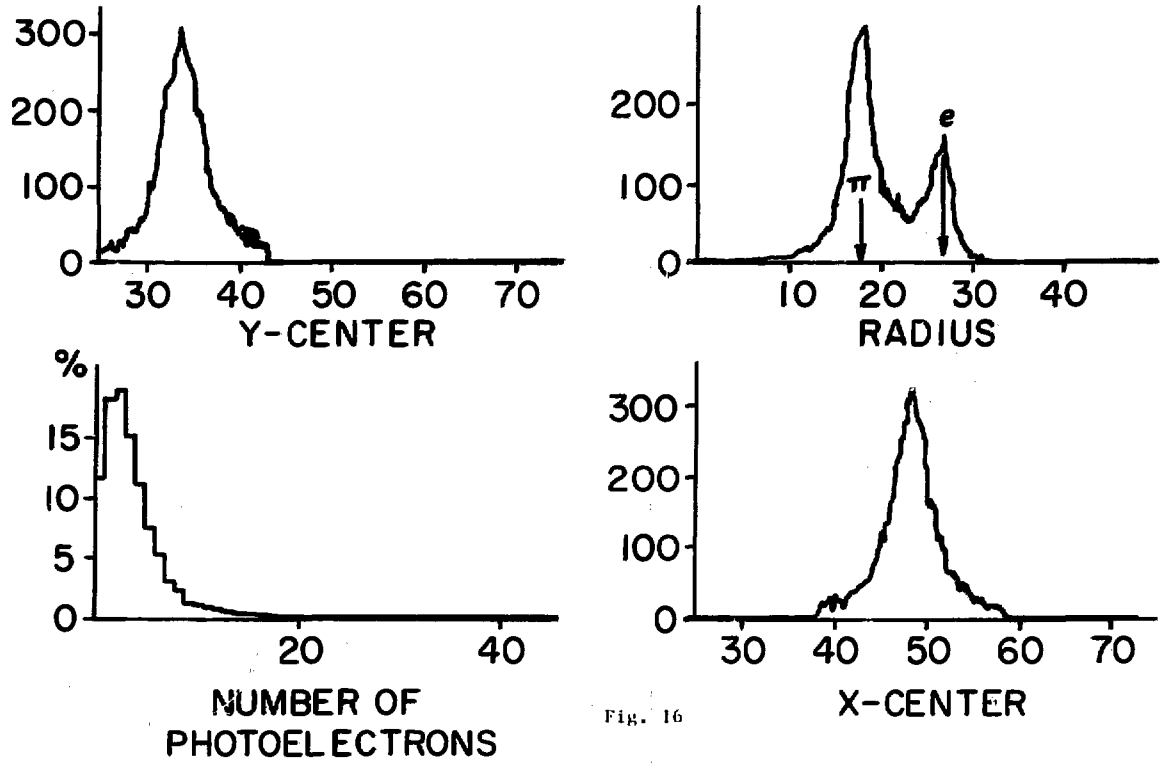
300
200
100
0
30 40 50 60 70
Y-CENTER
%
15
10
5
0
20 40
NUMBER OF
PHOTOELECTRONS
200
100
0
π
e
10 20 30 40
RADIUS
300
200
100
0
30 40 50 60 70
X-CENTER

Fig. 16

HOW WELL CAN WE MEASURE THE JET-JET INVARIANT MASS AT ISABELLE?

Kazuo Abe, University of Pennsylvania

We expect that the energy of jets coming out of ISABELLE interactions range anywhere from a few tens of GeV to a few hundreds of GeV with the charge multiplicity of up to 40. The question of how well these jets will be collimated is still unanswered. The QCD makes predictions of the P_T distributions within a jet, thus it should be straightforward to relate it to the opening angle of jet cone. However, it is not well defined so far and we need the clear definition of the opening angle in such a way that experiments should be able to measure it definitively and it is theoretically meaningful. If we take the attitude that the average sphericity measured at PETRA has some indications as to the jet size, then we can obtain the half opening angle defined as

$$\tan\theta = \left\langle \frac{P_T}{P_\parallel} \right\rangle$$

They are plotted in Fig. 1 versus the jet energy which is taken as one half of the e^+e^- energy. We should keep in mind that this angle comes from the average sphericity including all events and for some events the sharpness of jet-like behavior is more pronounced. The other experiment from which we can guess the jet size is the measurement of large P_T π^o's at ISR by the ABC group. Their measurement of the average angle of 9 GeV π^os from the axis on which the other 9 GeV π^o comes out on the other side is the indication of the jet size measured in terms of π^o components of the jet. The rms angle is $\sim 12^o$. Very roughly we can say that the measured π^o's carry about one half of the jet energy, so the 18 GeV jet has half opening angle of $\sim 12^o$, which is also plotted in Fig. 1. From these, we can reasonably expect the jet at ISABELLE to have a half opening angle of $\sim 10^o$ or less and up to 40 charged particles within its cone.

The invariant mass of jet-jet system is expressed as follows,

$$M \sim \sqrt{2E_1E_2(1-\cos\theta)}$$

where E_1 and E_2 are total laboratory energies of the first and the second jet and θ is their opening angle. The error in the mass is expressed as

$$\frac{\Delta M}{M} \sim \frac{1}{2}\sqrt{\left(\frac{\Delta E_1}{E_1}\right)^2 + \left(\frac{\Delta E_2}{E_2}\right)^2 + \left(\frac{\sin\theta}{1-\cos\theta}\right)^2 \Delta\theta^2}$$

The factor in front of $\Delta\theta^2$ becomes very large for θ below 60° and thus, in this θ region, angular resolution dominates the uncertainty of the mass. But as long as we stay in the region of $\theta > 60^\circ$, $\Delta\theta$ term can be reduced to the negligible level by making angular segmentations small. This can be achieved by finer segmentation of calorimeter blocks and knowing the interaction point with the help of tracking chambers.

In the design of a hadron calorimeter one must optimize i) longitudinal length for total energy containment, ii) sampling thickness, and iii) material. The energy containment in the transverse direction does not become a problem in most colliding beam detectors because they tend to cover 2π in the ϕ direction and large coverage in the θ direction. To contain 99% of energy of a 50 GeV particle, one needs 5.5 absorption length of steel, which is 30% thicker than the requirement for 95% containment. However one should be reminded that a loss of 5% energy broadens the energy resolution by 25% compared with the value of full containment. Making the sampling thickness finer improves the energy resolution especially at lower energies, but below 2.5 cm steel, there is no improvement as long as we are dealing with particles above 10 GeV.

After the above requirements are met for the longitudinal containment and the sampling thickness, the energy resolution is determined by the material used for the sampling. The best material so far found is uranium and its resolution is $\Delta E/E = 0.3/\sqrt{E}$ which is a factor of two better than most commonly used steel.

Among the large detectors proposed so far, the dipole detector emphasizes good jet detections using an uranium calorimeter. Its anticipated mass resolution at the Z^0 mass ($Z^0 \rightarrow$ jet + jet) when the jets opening angle is above 60° is $\Delta M/M \sim 3\%$. The mass resolution of this level would make it possible to sort out new particles decaying into multi jets final states from QCD backgrounds.

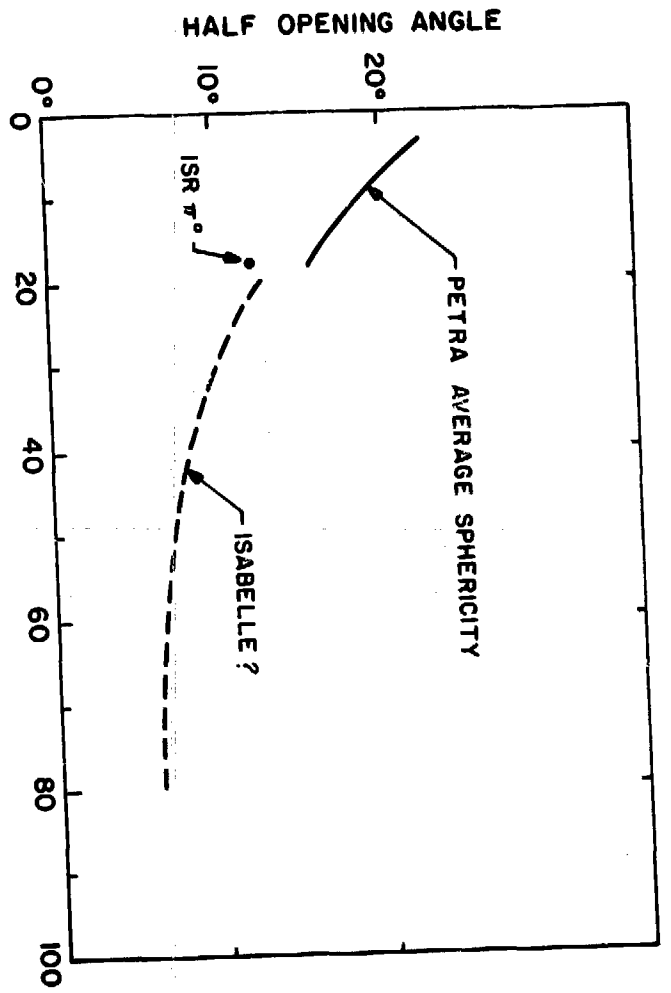
HALF OPENING ANGLE
0°
10°
20°
0
20
40
60
80
100
JET ENERGY (GeV)
ISR π°
ISABELLE ?
PETRA AVERAGE SPHERICITY

Fig. 1

INCLUSIVE LEPTON AND HADRON SPECTRA FROM QCD JETS

S. Csorna, Vanderbilt University

We have studied inclusive spectra of leptons and hadrons in order to

i) Better understand the design criteria for detectors at ISABELLE;

ii) Develop a quantitative understanding of how to measure semileptonic branching ratios of new flavored bare mesons (if they exist);

iii) Find signatures for new flavors apart from the well known dileptons coming from the bound state.

The work done here relies exclusively on the ISAJET monte carlo program.[1] We generated 1000 $T\bar{T}$, $B\bar{B}$, $C\bar{C}$ jets with

$$50 \text{ GeV} \leq (p_\perp)_{JET} \leq 150 \text{ GeV} \quad \text{and} \quad -3 \leq (y)_{JET} \leq 3$$

in order to compare cross sections and momentum distributions for leptons and hadrons.

In Table 1 we summarize the cross sections and integrated luminosity for each kind of flavored jet. Thus, according to theoretical expectations, there are 2/3 as many $T\bar{T}$ jets as there are $B\bar{B}$ or $C\bar{C}$ jets.

The number of leptons that are contained in these jets depends on assumptions about the K.M. angles. In the program we assumed

$$\left\{\begin{matrix} t \to b + W & 100\% \\ b \to c + W & 100\% \end{matrix}\right\} \quad \text{and} \quad 10\% \text{ semileptonic branching ratios.}$$

The number of leptons associated with each flavor is shown in Table 2. Thus the production of a new flavor such as $T\bar{T}$ is signaled by the doubling of the numbers of leptons in the inclusive spectra relative to what would be expected from the previously known flavors. In Fig. 1 we show the momentum spectrum of these leptons. What is immediately striking is the tremendous increase in low momentum leptons ($p \lesssim 5$ GeV). The detection of these leptons is clearly important for measuring semileptonic branching ratios. It appears then that one really needs a detector such as the dipole facility implemented with an image drift chamber and dE/dx for particle ID to measure the electron spectrum. It

would be much more difficult to work with the muons due to the low momentum range being considered.

In Fig. 2 we show π and K spectra from $T\bar{T}$, $B\bar{B}$, $C\bar{C}$ jets. Again the bulk of tracks came from a momentum range of $p < 5$ GeV, where particle separation is most conveniently done by dE/dx. The interpretation of these hadron spectra is clearly difficult, however the monte carlo does predict dramatic increases in the number of kaons (not the π/K ratio) from new flavored jets. This is shown in Table 3.

Our conclusion is (if the theoretical models for jet production and fragmentation are to be believed) that a dipole detector implemented with dE/dx and $\geq$ 1 m diameter drift chamber would be ideal for measuring and identifying the decay products of new flavored jets. Indeed if the predictions for the production cross section of bound $T\bar{T}$ states turns out to be too large, the inclusive electron spectra may be one of the most important handles for establishing new flavor production. Due to the suppression of the $Q\bar{Q}$ bound cross sections at high mass near the Z and above, inclusive studies may be the only way to detect new flavors (see Fig. 3).

We further believe that to measure these spectra, all that we need is a magnet and central drift chamber, the very detector elements which are most likely to be the first ones working as the facility comes on line.

REFERENCES

1. For a complete description of the ISAJET Program see BNL-29777 written by Frank E. Paige and Serban D. Protopopescu. Additional useful calculations can be found in BNL-27066 (author is Frank E. Paige) and an ISABELLE Workshop preprint titled "ISABELLE Physics: Some Useful Calculations" which is a handy collection of cross sections collected by Frank E. Paige.

Table 1

	σ(mb)	$\int \mathcal{L} dt$ for 1000 events (mb^{-1})
$T\bar{T}$ JET (M_T = 20 GeV)	0.23×10^{-7}	0.44×10^{11}
$B\bar{B}$ JET	0.33×10^{-7}	0.30×10^{11}
$C\bar{C}$ JET	0.34×10^{-7}	0.29×10^{11}

Table 2

	N_e or N_μ (from 1000 two jet events)
$T\bar{T}$ JET	782
$B\bar{B}$ JET	468
$C\bar{C}$ JET	218

Table 3

	$N_{\pi^{+-0}}$	$N_{K^{+-0}}$
	(from 1000 two jet events)	
$T\bar{T}$ JET	28,000	12,000
$B\bar{B}$ JET	20,000	8,200
$C\bar{C}$ JET	17,000	7,100

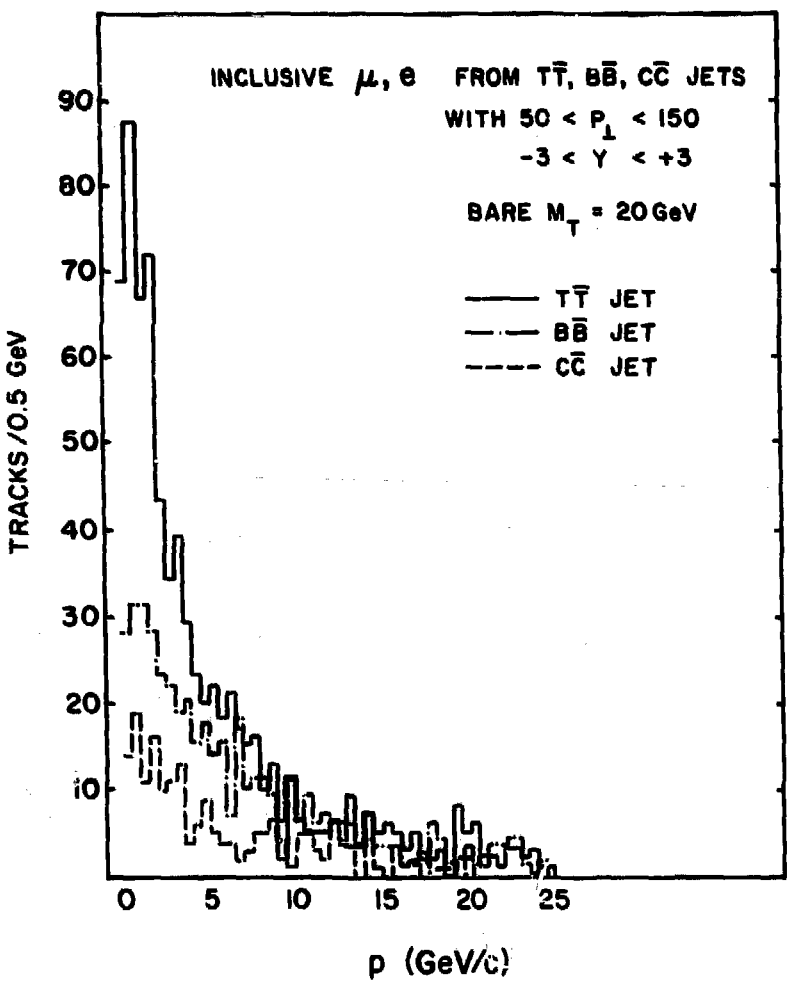
INCLUSIVE μ, e FROM TT̄, BB̄, CC̄ JETS
WITH 50 < P⊥ < 150
-3 < Y < +3
BARE M_T = 20 GeV
TT̄ JET
BB̄ JET
CC̄ JET
TRACKS/0.5 GeV
90
80
70
60
50
40
30
20
10
0
5
10
15
20
25
p (GeV/c)

Fig. 1

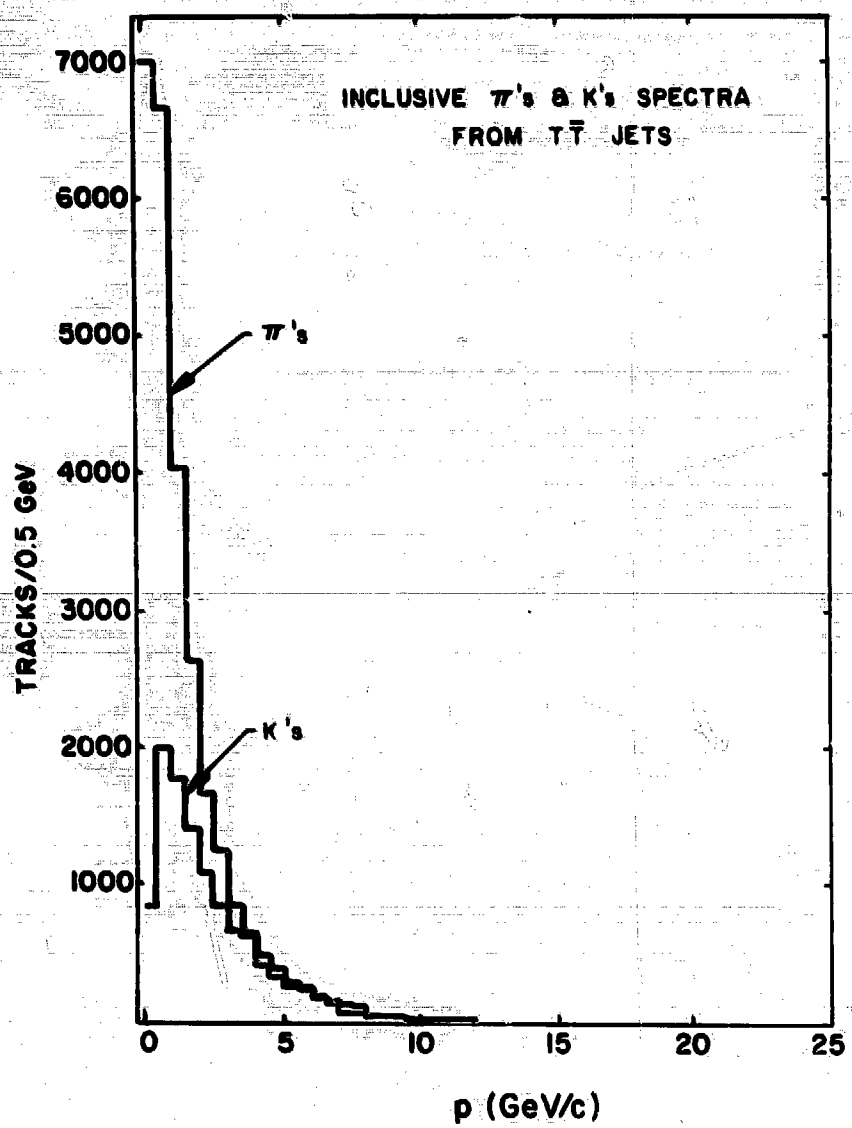
INCLUSIVE π's & K's SPECTRA
FROM T T̄ JETS
π's
K's
TRACKS/0.5 GeV
7000
6000
5000
4000
3000
2000
1000
0
5
10
15
20
25
p (GeV/c)

Fig. 2a

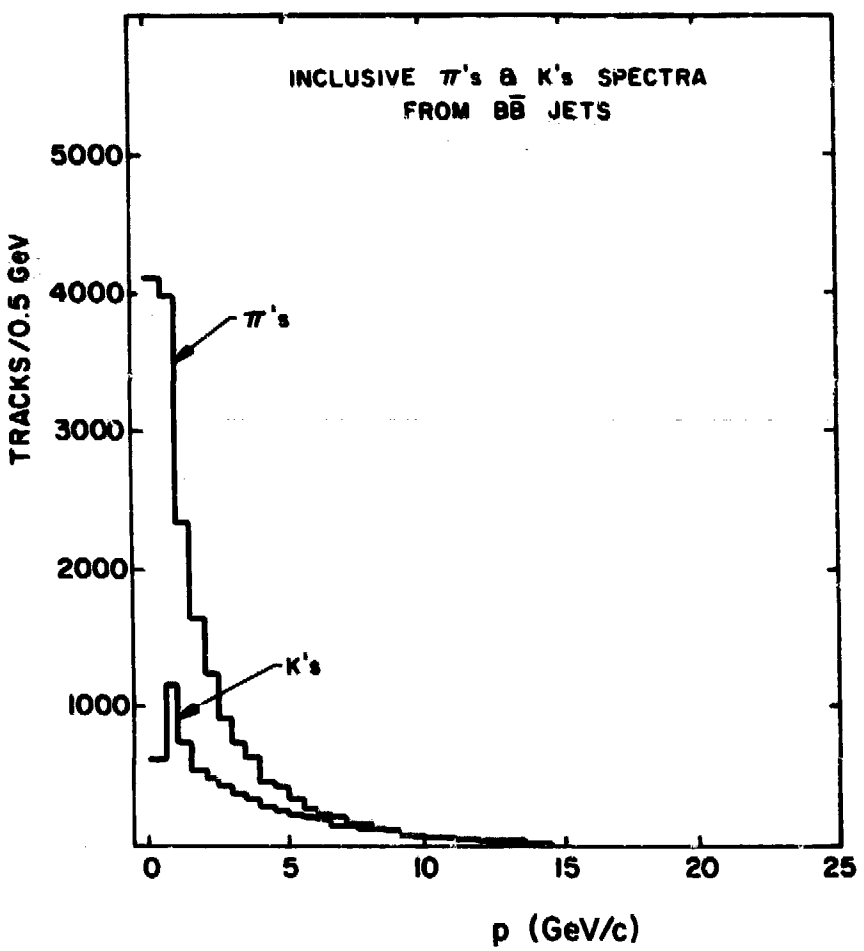
INCLUSIVE π's & K's SPECTRA
FROM BB̄ JETS
TRACKS/0.5 GeV
5000
4000
3000
2000
1000
π's
K's
0
5
10
15
20
25
p (GeV/c)

Fig. 2b

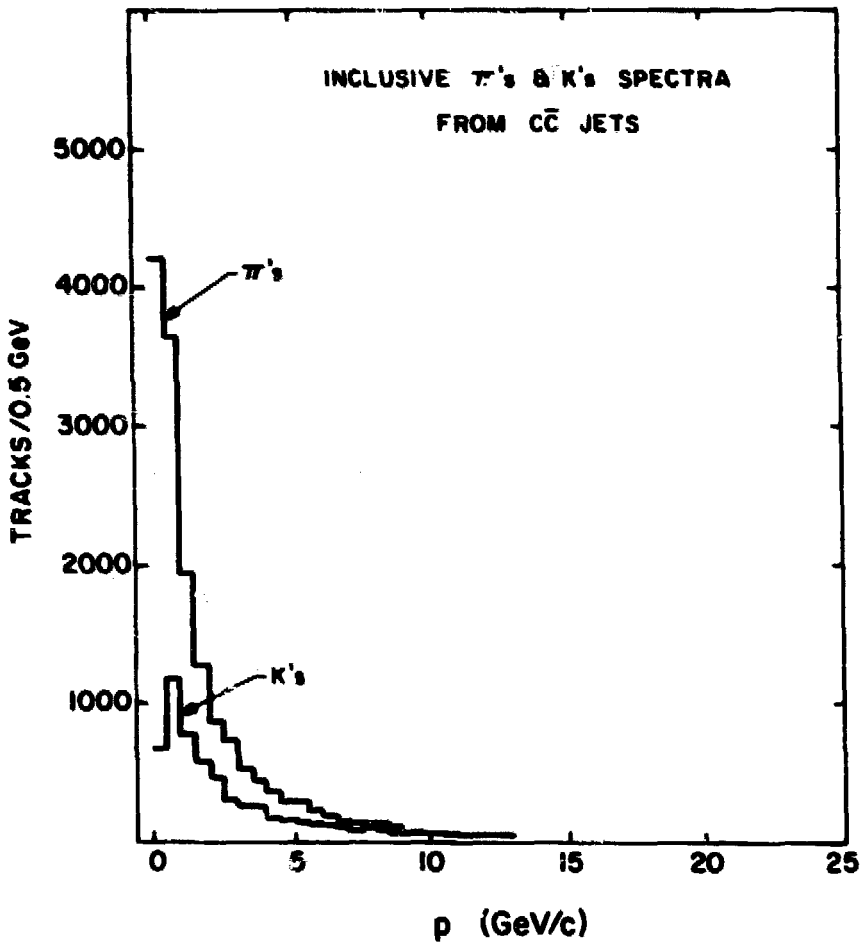
INCLUSIVE π's & K's SPECTRA
FROM CC̄ JETS
TRACKS/0.5 GeV
5000
4000
3000
2000
1000
π's
K's
0
5
10
15
20
25
p (GeV/c)

Fig. 2c

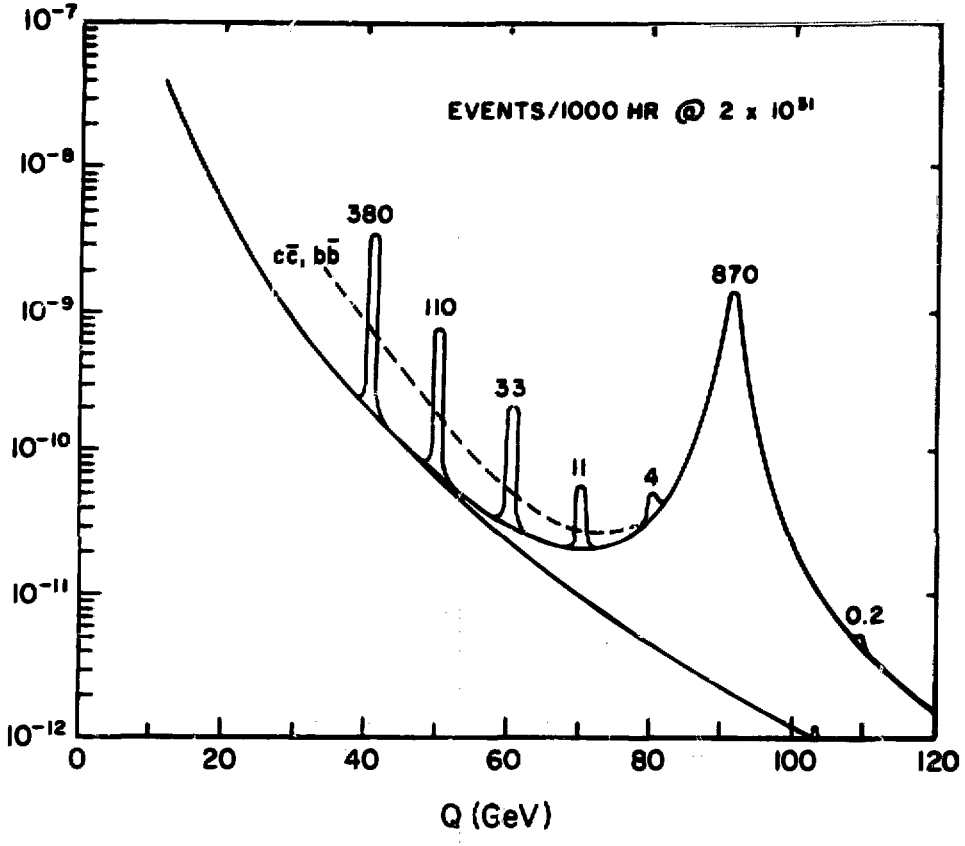
EVENTS/1000 HR @ 2 x 10^31
380
cc̄, bb̄
110
33
11
4
870
0.2
10^-7
10^-8
10^-9
10^-10
10^-11
10^-12
0
20
40
60
80
100
120
Q (GeV)

Fig. 3

MULTI-VERTEX DETECTION

T. Bacon, Imperial College

There are many postulated massive objects (Higgs mesons, technions, top quarks) which, depending on their masses, will decay predominantly to heavy flavours. The decay products will form jets which will generally look like those produced by light quarks. The events involving new objects can be signalled by lepton identification or by multiple jet production. The latter will require good calorimetry and/or particle tracking, possibly with particle identification, and will be subject to sizeable backgrounds.

Another signature of heavy flavours and their parents is the weak decay of the ground states of hadrons containing b, c or t quarks, yielding multiple vertices within a millimeter or so of each other. This note suggests that an inner detector of relatively low cost can provide an off-line filter for the heavy flavours which would also reduce combinatorial background in reconstructing the lowest charmed particle states. At present, there is only an upper limit for the lifetime of the lowest hadrons containing b-quarks of about 2×10^{-12} seconds (reflecting the spatial resolution of present detectors at e^+e^- machines) but the mean life of the D-mesons is known to be about 3×10^{-13} seconds.

REQUIRED RESOLUTION

A secondary vertex may be detected by finding a track (approximately 50% of $D^\pm$ decays give only one charged prong) which appears to miss the production vertex by a significant "impact" parameter. With the approximation that, on average, each decay product carries the same fraction of P_T and P_L in the decay, the mean impact parameter is approximately $c\tau$, (the mean decay distance $\ell = \frac{p}{m} c\tau$) essentially independent of the momentum of the D. For the D-mesons this is about 100 μm. The required resolution should be some fraction of this so that the majority of charm decays can be detected. Several multiprong charm decays, seen with detection probability of about 40%, were reported at the recent Lisbon conference for a bubble chamber experiment with about 50 μm resolution.

INNER DETECTORS

An appropriate inner detector could consist of high precision wire chambers of less than 50 μm resolution with anodes parallel to the beam pipe. The first layer would be wrapped closely round the beam pipe assumed to be of radius 5 cm. The charged particles would be tracked through more chambers out to about 30 cm radius, where the resolution requirements could be relaxed.

For speed, an event would be examined in the projection normal to the circulating beams (losing thereby a factor of $\sqrt{2}$ in resolution and more if the D-meson is not moving perpendicular to the beams) to reconstruct the production vertex using several tracks and to search for tracks with significant impact parameters. Unfortunately the lateral dimensions of the proton bunches are too large to determine the position of the production vertex with sufficient precision without reconstructing tracks (as is possible with e^+e^- rings). This again requires some improvement in the required resolution, dependent on the number of tracks reconstructed.

The length of the inner detector should be at least as long as the crossing region (approximately 50 cms). The geometrical acceptance will depend on the particular objects of study but, in the main, these are produced with high p_T and will register in the inner detector. The diffractive charm production observed at the ISR will not be observed easily, but is of less interest than charm production from heavy flavours.

The required resolution is worse than that attainable with a time expansion chamber (Approx. 10 μm. See report by Walenta, these proceedings). Solid state detectors can have similar resolution but are not considered here because, among other things, of the large size of the array required.

BACKGROUNDS

Since it is crucial that the chambers near the beam be free of background, beam halo should be reduced to a minimum. Also, for ease of reconstruction of high multiplicity events it would be best if the chambers were in a field-free region, avoiding p-ϕ correlations, so that a toroidal magnetic field or low field magnet would be preferred over a conventional solenoidal or dipole field. This would probably also reduce detector-generated background.

At the luminosity of ISA phase I, there will be a 30% chance of more than one event per crossing. At higher luminosities, the technique would require some refinement.

SUBCOMMITTEE REPORT ON THE SHAPE AND STRENGTH OF MAGNETIC FIELDS

B. Pope, Princeton, Chairman
M. Bregman, Columbia
P. Grannis, SUNY at Stony Brook
L. Littenberg, BNL
D. Luckey, MIT
L. Rosensen, MIT
T. Ypsilantis, Ecole Polytechnique

This subcommittee attempted to compare the properties of the canonical field shapes: dipole, solenoid and toroid. In addition, various options within each category were examined. For example, the perennial question of whether a dipole field should be horizontal or vertical was again raised. (The answer for this year appears to be that it does not make much difference, see the work of G. Parzen).[1] We had considerable difficulty in doing direct comparisons of general properties of the magnets and we refer the reader to the papers of Littenberg, Bregman, Grannis, Luckey, and Pope for their biased preferences for particular magnets.

An example of a calculation that tried to do a general comparison of the 3 field shapes is as follows. Consider a solenoid of field strength B, radius R and length L. Then the stored energy is

$U = 1.25\ L\ B^2\ R^2$ where U is in Mega Joules
B in Tesla and Lengths in meters

Similarly for a dipole of field strength B, a square cross section of $2R \times 2R$ and length L has a stored energy of

$$U = 1.6\ L\ B^2\ R^2$$

A toroid of inner field strength B_i, inner radius R_i, outer radius R_0 and length L has a stored energy of

$$U = 2.5\ L\ B_i^2\ R_i^2\ \ln(R_0/R_i).$$

We felt that a general comparison should be made for magnets of the same stored energy. Thus we can take B = 1.5 T, R = 1.5 m for the solenoid (as in the CDF detector at Fermilab) and obtain a stored energy per unit length of 6.3 MJ/m.

B = 1.3 T, R = 1.5 m for the dipole, and
B_i = 1.5 T, R_i = 1 m, R_0 = 3 m for the toroid

give similar stored energies.

Under these conditions, the sagitta for a 50 GeV particle has been calculated for these 3 fields as a function of the polar angle, θ, and the azimuthal angle, ϕ. The results are shown in Figures 1 and 2 and indicate some general properties of the field shapes.

A somewhat arbitrary and extremely tentative list of properties of the 3 field shapes is shown in Table 1.

REFERENCE

1. M. Cornacchia and G. Parzen, Effect of a Spectrometer Magnet on the Beam Beam Interaction, IEEE Transactions on Nuclear Science, Vol. NS-28, 2555 (1981).

Table 1

PROPERTY — MAGNET	DIPOLE	SOLENOID	TOROID	NO FIELD
Options	High/Low Field Vert/Horiz Field	High/Low Field Small/Large Field	Continuous inner coil Lumped inner coil	
Resolution in θ	Improves as $(\sin\theta)^{-1}$	Constant	Improves as $(\sin\theta)^{-1}$	
Acceptance of Magnet in θ	$0 \to 180°$	$20° \to 160°$	$30° \to 150°$	$0 \to 180°$
Resolution in ϕ	Dead cone around $\theta = 90°$, $\phi = 90°$	Uniform	Some Ripple	
Acceptance of Magnet in ϕ	$\gtrsim$ 90% of 2π	2π	$\simeq$ 70% of 2π	2π
Non-Uniformity of Field	$\lesssim$ 5% (For open dipoles)	$\leq$ 1%	$\simeq$ 5%	
Effect on Beams	Compensation of shielding needed "No difference between horiz and vert Field"	Compensation probably needed	No field on beams	No field on beams
Extract particles from Beam Pipe?	Yes	No	No	No
Return Yoke	Yes	Yes	No	No
Weight	Heavy	Heavy	Not so heavy	Light?
Access to Detectors	Good for open dipoles	Not so good	Good	Good
Construction	Easy, possibly conventional coil	Easy, probably superconducting	Superconducting. Difficult forces	
Physics	General 4π Physics, Jets, Bias towards high rapidity	General 4π Physics, Bias towards wide angles, $\mu\mu$	Wide angles, single particle inclusive, (Jets?) $\mu\mu$	Energy flow, Jets, e's, γ's

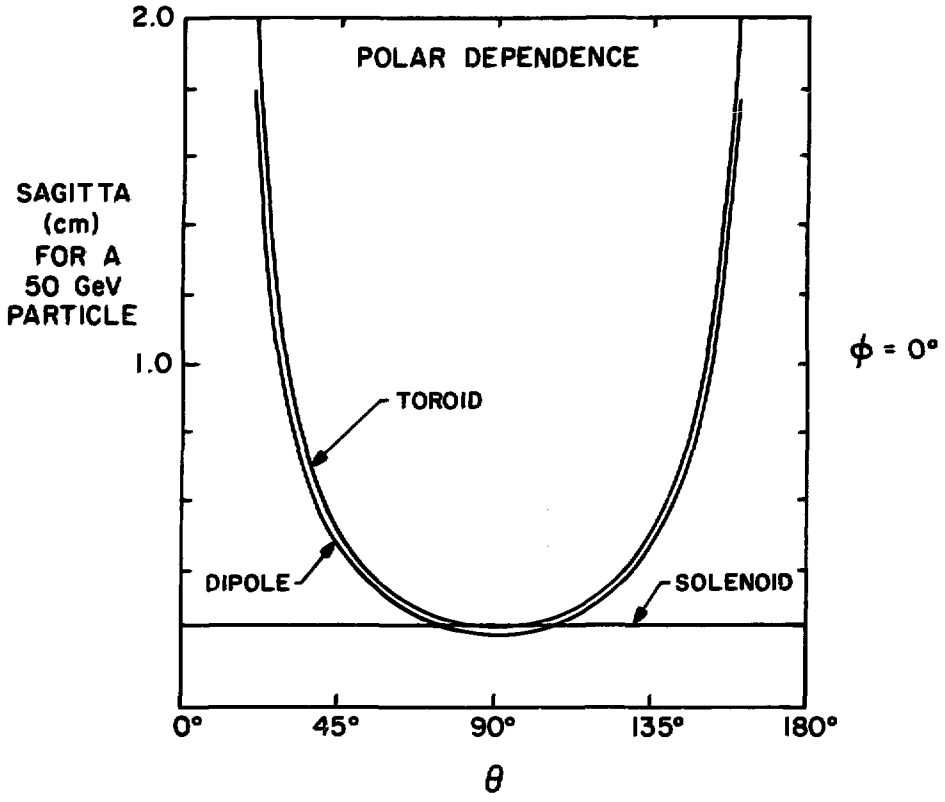
POLAR DEPENDENCE
SAGITTA (cm) FOR A 50 GeV PARTICLE
2.0
1.0
TOROID
DIPOLE
SOLENOID
φ = 0°
0°
45°
90°
135°
180°
θ

Fig. 1

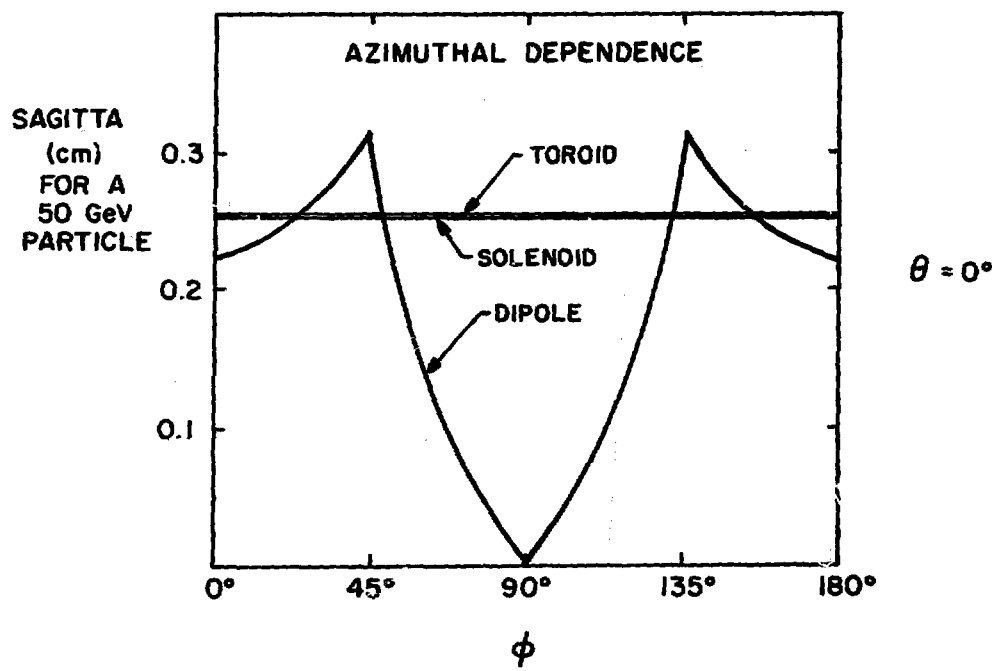
AZIMUTHAL DEPENDENCE
SAGITTA
(cm)
FOR A
50 GeV
PARTICLE
0.3
0.2
0.1
TOROID
SOLENOID
DIPOLE
θ = 0°
0°
45°
90°
135°
180°
φ

Fig. 2

PROGRESS REPORT ON THE DIPOLE DETECTOR MAGNET

L. Littenberg, BNL

This is a brief summary of the work done by the magnet design subgroup of the Dipole Detector Collaboration. Figure 1 shows the Dipole Detector. The subgroup, which consists of E. Kelly, J. Kopp, S. Ozaki, A. Prodell, R. Shutt and myself, is charged with designing a dipole spectrometer magnet which satisfies the following criteria:

1) A 5.5 m-diameter calorimeter must be accommodated within it.

2) The central field should be 5 kgauss, upgradable to 15 kgauss.

3) There must be adequate field uniformity within a radius of $\sim$1.5 m of the center of the magnet.

4) Forward going tracks must be unobstructed.

5) Stray fields must be kept within reasonable limits.

6) The magnet must be cryostable.

7) Access to apparatus within the magnet must be possible.

8) The dipole and any associated compensating, forward spectrometer, etc. magnets must be compatible with the requirements of the ISA.

The last criterion was originally thought to require that the dipole field lie in the horizontal plane. However, recent calculations[1] have shown that up to an excitation of 15 kgauss the dipole field may just as well be oriented in the vertical plane. Each orientation has advantages and at present we find the case for neither to be compelling. Thus we have studied both cases, and have developed two alternative (although very similar) designs.

A Helmholtz-like coil configuration was proposed with coil of i.d. 6m and profile 20 x 116 cm, the coils to be separated by 220 cm. Early versions had no iron. The resulting fields as calculated by GFUN3D[2] are those of Fig. 2. Uniformity is adequate but the fringe fields are rather large (e.g., $\sim$10% of central field at twice the coil radius). The addition of a shell of 80 cm of iron modifies the fields to those shown in Fig. 3. Note that the fringe field have been nearly eliminated. This thickness of iron is rather conservative and in fact has a significant effect on the fields even at 15 kgauss (see Figs. 4 and 5). The stray fields are reduced by a factor 2 or 3.

Other benefits of the iron are a reduction of the current necessary to reach 5 kgauss by 47% and a reduction of the maximum field in the coil by 26%. In addition of course, the iron provides a framework off which to hang the coils and the detectors. The iron is in the shape of a closed square box of i.d. 8m and o.d. 9.6m with 2x2m azimuthal holes at 0, 90, 190, and 270°. The end plates are also 80 cm thick and are separated by 5.5m (see Fig. 6).

The 80 cm spacing between the outer radius of the coil and the inner radius of the return yoke was determined via a study of the displacement force that arises when the coil is not centered in the iron. The coil is pulled toward the iron nearest it and if it can move in that direction, the attraction increases, leading to an instability. For an excusion of 1 inch, which is about the placement accuracy of a coil this large, this force is approximately 20000 lbs. The 80 cm spacing is optimal in the sense that the force decreases only slowly as this distance is increased, but increases rapidly as the distance is decreased. If the distance from coil to iron is halved, the force increases by a factor 20. There is also a force due to the presence of the azimuthal holes which tends to pull the coils square. At the 80 cm spacing, this force represents only a 3% effect.

Fig. 7 gives an idea of the forces involved at the 15 kgauss excitation (at 5 kgauss they are 5-9 times less). If there were no iron, the coils would attract each other with about 5 million pounds force. In the presence of the iron the coils are pulled in the opposite direction towards the end plates with a force of around 1 million pounds. This force is in fact the small residue of much stronger compressional forces. The end plates are drawn towards one another with a force of some 200 psi. There is a radial force on the coils of $\sim$ 4M lb/quadrant. For comparison the weights of the various magnet components are also listed on the figure.

The figure should be rotated through 90° to show the horizontal orientation. In this orientation supporting the coil and keeping it from distorting with both field on and the field off while endeavoring to minimize the heat transfer is quite a challenge. Ralph Shutt worked out a scheme using G-10 straps à la the ISA dipole supports which seems quite promising. We believe the cooling load can be kept to $\sim$ 200 watts.

The forces are, in general, not so great that the iron cannot be made to support itself. However, we are constrained by machining costs, the relatively small space available for assembly and the modest crane capacity. We feel that in the horizontal orientation, design and assembly of the iron would be much easier if the return yoke were given a square rather than the originally envisioned circular cross-section (see Fig. 6). The increased cost of the iron (≈ 20%) should be more than compensated for by savings in the cost of assembly. We note that in general the problems of assembly and support for both coil and iron are less in the vertical than in the horizontal orientation.

The magnet is meant to be cryostable. At present we plan to cool it with liquid He. Fig. 8 shows some details of the coil. There are 44 pancakes each of 18 turns (≈ 1200'). The size and low proportion of superconductor (2.2%) are given by the requirements of cryostability and self support against hoop stress. The octagonal cross-section of the conductor is a response to the horizontal field orientation. It increases the surface area available for heat transfer and reduces bubble trapping. We originally thought of the conductor as a monolith. However, representatives of AIRCO informed us that this would require a lot of expensive, unnecessary processing of copper. They suggested instead a kind of composite: a relatively small monolith (or even a cable) inset into a channel in pure copper. Such a configuration could easily carry the 5 kA required.

Compensation. Either the horizontal or vertical orientations can use the same compensators, e.g.,

	5 kgauss	15 kgauss
	28.2 kGm (0.85 GeV/c)	79.2 (2.38 GeV/c)
Compensator @ 8m	-18.7	-52.5
Compensator @ 29m	4.5	12.9

The trajectories in the two cases are shown in Figs. 9 and 10. For the 5 kgauss case the compensator @ 8m could be for example a 48D48. For the 15 kgauss case, we are talking about a substantial magnet which could be expensive. In fact, any realistic scheme requires a good deal more magnetic volume since it will have to accommodate forward spectrometry as well as compensation. Fig. 11 shows a possible scheme for the 5 kgauss horizontal

orientation. Calorimeters cover the forward direction down to ±4 mr, and forward going charged tracks with momenta up to 200 GeV/c are detected. The first two supplementary magnets are quite substantial, and considering that they will be duplicated on the opposite side of the interaction region, they represent a considerable investment, even on the scale of the main dipole.

While both horizontal and vertical symmetric schemes are acceptable to the machine physicists there is another set of vertical compensation schemes with several attractive features, which is not. This family of asymmetric compensation schemes throws virtually all the compensation onto one side of the intersection. Fig. 12 illustrates one such scheme. It allows access to the 0° neutral beam which otherwise is directed right back up the beam pipe. In addition forward charged tracks are dispersed rather than being refocussed, in contrast to both the horizontal and vertical symmetric schemes. Such dispersion could be crucial in the measurement of fast forward tracks. It's clear that these features represent physics advantages. For example one can envision situations wherein it would be very desirable to measure the total energy and momentum associated with a given class of events. One is much more likely to succeed in doing this with an asymmetric compensation scheme. The objections of the machine physicists are based primarily upon the fact that the crossing angle is changed in asymmetric schemes. Thus it is unlikely that we could initially turn on in such a configuration. However, after some experience in running Isabelle is gained, one would presumably get braver and as is the case a the ISR, accept the lower periodicity. If the horizontal orientation is chosen, asymmetric schemes are precluded.

Access

The most powerful arguments in favor of the horizontal field orientation have to do with access. Figure 13(a) gives an idea of the problem. Keep in mind that what seems to be free space in the figure is likely to be partly taken up with support systems, light guides, etc. The most difficult problem would seem to be getting access to the drift chambers in a reasonable time. In the horizontal orientation, access could be provided by allowing the two halves of the system, each containing one end plate, one coil and one calorimeter half to be independently movable. Similar loads ($\sim$1800 tons/half)

have successfully been made mobile via a system of rollers at PEP.[3] Simply moving the two sides apart would give access to almost everything within.

At first sight access in the vertical orientation seems much more difficult. However, we have found that with slight modifications to the design, a practical if somewhat complicated system of access can be envisioned. Fig. 13(a) shows the spectrometer in position in the research hall. The magnet has been modified somewhat; the coils have been made detachable and two opposing sides of the return iron have been removed. With the remaining two sides doubled in thickness, this results in only minor changes in the field and forces. Unlike the case of horizontal orientation, most of the magnet iron would stay in place - only the bottom end plate moves, carrying the calorimeter and the bottom coil with it. This carriage would be lowered about four feet on hydraulic cylinders to a roiler system. In this lowered position the calorimeter does not quite clear the upper coil. Therefore the upper end plate (to which he upper coil is affixed) can also be lifted hydraulically. The carriage is then free to move to one of two remote stations in the assembly hall (Figs. 13b & c). There is a movable 30 foot span gantry frame with a hydraulic lifting capacity of 700 T. Thus, for example, the top half of the calorimeter could be lifted off at the first station and the lower half and lower coil rolled to the second stations. In this way there is complete access to the interior of both halves of the calorimeter. In addition this scheme allows excellent access to the apparatus while it is still within the magnet. With the end plate in the low position, the top of the calorimeter is completely accessible. If the support of the top half of the calorimeter can be transferred to the top end plate, the bottom half of he calorimeter may be lowered independently exposing its interior and the bottom of the drift chamber package. If the top plate is raised both the inside of the upper calorimeter half and the top of the drift chamber package becomes accessible. If the top plate and coil are raised by themselves, the outside of the upper calorimeter becomes accessible without the necessity of breaking the beam pipe. If support of the lower calorimeter half is made transferable to the top plate, the carriage could be lowered without it, allowng access to the outside of this half of the calorimeter in situ. Thus almost any necessary access can be provided.

Both versions of this design meet the criteria listed above. They are technologically rather conservative and we foresee no great difficulty in building either one.

REFERENCES

1. M. Cornacchia and G. Parzen, Proceeding of the 1981 Particle Accelerator Conference, 1981.
2. M.J. Newman, C.W. Trowbridge and R.L. Turner. Proc. 4th Int. Conf. on Magnet Technology, Brookhaven (1972).
3. R.L. Blumberg HRS-180, 1980 (unpublished).

FIGURES

1) Layout of the dipole detector.
2) Field given by dipole coils without iron for 5 kgauss central field valve.
3) Field given by dipole coils with iron for 5 kgauss excitation.
4) Field given by dipole coils without iron for 15 kgauss excitation.
5) Field given by dipole coils with iron for 15 kgauss excitation.
6) Iron configuration for (a) horizontal and (b) vertical field orientations.
7) Magnetic forces for 15 kgauss excitation.
8) Details of the coils.
9) Compensation scheme for 15 kgauss horizontal dipole field.
10) Symmetric compensation scheme for 15 kgauss vertical dipole field.
11) Compensation and forward spectrometry for the 5 kgauss horizontal B-field case.
12) Asymmetric compensation for 15 kgauss vertical B-field case.
13) Access system for vertical field orientation.
    a) Spectrometer in position in research hall.
    b) Station 1 (in assembly hall).
    c) Station 2 (in assembly hall).

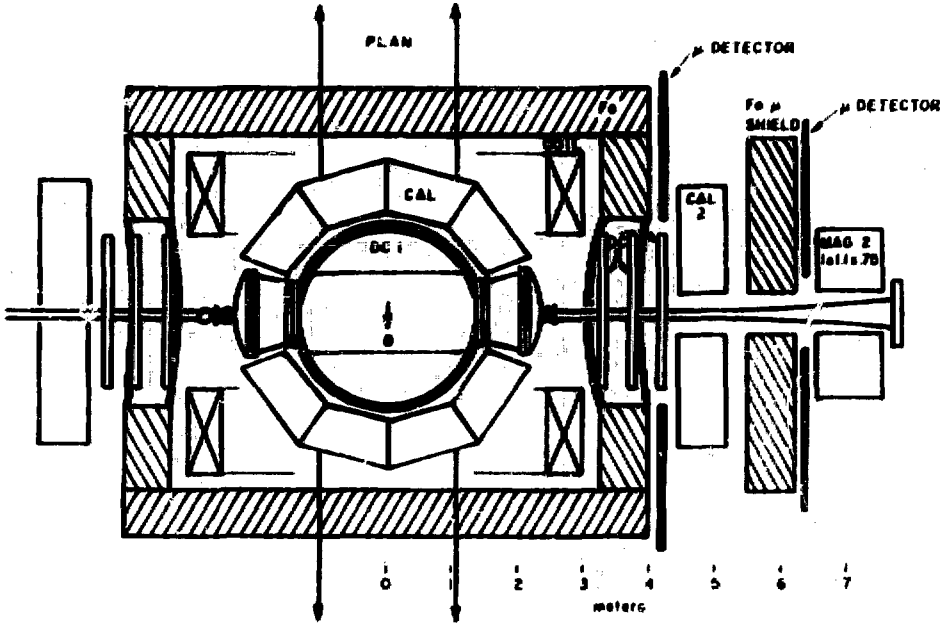
PLAN
μ DETECTOR
Fe
Fe μ SHIELD
μ DETECTOR
CAL
DC 1
CAL 2
MAG 2
0
1
2
3
4
5
6
7
meters

Fig. 1

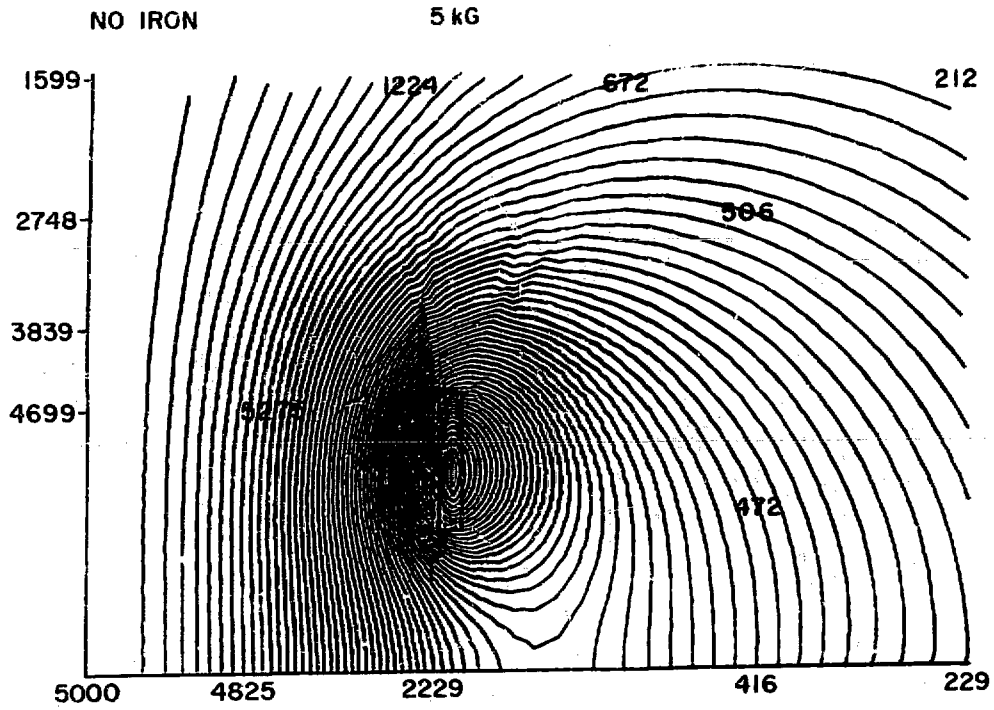
NO IRON
5 kG
1599
2748
3839
4699
5000
4825
2229
416
229
1224
672
212
306
472

Fig. 2

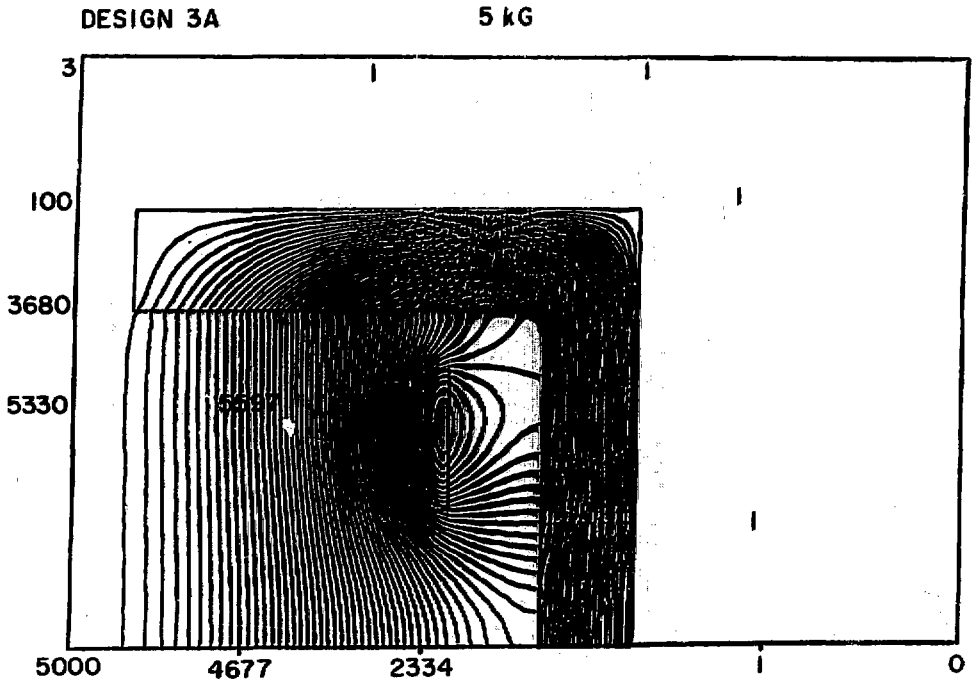

Fig. 3

FIG.4
NO IRON 15kG

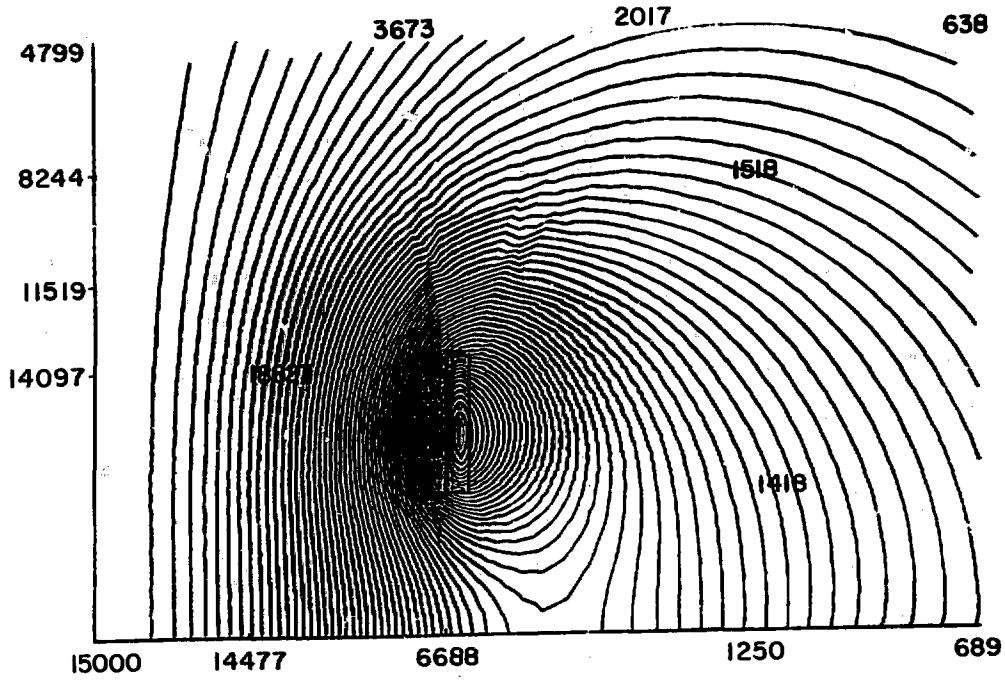

Fig. 4

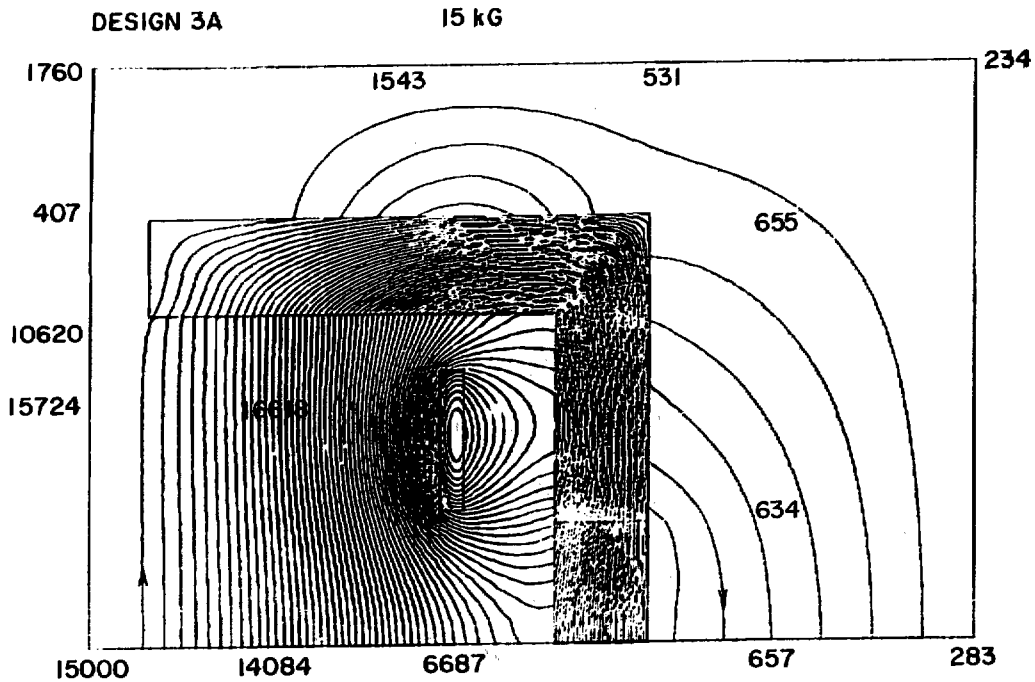
DESIGN 3A
15 kG
1760
1543
531
234
407
655
10620
15724
16618
634
15000
14084
6687
657
283

Fig. 5

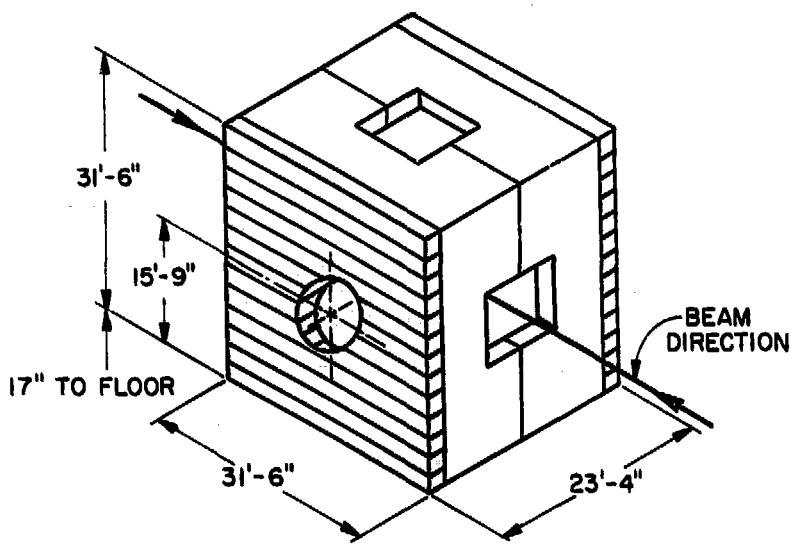

HORIZONTAL FIELD

Fig. 6a

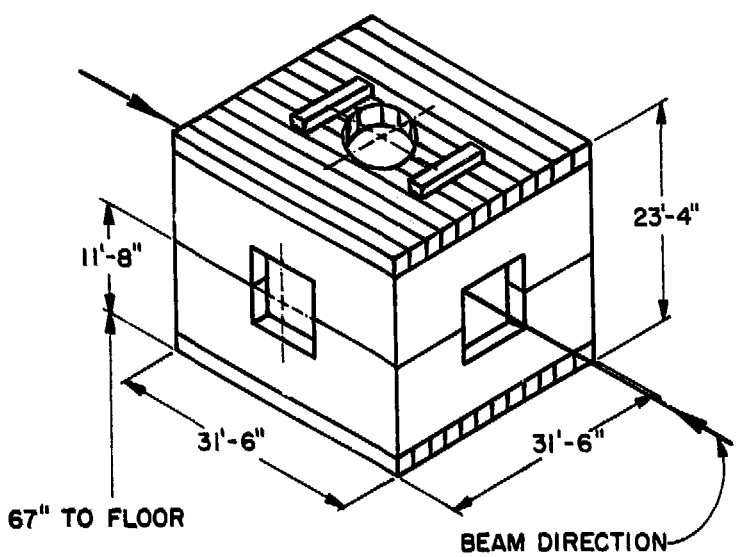

VERTICAL FIELD

Fig. 6b

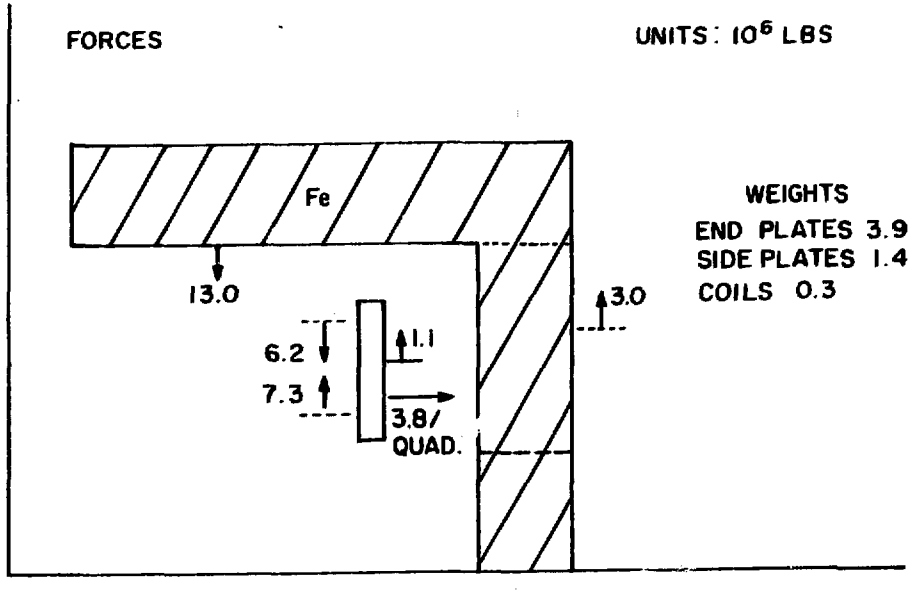
FORCES
UNITS: 10^6 LBS
Fe
13.0
3.0
6.2
7.3
1.1
3.8/
QUAD.
WEIGHTS
END PLATES 3.9
SIDE PLATES 1.4
COILS 0.3

Fig. 7

EACH COIL-44 PANCAKES, EACH 18 TURNS
5 MILES OF CONDUCTOR ~56,000 LBS

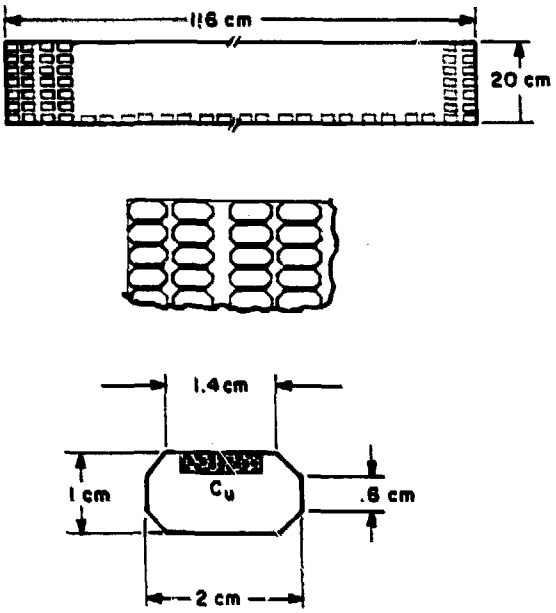

~2.2 % SUPERCONDUCTOR

Fig. 8

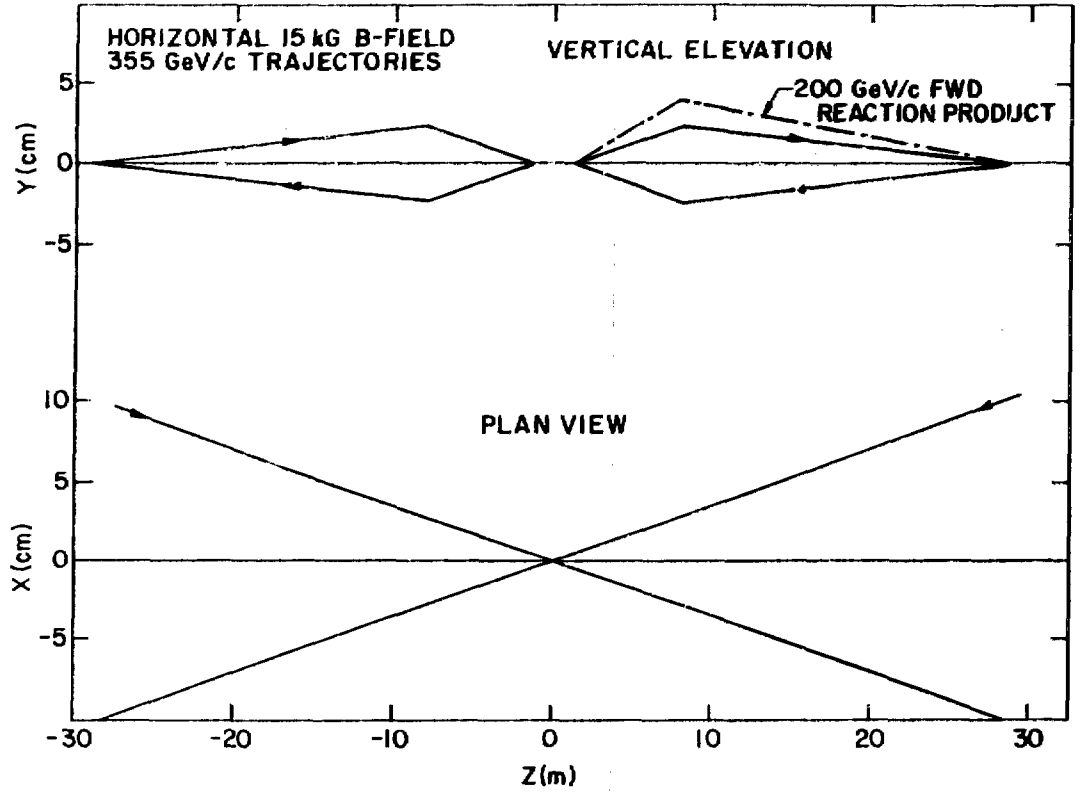
HORIZONTAL 15 kG B-FIELD
355 GeV/c TRAJECTORIES
VERTICAL ELEVATION
200 GeV/c FWD
REACTION PRODUCT
Y (cm)
5
0
-5
PLAN VIEW
10
5
0
-5
X (cm)
-30
-20
-10
0
10
20
30
Z(m)

Fig. 9

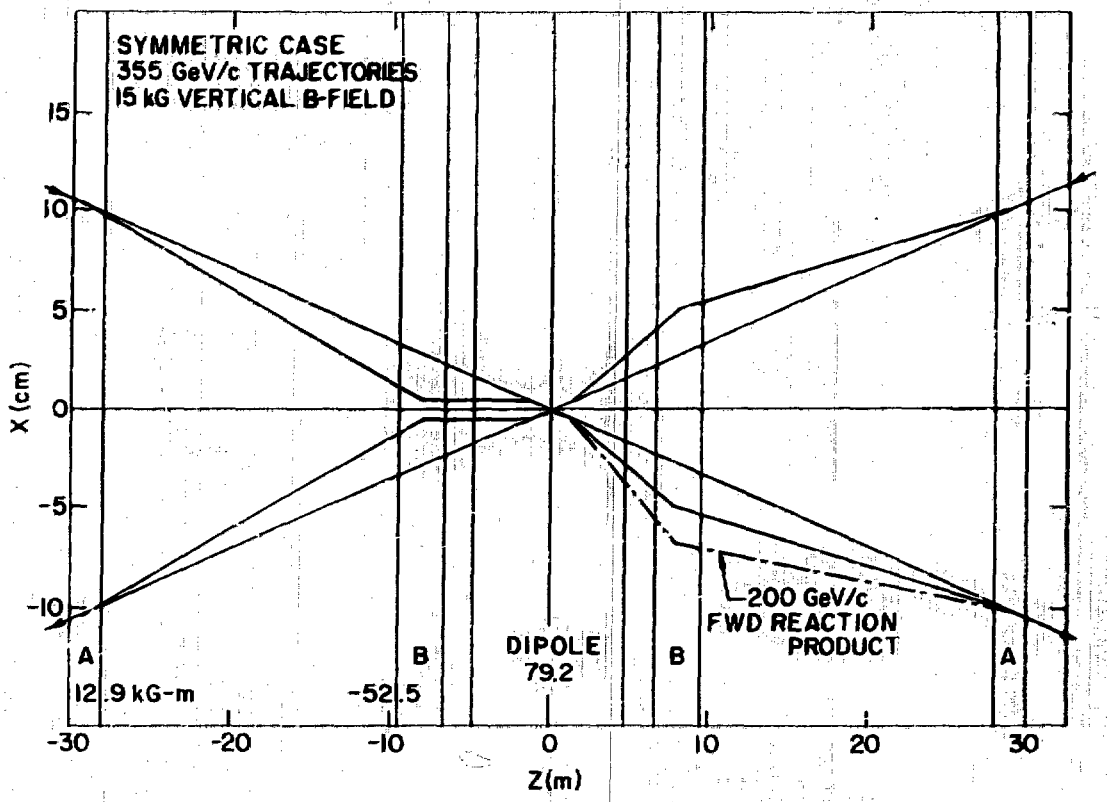
SYMMETRIC CASE
355 GeV/c TRAJECTORIES
15 kG VERTICAL B-FIELD
X (cm)
Z(m)
A
B
DIPOLE
79.2
B
A
12.9 kG-m
-52.5
200 GeV/c
FWD REACTION
PRODUCT

Fig. 10

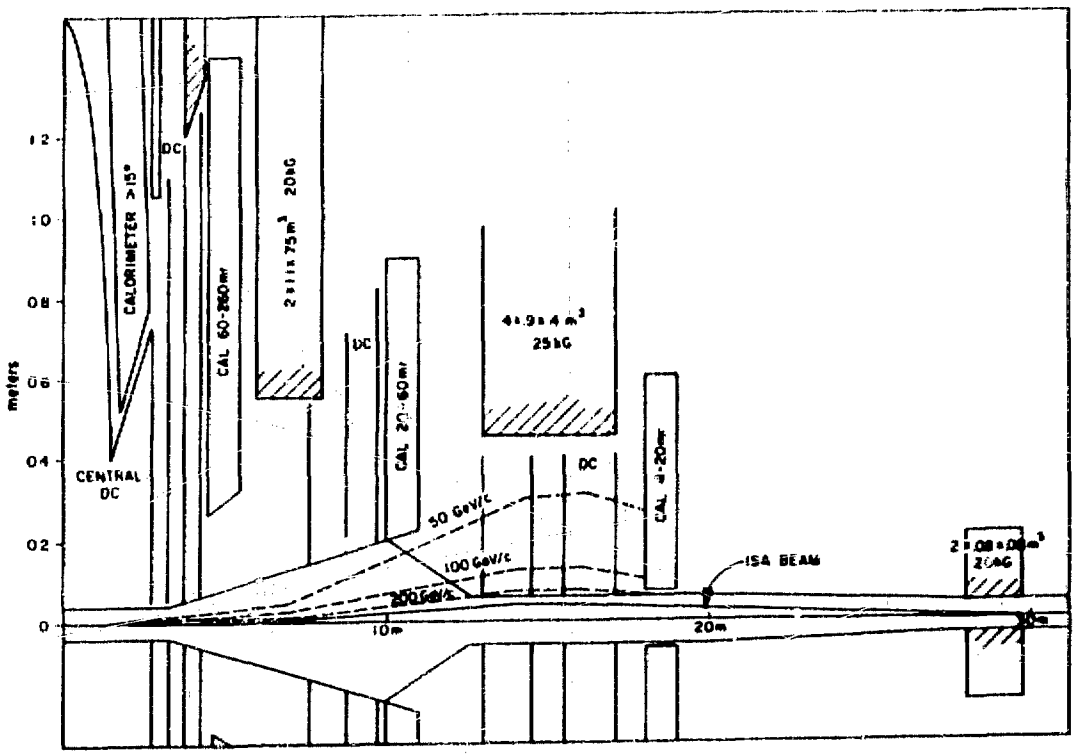
meters
1.2
1.0
0.8
0.6
0.4
0.2
0
CENTRAL DC
CALORIMETER >15°
DC
CAL 60-260mr
2 x 11 x 7.5m³ 20kG
DC
CAL 20-60mr
4 x 9 x 4 m³
25kG
DC
CAL 4-20mr
50 GeV/c
100 GeV/c
200 GeV/c
ISR BEAM
10m
20m

Fig. 11

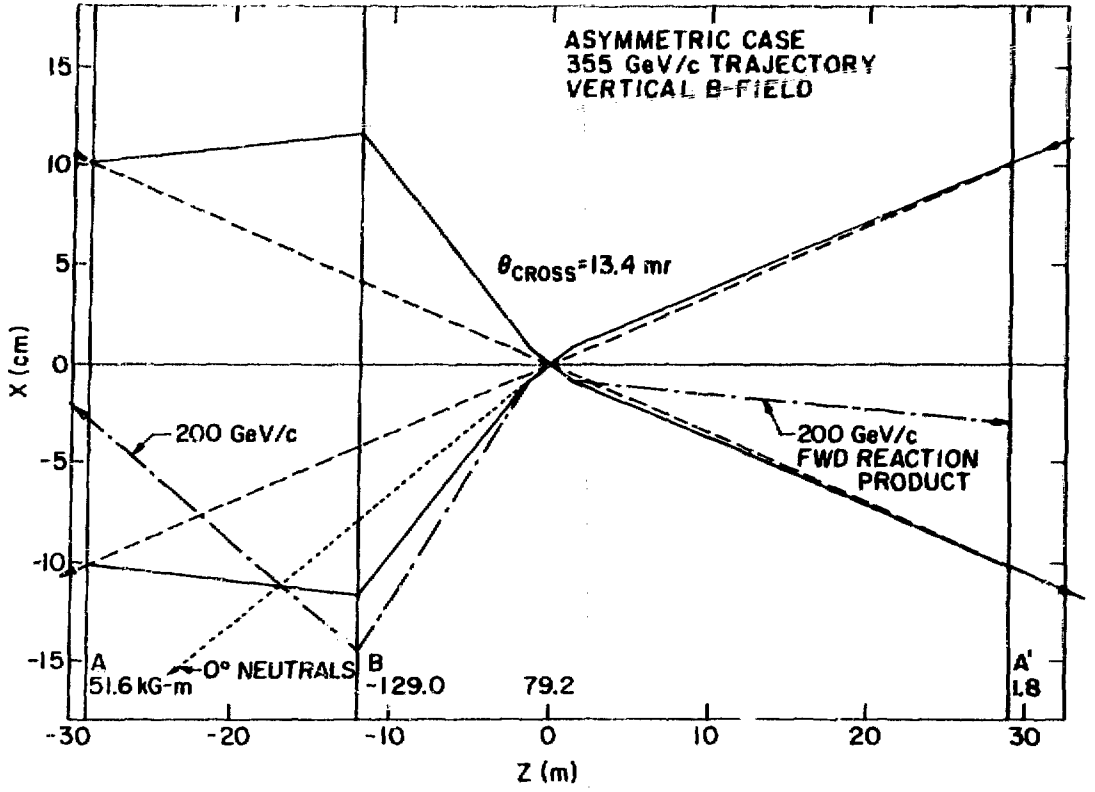
ASYMMETRIC CASE
355 GeV/c TRAJECTORY
VERTICAL B-FIELD
θCROSS=13.4 mr
200 GeV/c
200 GeV/c
FWD REACTION
PRODUCT
A
51.6 kG-m
0° NEUTRALS
B
-129.0
79.2
A'
L8
X (cm)
Z (m)
15
10
5
0
-5
-10
-15
-30
-20
-10
0
10
20
30

Fig. 12

a)

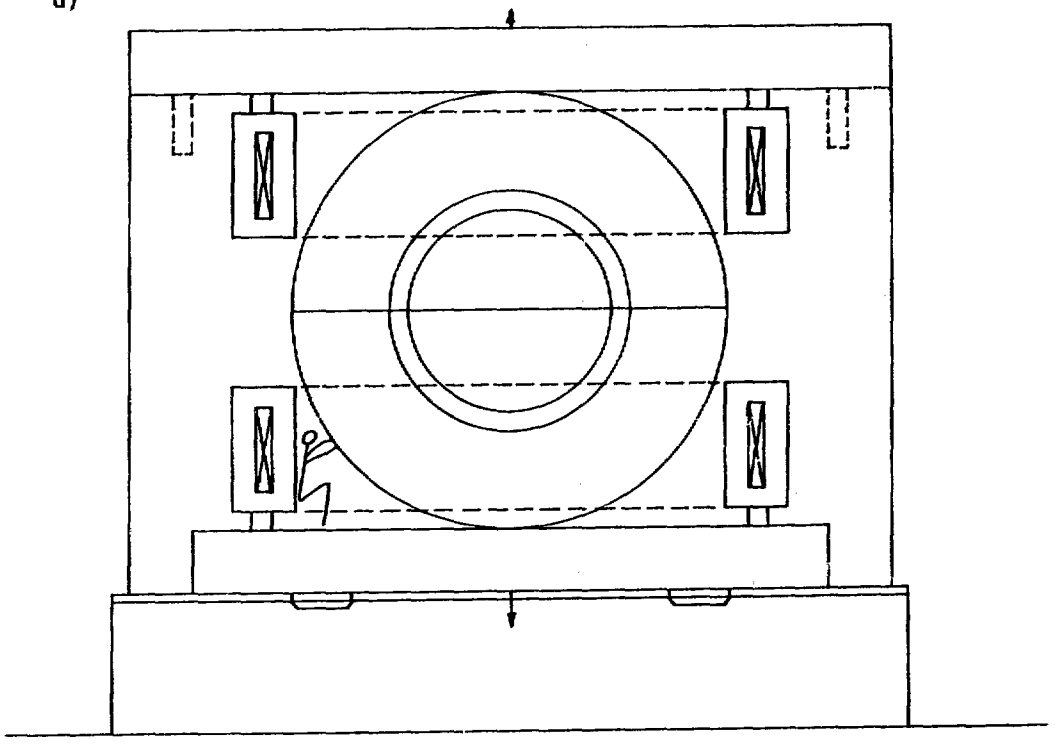

Fig. 13a

b) STATION I

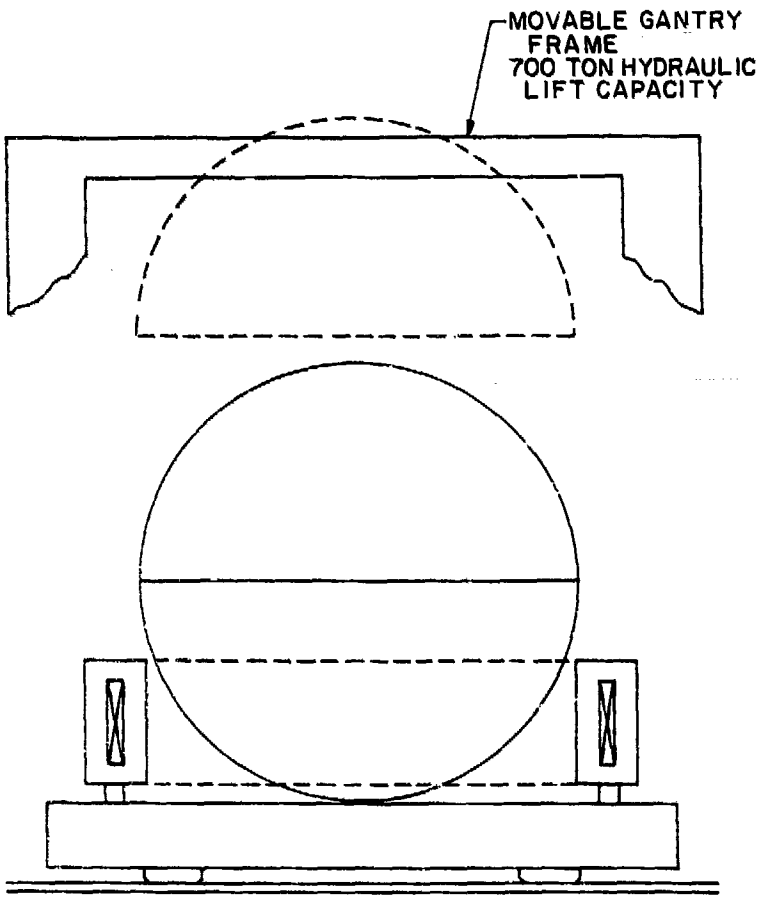

Fig. 13b

c) STATION 2

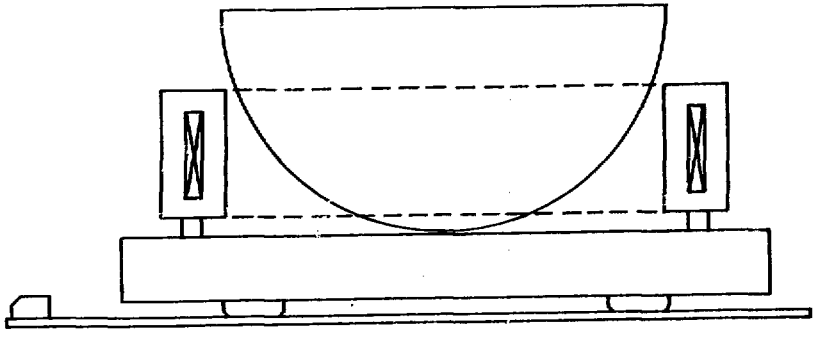

Fig. 13c

SOME THOUGHTS ON A DIPOLE DETECTOR

Mark F. Bregman, Nevis Laboratories

The dipole magnet considered for a large ISABELLE experiment has the following configuration: the field volume consists of a cylinder with diameter 5m and length 5m. It is envisioned as being constructed of two superconducting Helmholtz coils with a iron return surrounding them. The field is oriented perpendicularly to the beam.

The major motivation behind choosing a dipole field came from studying Z^o decay. At ISABELLE most objects produced in $q\bar{q}$ reactions are not produced at rest so they tend to decay assymmetrically in the lab frame. For dileptonic events one typically sees one high energy lepton close to the beam pipe and one of lower energy at a larger angle to the beam (See Fig.1). The dipole field has a great advantage here as it can make a good measurement of both leptons. The dipole is unique in that it has equally good bending power for all values of θ (for a given ϕ).

Some more general reasons for considering a dipole are the large coverage in rapidity that it affords, its good acceptance, and the fact that the dipole may allow analysis of the beam jets. Understanding of the beam jets may be important in searching for the η_t^c and some other states that may appear at ISABELLE energies. One expects events at ISABELLE to be symmetric in azimuth so that the dipole's lack of resolution along the field direction (inside of two cones perpendicular to the beam) does not introduce a bias in the acceptance of the dipole.

The major difficulties associated with the dipole stem from its strong interaction with the machine lattice. Studies have been made and at present it appears that the field could be oriented either horizontally or vertically. The dipole will require more complicated compensation schemes than some other magnet configurations, however, this has been studied and there are a couple of possible schemes. Another problem with the dipole is that it would probably have to be turned off during filling of the rings. Studies indicate that about 1.5 hours would be required for charging the magnet to a field of 15kG. During the early days of operation it is likely that the storage times of the beams will be shorter than designed. Short storage

times coupled with the charging time of this magnet might seriously reduce the amount of data taking for an experiment using a dipole. One further problem that must be faced by experiments using a dipole is that although the dipole can analyze small angle tracks one may have great difficulties in looking in this region due to the rates involved especially at the higher luminosities.

Finally in considering the dipole field configuration one must weigh the advantages of large acceptance, good resolution for small angle tracks, and the open geometry against the disadvantages associated with the dipole' interaction with the lattice.

Table 1

Acceptance of a dipole and a solenoid for $Z^o \to \ell^+\ell^-$. θ is the minimum angle that a ℓ^+ or ℓ^- makes with the field direction. (In the case of a dipole there is an additional cut of $\pm 5^o$ to the beam pipe).

Dipole		Solenoid	
θ	Acceptance	θ	Acceptance
15^o	92.4%	15^o	74.6%
30^o	81.7%	30^o	42.0%
45^o	65.3%	45^o	20.9%
60^o	44.1%	60^o	8.3%

Note: The cut on θ has the effect of requiring that the leptons be more and more nearly in the bending plane as θ is increased.

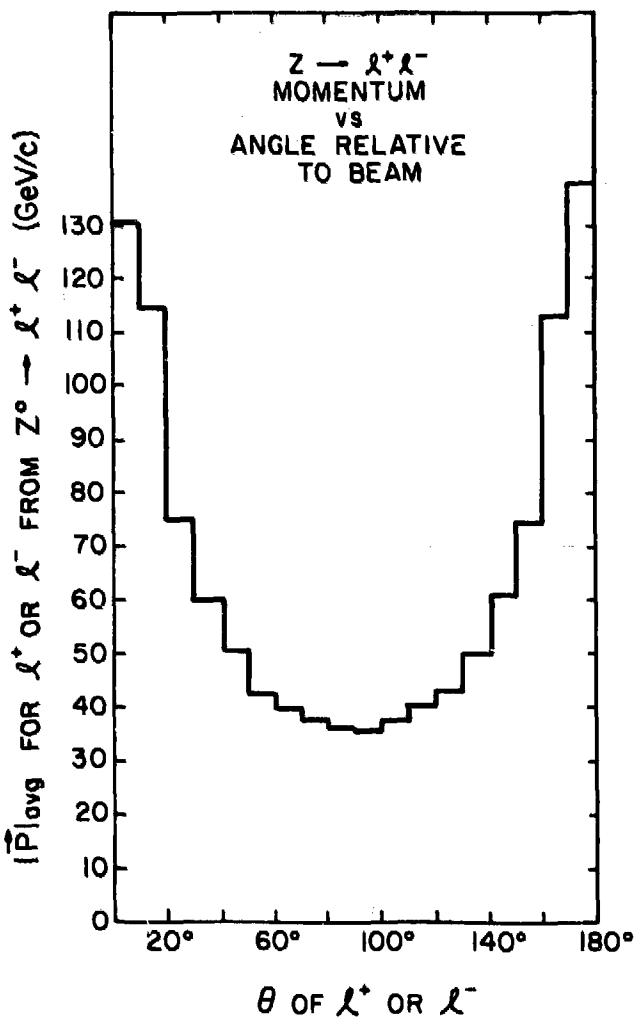
Z → ℓ⁺ℓ⁻
MOMENTUM
VS
ANGLE RELATIVE
TO BEAM
|P|avg FOR ℓ⁺ OR ℓ⁻ FROM Z° → ℓ⁺ ℓ⁻ (GeV/c)
130
120
110
100
90
80
70
60
50
40
30
20
10
0
20°
60°
100°
140°
180°
θ OF ℓ⁺ OR ℓ⁻

Figure 1

EVOLUTION OF THE MAGNET DESIGN FOR LAPDOG

L. Ahrens, BNL
S. Aronson, BNL
H. Foelsche, BNL
B. Gibbard, BNL
P. Wanderer, BNL
H. Weisberg, BNL
P. Yamin, BNL
D. Cutts, Brown U.
R. Lanou, Brown U.
R. Engelmann, SUNY Stony Brook
P. Grannis, SUNY Stony Brook
J. Kirz, SUNY Stony Brook
M. Marx, SUNY Stony Brook
R. McCarthy, SUNY Stony Brook

In designing an experiment focussing upon high resolution studies for electrons and photons, we have considered several possible configurations of magnetic field. This history, and some indication for the basis of choices made are given here. It must be realized that several specific constraints were imposed on this study. We wanted to optimize the energy resolution for electromagnetic detection and the magnet should dominate neither the effort nor cost. We did not foresee that we could afford full 4π solid angle coverage in EM detector and therefore the magnet need not cover all solid angle either. We expected to put the EM calorimeter outside the field in the large angle domain; thus we did not want thick material in the magnet coil (or return within active aperture).

We have considered both axial and dipole/toroidal field orientations, although we have never looked at the case of a dipole field on the circulating beams. We summarize below the advantages and disadvantages of both.

a) Axial field

Several versions have been examined: the original design had two window-frame magnets next to the collision point, or alternatively a single window frame magnet with a hole in the pole (see Figure 1 and Aronson et al., Isabelle Summer Study (1978), p 278). The chief advantage of the axial field is that the bend plane is perpendicular to the circulating beams, giving a very small source size and enabling one to make fairly precise momentum measurements with chambers outside the field only. The chief disadvantage of this version on the axial field is the very limited open (i.e., mass-free) solid angle, expecially in θ (or y).

Two other axial field configurations which were looked at were a

long, continuous thin solenoid (see Figure 2) and an open solenoid (or Helmholtz coil) magnet (see Figure 3). The drawbacks associated with the continuous solenoid were its relatively small bending power and the lack of any open solid angle. The coil was estimated to be $\tilde{\sim}$ 0.5 radiation lengths thick (and much thicker for forward-going particles). In the case of the open solenoid, massive conductors and very high stored energy were required to provide reasonable bending power in the open region at $\theta = 90^{o}$. The Helmholtz coil version was considerably more efficient but still had large coils (and coil shadows) and very limited θ coverage. The chief advantage of the solenoid-like axial fields is the "complete" 2π azimuthal coverage at $\theta = 90^{o}$. The solenoid-type magnets all have circular (i.e., easy to make) coils, although they all operate in the vertical position. Finally, since these magnets do not require momentum-measuring chambers near the collision point, they all afford some measure of containment of low-p_T charged particles, thereby reducing the rate-associated problems. (Even for the strongest solenoids considered, this rate reduction is probably not more than a factor of 3.)

b) Toroid/Dipole field

Two different toroid/dipole field configurations have been considered. First a 4-fold symmetric toroid, half iron and half air gap was considered. Later this was reduced to two-fold symmetry, for reasons of distributing a finite area of detectors more widely in θ. Figure 4 shows a cross-section of this version and Figure 5 compares the (θ,ϕ) coverage of this magnet with the Helmholtz magnet discussed above. The two are virtually identical in solid angle, with the toroidal geometry giving less $\Delta\phi$ but more $\Delta\theta$ than the solenoid.

For this type of magnet, the bend plane contains the long dimension of the interaction diamond, necessitating chambers near the beam pipe. Once this bullet is bitten, better momentum resolution can probably be obtained than in the axial field/external chambers case without pushing the state of the art in chamber resolution. While inner chambers could be employed in the axial field case to improve the momentum resolution, this involves tracking in the full-strength field. The inner and outer tracking regions contain about 8% and 19% of the total field integral respectively. The total field integral

out to r = 280 cm is 17.8 kG-m. An attractive feature of the toroidal field orientation is that the the "end" view (that view corresponding to Figure 4) the tracks are very nearly straight (or at least have very little net bending) through the field, facilitating tracking in this view (and perhaps triggering as well).

Figure 6 shows the same magnet in the beam plane. At approximately 5m overall length the θ-range $25^{\circ} < \theta < 165^{\circ}$ ($-1.5 < y < 1.5$) is covered with reasonable bending power. An interesting option to include in the installation is the possibility to move the magnet along the beams. Placing the magnet center 2m downstream of the crossing point, for example, gives θ coverage in the range $12.5^{\circ} < \theta < 102.5^{\circ}$ ($-0.2 < y < 2.2$).

Figure 7 shows some of the relevant parameters of the split dipole toroid magnet at 3 different values of central field = 10, 12, and 15 kG. Using the required current and iron for the 12 kG version we have estimated the cost very roughly, based on an estimate (by Ralph Shutt) of some possible general purpose dipoles for ISABELLE experiments (done in 1977). The required super conductor and iron for the magnet of Figures 4 and 6 are both scaled up from the Shutt design by an average factor 1.35. We have thus scaled all hardware by 1.35 and kept the same design/fabrication labor costs. The result for our case is \$1150K (including contingency) in 1977 dollars. Extrapolating to 1982 dollars (the earliest FY in which funds may be allocated) we used an inflation factor = 1.08 x 1.10 x 1.12 x 1.15 x 1.18 = 1.81, or a cost of \$2070K (FY 82). For discussion purposes it is proposed that we use \$2.5m for the total cost of the magnet, including transporter.

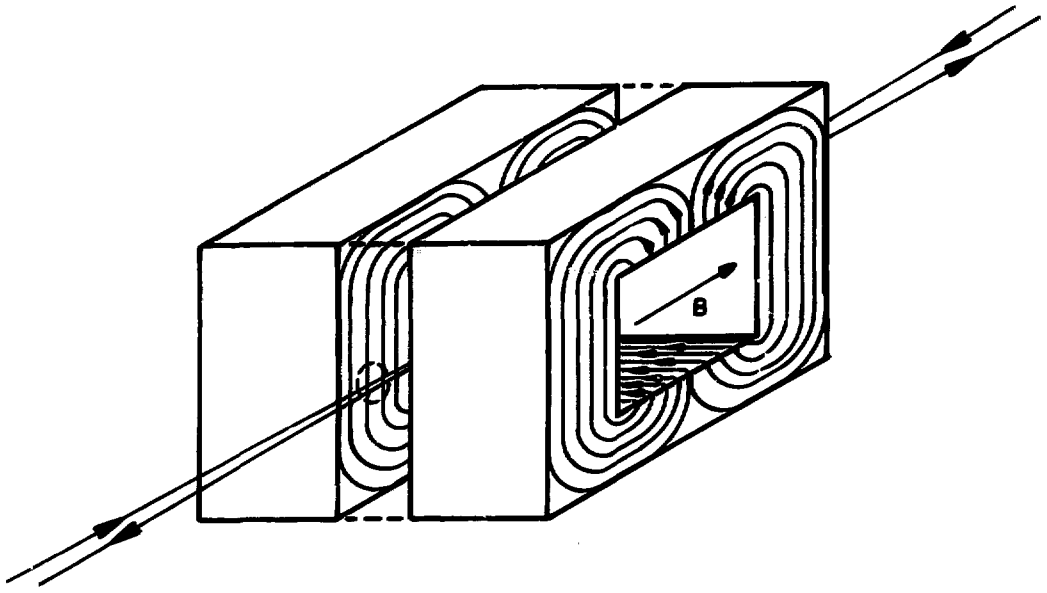

AXIAL DIPOLE

Fig. 1

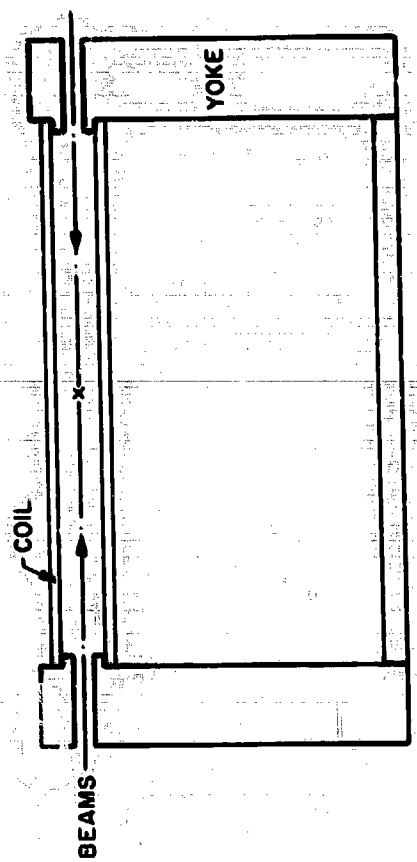

LONG THIN SOLENOID

Fig. 2

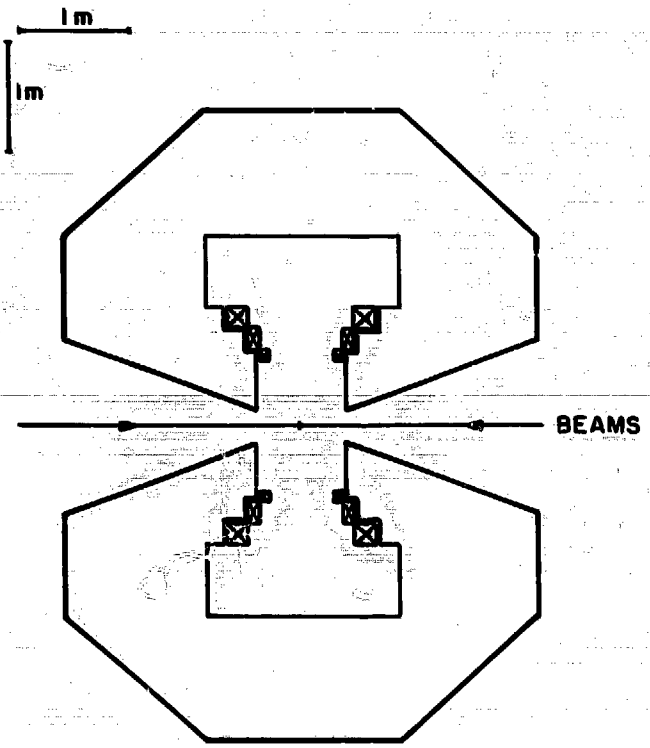

OPEN SOLENOID AXIAL FIELD MAGNET

Fig. 3

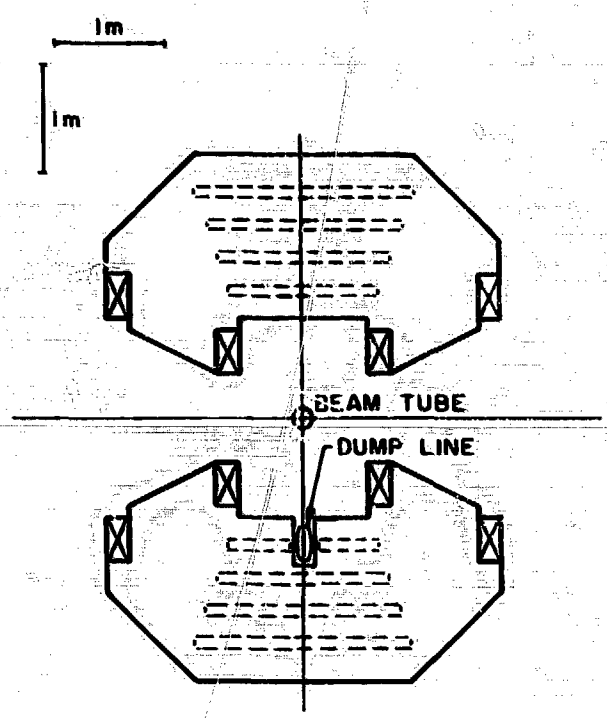

CROSS SECTION OF SPLIT TOROID/DIPOLE

Fig. 4

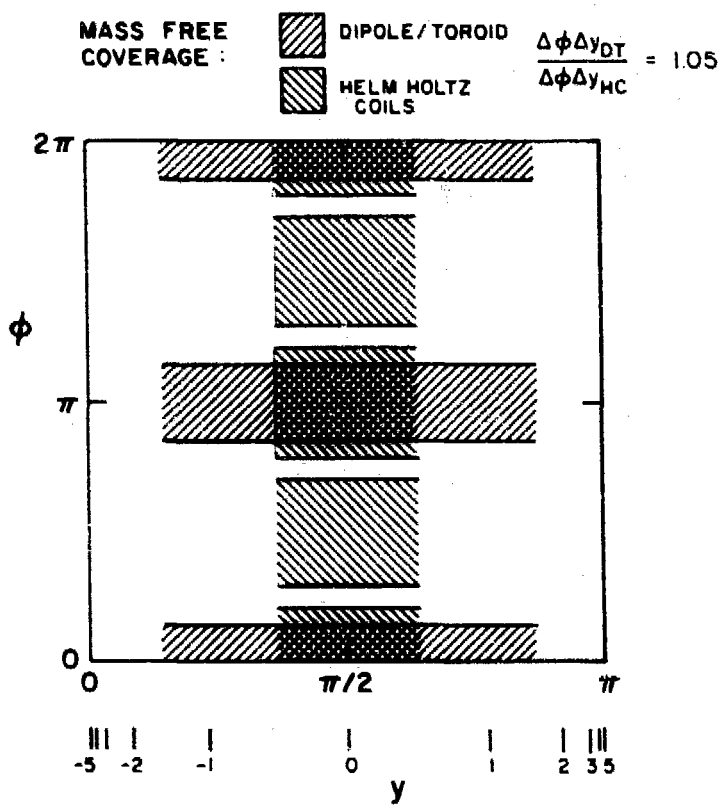
MASS FREE COVERAGE :
DIPOLE/TOROID
HELM HOLTZ COILS
$\frac{\Delta\phi\Delta y_{DT}}{\Delta\phi\Delta y_{HC}} = 1.05$
2π
φ
π
0
0
π/2
π
-5
-2
-1
0
1
2
3
5
y

Fig. 5

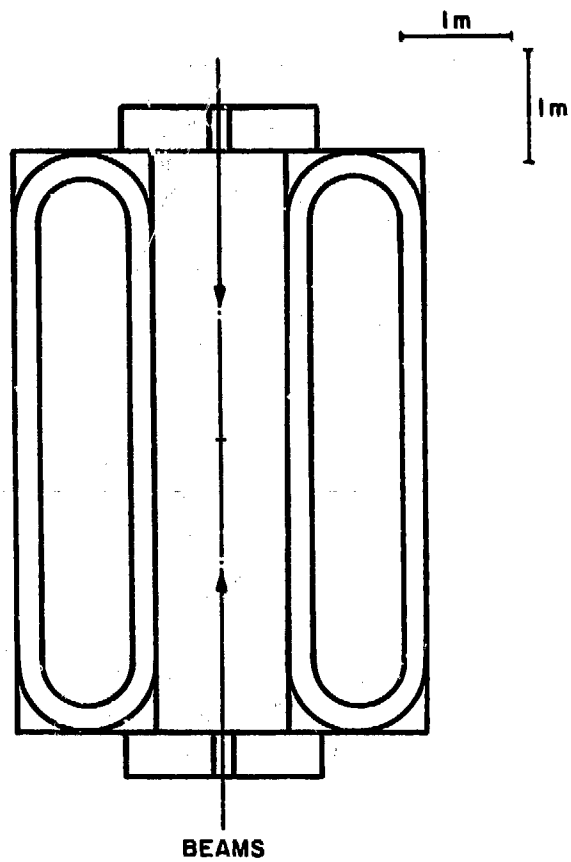

PLAN VIEW SPLIT DIPOLE/TOROID

Fig. 6

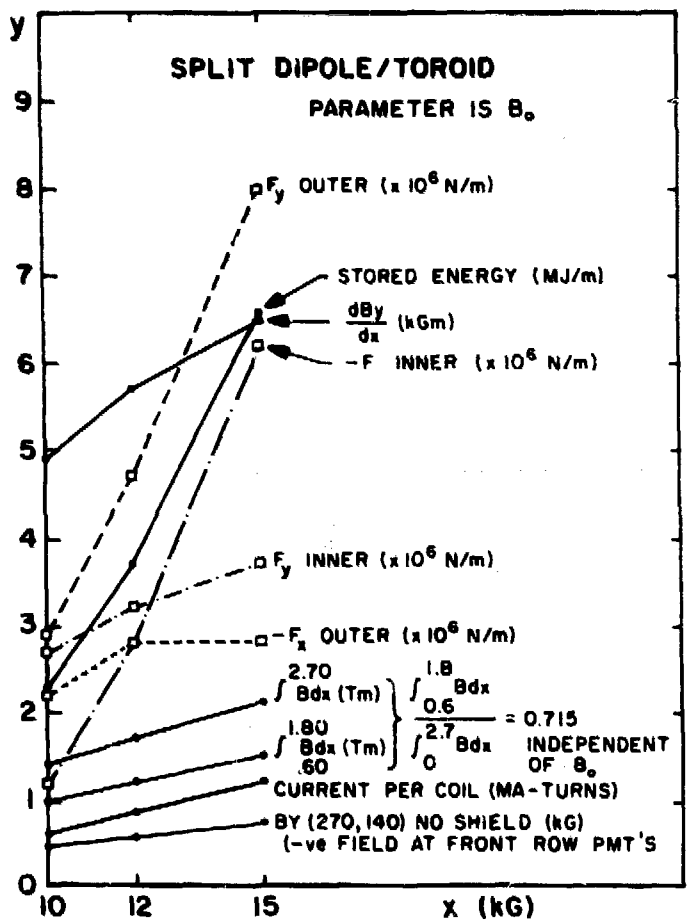
SPLIT DIPOLE/TOROID
PARAMETER IS B_o
F_y OUTER ($\times 10^6$ N/m)
STORED ENERGY (MJ/m)
$\frac{dBy}{dx}$ (kGm)
$-F$ INNER ($\times 10^6$ N/m)
F_y INNER ($\times 10^6$ N/m)
$-F_x$ OUTER ($\times 10^6$ N/m)
$\int_{.60}^{2.70} Bdx$ (Tm)
$\int_{.60}^{1.80} Bdx$ (Tm)
$\frac{\int_{0.6}^{1.8} Bdx}{\int_{0}^{2.7} Bdx} = 0.715$ INDEPENDENT OF B_o
CURRENT PER COIL (MA-TURNS)
BY (270, 140) NO SHIELD (kG)
(-ve FIELD AT FRONT ROW PMT'S
y
x (kG)
0
1
2
3
4
5
6
7
8
9
10
12
15

Fig. 7

THE USE OF CONVENTIONAL MAGNETS FOR 100 GEV PHYSICS

David Luckey and Samuel C. C. Ting

Laboratory for Nuclear Science
Massachusetts Institute of Technology
Cambridge, Massachusetts 02139

Some physicists[1] expect the energy range of 100 GeV, soon to be opened up by new accelerators, to be dominated by vector bosons associated with the weak interaction. Among these the Z_o is expected to have a mass near 90 GeV and a narrow width ($\Gamma \equiv 3$ GeV). If so, then new detectors will be hard pressed to achieve resolutions capable of resolving this width. Resolution will be important for low multiplicity decays like

$$Z_o \rightarrow e^+ + e^-$$

$$Z_o \rightarrow \mu^+ + \mu^-$$

$$Z_o \rightarrow \mu^+ + \mu^- + \text{Higgs}$$

where the particles could have momenta up to 45 GeV/c. The existence of a natural unit of resolution is an important change from recent physics where the multiplicity is high, and hence most momenta low.

We wish to discuss some aspects of obtaining such resolutions. We begin by obtaining an estimate of the resolution required. Suppose, by a clever combination of intrinsic mechanical accuracy, surveying with lasers, alignment with X-rays, and multiple measurements, etc., we could achieve an accuracy of 150 microns in measuring the sagitta of a circle. Then a 1% measure would require a sagitta of 15 mm and a BL^2 of 18 Tesla - m^2 for a 45 GeV/c particle. To set the scale, note

that the Big European Bubble Chamber (BEBC) has a BL^2 of 12T - m^2 (B = 3.5T and maximum L could be 1.85 m)[2]. In a practical detector the BL^2 would be reduced to about 8T - m^2 because of the beam pipe and supports for chambers. Similar or smaller numbers result from other large bubble chamber magnets. To reach the BL^2 of 18T - m^2 requires a radius of approximately 3.5 meters for a B of 1.5T.

A practical detector will have material; before proceeding we calculate how much material will cause a 150 micron Δs due to multiple scattering. Using the formula for a continuous medium

$$\Delta s = \frac{1}{4\sqrt{3}} L \cdot \frac{(.014)}{P(GeV/c)} \sqrt{t}$$

where t is the amount of material in radiation lengths, we find L < 10 meter if $\sqrt{t}$ = .3 for a 45 GeV/c particle. With the above BL^2 a useful field would have to be greater than 0.2 Tesla.

The optimization of a detector includes many non-analytic and perhaps non-rational choices and judgments. The instrumentation of the outer surface of a large volume is proportional to L^2. We note that many developments for large detectors have gone on in the past for cosmic ray experiments and recently that much activity and invention for large detectors is occurring in neutrino experiments and in proton-lifetime experiments[3]. We will assume such

techniques can be adapted and address ourselves mainly to the problem of obtaining a field over a large volume. We note that if the proton is found to decay, second or third generation experiments may need a magnetic field to study the various decay modes and that magnets such as we describe here will be useful.

The "difficulty" of making a magnet is related to the stored energy

$$E \sim B^2V \equiv B^2L^3$$

or the difficulty $\sim \frac{R^2}{L}$ where R is the resolution = BL^2. This would suggest that a large volume would be the best choice. There are, however, other limits. For example, a large superconducting magnet represents difficult transport problems and would be difficult to assemble <u>in situ</u>; refrigeration costs go as L^2; superconducting magnets with BL^2 like 18T-m^2 could cost 16M$ or more. Thus we would like to address the problem of conventional magnets assembled <u>in situ</u> which are as large as experimental halls, and which perhaps themselves comprise the experimental hall and the shielding.

In order to get some magnitudes, let us consider a cubic magnet with iron return yoke as shown in Figure 1. We take the side to be of length 2a. We assume a coil thickness T_o, assumed small compared to a. We will find that to utilize conductor we will have to make this assumption true in a real detector.

From Gauss's law, neglecting the field in the iron return,

$$\int B \cdot d\ell = 2Ba = 4\pi NI \times 10^{-7}\ T - m^2$$

where NI = number of ampere turns. If ρ is the resistivity of the coil, then the power $P = = 4(NI)^2 \rho/T_o$ and the coil volume $V = 16a^2T_o$. Combining, we find $R = Ba^2 = k\left(\frac{PV}{\rho}\right)^{1/2}$ where k is a constant ($.785 \times 10^{-7}$ in metric units). Let a = 3 meters and use aluminum .1m thick. Then the volume of the coil is 15 m^3, the mass 40 metric tons, and if we use 2 megawatts, we calculate B = .27 Tesla and $Ba^2 = 2.4\ T - m^2$. The iron return yoke at 1.7 T would weigh approximately 400 metric tons.

This conclusion is generally true and

$$R = Ba^2 = H(\text{shape})\left(\frac{P\lambda V}{\rho}\right)^{1/2}$$

where λ is the packing factor (the fraction of volume occupied by conductor) and H is a function of the shape. One can read about these shape functions in Montgomery[4] for coils without iron.

Since power is expensive, we keep it constant at 2 megawatts, and try more conductor. A proper calculation would minimize the overall cost by asking how long the magnet is run, etc., all worked at long ago by Lord Kelvin. We will, however, assume 660 tons of aluminum available and a volume (like that of the

proposed LEP halls) of 20 x 10 x 10 meters. We make the field in the difficult direction (20 m). Then we can obtain a field of .2 T with an aluminum coil of .3 m thickness and BL^2 of 5 T - m^2. The iron return yoke would weigh 2500 tons (for comparison, the iron shield on BEBC weighs 1600 tons). If we shorten the field to 10 meters we can double the resolution to the 10 T - m^2 region. We would require more iron since it is at a larger radial distance and because there is flux in the coil which must also be returned. A larger BL^2 would require a larger L to be efficient in conductor and iron.

Figures 2, 3, and 4 show some options on winding an aluminum coil. The current densities we are using are low, so that we need not necessarily use hollow tubing with the water in direct contact with the conductor.

Figure 2 shows a cross-section of a coil wound from standard aluminum cable. Here one could either spray water on the outside of the cable, or put cables in a common water or mud bath with some separate pipes carrying water to a heat exchanger. For a discussion of such heat exchange in great detail, see reference 5. The cable supporting structure must be able to cope with the forces of interaction with the magnet field, and the cables must be carefully located initially. Here one might use steel reinforced aluminum conductor, as is common for transmission

lines. For a recent discussion of various overhead cables see Ash et al.[6] For assembly in an inaccessible area this might be the preferred method.

Figure 3 shows a tape-wound coil. This geometry could be varied to put scintillators and wave bar shifters into the coil, thereby making it a shower counter. Aluminum tape coil can be obtained anodized and hence already insulated with a tough layer of aluminum oxide.

Figure 4 shows an easily constructed helix made from aluminum bar welded together at the corners as it is assembled. A water cooling pipe could be welded (or extruded) onto the outer and/or inner edges of the coil. This would most likely be the cheapest method of construction. Such bars might also be bolted, if the surfaces were prepared and protected during assembly. Reference 7 gives resistance per mm^2 for various surface preparations and applied loads, and shows that it would be possible to use such a bolted assembly.

Figure 5 shows a highly schematic view of a long magnet with possible drift chambers. The inserted iron pieces along the beam cause the field to bend in a manner that gives more resolving power at small angles (a magnetic bottle).

Figures 6a and 6b point out some possibilities other than solid iron for the return yoke. Rectangular steel tubing which could hold liquid scintillator or be

made into a drift chamber can be used. Much of the return yoke could be made out of the steel reinforcing rod used in all concrete buildings. One would simply use more steel rod and less cement. Handling such rod could be easier than working with large steel blocks in inaccessible places. Clearly, there are many choices more economical than the beautifully machined large pieces of ' on we are used to in experimental magnets.

If one is interested in building the cheapest conventional magnet, then one should consider sodium as an alternative to aluminum conductor. We would like to address some of the problems and advantages of using sodium metal.

Sodium has a resistivity ρ = 5.3 $\mu\Omega$-cm at 50°C; 4.3 $\mu\Omega$ cm at 0°C and 6.2 $\mu\Omega$-cm at 96°C, just below its melting point of 97.8°C. It has a density of 0.97, which makes its radiation length 282 mm. Like aluminum, it is produced by electrolysis, so its price relative to aluminum will remain the same. For the same number of ampere-turns, sodium is a factor of 2.6 cheaper. Special railroad cars equipped with external pipes for circulating heated oil (so that the molten sodium can be drawn out by vacuum) can be obtained in 80,000 lb net lots. Prices for raw material in June, 1981, were 57¢/lb for Na and 78¢/lb for Al.

Figure 7 shows a coil form of plastic or insulated aluminum which could be filled in situ by pumping molten sodium into the form. Inside the form would be a separate pipe for circulation of cooling fluid such as oil. Writes Peter Graneau[8], "On the basis of service record and economic merit of sodium metal (a factor of 2.6), sooner or later these (sodium) cables are likely to become a major factor in the underground transmission of electrical energy." This book describes existing sodium power cables and many of the tests made on them with respect to water and fires. For an earlier work see reference 9.

There are serious safety problems because of the reactivity of sodium with water and the halogens, but they are small compared to the hazards of using liquid NaK in both fusion and fission reactors. Much is known about the behavior of Na fires[10] and it may be possible to construct a hollow aluminum bar that could be bolted together and filled with Na which would be acceptably safe.

Finally, we would like to make some comments about air coil magnets of large size. The use of iron gives a saving in ampere-turns of a factor of about 1.5. If the increasing amount of iron is the problem, let us just make a massive coil, 2700 ton (metric) of aluminum or 1000 m^3. Using the tables of reference 4 we calculate the central field for a uniform current density solenoid of inside radius

5 meters, a length of 12 meters with 2 megawatts, to .5T for a BL^2 of 12.5T - m^2. Figures 8a and 8b show that we really should build a larger magnet to use the conductor efficiently.

An air coil is attractive in that the field can always be raised by adding more power. It has many problems; the most important is the stray field which would make operation of electron beam devices like photomultipliers and klystrons difficult or impossible. A homogeneous field can be obtained by suitable arrangement of the coils, and we give a long list of the possibilities studied by many experimental physicists[11].

We conclude that the problem of choosing between superconducting and conventional magnets will be answered largely by examining other boundary conditions. If one considers that the magnet structure could be the experimental hall or that the magnet must be constructed in a remote location, then a conventional magnet system could be the most economical.

REFERENCES

(1) For a recent summary, see:

P.Q. Hung and C. Quigg. Science 210, 1205 (1980).

For discussion of the original ideas see:

S. L. Glashow, Science 210, 1319 (1980).

S. Weinberg, Science 210, 1212 (1980).

A. Salam, Science 210, 723 (1980).

(2) H. Brechna, Superconducting Magnet Systems, Springer-Verlag, 1973.

(3) Steven Weinberg, "The Decay of the Proton," Scientific American 294, 64 (June 81).

(4) D. Bruce Montgomery, Solenoid Magnet Design, Wiley Interscience: New York, 1969.

F. H. Bullier, AIEE T 71, 634 (1952).

(5) G. Luoni, A. S. Morello, and A. E. Crockett, IEE Proc., Vol. 128, Pt. 3, 129 (1981).

(6) D.O. Ash, P. Day, B. Garland, R.R. Gibbon, Proc IEE, Vol. 126, 333 (1979).

( ) R. L. Jackson, IEE Proc. 128, Pt. 3, 45 (1981).

(8) Pet r C reau, Underground Power Transmission, John Wiley & Sons, 1979.

(9) L.E. Humphry, R.C. Hess and G.I. Addis, IEE, PAS-86 (1967).

REFERENCES

(continued)

(10) O. J. Foust, Sodium-NaK Engineering Handbook, Vol. III, Gordon and Breach, New York: (1979). Article on safety by C. W. Griffin and A. R. Piccot and other contributing authors.

(11) J. Clerk Maxwell, Treatise on Electricity and Magnetism, Vol. II, Sec. 714, 715, Clarendon Press (1873).

L. W. McKeehan, RSI 7, 150 (1936).

J. W. Clark, RSI 9, 320 (1938).

S. M. Rubens, RSI 16, 243 (1945).

J. P. Blewett, J. A. P. 18, 968 (1947).

M. W. Garrett, J. A. P. 22, 1091 (1951).

W. Franzen, RSI 33, 933 (1962).

J. E. Everett and J. E. Osemeikhian, J. Sci. Instrum. 43, 470, (1966).

S. T. Loney, J. Inst. Math. Applics. 2, 111 (1966).

L. Cesnak and D. Kabot, J. Phys. E 5, 944 (1972).

T. Kasuya, S. Ouchi, A. Minoh, Jap. J. App. Phys. 12, 1572 (1973).

K. Adamiak, Scientia Electrica 22, 128 (1976), 23, 48 (1977).

REFERENCES

(continued)

(11) D. Kabot, L. Cesnak, and J. Kokanel, J. Phys. E 12, 652 (1979).

J. S. Blicharski, J. Mag Resonance 43, 449 (1981).

L. S. J. M. Henkens, M. W. van Tol, H.J. L. vander Valt, and N. J. Poulis, Journal Phys. E. 10, 719 (1977).

FIGURE CAPTIONS

Fig. 1 A cubic magnet with side 2a. The coil thickness T_o is assumed small compared to a.

Fig. 2 A possible (low packing factor) conventional cable construction.

Fig. 3 Tape-wound aluminum coil construction. The winding could be spaced so that detectors could be inside the coil.

Fig. 4 Coil construction from aluminum bar, either welded or bolted.

Fig. 5 A possible low field detector. The iron poles at small angles cause the field to bend so that there is more resolving power at small angles.

Fig. 6a, b Some possible alternatives to large iron pieces in the return yoke.

Fig. 7 A casting form which could be filled with sodium metal. It is shown "exploded" so the winding can be visualized. In practice, it could be made of heavy-wall plastic pipe.

Fig. 8 a) Resolution vs. radius for air core magnets with various amounts of aluminum. The length of the coil is taken to 2.4 times the radius. Resolution is computed as central field times inside radius^2.

b) Same for sodium conductor.

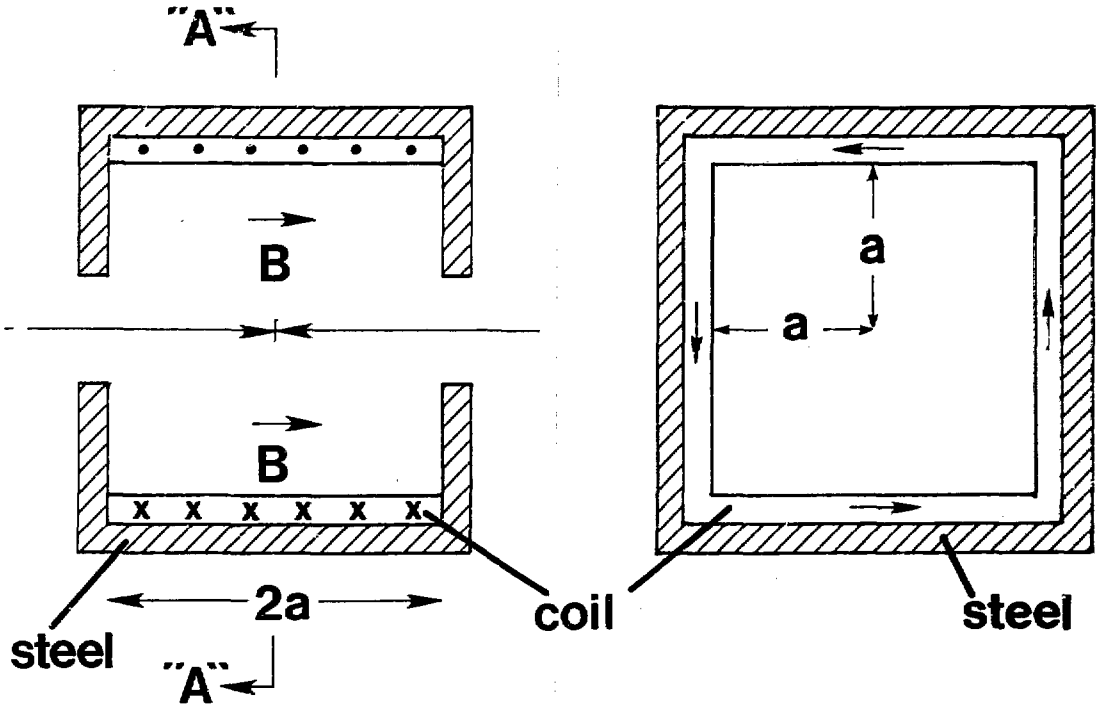
"A"
B
B
x x x x x x
2a
steel
"A"
Side View
coil
a
a
steel
Cross Section
"A-A"

Fig. 1

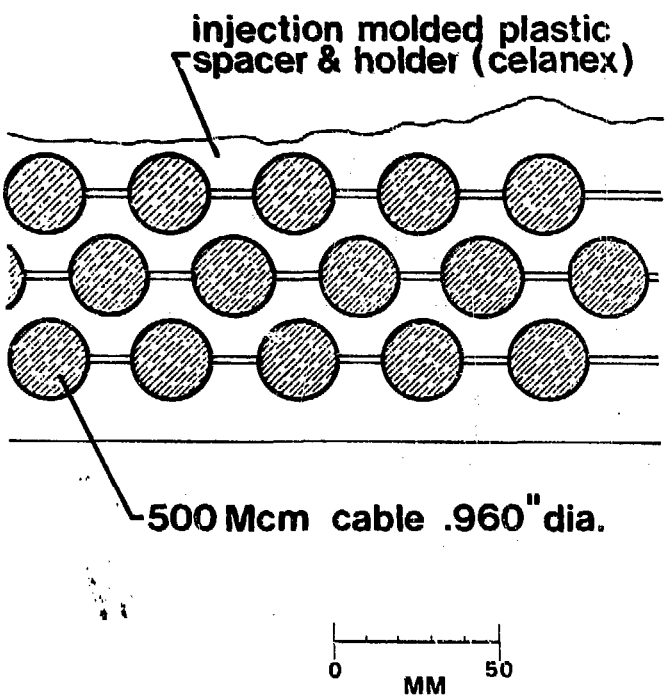
injection molded plastic
spacer & holder (celanex)
500 Mcm cable .960" dia.
0
50
MM

FIG. 2

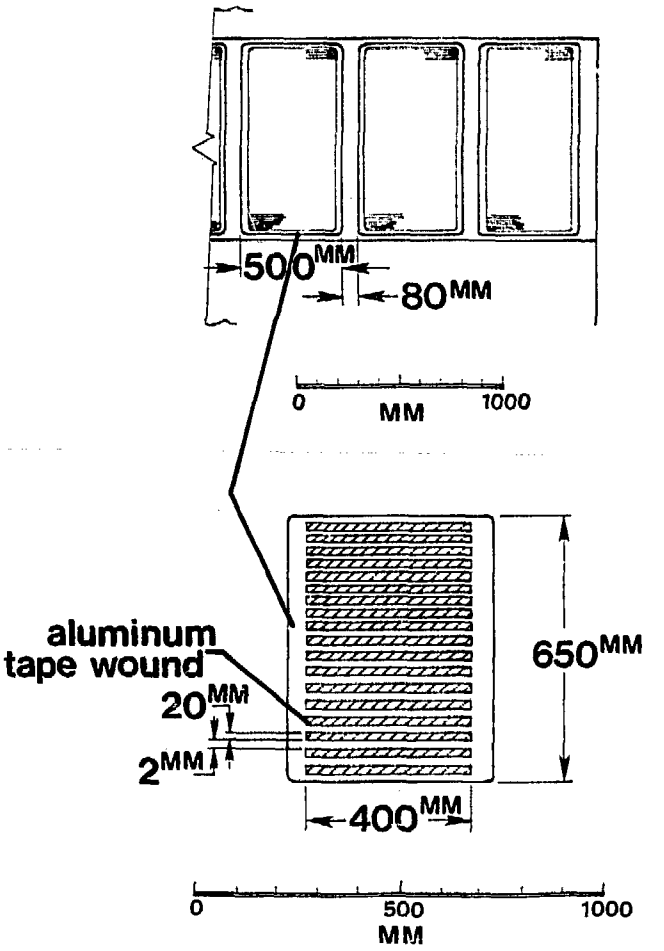
500MM
80MM
0
MM
1000
aluminum
tape wound
20MM
2MM
650MM
400MM
0
500
1000
MM

FIG. 3

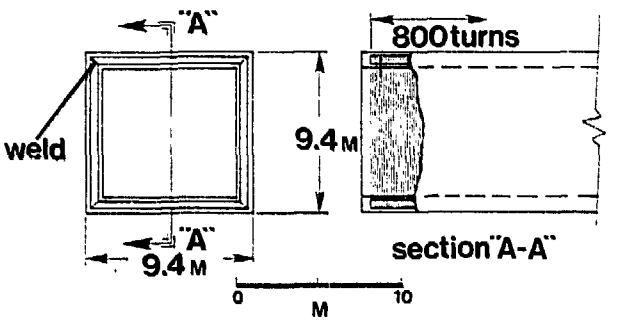
"A"
800 turns
weld
9.4 M
"A"
9.4 M
section "A-A"
0
M
10

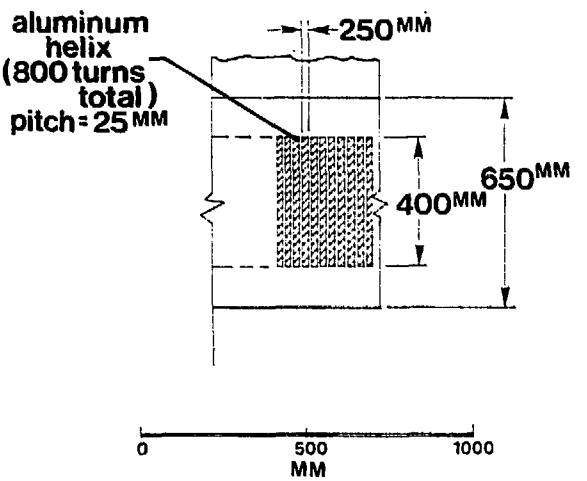
aluminum
helix
(800 turns
total)
pitch = 25 MM
250 MM
650 MM
400 MM
0
500
MM
1000

FIG. 4

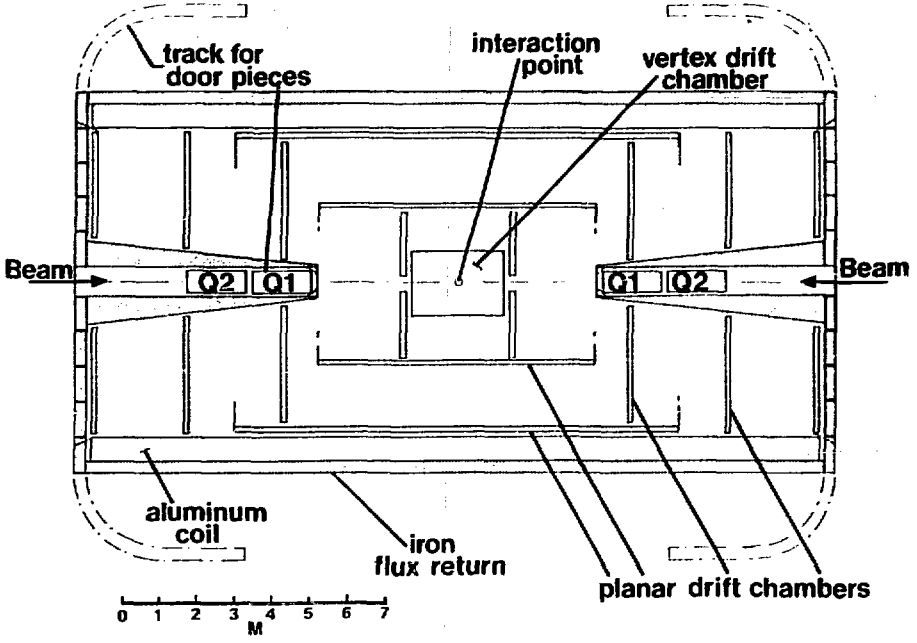
track for
door pieces
interaction
point
vertex drift
chamber
Beam
Q2
Q1
Q1
Q2
Beam
aluminum
coil
iron
flux return
planar drift chambers
0 1 2 3 4 5 6 7
M

FIG. 5

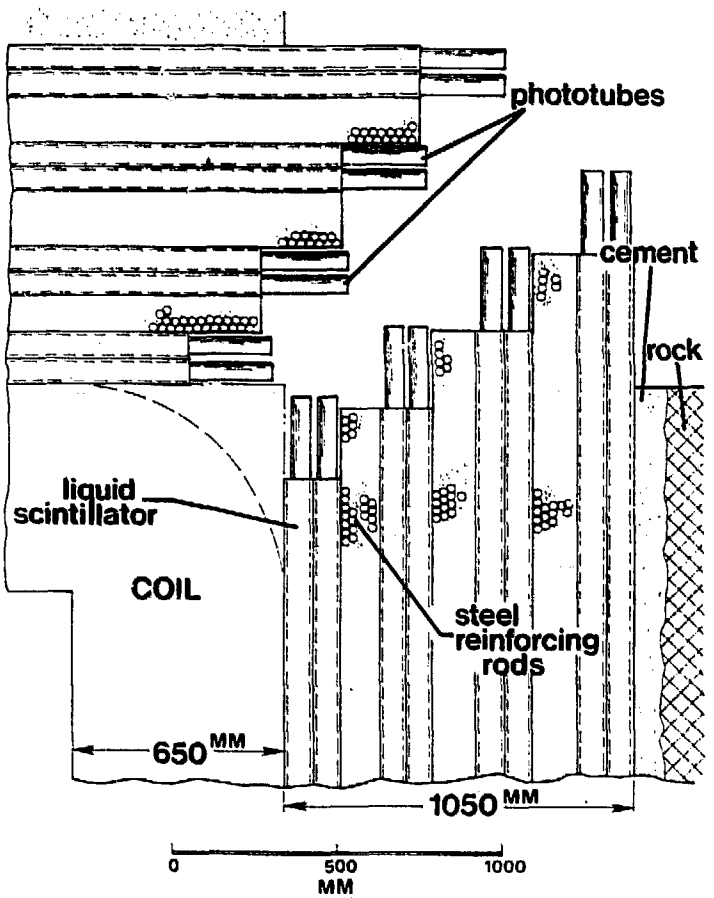
phototubes
cement
rock
liquid
scintillator
COIL
steel
reinforcing
rods
650 MM
1050 MM
0
500
1000
MM

FIG. 6A

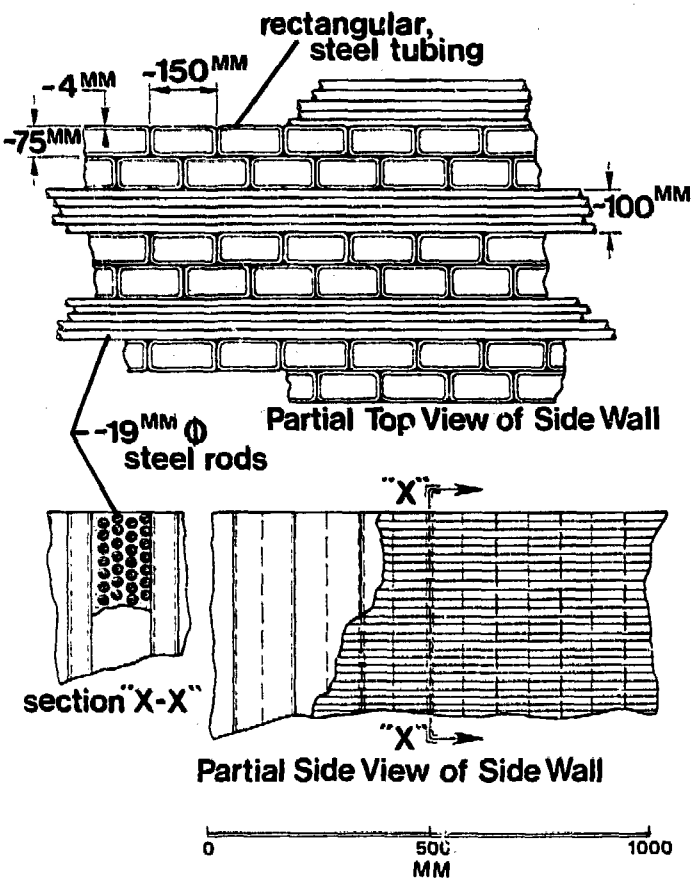
rectangular, steel tubing
~4 MM
~150 MM
~75 MM
~100 MM
~19 MM ϕ steel rods
Partial Top View of Side Wall
"X"
section "X-X"
"X"
Partial Side View of Side Wall
0
500 MM
1000

Fig. 6B

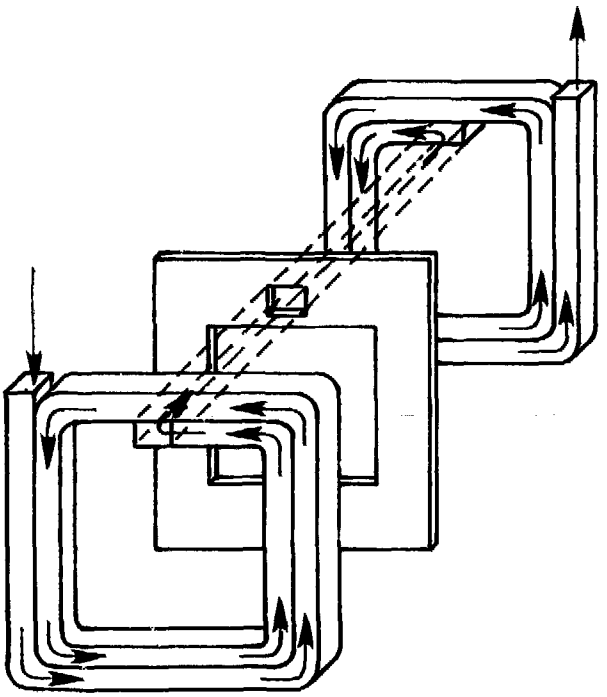

FIG. 7

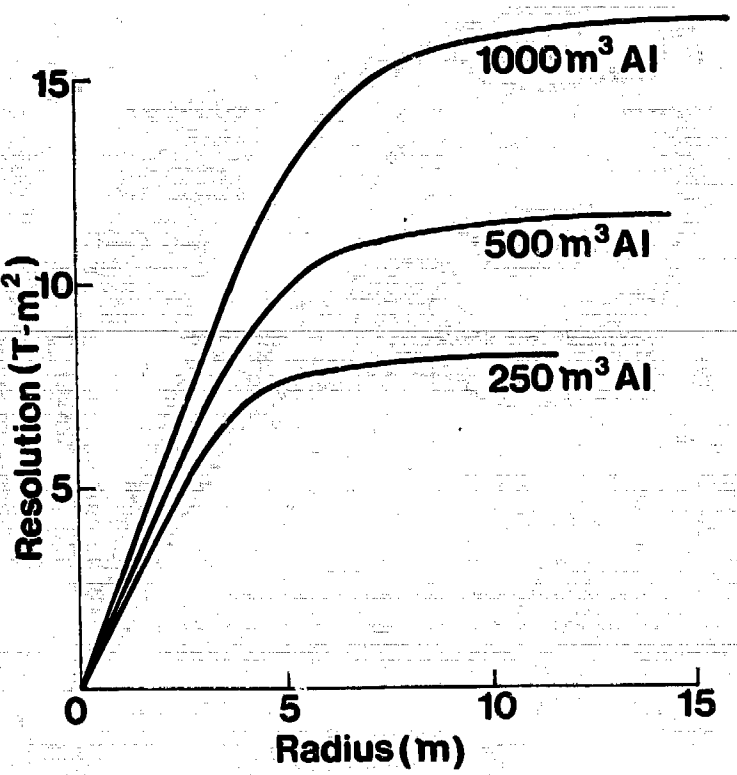
1000 m³ Al
500 m³ Al
250 m³ Al
15
10
5
0
Resolution (T-m²)
5
10
15
Radius (m)

FIG. 8A

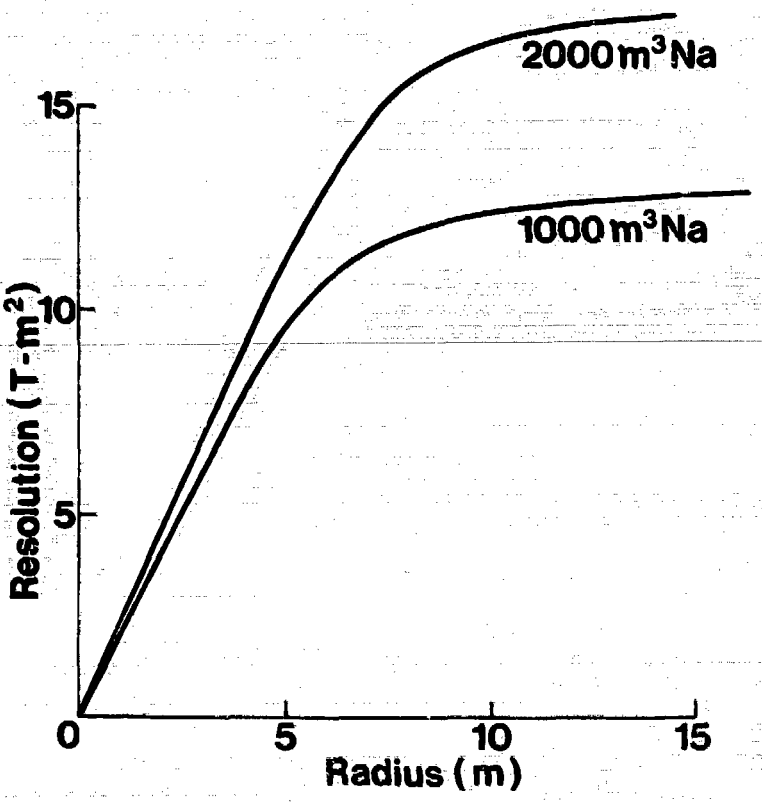

FIG. 8B

A GENERAL PURPOSE TOROIDAL DETECTOR

Bernard G. Pope
Princeton University

Peter Bonanos, Philip Heitzenroeder, Peter Materna
Princeton Plasma Physics Laboratory

In connection with a proposed search for muons and muon pairs at the ISABELLE storage rings, a preliminary design has been made for a superconducting toroidal magnet.* The purpose of a magnet at a colliding beam facility is to measure the momentum of charged particles by their bending in the magnetic field. As the momenta of particles produced in the next generation of colliding beams (proton-antiproton, electron-positron, electron-proton, as well as proton-proton) will be in the range 10-100 GeV/c, the highest magnetic fields are required. In addition, as the processes of greatest interest (for example, the production of the intermediate bosons, $W^{\pm}$ and Z^{0}) are expected to be extremely rare, detectors must have a large acceptance (centered at 90° to the colliding beams but extending down to angles of 30° to each beam). Thus the magnetic field must extend over a large volume.

Toroidal magnets when used at colliding beam facilities have the following advantages:

1. The magnetic field is always perpendicular to the flight path of the particles. This results in the field being used with maximum efficiency over the whole solid angle - no "dead" spots.
2. There is no magnetic field on the beams. Thus there is no wasted field and no perturbation of the beams.
3. There are no end-caps or iron return yokes. In addition to the saving in iron, (often a dominant factor in the cost and always a

*Proposal for a high sensitivity search for muons and muon paris using a toroidal magnet. B.G. Pope, Princeton University Publication COO-3072-97 (1979).

dominant factor in weight), this implies relatively easy access to the beam pipe and the possibility of combining large angle experiments with small angle detectors.

4. A toroid can be moved along the beams (so that the intersection region is no longer in the center of the magnet) so that studies can be made of production at smaller angles. The integrated B.dl will always be greater than for production at 90°. This advantage is also true for dipoles but not for solenoids.
5. The bending only changes the polar angle and leaves the original azimuthal pattern unmixed, allowing for a natural subdivision for the tracking chambers and easing pattern recognition problems.

In the original ISABELLE proposal that suggested the use of a toroidal magnet, muons were to have been studied by making use of a dense hadron absorber (~1 meter thickness of tungsten) surrounding the interaction region. The momenta of muons or muon pairs emerging from this absorber could then be measured with a system of drift-chambers operating inside the magnetic field. This results in a sensitive high-resolution apparatus capable of exploiting the highest energies and luminosities expected at ISABELLE.

The scope and flexibility of this apparatus can be increased by making the primary absorber into a calorimeter and adding a high precision drift chamber array around the interaction region to permit the angles and multiplicities of particles to be measured. The calorimeter would consist of alternating layers of tungsten and scintillation counters. In this way electrons, protons and hadrons could be distinguished and their energies measured. In addition, of course, muons would be identified by their ability to penetrate the calorimeter without interacting.

Clearly, muons, having passed through the dense calorimeter, would not be affected by passing through the coils of the magnet. However, if the magnet were constructed such that there was a reasonable probability of particles from the interaction region passing unobstructed between the coils, the apparatus would become a powerful hadron or electron detector. The ratio of unobstructed azimuth divided by total azimuth (2π) is referred to as the transparency of the coils. A reasonable transparency (say $\geq 60\%$) implies that the magnet could be used in a totally different mode, where the calorimeters

are removed and the momenta of hadrons and electrons could be measured with the magnetic spectrometer. In this case the clear central bore of the magnet could be equipped with Cerenkov counters for particle identification.

For the above reasons a toroidal magnet has been designed with a central warm bore of 1 meter radius, a bending power of 3.5 Tesla-meter, an outer radius of less than 5.5 meters (the beam height suggested for the major facility hall at ISABELLE), a transparency of greater than 60%, and a length such that a polar angular range of 30°-150° could be studied.

The principal features of the design are summarized in Table 1 and Figs. 1-3.

Table 1

Toroidal Superconducting Magnet

Principal Design Features

Bending Power	3.5 T-m
Minimum Useful Detection Angle	30°
Central Transparency	60%
Central Warm Bore Radius	1m
Toroidal Warm Volume	
Inner Radius	1.8m
Outer Radius	4.0m
Axial Length	9.3m
Outer Radius	4.9m
Overall Length	~15.0m
Total NI of Toroid	21.6 MAt
Number of Coils	8
Turns per coil	420
Turns per pancake	30
Number of pancakes	14
BR Product	4.32 T-m
Design Current	6430A
Total length of superconductor required	81 km
Superconductor Type	Filamentary NbTi
Stabilizer	Copper
Stabilization Limit	6730A
Critical Current @ 5T, 4.2°k	~18,000A
Peak Field at Superconductor	5T
Cooling Method	Pool Boiling
Coil Cavity Area: Conductors, Insulation and Cryogen	950 sq. cm./coil
ni	2.7 MAt/coil

Table 1 - continued

Gross Current Density in coil cavity	2840 A/sq. cm.
Electrical Insulation	Glass-Epoxy-Cryogenic Grade
Thermal Insulation	Aluminized Mylar and Paper
Insulated Surface Area	600 sq. meters
Thermal Transfer Rate: Total	720 W
Structural Supports: Heat Leak	150 W
Electrical Leads: (8) pairs	150 liters/hours
Suggested Refrigeration Capacity	1.5 kW
Suggested Liquefier Capacity	300 liters/hours
Weights:	
Coils	104 tons
Coil Cases	230 tons
Structures	260 tons
Total cold mass	594 tons
Dewar	106 tons
Total weight	700 tons
Maximum Crane Lift Required	45 tons
Structural Material	TP304 or TP316 LN Stainless Steel
Material Properties @4.2°K (TP 316 LN)	
Ultimate Tensile Stress	200 ksi
Yield Stress (0.2%)	125
Fracture Toughness	150 ksi $\sqrt{in.}$

Two important features of the design that are not shown in Table 1 are the construction schedule which indicates a lead time of about 5-1/2 years and the overall cost which is likely to be in excess of $20M.

This latter figure has suggested that we modify some of our grand aspirations and we have considered a more modest magnet with parameters as shown in Table 2. This magnet is illustrated in Figs. 4 and 5.

Table 2

r_{inner} = 1 m r_{outer} = 3 m
B_{inner} = 20 kG B_{outer} = 7 kG
$\int_{r_{inner}}^{r_{outer}} B.dr$ = 22 kG.m
NI = 10^7 Ampere turns
Stored energy = 65 MJ
Estimated momentum resolution $\Delta p/p$ = 0.05 p %
Transparency = unobstructed azimuth = 75%

FIGURE CAPTIONS

Fig. 1. Model of a 3.5 T-m superconducting toroidal magnet.

Fig. 2. Elevation view of toroid.

Fig. 3. Details of toroid.

Fig. 4. End view of a detector based on a 2.2 T-m superconducting toroidal magnet.

Fig. 5. Cross section of the detector.

Fig. 1

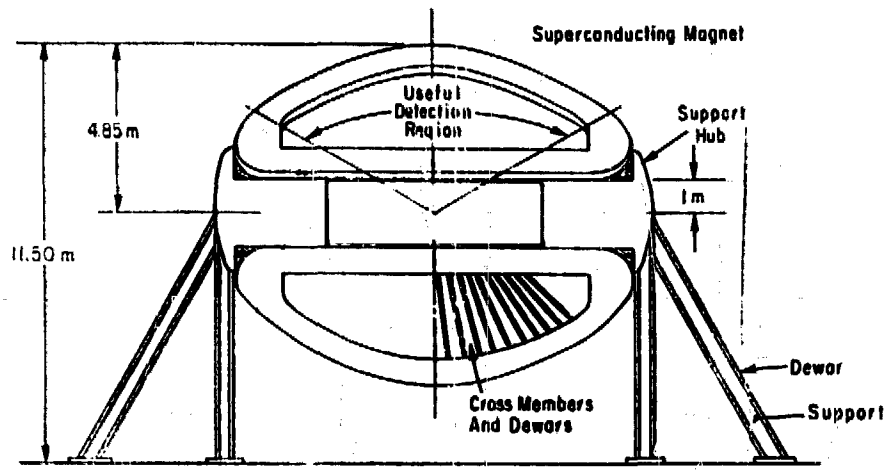
Superconducting Magnet
Useful
Detection
Region
Support
Hub
4.85 m
1 m
11.50 m
Dewar
Support
Cross Members
And Dewars
Section A-A

Fig. 2

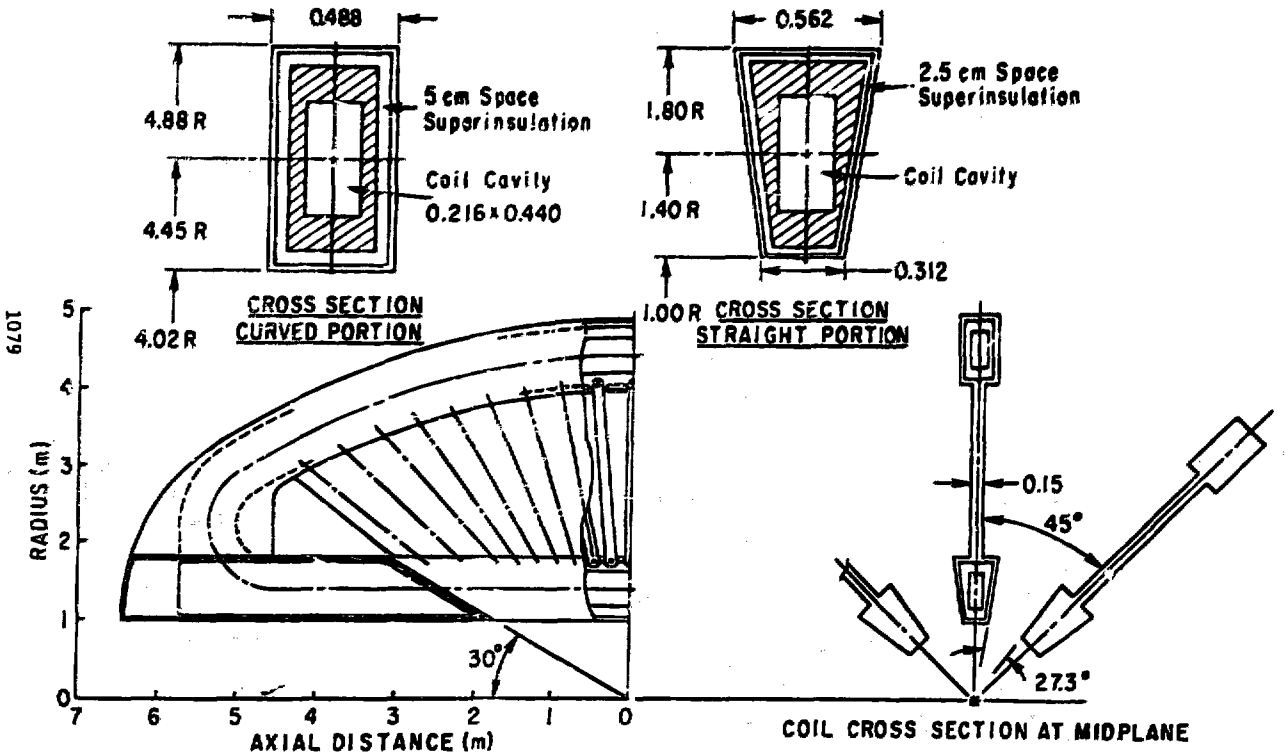

GENERAL ARRANGEMENT

Fig. 3

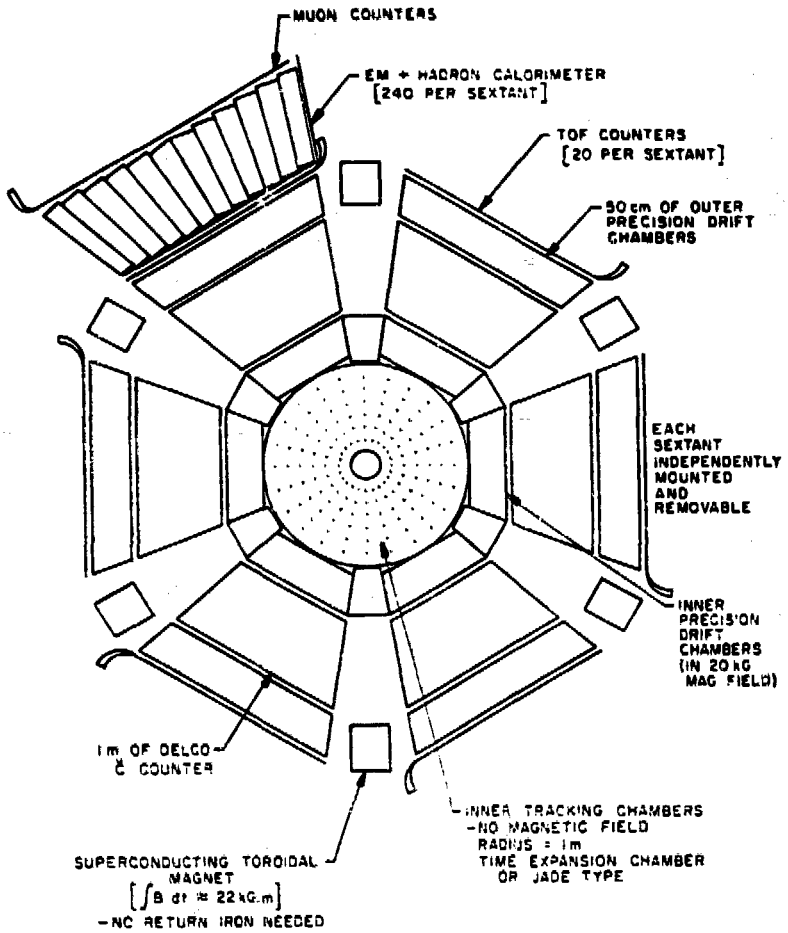
MUON COUNTERS
EM + HADRON CALORIMETER
[240 PER SEXTANT]
TOF COUNTERS
[20 PER SEXTANT]
50 cm OF OUTER
PRECISION DRIFT
CHAMBERS
EACH
SEXTANT
INDEPENDENTLY
MOUNTED
AND
REMOVABLE
INNER
PRECISION
DRIFT
CHAMBERS
(IN 20 kG
MAG FIELD)
1m OF DELCO
C COUNTER
INNER TRACKING CHAMBERS
-NO MAGNETIC FIELD
RADIUS = 1m
TIME EXPANSION CHAMBER
OR JADE TYPE
SUPERCONDUCTING TOROIDAL
MAGNET
[∫B dr ≈ 22 kG.m]
-NO RETURN IRON NEEDED

Fig. 4

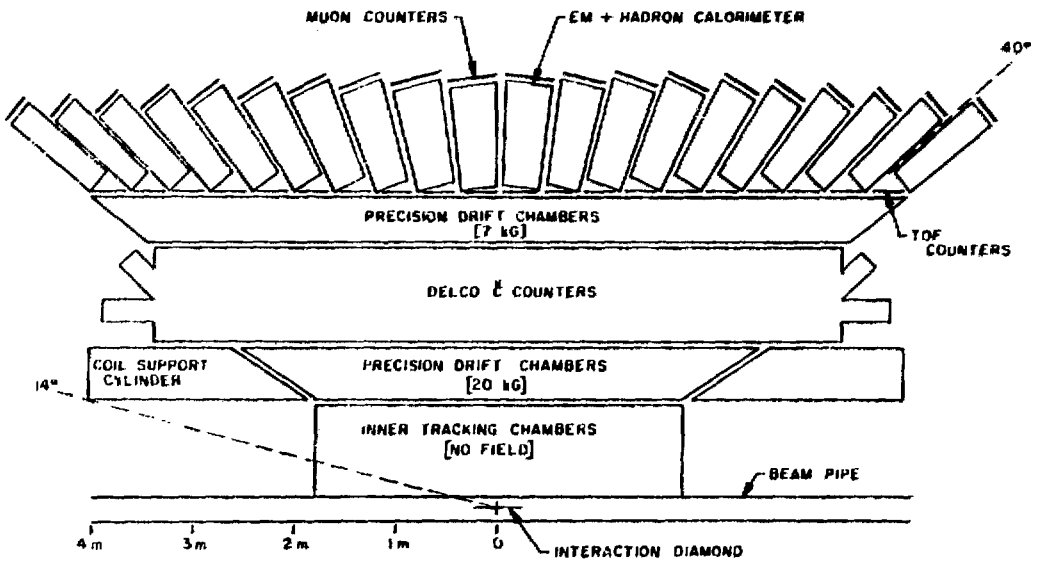
MUON COUNTERS
EM + HADRON CALORIMETER
40°
PRECISION DRIFT CHAMBERS
[7 kG]
TOF
COUNTERS
DELCO ℓ COUNTERS
COIL SUPPORT
CYLINDER
PRECISION DRIFT CHAMBERS
[20 kG]
14°
INNER TRACKING CHAMBERS
[NO FIELD]
BEAM PIPE
4 m
3 m
2 m
1 m
0
INTERACTION DIAMOND

Fig. 5

REPORT OF THE WORKING GROUP ON DATA TAKING WITH BUNCHED BEAMS

R. Blumenfeld, Johns Hopkins
R.C. Fernow, BNL
J.C. Herrera, BNL
S. Kabe, KEK
M. Marx, SUNY, Stony Brook
A. Nappi, PISA
M. Tannenbaum, BNL

The purpose of this working group was to consider the problems created for experimenters under the bunched beam running conditions of ISABELLE Phase I. We will attempt to give some indication of the nature of the problem, identify the kinds of experiments that will have difficulties, and then consider some of the possibilities for dealing with them.

I. ISABELLE PHASE I ENVIRONMENT

First, we present the "facts of life" for running at ISABELLE Phase I with bunched beams, and some of the implications of this environment.

We assume for purposes of calculation that each ring is filled with 57 AGS buckets whose centers are 224 nsec apart, and that the buckets are 3-dimensional gaussian charge distributions with vertical, horizontal and longitudinal rms distributions of 0.2 mm, 0.5 mm and 1400 mm respectively. The crossing angle is taken as 7 mrad. Presented in Figures 1 and 2 are the instantaneous luminosity as a function of time during the beam crossing and the longitudinal luminosity integrated over time. Both of these distributions are sharply peaked with rms widths of 3.4 nsec in time and 11 cm along the diamond. These widths reflect the assumption of gaussian shape and will probably vary depending on the actual charge distributions. They do, however, indicate that resolving multiple interactions in a single bunch-bunch crossing will be non-trivial.

We next consider the probability of getting two or more events in that single bunch-bunch crossing. This is simply calculated by Poisson statistics. The probability of having n interactions in a given bunch crossing when you expect an average μ is:

$$P_\mu(n) = \frac{\mu^n}{n!} e^{-\mu}$$

Presented in Table 1 as a function of the mean number of events per bunch collision are the average luminosity that correaponds for ISABELLE Phase I (50

mb assumed), the probability of no event occurring, and the effective average luminosity which is defined below.

We first say that the average number of "interesting" events per bunch collision is given by the physics cross-section for that process times the average luminosity per bunch crossing:

$$N_{int} = \sigma_{int} \mathcal{L}_{BC}$$

If, because of the nature of the experiment, we must now require that the interesting event was the only one in its bunch crossing, we must multiply N_{int} by probability that it was alone to get N_{clean}. This probability is given by

$$\frac{1 \cdot P(1)}{1 \cdot P(1) + 2 \cdot P(2) + 3 \cdot P(3) + \ldots}$$

or

$$\frac{P(1)}{\sum_{n=1}^{\infty} n\, P(n)} = \frac{\mu e^{-\mu}}{\mu} = e^{-\mu}$$

where P(n) is the Poisson probability of having n. Thus we have

$$N_{clean} = N_{int}\, e^{-\mu} = \sigma_{int} \mathcal{L}_{BC}\, e^{-\mu}$$

Thus we define the effective average luminosity as

$$\mathcal{L}_{eff} = \mathcal{L}_{av}\, e^{-\mu}$$

Note that $e^{-\mu}$ is numerically equal to P(o). We see from the table that the maximum effective luminosity occurs for $\mu = 1$, although the nominal ISABELLE Phase I effective luminosity is only some 30% lower. However, we also note that for $\mu = 1$, the cleanliness factor is only 0.37 so that the observed events will have to be multiplied by a factor of 2.7 to get the correct cross-section. Even for $\mu = .33$ there is still a 41% correction. This will make the measurement of absolute cross-sections very difficult in as much as μ is continuously changing during one fill of the machine. In addition, these considerations are in the absence of any trigger bias effects which may tend to enhance the number of multiple events. This is because the high peak luminosity forces extra events to be identically in time. With DC

beams (and the same average luminosity) the extra events will be more spread out in time so that scintillators can resolve them, drift chambers will have extra hits but not extra reconstructable tracks and energy dumped in calorimeters will be off-center from their gates and so lose some of their potential for making trouble. Clearly any step toward DC beams, such as increasing the number of bunches per beam while reducing the charge per bunch, would be a step in the right direction.

In an attempt to compare the effective luminosity for bunched beams with what could be attained in a continuous machine, we also quote in Table 1 the luminosity in an unbunched machine that would yield the same effective luminosity(*). This would depend on the resolving time of the experiment, for which we assume, as a benchmark figure, 100 μsec. We note that the highest luminosity attainable with the bunch scheme of Phase I could be attained in a continuous machine with a lower luminosity (~ factor 2) and therefore with a bigger "cleanliness factor", but with a larger beam current. We also note that the effective luminosity corresponding to ISABELLE Phase II (unbunched) could never be reached with the duty cycle of Phase I. A more detailed comparison of the effective luminosity in unbunched versus bunched beams is tried in Appendix III. Its conclusions are that, for a given average luminosity, the best effective luminosity corresponds to no bunching, independent of the detector resolution. If, on the other hand, the comparison is performed at a given average beam current, trying to account for the dependence of the luminosity on the bunch length, an optimal bunch length exists.

Even though the improvements in effective luminosity in the case of DC beams may not appear dramatic, we wish to stress that bunched beams are, in any case, potentially troublesome compared to DC beams.

II. EXPERIMENTAL SENSITIVITY TO MULTIPLE EVENTS

The amount of trouble caused by the occurrence of more than one event in a bunch-bunch collision is clearly dependent on the experiment. Since the vast majority of interactions are diffractive in nature we may expect a shower of hadrons along the beam direction to accompany a trigger event of any type.

(*) In a continuous machine $L_{eff} = Le^{-\sigma L}\, t_{res}$.

In general experiments with small angular acceptance away from the forward direction, single particle experiments at large transverse momentum, or experiments which are only interested in measuring single particle spectra will not be hurt by the presence of multiple events. Experiments with 4π acceptance or which attempt to measure very small angle scattering may have a serious problem unless they are able to know when a multiple event has occurred.

Multiple events do not appear to be a problem for most of the program with the M.I.T. spectrometer. This detector will be triggered on large p_t muons with an inner calorimeter to absorb hadrons. The major triggering difficulty may be accidentals between single muon events and hadron punch throughs faking a muon pair event. Multiple events could eliminate tracking information from the drift chambers since there would no longer be an unambiguous time origin to measure from.

The large dipole detector may be more susceptible. Here the emphasis is on hadronic jet production and the trigger involves the total energy deposited in some region of the calorimeter. The gate interval is 120 ns to allow sufficient time for waveshifting the scintillator light. A second event would effectively lower the trigger threshold. Since the p_t distribution is very steep this could lead to a substantial increase in the trigger rate. The angular distribution would also be shifted away from 90°.

III. REMOVAL OF MULTIPLE EVENTS

If ISABELLE operates in a bunched beam mode, there will be multiple proton-proton collisions in one beam crossing. For those experiments that are sensitive to multiple interactions the problem arises as what to do about them. Although it is possible in some cases to actually separate the particles coming from multiple events, it will be assumed that in general the goal will be to identify the presence of multiple events and then discard them all.

The ways that have been suggested of attacking the problem are the following:

1. Excellent time resolution. Because a second event is expected to be within a couple of nanoseconds of the main event, this is not considered to be of significant help.

2. Finding multiple vertices in the interaction diamond. This method

should work in removing multiple events, however, it has the disadvantage of being a relatively slow means of event rejection. In order words, all the tracks in an event must be reconstructed and the vertices found before the whole thing is thrown away. This can be a significant waste of computer time.

3. 4π hadron calorimetry. This method would throw away events with significantly more visible energy than that available in a single beam-beam interaction. This appears to be relatively fast, but needs detailed study to determine the sensitivity to loss of particles staying in the vacuum pipe.

4. Small hadron calorimeters. This method places relatively small hadron calorimeters on the downstream arms of experiments without general hadron calorimetery. The idea is to discard events with particles of more than the single beam energy near the vacuum pipe of either beam. This is similar to the previous method, but makes use of the fact that extra events will tend to be diffractive in nature, and therefore, of relatively small angle.

The last two methods also have the advantage in helping to remove background due to beam-gas or beam-wall interactions in coincidence with a beam-beam event, in as much as these will tend to have extra visible energy but only a single reconstructable vertex.

TABLE I

Average Luminosity (Bunch)	Average Current	Mean Number of Events Per Bunch Collision	Efficiency for Clean Event	Effective Luminosity for Clean Event	D.C. Luminosity for Same Effective Luminosity for Resolving Time τ_2 = 100 ns	Continuous Current
$L_{AV}(cm^{-2}s^{-1})$	$I_{AV}(A)$	μ	$P(0) = e^{-\mu}$	$L_{eff}=L_{AV}e^{-\mu}$	$L_{eff}=L_{DC}e^{-\sigma L_{DC}\tau_R}$	$I_{DC}(A)$
0.9×10^{31}	0.33	0.1	0.90	0.8×10^{31}	$L_{DC}=0.85\times10^{31}$	1.6
2.9×10^{31}	0.6	0.33	0.72	2.1×10^{31}	$L_{DC}=2.4\times10^{31}$	2.8
4.5×10^{31}	0.74	0.5	0.61	2.7×10^{31}	$L_{DC}=3.2\times10^{31}$	3.2
9×10^{31}	1	1	0.37	3.3×10^{31}	$L_{DC}=4\times10^{31}$	3.6
1.8×10^{32}	1.5	2	0.14	2.4×10^{31}	$L_{DC}=2.8\times10^{31}$	3.0
2.7×10^{32}	1.8	3	0.05	1.3×10^{31}	$L_{DC}=1.4\times10^{31}$	2.1
			DC BEAMS	7.4×10^{31}	$L_{DC}=2\times10^{32}$	8

FIGURE CAPTIONS

Figure 1. Instantaneous luminosity as a function of time.

Figure 2. Integrated luminosity along the length of the diamond.

Figure 3. Geometry of the beam crossing.

APPENDIX FIGURES

Figure A2. Probability for an event to come unaccompanied by any other event within the detector resolving time, plotted as a function of resolving time. The full line corresponds to the parameters of ISABELLE Phase I and C = 50 nb, the dashed line to a D.C. machine with the same luminosity as ISABELLE Phase I.

Figure A3. Effective luminosity plotted as a function of the bunch length, assuming the parameters of the ISABELLE "superbunch" option but letting the luminosity change inversely with the bunch length.

In the full curve a resolving time larger than the bunch length and smaller than the bunch spacing is assumed, in the dashed line the resolving time is fixed at 100 nsec.

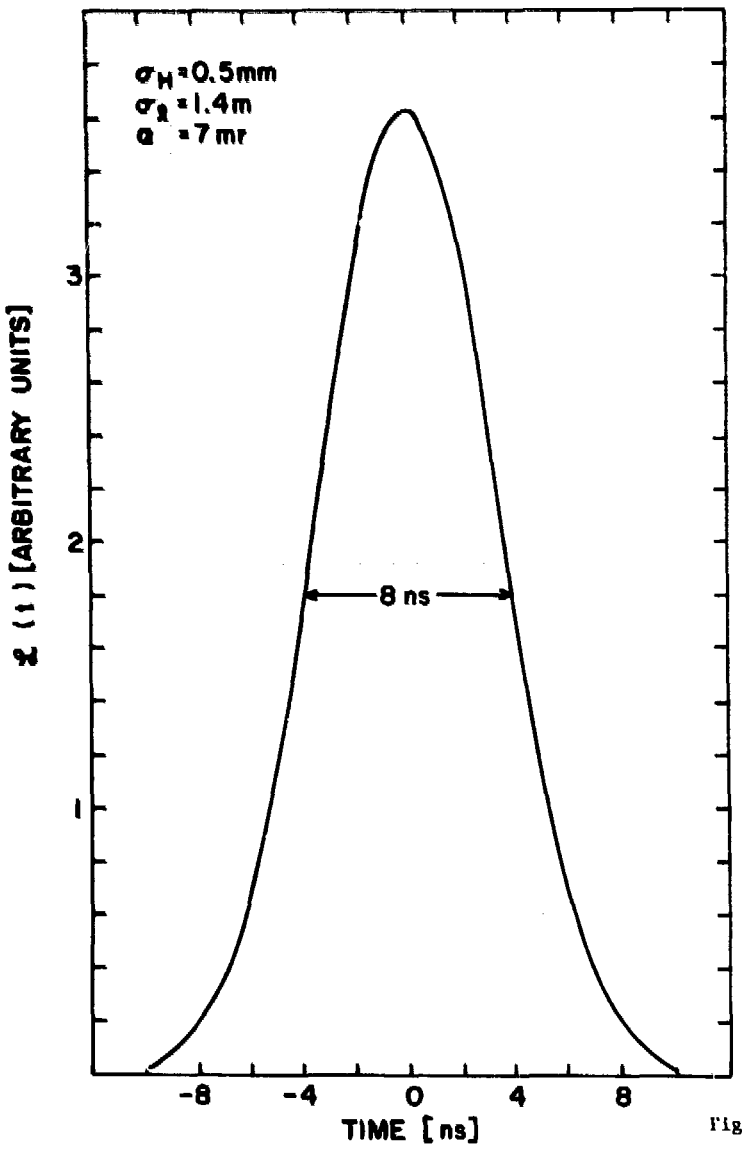
σ_H=0.5mm
σ_ℓ=1.4m
α =7 mr
8 ns
ℒ (t) [ARBITRARY UNITS]
TIME [ns]
-8
-4
0
4
8
1
2
3

Fig. 1

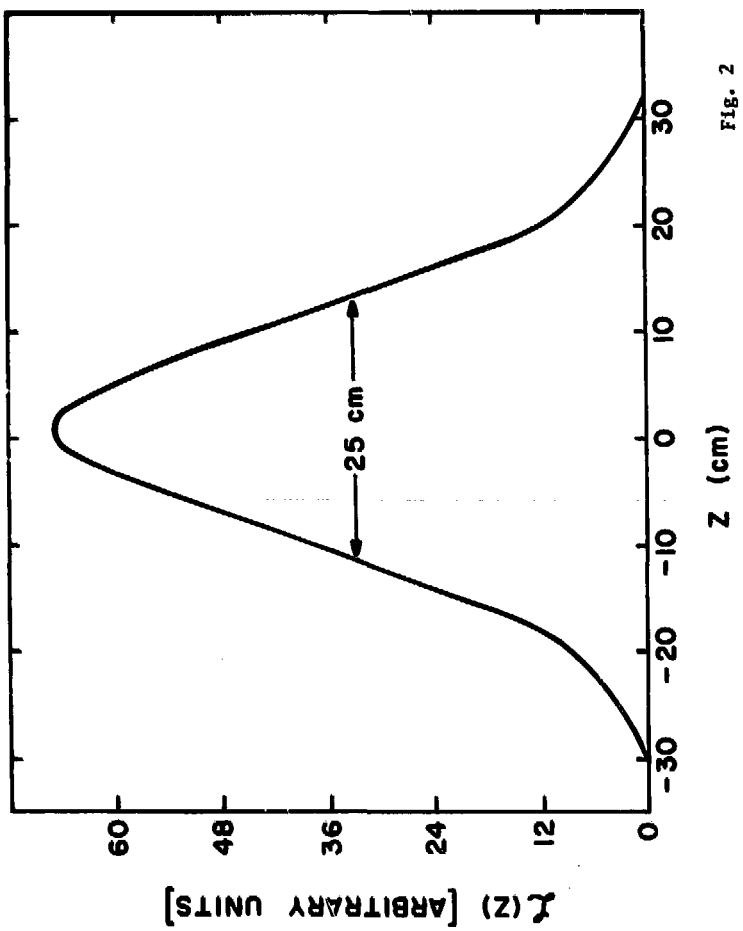
$\mathcal{L}(Z)$ [ARBITRARY UNITS]
0
12
24
36
48
60
-30
-20
-10
0
10
20
30
Z (cm)
25 cm

Fig. 2

APPENDIX I

LUMINOSITY FOR BUNCHED BEAMS

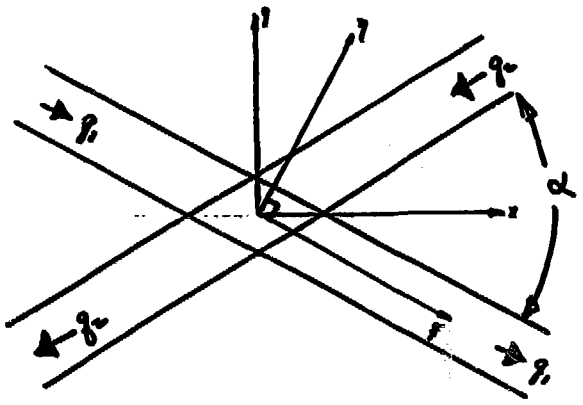

Fig. 3

$$L = 2c \cos^2 \frac{\alpha}{2} \int \rho_1 \rho_2 dV \qquad (1)$$

Figure 3. Geometry of the beam crossing

Gaussian in width, height, and along bunch (η, z, ξ)

Displacement of bunch peak from crossing $\delta_1 = ct$, $\delta_2 = c(t-t_o)$

Total charge per bunch (q_1, q_2)

Particle densities:

$$\rho_1(\eta,z,\xi) = \frac{q_1}{e\pi^{3/2} a_1 b_1 \ell_1} e^{-\frac{\eta^2}{a_1^2} - \frac{z^2}{b_1^2} - \frac{(\xi-\delta_1)^2}{\ell_1^2}}$$

$$\rho_2(\eta,z,\xi) = \frac{q_2}{e\pi^{3/2} a_2 b_2 \ell_2} e^{-\frac{(\eta \cos\alpha - \xi \sin\alpha)^2}{a_2^2} - \frac{z^2}{b_2^2} - \frac{(\xi \cos\alpha + \eta \sin\alpha + \delta_2)^2}{\ell_2^2}}$$

INSTANTANEOUS LUMINOSITY

$$L(t)=2c\cos^2\frac{\alpha}{2}\frac{q_1q_2}{e^2\pi^{3/2}}\frac{\exp-\left\{\frac{a_1^2(t[1+\cos\alpha]-t_o\cos\alpha)^2+a_2^2c^2(t[1+\cos\alpha]-t_o)\cos\alpha\,t_o^2c^2(t^2[t_1^2+t_2^2]-2t_1^2tt_o+t_1^2t_o^2)\sin^2\alpha}{(a_1^2+a_2^2)(t_1^2+t_2^2)+(a_1^2-t_1^2)(a_2^2-t_2^2)\sin^2\alpha}\right\}}{\sqrt{a_1^2+b_2^2}\sqrt{(a_1^2+a_2^2)(t_1^2+t_2^2)+(a_1^2-t_1^2)\sin^2\alpha}} \qquad (2)$$

rms sizes:

$$\left.\begin{aligned} a_1 &= \sqrt{2}\,\sigma_H(1)\\ b_1 &= \sqrt{2}\,\sigma_V(1)\\ \ell_1 &= \sqrt{2}\,\sigma_L(1)\end{aligned}\right\}\ \text{beam 1}$$

LUMINOSITY PER BUNCH COLLISION (cm^{-2})

$$\mathcal{L}_{(B.C.)}=\int_{-\infty}^{\infty}L(t)\,dt$$

$$\mathcal{L}_{(B.C.)}=\frac{q_1q_2}{e^2 2\pi}\frac{\cos\frac{\alpha}{2}}{\sqrt{\sigma_V^2(1)+\sigma_V^2(2)}}\frac{e^{-\frac{C\,t_o^2\sin^2(\alpha/2)}{2\left[(\sigma_N^2(1)+\sigma_N^2(2)\cos^2\frac{\alpha}{2}+(\sigma_2^2(1)+\sigma_L^2(2)\sin^2\frac{\alpha}{2}\right]}}}{\sqrt{\sigma_R^2(1)+\sigma_R^2(2)\cos^2\frac{\alpha}{2}+(\sigma_L^2(1)+\sigma_L^2(2)\sin^2\frac{\alpha}{2}}} \qquad (3)$$

AVERAGE LUMINOSITY (cm^{-2} sec^{-1})

Number of bunch collisions per second = $f_B = n_B f_o$

$$L = f_B \mathcal{L}_{(B.C.)} \qquad (4)$$

APPENDIX II

FORMAL DERIVATION OF EFFECTIVE LUMINOSITY

$\mathcal{L}_{BC}$ - luminosity per bunch collision

σ_i - cross section for interesting event

$\sigma_i \mathcal{L}_{BC} = \mu_i$ - mean number of interesting events/bunch collision

$P_i(1) = \mu_i e^{-\mu_i}$ - probability of getting one and only one interesting event per bunch collision

$$P_i(1) = \sigma_i \mathcal{L}_{BC} e^{-\sigma_i \mathcal{L}_{BC}}$$

$(\sigma_T - \sigma_i)\mathcal{L}_{BC}$ - mean number of noninteresting events per bunch collision

$P(0) = e^{-(\sigma_T - \sigma_i)\mathcal{L}_{BC}}$ - probability of getting zero noninteresting events per bunch collision

$$P(1) = P_i(1)\, P(0)$$

$P(1) = \sigma_i \mathcal{L}_{BC} e^{-\sigma_T \mathcal{L}_{BC}}$ - probability of gathering one interesting event per bunch collision and nothing else.

$n_B f_o$ - number of bunch collisions per second

$N_i = \sigma_i n_B f_o \mathcal{L}_{BC} e^{-\sigma_T \mathcal{L}_{BC}}$ - mean number of single interesting events per second

$N_i = \sigma_i L_{eff}$ - <u>by definition</u>

$$\therefore L_{eff} = n_B f_o \mathcal{L}_{BCe}^{-\sigma_T \mathcal{L}_{BC}}$$

Bunched

$L_{eff} = L_{AV} e^{-\sigma_T \mathcal{L}_{BC}}$ - effective average luminosity for bunch beams.

τ_R - resolving time

L_{AV} - average dc luminosity

$\mu_i = \sigma_i L_{AV} \tau_R$ - mean number of interesting events per resolving time.

$P_i(1) = \sigma_i L_{AV} \tau_R e^{-\sigma_i L_{AV} \tau_R}$ - probability of getting one interesting event per resolving time.

$P(0) = (\sigma_T - \sigma_i) L_{AV} \tau_R$ - mean number of noninteresting events per resolving time.

$P(0) = e^{-(\sigma_T - \sigma_i) L_{AV} \tau_R}$ - probability of getting zero noninteresting event per resolving time.

$$P(1) = P_i(1) P(0)$$

$P(1) = \sigma_i L_{AV} \tau_R e^{-\sigma_T L_{AV} \tau_R}$ - probability of getting one interesting event per resolving time and nothing else.

$\frac{1}{\tau_R}$ = number of resolving times per second.

$N_i = \frac{1}{\tau_R} P(1)$.

$N_i = \sigma_i L_{AV} e^{-\sigma_T L_{AV} \tau_R}$ - mean number of interesting events per second.

$N_i = \sigma_i L_{eff}^{D.C.}$ - by definition

$L_{eff}^{D.C.} = L_{AV} e^{-\sigma_T L_{AV} \tau_R}$ - effective average luminosity for continuous beams.

APPENDIX III

DEAD TIME FROM PILE-UP

We will work in the rather simplified assumptions that:

a. Multiple events occurring within the time resolution of the slowest detector can be identified as such;

b. events accompanied by other events within the time resolution are discarded.

We will try to evaluate how the efficiency connected with this loss of events depends on the bunch structure.

Let us assume that the interaction probability per unit time, as a function of time is constant during bunch crossing and zero otherwise (Figure 1.)

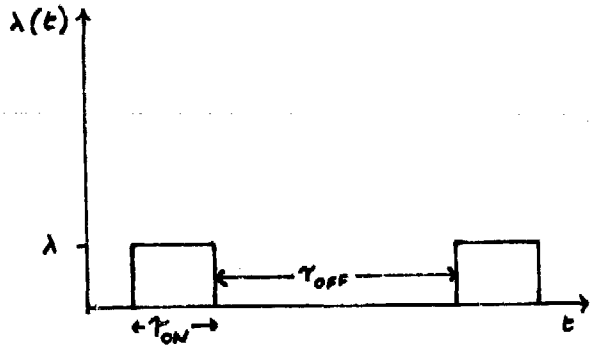

Fig. 1

where

$$\lambda = \sigma L_{peak}$$

$$\tau_{on} + \tau_{off} = \frac{1}{n_{Bf}}$$

$n_B \equiv$ number of bunches

$f \equiv$ revolution frequency

and τ_{on} is defined as

$$\tau_{on} = \frac{\text{Mean luminosity}}{\text{Peak luminosity}} (\tau_{on} + \tau_{off})$$

The efficiency that we are trying to evaluate is given by the probability that no event occurs in a time $t^{(*)}$ after the interesting event, call it P(t). Therefore

$P(t) \propto e^{-\lambda t}$ during the on intervals

$\propto$ const during the off intervals.

If we neglect the displacement of the event time within the bunch, this will lead to the solid line in Figure 2, where the parameters of ISABELLE phase I and a cross section of 50 mb are assumed. Also shown on the same figure is the efficiency for a continuous machine with the same average luminosity. Note that for $t_{res} = n\,(\tau_{on} + \tau_{off})$ the two curves touch.

The efficiency curve for any τ_{on} and τ_{off} can be drawn according to the following recipe:

a. Draw the efficiency curve for a continuous machine with the same average luminosity;

b. the efficiency for t_{res} between $\tau_{on} + n\,(\tau_{on} + \tau_{off})$ and $\tau_{off} + \tau_{on}$ $\tau_{on} + n\,(\tau_{on} + \tau_{off})$ is a constant corresponding to the efficiency for a continuous machine at $t_{res} = \tau_{on} + \tau_{off} + n\,(\tau_{on} + \tau_{off})$

c. the efficiency between $0 + n\,(\tau_{on} + \tau_{off})$ and $\tau_{on} + n\,(\tau_{on} + \tau_{off})$ is the line connecting the point at $t_{res} = \tau_{on} + N\,(\tau_{on} + \tau_{off})$ previously drawn with the point at $t_{res} = n\,(\tau_{on} + \tau_{off})$ of the continuous machine.

It is clear that, from this point of view, for any resolving time, a bunched operation is worse than continuous operation <u>at the same average luminosity</u>, except where $t_{res} = n\,(\tau_{on} + \tau_{off})$, in which case the efficiency is the same.

However a more realistic comparison of bunched versus unbunched operation should take into account the dependence of the luminosity on the bunch longitudinal size. We will assume that, for a given charge in the bunch, the luminosity per bunch crossing varies inversely with the longitudinal bunch width and hence with τ_{on}:

$$\lambda_{B.C.} = \frac{k}{\tau_{on}} \qquad (1)$$

(*)Equal to the resolving time of the slowest detector.

so that

$$\lambda_{AV} = \frac{\lambda_{B.C.}}{\tau_{on} + \tau_{off}} = \frac{k}{\tau_{on}} \frac{1}{\tau_{on} + \tau_{off}} \qquad (2)$$

$$\lambda_{Pk} = \frac{\lambda_{B.C.}}{\tau_{on}} = \frac{k}{\tau_{on}^2} \qquad (3)$$

For definiteness we shall assume the parameters of the ISABELLE "superbunch" option.

$n_B = 57$

$L_{mean} = 1.4 \times 10^{32}\ cm^{-2}\ sec^{-1}$ $\qquad$ $\tau_{on} + \tau_{off} = \frac{1}{f n_B} = 225$ nsec

$L_{peak} = 8 \times 10^{32}\ cm^{-2}\ sec^{-1}$ $\qquad$ $\tau_{on} = \frac{L_{mean}}{L_{peak}} (\tau_{on} + \tau_{off}) = 39.4$ nsec

The parameter k in formula (1-3) is given by

$$k = \lambda_{Pk} \tau_{on}^2 = \sigma L_{Pk} \tau_{on}^2 = 50 \times 10^{-27} \times 8 \times 10^{32} \times 15.52 \times 10^{-16}\ sec =$$

$$= 6.2 \times 10^{-8}\ sec = 62\ nsec.$$

We further assume (academically) that the bunch length can be varied at will and that the resolving time of the experiment is always between τ_{on} and $\tau_{on} + \tau_{off}$, and compute the effective luminosity as a function of τ_{on}, effective luminosity being defined as average luminosity multiplied by the efficiency computed above. We have

$$L_{eff} = L_{av} e^{-\lambda_{AV} (\tau_{on} + \tau_{off})} = \frac{k}{\sigma \tau_{on}} \frac{1}{\tau_{on} + \tau_{off}} e^{-\frac{k}{\tau_{on}}} =$$

$$= \frac{k}{\tau_{on} + \tau_{off}} \frac{1}{\sigma} \frac{1}{\tau_{on}} e^{-k/\tau_{on}}$$

$L_{eff}\ (\tau_{on})$ has a maximum for $\tau_{on} = k^{(*)}$. In fact

$$\frac{d}{d\tau}\ \frac{1}{\tau}\, e^{-k/\tau} = -\frac{1}{\tau^2}\, e^{-k/\tau} + \frac{1}{\tau}\,\frac{k}{\tau^2}\, e^{-k/\tau} = \frac{1}{\tau}\, e^{-k/\tau}\ \frac{k}{\tau^2} - \frac{1}{\tau}$$

The curve $L_{eff}\ (\tau_{on})$ is shown in Figure 3.

(*)For ISABELLE Phase I k = 3.5 nsec.

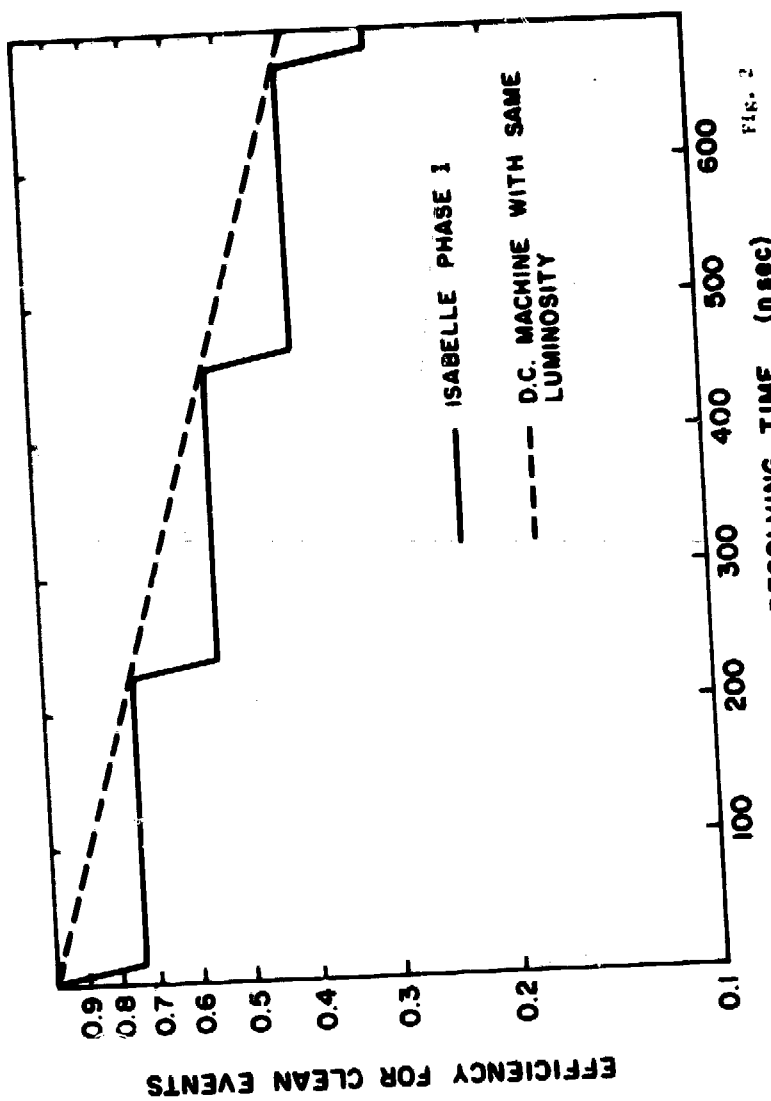
EFFICIENCY FOR CLEAN EVENTS
0.9
0.8
0.7
0.6
0.5
0.4
0.3
0.2
0.1
100
200
300
400
500
600
RESOLVING TIME (n sec)
ISABELLE PHASE 1
D.C. MACHINE WITH SAME LUMINOSITY

Fig. 2

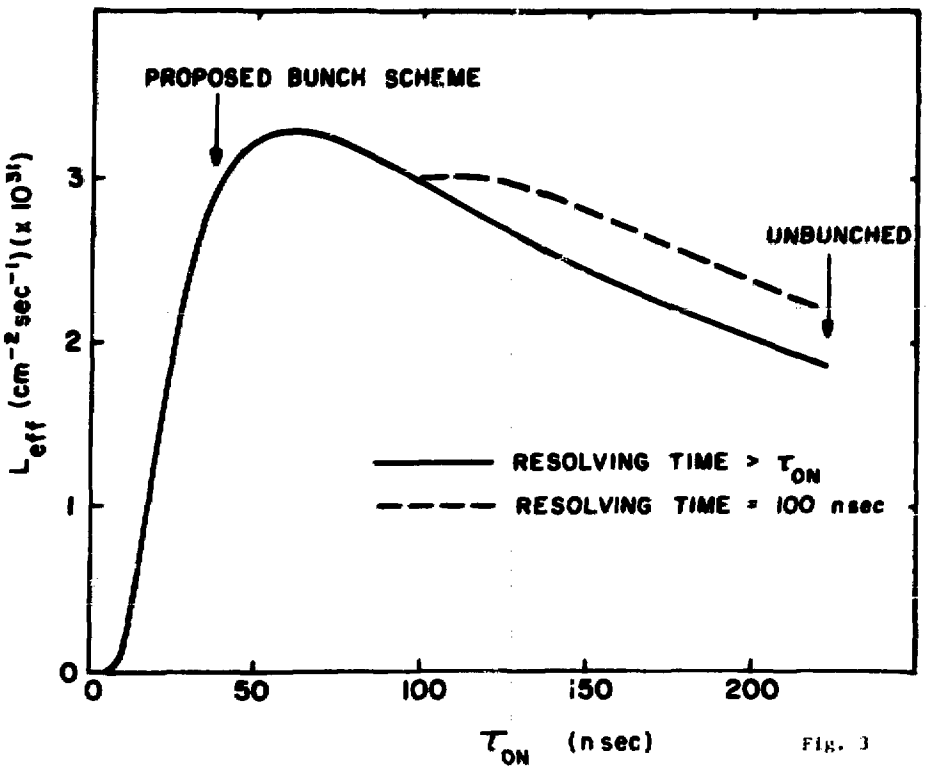
PROPOSED BUNCH SCHEME
UNBUNCHED
RESOLVING TIME > τ_{ON}
RESOLVING TIME = 100 nsec
L_{eff} ($cm^{-2}sec^{-1}$)(x 10^{31})
0
1
2
3
0
50
100
150
200
τ_{ON} (n sec)

Fig. 3

A COMMENT ON RESOLVING DOUBLE INTERACTIONS AT ISABELLE

R.A. Johnson - BNL

As smaller and smaller cross sections are investigated at Isabelle, backgrounds from double interactions become a larger and larger problem. There are two methods of distinguishing multiple interactions in a single bunch crossing: resolving the two interaction vertices and/or resolving the different interaction times. The purpose of this note is to show that the two methods provide orthogonal information and that both should be present in large Isabelle detectors.

The number of interactions at a given position in the interaction diamond at a given time is proportional to the product of the particle densities in each bunch at that point and time

$$N\ dx\ dt \propto P_{Beam\ 1}(x,t)\ P_{Beam\ 2}(x,t)\ dx\ dt$$

Taking $x = 0$ at the center of the interaction region, $t = 0$ at the center of the bunch crossing, and the two bunches to be mirror images of each other

$$P_{Beam\ 1}(x,t) = P(x + \beta ct) = P_{Beam\ 2}(-x, -t)$$

then

$$N\ dx\ dt \propto P(x + \beta ct)\ P(-x - \beta ct)\ dx\ dt \qquad (1)$$

For purposes of illustration take

$$P(x,0) = 1 \text{ for } |x| < a\ .$$

$$P(x,0) = 0 \text{ elsewhere.}$$

This is the boxcar bunch illustrated in Figure 1(a). The probability density is flat over the region outlined in Figure 1(b). When this probability distribution is put into equation (1) and integrated over either the position or the time, the resulting probability distribution is the triangular distribution given in Figure 1(c). Although the two distributions look the same, the peaks come from different events. Events in the peak of the time distribution come from the entire interaction region while events in the center of the interaction region come from all times during the bunch crossing. Therefore,

measurement of both gives two pieces of orthogonal information about the event. Real Isabelle bunches will be much more peaked than this simple example making the confusion in either variable, position or time, much greater. Therefore, measurement of both is much more important.

FIGURE CAPTION

Figure 1. a) Particle density for a boxcar bunch; b) area of constant interaction probability for crossing of boxcar bunches; and c) interaction probability distribution as a function of either vertex position or interaction time.

INTERACTION DENSITY
(c)
β_{c1} or x
1
0
PARTICLE DENSITY
(a)
β_{c1} →
(b)
x
1
0
x
1
0

Fig. 1

CAN PHASE I DETECTORS BE UPGRADED TO PHASE II

E. Beier, University of Pennsylvania
R. Johnson, BNL
H. Kasha, Yale University
W. Morse, BNL

The luminosity in phase I will be 2 x 10^{31}-10^{32} $cm^{-2}sec^{-1}$. The beam is bunched with the bunches separated by approximately 220ns. Generally there will be less than two events per beam crossing. It is appealing to optimize the detector to make use of this time separating events. For example the ion collection time of the central drift chamber could be equal to the bunch separation. This would give drift chamber cells of approximately 1.7 cm x 1.7 cm and approximately 13000 cells for the 50 layers of the cylindrical central detector suggested by the Dipole design. The drift chamber cell size could be larger since the time resolution is very good for the "double chamber" design, however this may preclude using the drift chamber information in one of the levels of triggering. For example if the fast trigger is a large deposit of energy in the central calorimeter, the drift chamber data would then be interrogated to make sure the interaction came from the interaction diamond.

Could a general purpose detector optimized for phase I be upgraded to phase II? First of all the new physics results of phase I will almost certainly suggest changes to be made in the detector. Indeed it may be decided to completely reconfigure the apparatus to build a new specific purpose detector. However if it is decided to upgrade a general purpose detector to phase II, some of the inner tracking drift chambers should probably be replaced with detectors which can be used in the trigger. One possibility is the scintillating optical fibers being developed by R. Strand and S. Borenstein. It may also be possible to upgrade the drift chamber electronics to accept multiple hits per cell. Then the central detector will probably be able to accept phase II luminosities. However the forward detectors will almost certainly be unable to accept the highest luminosities of phase II.

Appendix - Multiple Interaction in a Bunch Crossing

In our discussion, the probability of multiple interactions in a single bunch crossing came up repeatedly. The figure accompanying this appendix was useful for those discussion. In phase I ISABELLE with an average luminosity of 2×10^{31}, 4.2 mhz crossing rate, and a 60 mb cross section, we will expect .3 interactions/crossing. Under these conditions we should expect that 74% of the crossings will have no interactions and that (and this is what is frightening) of those that do have interactions 14% will have two interactions.

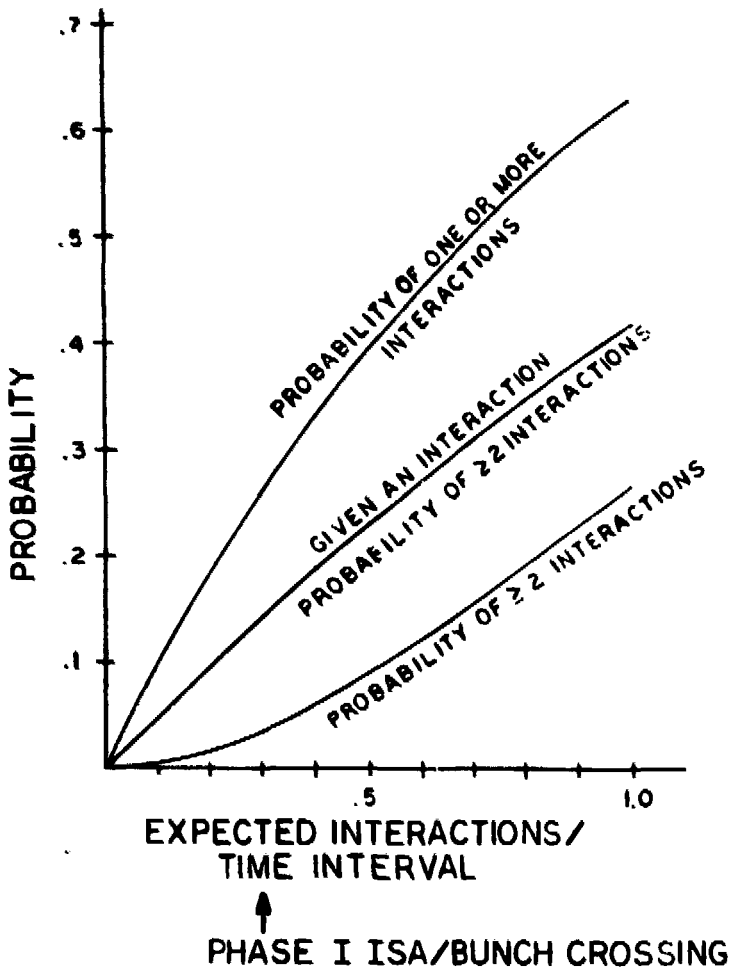
PROBABILITY
.7
.6
.5
.4
.3
.2
.1
PROBABILITY OF ONE OR MORE INTERACTIONS
GIVEN AN INTERACTION
PROBABILITY OF ≥2 INTERACTIONS
PROBABILITY OF ≥2 INTERACTIONS
.5
1.0
EXPECTED INTERACTIONS/
TIME INTERVAL
PHASE I ISA/BUNCH CROSSING

Fig. 1

SOME LESSONS LEARNED FROM A HIGH INTENSITY EXPERIMENT AT THE AGS

R.A. Johnson - BNL

In 1978 when the BNL-Princeton-Illinois collaboration first proposed an η_c search to the high energy advisory committee at Brookhaven, one of our hopes was that this experiment would provide an existence proof that photomultiplier calorimetry could operate in high rate environments. That proof was not as easy as we anticipated. In our first run in 1979 rate effects killed the experiment for approximately 95% of the time and at the same time killed any chance we had of measuring small cross sections. I foresee a similar danger for first round Isabelle experiments as they try to cope with high intensities. In this report I will discuss some of our problems and solutions that allowed us to do calorimetry in an environment of 10^7 particles/sec in our second run in 1980. These are presented in the spirit of a warning about areas of concern and not as the ideal solution for all experiments. There is no substitute for actual experience in a hostile environment.

Figure 1 is a schematic diagram of our apparatus. The aim of the experiment was to measure the exclusive reaction $\pi^- p \to \eta_c n$ by detecting the two photon decay of the η_c. The intensity of the pion beam was 10^7 particles/sec. The counters that encountered the high rates were the following: the beam counters (B_1, B_2, and A_2) which detected the incident beam particle and vetoed uninteracting particles, the segmented scintillator target counter which indicated where the interaction occurred, the downstream photon vetoes (V counters) and the inner edge of the detector. The beam counters and the segmented target counters were running at 10 MHz, the photon vetoes (which were not in the beam), up to 4 MHz and the inner edge of the detector, at approximately 1 MHz.

First and foremost, to do calorimetry at these rates you must have a photomultiplier base that can supply enough current to the dynodes. A.M. Halling, one of my collaborators at Princeton, designed for us the base shown in Figure 2. It is a transistor base designed for pulsed operation. Between spills it draws approximately 1/2 ma split equally between the transistors and the resistor string. During the spill the transistors carried up to 7 ma. In the laboratory, the base was tested up to 20 ma with

no adverse effects. With these currents going through the photomultiplier the gain was constantly changing (it normally doubled during the first day of running and then slowly decreased) making constant in situ calibration necessary. I would expect the same to be true at Isabelle.

Mike's base is by no means the first transistor base[1,2] nor the best for the Isabelle. It does have the novel feature of using Darlington pairs in the final stages to direct essentially all of the current into the photomultiplier. Bases with this feature would save a great deal of high voltage power at Isabelle.

The next problem in high rate calorimetry is transporting the signals to the electronics. When a nice crisp signal comes out of 100 m of RG58, it has developed a long tail which has amplitudes greater than 1% of the peak for a few hundred nanoseconds. For calorimetry where large dynamic ranges are important, this is a disaster. The signals must recover to below the range of interest before the next interaction occurs. One method to get around this problem is to use better cables. In our case we used RG8 which has approximately 1/5 the attenuation at 1 GHz that RG 58 has. With this addition we were able to use 100 nsec gates on our photon detector elements. RG8 cable is approximately 5 times as expensive as RG58 and, therefore, is not the solution for Isabelle. However, RG62, a 93 Ω cable, has the same attenuation properties as RG8 and is priced in the range of RG58. It has the additional advantage of giving twice the voltage for a given charge. Even though it would change the standard for the front ends of electronics, it is a good choice for the cable standard at Isabelle.

For counters running faster than 1 MHz, changing cables is not enough. The signals must be shaped at the photomultiplier to cancel the tail that develops in the cable. Unfortunately, a clip line is not enough because it does not provide protection against signals reflected from the electronics. Back termination is necessary. Figure 3 shows the shaping network that A.M. Halling and K.T. McDonald developed. The resistors R_1 and R_2 and the capacitor C_1 were chosen to match the photomultiplier signal to the cable. In a typical example, $R_1 = R_2 = 240\ \Omega$, $C_1 = 150$ pf, the attenuation through the shaper was 8 db and the time to return from the maximum pulse height to 1% of that pulse height was reduced from 400 nsec to 50 nsec.

In the η_c experiment, the most ambitious calorimetry was in determining the interaction vertex in the target. Here we were able, with the stiff base and pulse shaping, to integrate over a 40 nsec gate and get only a 10% distortion from pile up. This is to be compared with a 25% intrinsic width. In the photon vetoes we were able to identify photons in a dynamic range from 100 MeV to 10 GeV.

Finally, we found it essential to get timing information from each calorimeter element along with pulse height information. High rate environments imply high singles rates which, in turn, imply high noise levels. In addition, in a typical event we found remnants of previous events. Timing information was necessary for sorting the in-time hits from all other extraneous information.

What are my recommendations for high rate calorimetry at Isabelle? First and foremost, test the entire system from counters to readout electronics in an equivalent rate environment before final installation. We have shown that rate problems can be overcome, but the weak links must be identified. Second, plan to get adequate information such that the off-line analysis can sort out in-time and out-of-time elements. Environments of 10^7 particles/second are difficult, but if great care is taken, they are livable.

REFERENCES

1. C.R. Kerns, IEEE Trans. on Nucl. Sci., Vol. NS-24, No. 1, 1977.
2. H. Jung and M. Brüllmann, Nucl. Inst. and Meth. 65, 178 (1968).

FIGURE CAPTIONS

Figure 1. The apparatus used in the η_c search. B_1 and B_2 are beam counters. The A counters are charged particle anticounters. S and V are photon vetoes. The elements on the right comprise the photon detector (a lead scintillator sandwich followed by lead glass).

Figure 2. A transistor base developed by A.M. Halling.

Figure 3. A typical pulse shaper for photomultiplier signals into long cables.

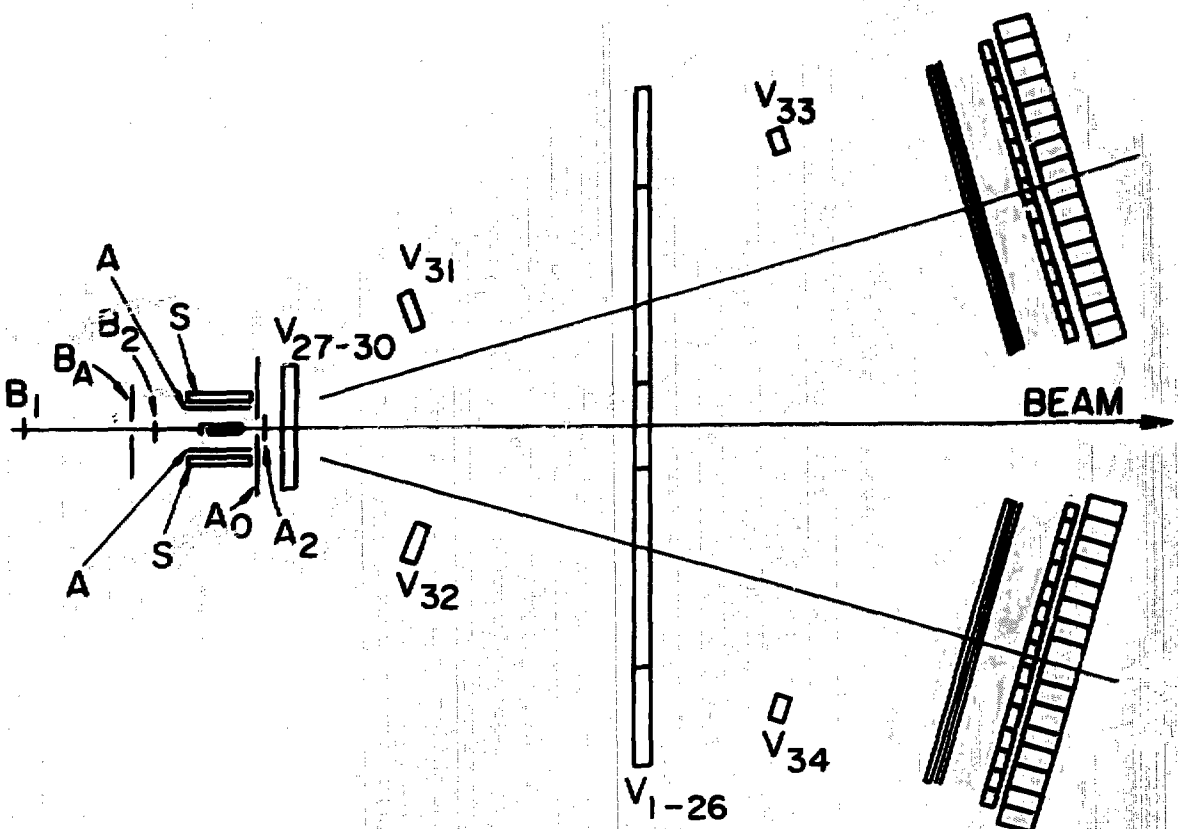

Fig. 1

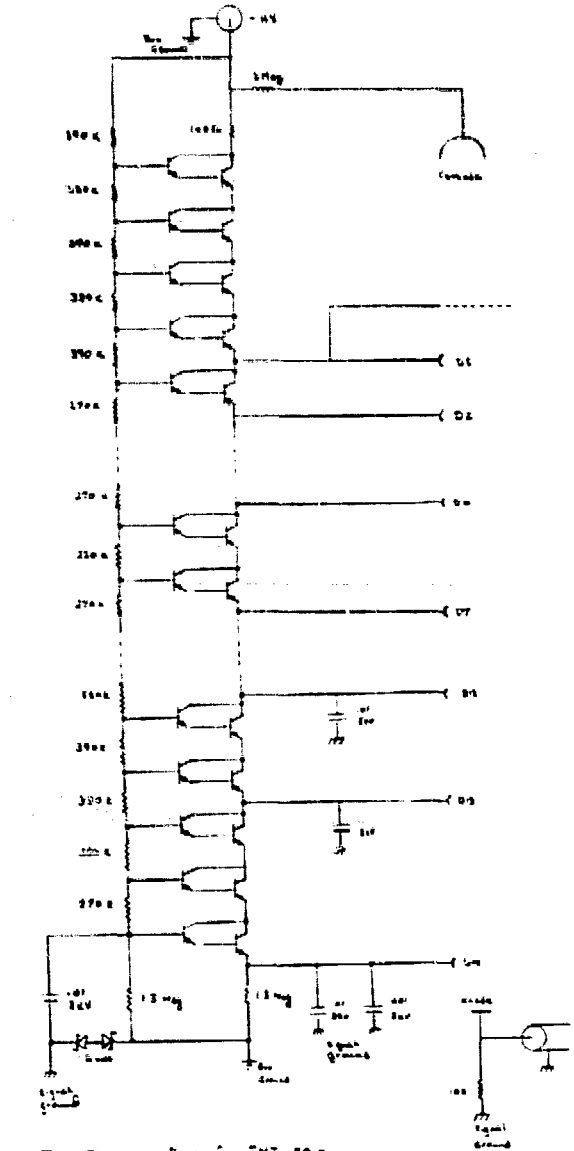

High Rate Transistor Base for EMI 9813
Transistors are Motorola 2N3640
10 Meg base biasing resistances

Fig. 2

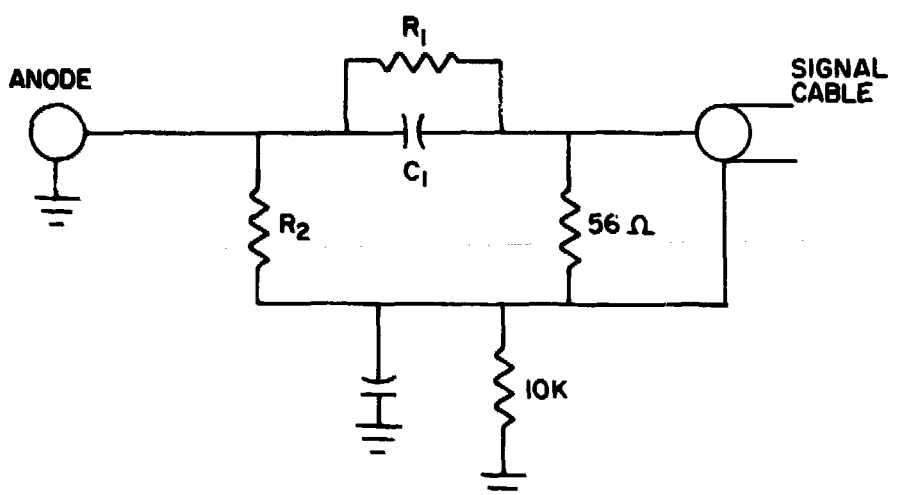

Fig. 3

MACHINE AVAILABILITY VS MAGNET RELIABILITY

G.E. Bozoki, BNL

I. INTRODUCTION

The purpose of the present note is to discuss briefly the availability of ISABELLE for physics experiments. Investigating problems like these is not too important at conventional accelerators, but its discussion in superconducting magnet environment seems to be inevitable. Nowadays, laboratories that are using superconducting magnets for accelerators are having to learn a completely new set of concepts and methods.

The reason for special attention is the special behavior of superconducting magnets. Namely, they become "normal" if small, heat generating disturbances upset their stabilities. The disturbances can have various origins: magnetic field jumps, mechanical motions of the conductor, eddy-current heating, coolant warm-up, radiation heating, etc. Such magnet failures, or quenches, can happen randomly because of the interplay of the above sources. Whenever they occur, they represent fatal failures for continuous machine availibility. In other words, the availability of a machine for physics experiments is inherently related to the reliability of its magnets for quenchless operation. Since there are now two types of magnets under consideration for ISABELLE purposes, it is interesting to compare the availabilities of the machines to be built from them.

II. AVAILABILITY CALCULATION

To treat the problem as simply as possible, we assume that, except for the superconducting magnets, all systems and subsystems of the machine (as well as the operators) perform without failure during unlimited operational time. To characterize the magnet failure-rate, in the present context the quench rate, we define a $\lambda(I,g,t,s)$ quench-rate function. It describes a

probability $\lambda(I,g,t,s)\Delta t$, that a magnet with a given geometry g, operating up to a maximum current I until a time t at a given location s of the machine, will have a quench during an operational time interval $(t, t+\Delta t)$. We assume furthermore, that for a "trained magnet" this probability is independent of time and location.* Since the magnets can recover relatively quickly ($\sim$1/4 hr) after a quench, the most often applied failure density distribution, the exponential one, can be taken as quench density distribution:

$$q(I,g,t) = \lambda(I,g)e^{-\lambda(I,g)t} \qquad (1)^{**}$$

The magnet reliability i.e., the probability, that a magnet does not quench during a time interval $[0,t]$, is defined as:

$$R(I,g,t) = \int_0^t q(I,g,\tau)d\tau = e^{-\lambda(I,g)t} \qquad (2)$$

For exponential quench density distribution, there is a simple relation between quench rate and mean quench-free time, MQFT(I,g):

$$MQFT(I,g) = \int_0^\infty tq(I,g,t)dt = \lambda^{-1}(I,g). \qquad (3)$$

From the point of view of the machine availability, the magnets are in "series" logical connection. It means, when for any reason, an individual magnet quenches, the physics experiments at the measuring regions are discontinued.

Assuming that the dipoles and quadrupoles for a given magnet design have the same quench rate function and they are able to initiate quenches independently, the probability that an ISABELLE ring will operate continuously during a time interval of $[0,t]$, is:

$$A^{RING}(I,g,t) = \prod_{i=1}^{N} R_i(I,g,t) = e^{-N\lambda(I,g)t} \qquad (4)$$

---

*Additional variables like coolant parameters etc., are neglected for the present considerations.

**The exponential quench density distribution implies that the magnet "does not age". Presently, there is practically no data available about the useful lifetime of superconducting magnets.

where N is the number of magnets in a ring. Consequently, the probability that the whole machine will be available for physics measurements in a [0,t] interval, uninterrupted by quenches, is

$$A^{MACHINE}(I,g,t) = \prod_{k=1}^{2} A_k(I,g,t) = e^{-M\lambda(I,g,t)} \qquad (5)$$

where M = 2N is the total number of magnets in the machine.

The mean quench-free time for the whole machine is:

$$MQFT^{M}(I,g) = \frac{1}{M}\, MQFT(I,g) = \frac{1}{M\lambda(I,g)} \,. \qquad (6)$$

If ISABELLE is built from FNAL magnets the total number of magnets (dipoles and quads) is $M^{FNAL} = 984$ (tentative value, see[1]). If BNL magnets are used[2], $M^{BNL} = 1138$. (Superconducting correction magnets, spoodles, are considered to be failsafe, because they are operated at relatively low currents.)

Figures 1 and 2 show the availability of a ring and the whole machine, respectively, as a function of quench-free operation time for various MQFT(I,g) values. The broken and solid lines indicate respectively, the standard ISA-design and the new version. The ring data may represent the availability of the ep-option.[3] The quench rate functions for the FNAL and BNL magnets are different, but taking them tacitly to be equal [i.e. MQFT(I,g = FNAL) = MQFT(I,g = BNL) = MQFT(I)], the graphs directly provide the magnet number dependency.

III. DISCUSSION AND CONCLUSIONS

Comparing the graphs on Fig. 1 with those of Fig. 2, it is clear that the availability of a ring for physics measurements is trivially superior than that of the whole machine. In other words the "ep-option" certainly has definite advantages from the point of view of availability.

For the whole machine, the availability is not entirely favorable. Consider e.g. our chances to run an experiment during a decent 10 hour period uninterrupted by quenches. As Fig. 2 shows, the requirement to have a 90% chance of success is that the average quench-free time for a magnet should be

around 12 years! To achieve such a situation the magnets should be extremely stable and the machine operating conditions should be absolutely safe. Thus, it can happen, that the present maximum operating current of the magnets (I), the temperature of the coolant should be reduced and/or conventional magnets have to be used at critical beam loss locations of the machine. This conclusion is valid for any machine version.

The slightly smaller availability of the standard ISA-design compared to that of the new version reflects the fact that in that design there are more superconducting magnets ("potential time-bombs").

One would get a marked difference, if one could demonstrate, that MQFT(I,R = FNAL) >> MQFT(I,R = BNL). At present, the validity of this condition, can only be guessed at: the better quench-characteristics of the FNAL magnets compared to those of BNL-ones and the bunched beam operation which results in less beam spill, speak for the validity of the condition. However, the smaller aperture of the FNAL magnets speaks against it. As usual, more study is needed to clarify the situation.

The obvious advantage of the new version, is that fewer magnets result in a shorter total time for recycling the machine after quenches. The number of spare magnets is also smaller. In other words, the maintainability of the machine looks better (at least from the point of view of quenches). This condition, results in a larger total useful operating time.

The result of the present preliminary and oversimplified availability estimate illustrates the necessity and usefulness of more detailed operational analyses of machines with superconducting magnets.

REFERENCES

1. M. Cornacchia, E. Courant, K. Johnsen; ISABELLE with FNAL Magnets; Proc. of ISABELLE Summer Workshop; July 20-31, 1981.
2. ISABELLE: A 400 GeV x 400 GeV P-P Colliding Beam Facility, BNL 50718, 1978.
3. W. Lee and R.R. Wilson: The ep Option, Proc. of ISABELLE Summer Workshop, July 20-31, 1981.

FIGURE CAPTIONS

Fig. 1. Availability of an ISA-ring vs quench-free operation time. Parameter: average quench-free time for a magnet, MQFT(I). Solid lines: FNAL magnets. Broken lines: BNL-magnets.

Fig. 2. Availability of the whole machine vs quench-free operation time. Parameter: average quench-free time for a magnet, MQFT(I). Solid lines: FNAL magnets. Broken lines: BNL-magnets.

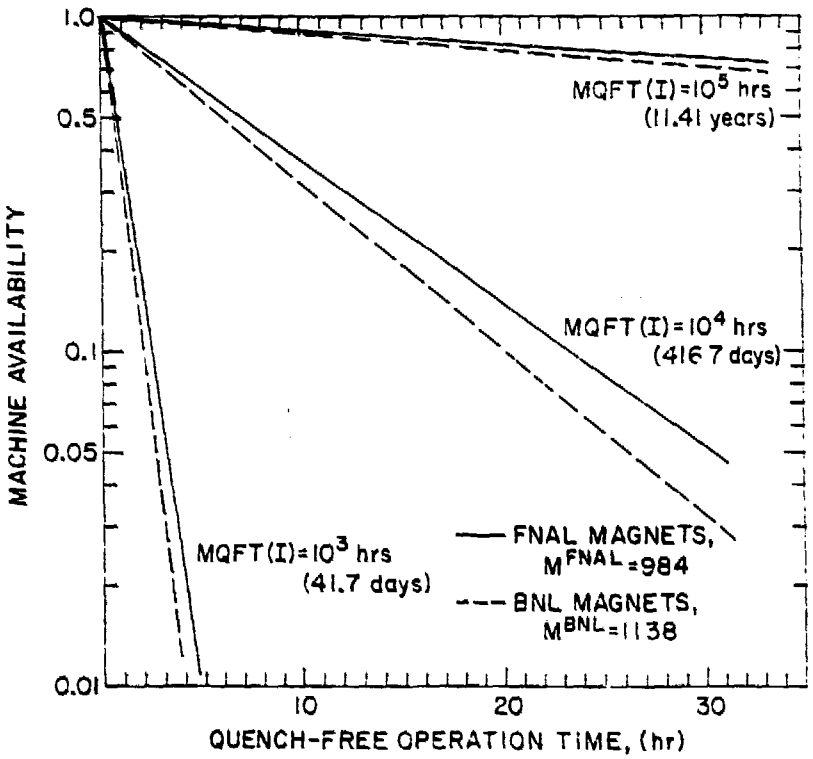
1.0
0.5
0.1
0.05
0.01
MACHINE AVAILABILITY
MQFT(I)=10^5 hrs
(11.41 years)
MQFT(I)=10^4 hrs
(416.7 days)
MQFT(I)=10^3 hrs
(41.7 days)
FNAL MAGNETS,
M^FNAL=984
BNL MAGNETS,
M^BNL=1138
10
20
30
QUENCH-FREE OPERATION TIME, (hr)

Fig. 1

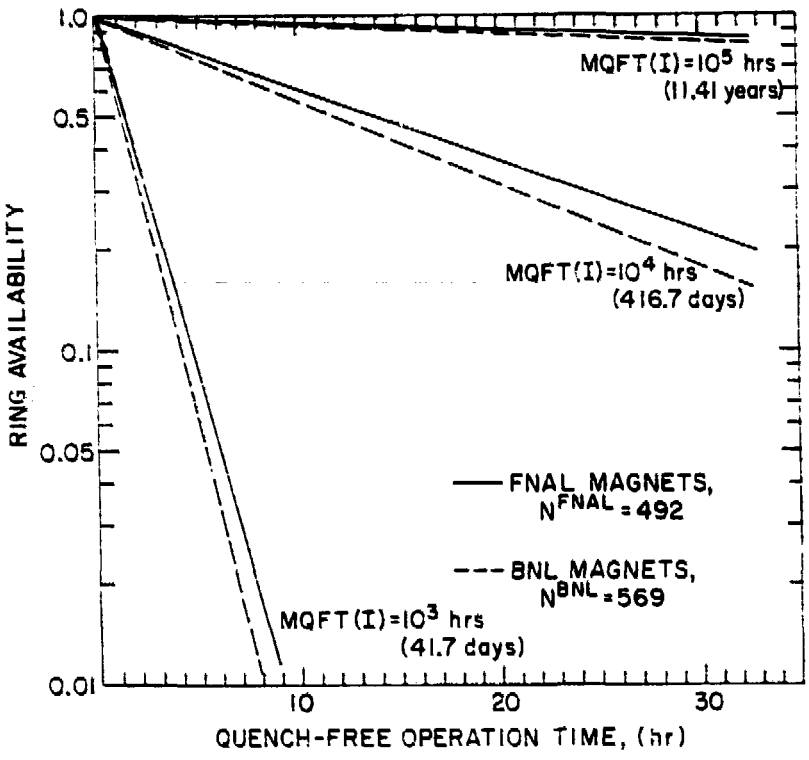
1.0
0.5
0.1
0.05
0.01
RING AVAILABILITY
MQFT(I)=10^5 hrs
(11.41 years)
MQFT(I)=10^4 hrs
(416.7 days)
FNAL MAGNETS,
N^FNAL=492
BNL MAGNETS,
N^BNL=569
MQFT(I)=10^3 hrs
(41.7 days)
10
20
30
QUENCH-FREE OPERATION TIME, (hr)

Fig. 2

CALIBRATION AND MONITORING OF LARGE DETECTORS

E. Beier, Univ. of Penn.
V. Hagopian, Fla. St. Univ.
H. Jensen, FNAL
J. Marraffino, Vanderbilt Univ.
H. Sticker, Rockerfeller Univ.
K. Sumorok, Univ. of Birmingham
D.H. White, BNL

I. INTRODUCTION

The general problem of calibration and monitoring of an experimental setup has become increasingly more important and troublesome as detectors have become larger and more complex. Nonetheless, the physical quantities actually measured by any detector are simple, namely a charge or pulse height, a time interval or a position. It may be necessary to obtain either absolute or relative measurements of these quantities. The problems associated with that fall under the heading of calibration. It is also necessary to measure these quantities over an extended time with a presumption of both long term and short term stability. The establishment of this knowledge falls under the heading of monitoring. These two functions obviously overlap, but the distinction between them can be kept clear at least in an operational sense.

Generally, absolute calibrations are needed only once, or perhaps twice for cross checking purposes. Such absolute measurements include for example, magnetic field mapping, detector alignment or survey, energy deposition in calorimeters or shower detectors and linearity and resolution of various detector elements. On the other hand relative calibrations should be made periodically, with a frequency determined by the stability of both the detector and the calibration device itself. In this context, it is important to recognize that the calibration device (whatever it may be) is not perfect, but often suffers at least as many deficiencies as the detector itself. Some specific examples of such deficiencies are mentioned below. The advantages of relative calibrations are that they need not be made "in place", are comparatively quickly performed, may be integrated with the online monitoring system and are easily related to some small number of absolute standards.

Ideally, monitoring standards should be significantly more stable than the system being monitored over the necessary time period. This need is far

more easily stated than achieved, but we emphasize its importance. It is only one of many tactical choices to be made early in the design of any large detector. Another such tactical decision concerns just what to monitor. It is possible to monitor each individual element, selected individual elements, logically related groups of elements or global properties of the entire detector. This choice is closely related to the relative calibration procedures adopted. That is, the monitoring and calibration functions overlap most markedly here, provided the monitoring standard has been calibrated. We note that the data itself can be used, as opposed to some other special input to the system, depending on the sensitivity required, and on the data rate. In either case, monitoring needs to be continuous and at a rate commensurate with a short monitoring time.

If we regard the calibration of a detector as the evaluation of a set of coefficients which transform measured parameters such as pulse heights, wire numbers and drift times into physical variables such as energy and position, it is convenient to assume that there are two levels of analysis with different accuracy requirements. For the sake of argument, we take the first level of precision to be 10% and the second to be 1%. Then, the first level is appropriate for use as part of an event trigger or to evaluate gross features of a large event sample. The transformation of measured parameters into physical variables at this level of analysis should be linear, e.g.

$$\text{Energy} = \text{slope} \times (\text{ADC reading} - \text{Pedestal})$$

$$\text{Time} = \text{slope} \times (\text{TDC reading} - t_0)$$

For ease of data handling, we further require that the second order corrections needed to achieve the 1% precision be factorizable from those used for the first level. This means that the second order coefficients should be slowly varying functions of the environmental factors such as temperature, pressure, voltage, gas mixture, etc. These coefficients should probably be obtained before and/or after a data taking period in dedicated runs in order to obtain the required statistics, since they are, by construction, small and slowly varying. In contrast, the slopes used in the first level transformations are strong functions of the environmental factors. For example, the slope might be a photomultiplier tube gain, or the amplification on a wire in a gas detector, both of which have exponential dependence on

applied voltage. Because of the complexity and large number of channels in most new detectors, it would seem inadvisable to leave these strong dependences free, but rather to use some sort of feedback loop system to keep these parameters under control.

II. EXAMPLES OF LARGE DETECTOR SYSTEMS

In order to understand some of the problems encountered by large detector systems the calibration systems employed by three different experiments are described. a) The UA1 experiment at the SPS $p\bar{p}$ collider,[1] b) E734, ν_e, ν_μ elastic scattering experiment at BNL, c) The lead glass wall experiment at SLAC.[2] Table 1 summarizes the systems employed by UA1 and Table 2 those used in the BNL ν experiment.

III. CALIBRATION SYSTEMS USED BY UA1

III.1 Electromagnetic Calorimeters

Electromagnetic calorimeters are all Pb-scintillator sandwiches with 4 depth samplings with total depths between 26 and 30 radiation lengths. They all employ BBQ readout. The gains of tubes are monitored with a dye laser system, the light being transmitted to the light guide just before the PMT by an optical fiber. The laser light intensity is monitored by special PMTs which also view Am^{241} doped NaI crystals. The gains are set by measuring the calorimeter response to either

a. 4.2 Curie Co^{60} source

b. 18 MeV Betatron Bremsstrahlung Beam

which has been cross calibrated with calorimeter modules in an e^- test beam. The fine detailed response over the calorimeter is mapped using the Co^{60} source.

The 4.2 Curie Co^{60} source calibration requires the measurement of a dc current in the PMT which needs an additional "picoamplifier", which in turn needs cross calibration using an LED system.

The betatron calibration is done in single shots though there are problems to reduce noise pickup from the betatron.

III.2 Hadron Calorimeter

The magnet return yoke and the endcap down to 5° are constructed out of 5 cm iron plates interspaced with 1 cm thick plexipop scintillator read out with BBQ waveshifter bars. The energy response is defined in terms of the pulse height of a 5 GeV muon per scintillator plate. The number of equivalent particles per GeV (nep) was found to be 11.2 from measurements in a test beam. The gains of the PMTs were set by measuring the response of the calorimeter to cosmic ray muons, and adjusting the high voltage to give the appropriate pulse height. This gain was then recorded by inserting Ru^{106} β sources into the calorimeter and then measuring the dc current in the PMT chain with a digital voltmeter (DVM). Knowing the half life of these sources it was then possible to reset the gain at a later date by reinsertion of the same sources. At this point onwards the laser monitoring system was used to track the gain of the PMTs. This monitoring system consists of two uv nitrogen lasers (λ = 337 nm) each illuminating ~ 3500 (25m, 200 μm diameter) quartz fibers by means of a large diffuser box. The light is therefore transmitted to the center of every sheet of scintillator where it is absorbed within 1-2 mm of the surface and remitted isotropically as scintillation light. As there are between 6 and 12 sheets of scintillator viewed by each PMT, there is a corresponding number of light fibers and hence a sufficient redundancy in the system to allow detailed cross checks between the fibers. The absolute light level from the laser is monitored by special PMTs which also view Am^{241} doped NaI crystals. The major advantage of exciting the scintillator directly is to check the whole light collection chain. The gain of the PMTs may be monitored independent of the laser intensity by measuring the standard deviation σ of the laser distribution. We then have

$$\#\text{ of photoelectrons} = (\text{peak}/\sigma)^2$$

$$\text{gain} = (\text{peak}/\#\text{of photoelectrons}) = (\sigma^2/\text{peak})$$

III.3 Central Detector

The central detector used in UA1 is a large cylindrical drift chamber

with image readout.[3] This means that every 32 ns of drift time the total charge and the current division is digitized with flash ADC's. Typical pulses will be 3-4 bins wide and the time pick off of the leading edge is done by interpolating to 3 bits precision within the first bin, i.e., 4 ns or ~ 200 μ in space. For calibration of the flash ADCs, charge is injected at the input of each preamplifier at the end of each wire. In the charge and time digitization modules (CTDs) the amplifier gains are equalized and the offsets and levels adjusted until the correct responses for given inputs are obtained.

In addition to the calibration of the electronics two schemes for producing neutral straight tracks in the drift chambers are to be used. The first will utilize a collimated x-ray beam generated from an x-ray flash tube pulsed at 150 kV.[4] Two types of processes occur. Firstly, there is approximately 60% photo-ionization which occurs mostly from the Argon K-shell where the ejected electron carries essentially the initial x-ray energy and is long ranged. Secondly, the remaining 40% Compton scatter which gives rise to ejected electrons of low energies and a deflected beam. As these electrons provide the best localization, a necessary cut is that there should be only one interaction per drift cell in the chamber. It is therefore necessary to accumulate many x-ray shots to define a beam profile. The big advantage is that it is possible to link chambers and drift cells over tens of meters.

A second scheme to produce neutral straight tracks is to use a uv N_2 laser. This method has been discussed by several authors[5] and is currently being developed for use in UA1. A laser beam is fired through quartz windows into the chamber gas volume and can produce tracks of up to several hundred ion pairs per cm. The ionization mechanism would appear to be by double photon absorption via a metastable state which saturates during the initial passage of the beam giving rise to a linear dependence of the pulse height with laser intensity. An extremely low level of impurity is all that is required to explain the observed phenomena. Tracks with a localization precision of 50 μ should be obtained in a magnetic field. By splitting the beam with a prism or a diffraction grating it should be possible to measure the drift velocity and drift angle in a magnetic field and also study two track resolutions.[6]

The monitoring of the gas gain is important as the amplification process has an exponential dependence on the temperature, pressure, applied voltages, gas mixture, etc. While the monitoring of each of these should be done, a global monitoring using a small chamber and a source provides an easier way to apply correction for the dE/dx measurement. This can also be important if time slewing is a serious problem. For UA1, as with other experiments, two small chambers are used, one on the input to the large chambers and one on the output. Fe^{55} sources are painted on the walls of the chamber and the pulse height obtained is an absolute monitor of the gain.

IV. THE BNL NEUTRINO EXPERIMENT

This experiment consists of a series of identical modules which are alternately liquid scintillator calorimeters and proportional drift tube planes (PDT). The liquid scintillator planes have 32 PMT outputs and energy and event time is measured for each tube. A PDT plane measures x and y separately with 108 outputs which measure time (position) and pulse height. This experimental system is repeated 118 times with independent devices for photon detection and a muon spectrometer based on the same detecting elements. This detector is conceptually simple, although the 20K analog elements is a large number, and it may be instructive to consider the calibration problems that occur even in a geometrically straightforward device.

IV.1 Calorimeter

A calorimeter wall consists of sixteen liquid scintillator cells 4m long and 25 x 7.5 cm in cross section. Each end is viewed by a PMT and each end may be illuminated by a light flasher through a permanently fixed flexible light pipe. There are concerns that the liquid scintillator may deteriorate, the PMT gain may change and the electronics may drift in gain. The time constants for each channel must be established and monitored to nanosecond accuracy. The electronic check is conducted by using a pulser at each amplifier input, although this is principally used for diagnostic purposes.

The principal calibrating source is the light flasher. The light source is a spark gap which is viewed also by a vacuum photo diode to monitor the fluctuating amplitude and time of the light pulse after an initiating signal. These fluctuations, although removable by the vacuum photo diode signal are certainly inconvenient. The linearity and pedestal of the system are determined by inserting calibrated filters in front of the light source and fitting the output data points. Overall calibration, i.e. the transformation of ADC counts into MeV of deposited energy is accomplished by reconstructing cosmic ray muons in the detector. We will discuss this further below.

IV.2 PDTs

The proportional drift tubes are operated in a linear gain region so that an extensive range of dE/dx is measurable. At the front end of each electronic channel a pulser variable in amplitude and time under digital control is used for calibration and diagnosis of the data acquisition system. The pedestals and gain of each channel are determined from this pulser. The drift time vs position for the appropriate gas mixture has been measured in a test beam, although establishing this function from cosmic ray muons is feasible. The gas is circulated rapidly enough that the gas mixture is expected to be uniform throughout the apparatus. The gas gain of each module is measured in the production process and controlled to 10% which is adequate for this experiment.

These PDT planes are 4m x 4m and we expect a position resolution of 0.7 mm. The purely geometrical limits on position determination are controlled as follows. The wire spacing and the orthogonality of the x and y measuring planes are controlled in manufacture to 250 μ and 3 μrad respectively. Four fiducial points are external to the chamber area and are used to check the internal dimensions. After installation, the external survey is conducted also using these fiducial points. The surveys, both internal and external, are overconstrained reducing the probability of error remaining.

After individual elements and modules are calibrated the entire detector is connected using cosmic ray muons. These particles are used to make the

connection between the constant which describes the gain of each channel and deposited energy in MeV. The attenuation length of the scintillator cells is also derived. Relative timing is also verified with muons.

V. LEAD GLASS WALL SLAC

This experiment consisted of approximately 250 lead glass blocks in which the energy measurement was maintained to ± 1%. This was achieved by ensuring the following

A. The high voltage of the PMTs was kept to ± 1 volt by using stable power supplies and a monitoring computer reading the potential across each power supply.

B. The equipment temperature was stabilized to within ± 1°C. A variation of the energy readout of about 1% per °C was observed.

The system was monitored by a system of fiber optics and a single LED. Each lead glass block had one 1mm diameter fiber attached via a 45° prism glued to the block. The LED was monitored by three monitor PMTs which also viewed Am^{241} doped NaI crystals. Gain changes of 1% were monitored.

The absolute calibration was achieved by exposure of each lead glass blocks to an electron beam.

In addition a few of the blocks also viewed Am^{241} doped NaI crystals. The energy resolution of the system obtained was

$$\frac{\sigma}{E} = \left(0.84 + \frac{4.8}{\sqrt{E}}\right)\% \text{ with E in GeV.}$$

Two electron beam calibrations 4 months apart showed that each block was stable within 1% to 2%.

VI. GENERAL RECOMMENDATIONS

VI.1 Calorimeters

It will not always be possible in these large detectors to put every calorimeter stack into a particle beam of the type or energy range required. For calibration other methods of energy deposition will be required. For

electromagnetic calorimeters γ sources appear to be the most promising, c.f. PAI who use a 4.2 Curie Co^{60} source or an 18 MeV betatron. For hadronic calorimeters muons provide a calibration for most devices. Uranium calorimeters have the advantage that they are self calibrating. If radioactive sources could be built into other types of calorimeters without presenting a safety hazard, or a degeneration of performance, then this would be a considerable advantage in calibration.

The monitoring of PMTs used in many of these calorimeters generally rely on light flasher systems.

1. LEDs can give satisfactory results if all the environmental factors are carefully monitored.

2. Laser systems may be divided into two categories.

a. Systems which monitor the PMT gains by shipping blue or visible light to the PMTs

b. Systems which attempt to excite the scintillating medium. These systems have the ability of monitoring the whole light collection chain.

The difficult part with both the above systems is the monitoring of the light intensity. Three methods are considered.

a. PMT monitors viewing the light source and also an absolute light source such as an Am^{241} doped NaI crystal.

b. Drifts inherent in PMT tubes can be eliminated by using unity gain systems such as vacuum photodiodes. Their limitation is in the temperature stabilization required.

c. Silicon p-i-n diodes are, in principle, more stable than vacuum photodiodes. The photoconversion and charge collection take place within the silicon and have a weak temperature dependence.

VI.2 Drift Chambers

The accurate reconstruction of charged tracks in drift chambers requires a complete knowledge of the following:

a. Accurate survey measurements of the sense wire locations

b. Accurate measurements of the drift properties of the gas employed.

c. The magnitude, shape and direction of the applied electric and magnetic fields. Uniform fields make analysis much easier.

A. Much of the internal survey information is generated through the application of quality control in mechanical assembly. The need for well-defined electric fields often imposes greater internal accuracy than is required by the survey. However, the transfer of the coordinate system from the sense wires to an external fiducial often causes difficulty. In large scale apparatus a change of 10°C can cause noticeable change in dimension but these concerns are generally superceded by concerns for gas gain and other stabilities. The use of standard survey methods becomes so onerous in detectors with a high density of disparate elements that mechanical assembly methods become desirable as locating definitions rather than subsequent optical methods. The use of lasers and x-rays to produce linear ionizing deposits supplements these traditional methods by producing a verification but the need for careful attention to assembly is still required.

B. In systems that require measurements of dE/dx in the gas, the need for gain stability overrides the drift velocity problem. Many groups measure the drift velocity using a test beam and then devote attention to quality control of the gas. The choice of operating voltage is used to minimize the variation of distance with drift time.

C. A compromise between a straightforward mechanical arrangement of electrodes and a simple algorithm connecting the arrival time of the electrons and distance of track requires a compromise between the two considerations. Many schemes have been tried without a single scheme achieving pre-eminence. The structure of UA1 is affected by the bunch structure of the beam and the extended drift space depends on the uniform electric and magnetic fields. The neutrino experiment has a simple mechanical structure, but is limited in spatial accuracy and has no significant magnetic field. R807 at the CERN ISR has a complex electrode structure in which a nonuniform magnetic field is used, and in spite of considerable calculational effort it appears that a price is paid in ultimate spatial resolution from the nonuniform magnetic field and from the features which resolve the left-right ambiguity.

REFERENCES

1. A. Astbury et al., a 4π Solid Angle Detector for the SPS Used as a Proton-Antiproton Collider at a Center of Mass Energy of 540 GeV, CERN/SPSC/78-06/SPSC/p.92
2. R. Madaras et al., Nucl. Instrum. and Methods 160, 263 (1979); R. Diamond et al., Lead Glass Wall Trigger for the SLAC 40 Inch Bubble Chamber, Florida State University Preprint (1981); J. Brau et al., Lead Glass Column, A Large Shower Detector at the SLAC Hybrid Facility, SLAC Preprint 2773 (1981).
3. M. Barranco-Luque et al., Nuclear Instrum. and Methods 176 (1980) p.175; M. Calvetti et al., Nuclear Instrum. and Methods 176 (1980) p.255.
4. M. Rijssenbeek, Status of the X-Ray Calibration System UA1 Technical Note 80/55.
5. H. Aderhub et al., Nuclear Instrum. and Methods (1979) p.581; J. Bourotte and B. Sadoulet, Nuclear Instrum. and Methods 173 (1980) p.463; H.J. Hilke, Nuclear Instrum. and Methods 174 (1980) p.145.
6. K. Sumorok, Monitoring of Central Detector Parameters Determining Track Reconstruction and Pulse Heights, UA1 Technical Note 81/25

Table 1
Summary of Calibration Systems Used by UA1

	Apparatus	Method	Calibration
1	Electromagnetic Calorimeters	Co^{60} Source (4.2 Curies) response compared with e^- test beams	PMT tube gains
2	Electromagnetic Calorimeters	Betatron bremsstrahlung spectrum 18 MeV maximum (as above)	PMT tube gains
3	Electromagnetic Calorimeters	N_2 dye laser and optical fibers to each PM light guide	Monitor PM tube gains when calibrated
4	Hadronic calorimeter down to 5°	N_2 laser with quartz fibers exciting the plexipop scintillator	Measure and monitor PMT tube gains
5	Central detector	Injection of charge at the input of each preamplifier	Calibrate flash ADCs for dE/dx and current division
6	Track chambers throughout experiment	X-ray beams from 160 KV pulsed flash tube	Spatial linking of drift cells and chamber over tens of meters
7	Central detector	Collimated uv laser beams fired through quartz windows	Linking of drift cells and measurement of V_D and θ_D
8	Track Chambers	Fe^{55} sources monitored in two small chambers on the input and output of the gas supply	Absolute monitoring of gas amplification gain

Table II
Calibration Systems in Neutrino Experiment

Apparatus	Method	Calibration
Particle Calorimeter (liquid scintillator PMT)	Pulser at input of electronics	Channel and system diagnosis
	Light flasher, spark gap with vacuum photodiode and light pipes	Pedestal and gain of total channel. Mean t_o of calorimeter wall
	Cosmic ray muons	Absolute energy scale in MeV
Proportional Drift Tubes	Pulser at input to electronics	Channel and system diagnosis
		Pedestal and gain, relative t_o
	Cosmic ray muons	Absolute dE/dx scale, verify geometry from residuals
	Survey internal and external to plane in experiment	Absolute location of wires, defining geometry
	Relative gas gain monitored separately	Diagnosis

AUTHOR INDEX

Volume 1 contains pages 1-402 + 8
Volume 2 contains pages 403-804
Volume 3 contains pages 805-1134
Volume 4 contains pages 1135-1488

U.S. GOVERNMENT PRINTING OFFICE: 714-037#16